

Comparison of Iron and Tungsten Absorber Structures for an Analog Hadron Calorimeter

Dissertation

zur Erlangung des Doktorgrades
des Department Physik
der Universität Hamburg

vorgelegt von

CLEMENS GÜNTER

aus Hamburg

Hamburg
2014

Gutachter der Dissertation: Prof. Dr. Erika Garutti
Dr. Felix Sefkow

Gutachter der Disputation: Prof. Dr. Eckhard Elsen
Prof. Dr. Johannes Haller

Datum der Disputation: 04.02.2015

Vorsitzender des Prüfungsausschusses: Dr. Georg Steinbrück

Vorsitzende des Promotionsausschusses: Prof. Dr. Daniela Pfannkuche

Dekan der MIN-Fakultät: Prof. Dr. Heinrich Graener

Leiter des Department Physik: Prof. Dr. Peter Hauschildt

Abstract

Future electron-positron-collider experiments will require unprecedented jet-energy resolution to complete their physics programs. This can only be achieved with novel approaches to calorimetry. One of these novel approaches is the Particle Flow Algorithm, which uses the best suited sub-detector to measure the energy of the particles produced by the electron-positron collision. The CALICE Collaboration evaluates different read-out technologies for Particle Flow Calorimeters. This thesis describes the comparison of two different absorber materials, iron and tungsten, for the CALICE Analog Hadron Calorimeter. It is described how testbeam data, that has been recorded in the range from 2 GeV to 10 GeV with the Analog Hadron Calorimeter is calibrated, and how samples are selected containing showers from just one particle type. The data is then compared to simulations and the remaining disagreement between data and simulation is discussed. The validated simulations are then used to decompose the showers into different fractions. These fractions are compared for the two absorber materials to understand the impact of the absorber material choice on the calorimeter performance.

Zusammenfassung

Zukünftige Elektron-Positron-Collider Experimente erfordern eine nie zuvor erreichte Jet-Energie Auflösung für ihre Physik Programme. Dies kann nur mit neuen Ansätzen für die Kalorimeter erreicht werden. Einer dieser neuen Ansätze ist der Particle Flow Algorithmus, der den jeweils bestgeeigneten Unterdetektor nutzt, um die Energie von den in der Elektron-Positron Kollision produzierten Teilchen zu messen. Die CALICE Kollaboration evaluiert verschiedene Auslesetechnologien für Particle Flow Kalorimeter. Diese Arbeit beschreibt, den Vergleich von zwei verschiedenen Absorbermaterialien, Eisen und Wolfram, für das CALICE Analoge Hadron Kalorimeter. Es wird beschrieben, wie Test-beamdaten, die bei Energien von 2 GeV bis 10 GeV mit dem Analogen Hadron Kalorimeter aufgenommen wurden, kalibriert werden und wie Datensätze, die nur Schauer von einer Teilchenart enthalten, selektiert werden. Die Daten werden mit Simulationen verglichen und die verbleibenden Unterschiede zwischen Daten und Simulationen werden diskutiert. Die validierten Simulationen werden dann genutzt um die Schauer in verschiedene Komponenten zu zerlegen. Diese Komponenten werden zwischen den beiden Absorbermaterialien verglichen, um zu verstehen, welchen Einfluss die Wahl des Absorbermaterials auf die Kalorimeterleistung hat.

CONTENTS

Introduction	9
1 Future Linear Collider Experiments	13
1.1 The International Linear Collider	14
1.2 The Compact Linear Collider	15
1.3 Detectors	17
2 Particle Showers and Calorimetry	21
2.1 Electromagnetic Cascades	21
2.2 Charged heavy Particles traversing Matter	24
2.3 Hadron Showers	26
2.4 Calorimeters	27
2.5 Particle Flow concept	29
3 The CALICE AHCAL Physics Prototype	33
3.1 The Active Layers	33
3.2 Read-out Electronics	34
3.2.1 Silicon Photomultiplier	37
3.2.2 Very-frontend Electronics	38
3.2.3 The Data Acquisition	39
3.2.4 The Calibration and Monitoring Boards	39
3.3 The Absorber	41
4 The Testbeam Setups	43
4.1 The FNAL 2008 and 2009 Testbeams	43
4.2 The CERN 2010 Testbeam	44

5 Physics Simulation	49
5.1 Hadron Cascade Simulation	49
5.1.1 Cascade Models	50
5.1.2 String Parton Models	51
5.1.3 Chiral Invariant Phase-space Model	52
5.1.4 LEP	53
5.2 GEANT4 Pre-compound and De-excitation Models	53
5.3 Physics Lists	54
5.4 Precision Neutron Calculations	54
6 Detector Calibration and Characterization	55
6.1 Offline Calibration of the Temperature Sensors	56
6.2 Pedestal Subtraction	56
6.3 Gain Calibration	58
6.4 Inter-Calibration	58
6.5 Saturation Correction	60
6.6 Cell Equalization with Muons	63
6.7 Identification of Bad Channels	68
6.8 Noise after Calibration	69
6.9 Inter-tile Crosstalk	70
7 Event Selection	77
7.1 Beam Events	77
7.2 Events with LED flashes	78
7.3 Empty Events	78
7.4 Upstream Interactions	79
7.5 Additional Algorithms	79
7.6 Particle Identification	80
7.7 Multi-Particle Events	83
7.8 Selection of the Tungsten Data Samples	85
7.9 Selection of the Iron Data Samples	86
8 Detector Simulation	91
8.1 Simulation of the Physics Processes	91
8.2 Simulation of the Detector Response	92
8.3 Beam Profiles	94
8.4 Simulation of the Detector Noise	95
8.5 Hadron Shower Decomposition	97

9 Validation of the Simulation	101
9.1 Detector Validation with Muons	101
9.2 Detector Validation with Electron Showers	104
9.3 Validation of the Pion Shower Simulation	110
10 Comparison	121
10.1 The First Hadronic Interaction and the Electromagnetic Fraction	121
10.2 Comparison of Shower Profiles	124
10.3 Time evolution of the Shower	125
10.4 Comparison of the Shower Components for different Physics Lists	128
10.5 Comparison of the Calorimeters	131
11 Summary and Outlook	139
A Data Sets and Calibration	145
B Event Selection Parameters	147
C Simulation Parameters	153
D Additional Results	155
Bibliography	163
Acknowledgements	169

INTRODUCTION

Roughly a century after the beginning of modern physics with the discovery of quantum theory and relativity, particle physics has formed a theoretical model, which can explain the overwhelming majority of all measurement results: the Standard Model of particle physics [1, 2, 3]. The Standard Model describes the constituents of matter as twelve fermions, six quarks, which form the hadrons, and six leptons. For each of the particles, there is an anti-particle, having the same mass, but opposite quantum numbers. Hadrons like protons, neutrons, pions and others are formed from either combinations of three quarks or quark-anti-quark pairs. The twelve fermions are further divided into three generations, where the properties of the generations are similar, except for the mass. The gauge bosons of the strong and electroweak interaction mediate the forces between these fermions. All these particles have been observed in experiments. Not included in the standard model of particle physics is the gravitational force, which can typically be neglected in the quantum regime due to the small involved masses.

The standard model particles have zero mass in this theory, which obviously contradicts the measured masses of these particles. This shortcoming of the standard model can be overcome by breaking of the electroweak symmetry, which can be done by adding a new scalar field, the Higgs field. The Higgs-field generates the particle masses by its couplings to the standard model particles [4, 5, 6]. By the introduction of this field a new particle, the Higgs particle is also introduced. The search for this particle lasted for several decades without success and the possible mass of the Higgs, which is not fixed by theory, was already severely constrained by earlier experiments at the LEP and Tevatron colliders (and other experiments). However, a new boson with a mass around 125 GeV, that is so far consistent with this Standard Model Higgs, has recently been discovered by both the ATLAS and CMS collaborations at the Large Hadron Collider at CERN [7, 8].

Despite the enormous success of the standard model to explain experimental results, it is clear, that the standard model has limitations. At the moment it is not clear, how neutrino masses, that are measured in neutrino oscillation experiments can be consistent with the experimental absence of right-handed neutrinos (and left handed anti-neutrinos). Another example that can point at physics beyond the standard model are the measured rotational spectra of galaxies and larger cosmological objects, that are not in agreement with the visible matter distributions of these objects. The additional matter needed to explain the rotational spectra is called dark matter, since it underlies gravity but is not visible in the electromagnetic spectrum. A possible candidate for this matter is one or more unknown particles.

The capability of the Large Hadron Collider for precision measurements of this new particle, and others that might be found in the future, is limited, since the collisions parameters are not well defined due to the compound nature of the collided protons and the strong backgrounds from proton collisions. Therefore, a next generation of electron-positron colliders, which have the capability for precision measurements of the Higgs particle, has been developed and proposed. Besides precision measurements of the Higgs-like particle, these physics programs also foresee searches for physics beyond the Standard Model, precision measurements of the top quark mass and many others [9, 10].

Besides new accelerator technology that has to be developed for the next generation colliders to achieve the desired collision energy and collision rate, the precision requirements set also unprecedented performance goals for the detectors that record the collisions. The required jet-energy resolution of a few percent at around 100 GeV (to distinguish W-boson and Z-boson decays), can only be achieved with new detector concepts as the Particle Flow concept. This concept aims to measure each collision product with the sub-detectors which offers the best measurement. It is used in a simple version, called energy flow, at the CMS detector. It requires optimized sub-detectors as tracking systems and calorimeters, with high granularity to disentangle the signals from the individual collision products. The CALICE collaboration has developed several high-granular calorimeter prototypes with different read-out technologies: Digital, semi-digital and analog high-granular sandwich calorimeters. However, the choice of the absorber material is not fixed by the read-out technology. Therefore this thesis will investigate the differences of hadron showers in an analogue high-granular sandwich calorimeter equipped with either tungsten or iron absorber plates.

Chapter 1 will give a brief introduction to the two most advanced next generation electron-positron collider projects and their detectors.

Chapter 2 will introduce the physics of particle showers and the underlying mechanisms for different particles. This chapter will also give a summary on the most important principles in calorimetry and an introduction into the principles of Particle Flow calorimetry, which is the design paradigm of the detectors for the next generation of electron-positron linear colliders.

Chapter 3 is a description of the Analog Hadron Calorimeter used to record the data which is evaluated in this thesis. It is one of the CALICE collaboration prototype calorimeters and constructed as a sandwich calorimeter with layers of scintillator tiles which are read out by Silicon Photomultipliers. These active layers are interleaved with metal absorber layers which induce particle showers. The active layers are described in detail as well as the two different absorber materials used and the read-out electronics needed to record shower data.

The shower data which is evaluated in this thesis has been recorded during two different testbeam campaign at the Fermi National Accelerator Laboratory and at CERN. The two experimental setups are described in chapter 4.

The recorded data is compared with different hadron shower simulations. Chapter 5 gives a brief overview on the different hadrons physics simulations from the GEANT4 software framework, which are used for the thesis.

The data which has been recorded needs to be calibrated and corrected for effects like saturation of the Silicon Photomultipliers. The calibration procedure is explained in chapter 6. Also explained are the extraction of the calibration constants and the required measurements. Although, both datasets have been analyzed before [11, 12], several problems in the calibration of both data sets have been spotted and fixed. Additionally the inter-tile crosstalk, an important parameter for the detector simulation of the Analog Hadron Calorimeter, has been measured.

The recorded data sets include showers from electrons and hadrons as well as muons and have to be separated into samples containing only shower data from one particle type. The existing event selections for both analysis has been harmonized for both datasets. Additional criteria to improve the data quality, especially for a multi-particle contamination of the FNAL data, which has not been reported before, are described in chapter 7.

The simulation parameters used for the existing analysis differ and lead to unreasonable results if applied to the other analysis. Chapter 8 describes how detector effects are simulated and the input parameters to the simulation are discussed. Also a shower decomposition algorithm developed for this thesis is described. It searches in the shower history backwards from the energy deposition inside the calorimeter to the first inelastic scattering for certain processes and assigns the scintillator energy depositions to different showers components according to the found intermediate interactions.

The simulated data is then compared to recorded data in chapter 9. The data from muons and electrons is used to validate the detector simulation. Once the uncertainty of the detector simulations is quantified, the simulated pion showers are compared to experimental shower data for both iron and tungsten absorber.

Additional details of the shower development can then be extracted from the verified pion shower simulation to understand the differences of the shower development between iron and tungsten absorber configurations of the Analog Hadron Calorimeter. In chapter 10 the simulated data is used to decompose the showers into different components, which are then compared for the two absorber types. These differences of the shower components can be used to understand and explain the differences of the single particle energy resolution for the two absorber configurations of the Analog Hadron Calorimeter.

The thesis will close with a summary and discussion of the results and a outlook.

The results contained in this thesis have not yet been approved by the CALICE collaboration.

CHAPTER I

FUTURE LINEAR COLLIDER EXPERIMENTS

The Large Hadron Collider (LHC) [13] is up to the present day the most powerful particle accelerator. It is a proton-proton ring collider which can accelerate and collide protons up to a center-of-mass energy of $\sqrt{s} = 14$ TeV. Additionally it offers the possibility to accelerate and collide also heavy ions. The main purpose was to extend the Higgs search to higher energies as well as to search for physics beyond the standard model. However, due to the composite nature of the protons, neither the exact energy of the colliding particles, nor other collision parameters like the spin orientation of the colliding particles is well defined.

These limitations can be overcome by colliding leptons instead of hadrons, as these are particles without any known substructure. Therefore, the collision energy of a lepton collision is known with significantly higher precision. Additionally the lepton beams can be polarized, so that also the spin orientations of the colliding particles are well known. Therefore an e^+e^- collider is the natural candidate to complement the discovery machine LHC for precision measurement.

The maximum achievable collision energy of a ring collider is limited by energy losses of the accelerated particles due to synchrotron radiation, which scales in power P_{sync} as:

$$P_{sync} \propto \frac{E^4}{r \cdot m^4}, \quad (1.1)$$

with E as energy, m as mass of the accelerated particle, and r as acceleration ring radius. The radiation losses are significantly higher for electrons than for protons, due to the strong mass dependence. So far, the maximum energy for electrons was achieved with the LEP accelerator at CERN ($\sqrt{s} = 209$ GeV with a ring circumference of around 27 km), taking into account nowadays acceleration technology and a reasonable ring radius in terms of building costs.

Therefore the next electron-positron collider will most likely be a linear accelerator with collision energies near the TeV region, and with a physics program concentrated of precision measurements of the Higgs-like particle found at the LHC, since this energy regime gives access to several production channels (see fig. 1.1). Also the search for possible new physics beyond the standard model will continue. Two different linear accelerators are currently discussed as the most promising and mature projects: the International Linear Collider (ILC) and the Compact Linear Collider (CLIC). Although both differ drastically

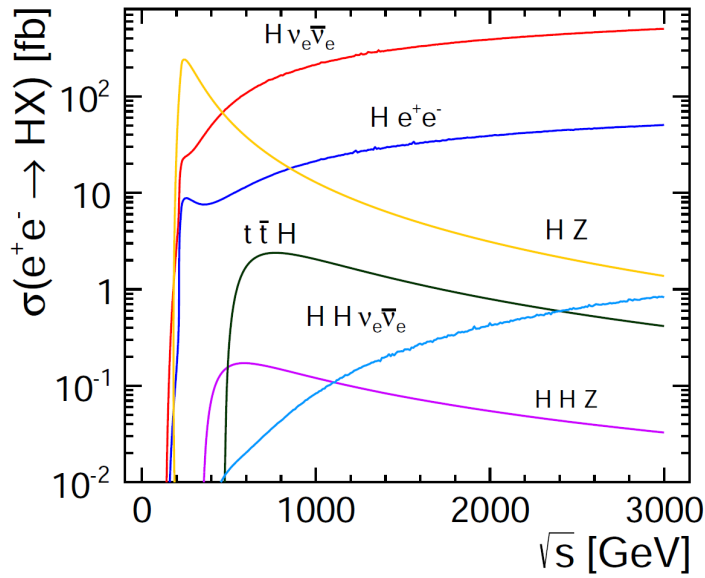


Figure 1.1: Cross sections for different production mechanisms for a 125 GeV Higgs boson as a function of the e^+e^- center-of-mass energy [14].

in the used accelerator technology and the resulting beams, the foreseen detectors to record the collision data are similar. In fact the CLIC detectors have been adapted from the ILC ones and have been modified for the different collision environment. The following chapter will give a brief summary of the two accelerators and their detectors.

1.1 The International Linear Collider

The International Linear Collider is a planned electron-positron linear collider based on super-conducting acceleration cavities and with a design luminosity of $1.8 \cdot 10^{34} \text{ cm}^{-2}\text{s}^{-1}$ at a center-of-mass energy of 500 GeV [15]. A possibility for a later upgrade of the center-of-mass energy to 1 TeV and higher luminosity is foreseen. The project has reached a level of maturity where a site for the construction has been identified.

Figure 1.2 shows a schematic overview of the ILC accelerator. Bunches of polarized electrons are ejected by laser pulses from a photocathode in the electron source. The bunches are accelerated to 5 GeV in a superconducting linac and then collected in the electron damping ring. Bunch trains are formed and the beam emittance is reduced by the use of superconducting wiggler magnets which induce synchrotron radiation.

The electron bunch trains are transported from the damping rings to the main linac by the Ring to Main Linac. It accelerates the electrons from 5 GeV to 15 GeV, while compressing the bunches from a bunch length of several millimeters to a few microns as required in the region where the electrons and positrons interact (IR). It also features magnets to orient the spin polarization in the desired direction.

The ILC Main Linacs accelerate the electrons (and positrons) from 15 GeV to a maximum energy of 250 GeV. The acceleration is achieved with superconducting niobium cavities which are powered by clystrons. The cavities are operated at 2 Kelvin and are housed in

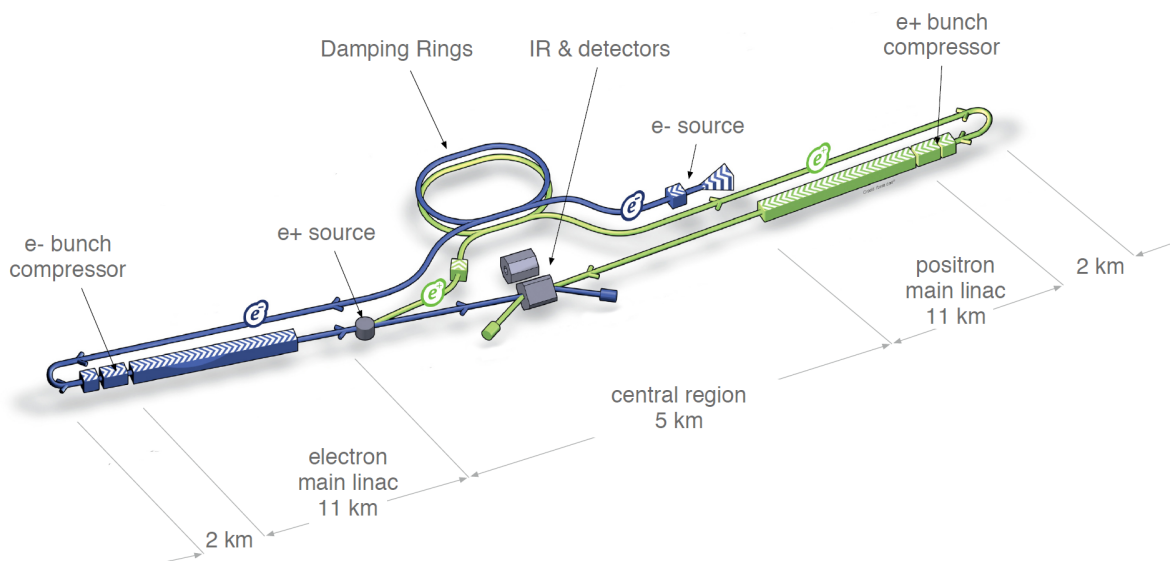


Figure 1.2: Overview of the ILC layout (not to scale)[15].

cryomodules. The cavities provide acceleration gradients of more than $30 \frac{\text{MV}}{\text{m}}$, which was only achieved for mass production techniques after a decade of extensive R&D.

After the acceleration to 250 GeV the electrons are transported through a superconducting helical undulator that generates photons with maximum energies up to around 30 MeV. Then the electron beam is separated from the generated photon beam by using a low-emittance-preserving chicane and transported by the Beam Delivery System (BDS) to the IR where two detectors can be operated alternately in a push-pull configuration. The BDS focuses the beam to the size needed to meet the design luminosity goals and also dumps the beams after the collision.

The photon beam generated by the undulator is directed to a titanium target, where electron-positron pairs are produced. The electrons and remaining photons are dumped, while the positrons are accelerated in a first step to 400 MeV. The positron bunches are then also accelerated to 5 GeV with a superconducting linac as the electrons. Afterwards the positrons are injected into a second damping ring parallel to the electron ring, from where they follow a similar line as the electron beams until they are brought into collision with the electrons. The foreseen beam-structure will result in bunch trains, that allow roughly one collision per $0.5 \mu\text{s}$ for more than 1000 bunches, but with a long spacing of almost 200 ms between the bunch trains.

1.2 The Compact Linear Collider

The second project for a planned electron-positron linear collider, which has reached a reasonable level of maturity, is the Compact Linear Collider (CLIC) [14]. However, it is not as advanced as the ILC project, since a new acceleration concept for the electron and positron beams is foreseen, which requires still ongoing R&D: Additional low energy, high current beams, called drive beams, are decelerated and the energy is transferred to copper

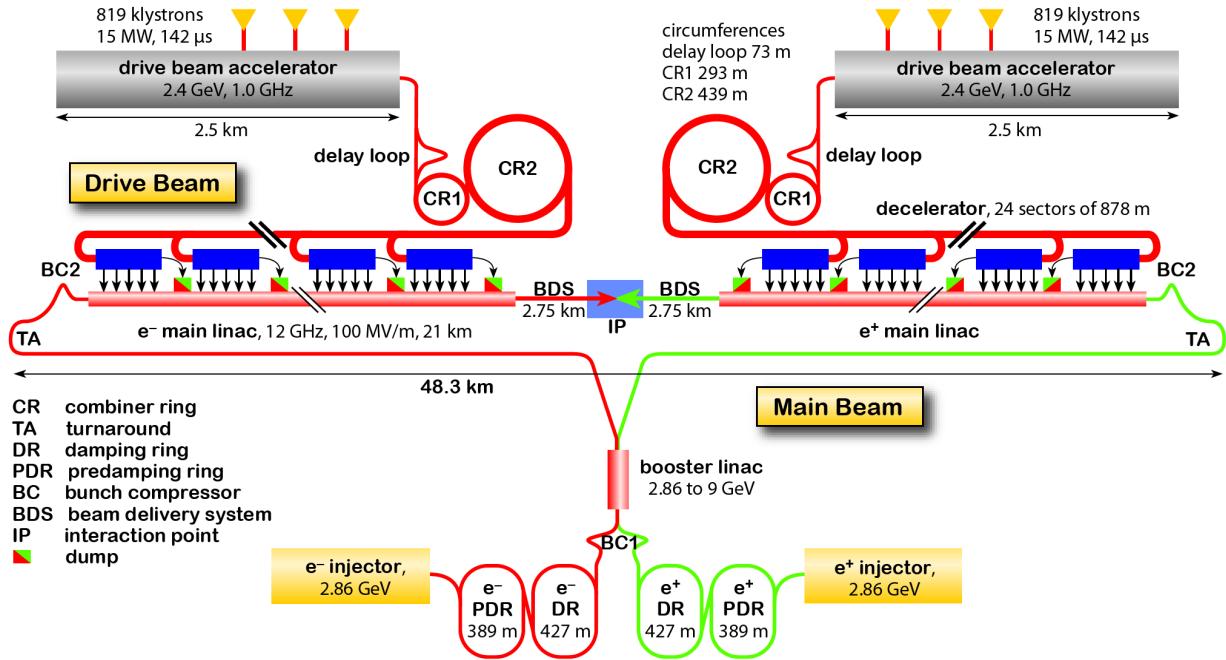


Figure 1.3: Overview of the CLIC layout at $\sqrt{s} = 3$ TeV [14].

cavities to accelerate the colliding electron and positron beams. The center-of-mass energy is foreseen to be initially at 500 GeV. An extension of the acceleration region could upgrade the accelerator to a center-of-mass energy of up to 3 TeV.

Figure 1.3 shows a schematic overview of the accelerator. The colliding beams are produced in conventional electron and positron sources and accelerated to 2.86 GeV until they are injected into two consecutive damping rings, the pre-damping rings (PDR) and the damping rings (DR), where the beam emittance is reduced. The main beams are transferred from the damping rings to the main linac by the Ring to Main Linac, where the beams are compressed longitudinally and accelerated to 9 GeV. The main linac uses cavities made of copper to achieve acceleration gradients of around $100 \frac{\text{MV}}{\text{m}}$.

The RF power needed to achieve the acceleration is extracted from high-current, low-energy drive beams, that run parallel to the colliding beams through a sequence of power extraction and transfer structures. A 500 GeV CLIC would only need a single drive beam that can power both the main electron and the main positron beam.

Once the beams have been accelerated to the collision energy, they are transported by the Beam Delivery System (BDS) to the Interaction Region, where they are brought into collision. Prior to the collision the beams are further compressed by the BDS. The collisions are recorded by either one of two detectors in a push-pull configuration. The beam-related backgrounds for the collisions are stronger compared to ILC due to the even more compressed bunches and therefore stronger fields.

1.3 Detectors

Both accelerators are foreseen to have two multi-purpose detectors recording the e^+e^- collisions, where either one records data, while the other detector can be accessed for maintenance. The two planned detectors for the ILC are the International Large Detector (ILD) and the Silicon Detector (SiD) [16]. Schematic overviews of both detectors are shown in figure 1.4 and figure 1.5. The two detectors currently foreseen for the CLIC accelerator are CLIC-ILC and CLIC-SID [10], which are adaptations of the ILC detectors for the different collision environment at CLIC. Some of the key parameters for the detectors are summarized in table 1.1.

The detectors have been optimized for unprecedented jet-energy resolution of 3-4 % at the jet-energies between 50 GeV and 500 GeV, maximized hermeticity and minimized dead material budget, while providing also good vertex reconstruction. The requirement for the jet-energy resolution is fulfilled by designing the detectors for the Particle Flow algorithm (see chap. 2), which uses the best suited sub-detector to precisely measure the energy of each of the collision products to optimize the overall jet-energy resolution. This requires excellent tracking resolution and highly granular calorimeters. The tracking and calorimeter system are placed inside the magnet coil to minimize uninstrumented volumes. Additionally the flux return yoke is also instrumented, which can be utilized for muon tracking and as tail catcher for the calorimeter.

The SiD detector concept is based almost completely on silicon read-out technologies and features an all silicon tracking system and an electromagnetic calorimeter based on silicon chips as active material. For the hadron calorimeter gas is foreseen as active material. In contrast to this, the ILC concept foresees a Time-Projection-Chamber (TPC) combined with a silicon vertex detector as tracking system. The electromagnetic calorimeter for this detector is planned with scintillator and silicon as active material. The hadron calorimeter is planned to use either scintillator or gas as active material. The detectors have been designed with a central barrel regions with two end-cap plugs.

The modification for the CLIC detectors include higher performance constraints on the vertex detectors, due to the stronger backgrounds, and an increased magnetic field, due to the higher average particle momentum of the collision products. Additionally the calorimeters have to be thicker in terms of interaction lengths (see chap. 2), which can be achieved by a change of the absorber material for the hadronic calorimeter from iron to tungsten. It is crucial to understand the differences of the shower development in iron and tungsten to estimate the impact of this absorber change.

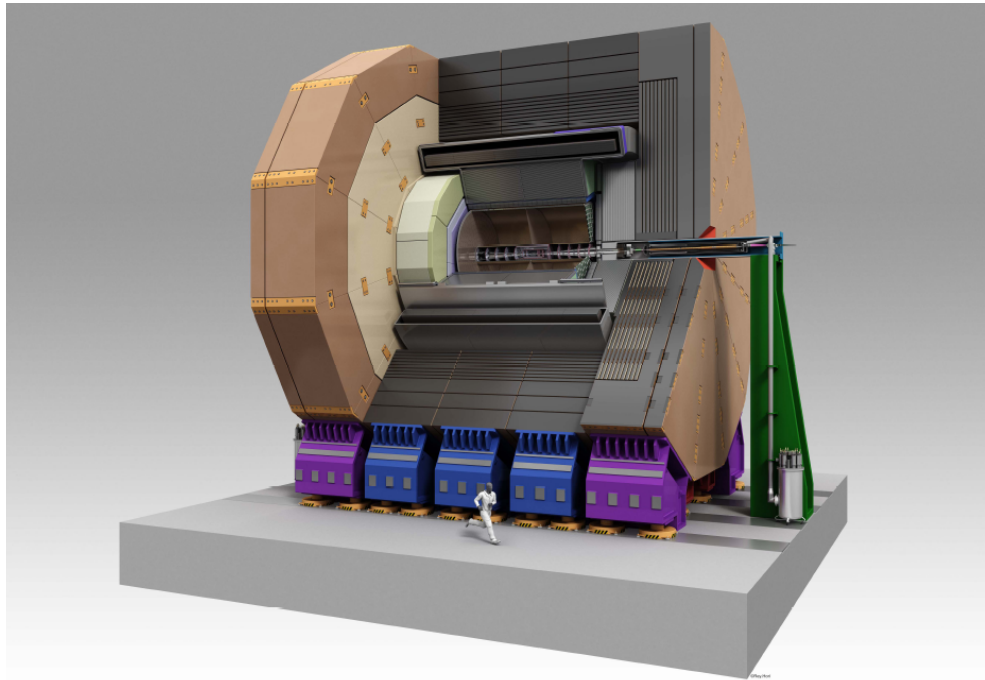


Figure 1.4: View of the ILD detector concept on its platform [16].

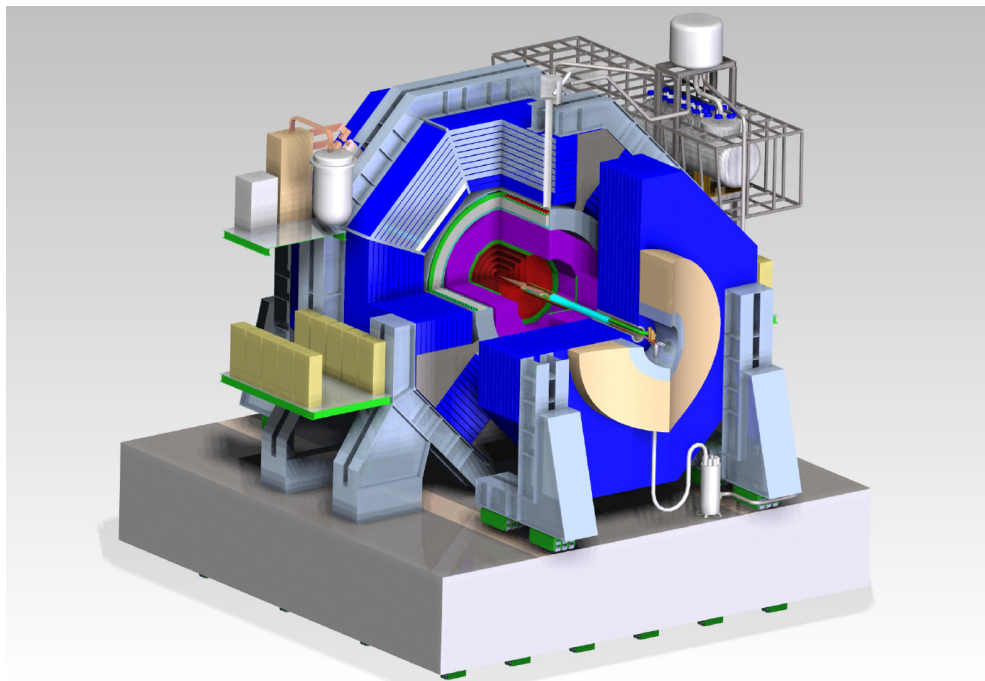


Figure 1.5: View of the SiD detector concept on its platform [16].

Concept	ILD	CLIC_ILD	SiD	CLIC_SiD
Tracker	TPC / Silicon	TPC / Silicon	Silicon	Silicon
Solenoid Field [T]	3.5	4	5	5
Solenoid Free Bore [m]	3.3	3.4	2.6	2.7
Solenoid Length [m]	8.0	8.3	6.0	6.5
Vertex Inner Radius [mm]	16	31	14	27
ECAL r_{\min} [m]	1.8	1.8	1.3	1.3
ECAL δr [mm]	172	172	135	135
HCAL Absorber B / E	Fe / Fe	W / Fe	Fe / Fe	W / Fe
HCAL $[\lambda_{int}]$	5.5	7.5	4.8	7.5
Overall Height [m]	14.0	14.0	12.0	14.0
Overall Length [m]	13.2	12.8	11.2	12.8

Table 1.1: Some key parameters for the ILC and CLIC detector concepts [10]. The inner radius of the electromagnetic calorimeter is given by the smallest distance to the main detector axis. Materials for the HCAL absorber are given for the barrel (B) and end-cap (E) sections.

CHAPTER II

PARTICLE SHOWERS AND CALORIMETRY

When high energetic particles traverse dense matter, they will typically interact with the atoms of the matter. Calorimeters in high energy physics, which are used to measure particle energies, make use of this fact by measuring signals from the remnants of these interactions. This chapter gives a brief overview of the physics that describe the interactions of the traversing electrons, muons, and hadrons with the atoms of the traversed matter. It will also give a short summary of the aspects of calorimetry that are relevant for this thesis, the energy resolution of calorimeters and an introduction to Particle Flow calorimetry.

2.1 Electromagnetic Cascades

High-energy electrons, positrons, and photons traversing dense matter, like the absorber material of a calorimeter, lose their kinetic energy by electromagnetic processes. The contributions of these processes to the total energy loss depend on the kinetic energy of the electron (or positron) as shown in figure 2.1.

At energies above roughly 100 MeV, and in many materials already at lower energies, the principal source for energy loss is the emission of Bremsstrahlung photons, which is due to deflections of the electron in the electric field of the absorber atoms. At lower energies the principal source of energy loss is ionization. There are also minor contributions from other processes like low-energy electron-electron scattering (Møller scattering), and low-energy electron-positron scattering and annihilation processes for positrons (Bhabha scattering). The transition point, where the energy losses from ionization and Bremsstrahlung contribute equally to the total energy loss, is usually referred to as the critical energy E_c . However, there is a different definition of the critical energy used by the PDG. In this definition E_c is the energy at which the ionization loss per radiation length X_0 (see below) equals the electron energy E [17]:

$$(\Delta E)_{ion} = \left[\frac{dE}{dx} \right]_{ion} X_0 = E. \quad (2.1)$$

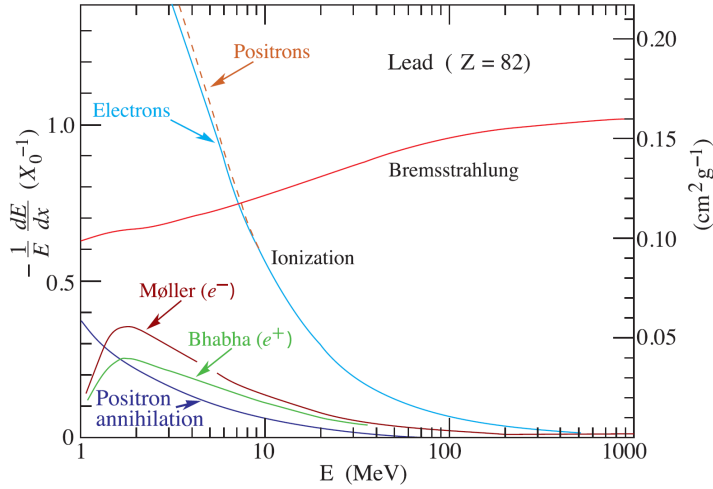


Figure 2.1: Fractional energy loss per radiation length in lead as a function of electron or positron energy [17]. Electron (positron) scattering is considered as ionization when the energy loss per collision is below 0.255 MeV, and as Møller (Bhabha) scattering when it is above.

The critical energy for iron is about 22 MeV and for tungsten about 8 MeV (see table 3.1).

Photons traversing dense matter lose their energy by the following processes: At highest energies the most likely process to occur is pair production where the photon creates an antiparticle-particle-pair (typically e^+e^- -pair) in an external electromagnetic field. However, this process needs photon energies of at least the rest mass of the electron-positron-pair. At energies below the e^+e^- -pair-production threshold Compton scattering is the most likely process where the photon is scattered incoherently by an electron. The energy regime where this process is dominant depends on the proton number Z of the material, and is smallest for high- Z materials [18]. At lowest energies the Photoelectric Absorption is dominant, the absorption of the photon by an atom, where the cross sections depend crucially on the electron shell structure of the hit atom. Figure 2.2 shows the cross sections for the processes for iron and tungsten (data from [19]).

The combination of these effects leads to the development of small showers already at relatively low energies of a few MeV, a typical energy for γ s from nuclear de-excitation. Such a γ may create an e^+e^- -pair, which loose their energy via ionization of the medium. The positron may then annihilate with an electron at rest leading to two 511 keV γ s, which may undergo a series of Compton scatterings until they are photoelectrically absorbed. The Compton electrons and the photoelectron loose their energy via ionization. This way the initial γ deposited all its energy in the medium via ionization of daughter particles.

An electromagnetic cascade initiated by a multi-GeV electron underlies the same principles as this example. But in addition, Bremsstrahlung plays a major role in electromagnetic cascades. As mentioned above, the most significant energy loss for high energy electrons is Bremsstrahlung, and a multi-GeV electron will immediately start to emit huge numbers of Bremsstrahlung photons once it starts to traverse dense matter. Although the vast majority of these photons is very soft, there is still a considerable number of photons exceeding

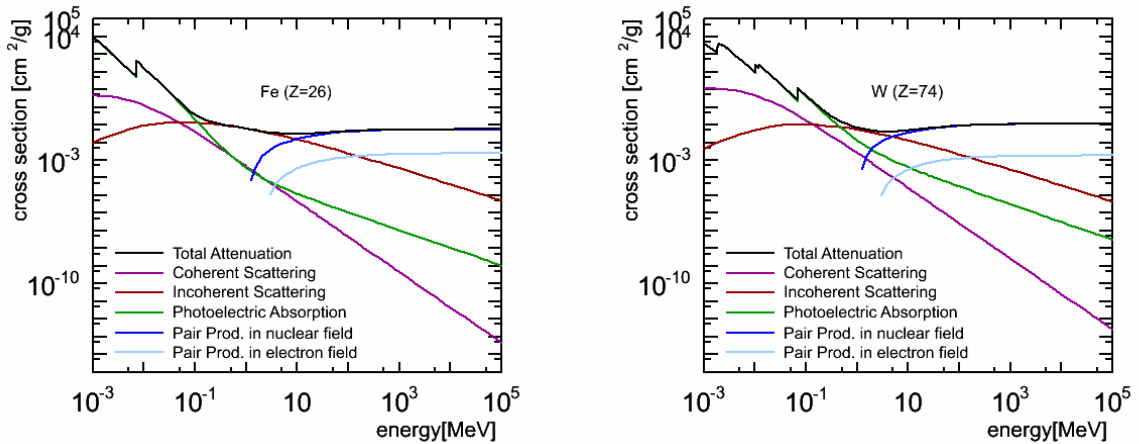


Figure 2.2: Photon total cross section and contributions for iron(left) and tungsten(right). Data obtained from [19]

the necessary energy for pair production, resulting in a much higher shower particle multiplication than in the simple example above. The cascade has reached its peak multiplicity when the average electron energy is approximately E_c . The depth where the peak multiplicity is reached is called shower maximum and shows a logarithmic dependence on the energy of the electron initiating the cascade.

The typical scale to describe these electromagnetic cascades in a material-independent way is the radiation length X_0 , which is the distance after which the traversing high energy electron has lost on average $(1 - e^{-1}) = 63.2\%$ of its initial energy. It can be approximated within 3 % by [17]:

$$X_0 = \frac{716.4A}{Z(Z+1)\ln(287/\sqrt{Z})} \frac{\text{g}}{\text{cm}^2} \quad (2.2)$$

where A denotes the number of nucleons and Z the number of protons in a nucleus of the material.

Typically the energy deposit E in the longitudinal direction x in electron showers is parametrized as:

$$\frac{dE}{dx} = E_0 \cdot x^\alpha \cdot e^{-\beta x} \quad (2.3)$$

with the two free fit parameters α and β and the total energy deposit E_0 [20].

The radiation length of a mixture of materials can be calculated with

$$\frac{1}{X_0} = \sum_i \frac{V_i}{X_{0,i}} \quad (2.4)$$

with V_i and $X_{0,i}$ being the fraction of the volume and the radiation length in mm of the i th component of the mixture [18].

In contrast to the continuously Bremsstrahlung emitting electrons, a photon will travel some distance before it is converted to a particle-antiparticle-pair. The mean free path

length I_γ of a photon is related to the radiation length:

$$I_\gamma = \frac{9}{7} X_0. \quad (2.5)$$

This also means, that the photon total cross section is related to the radiation length by

$$\sigma(E \rightarrow \infty) = \frac{7}{9} \frac{A}{N_A X_0} \quad (2.6)$$

with A as atomic weight and N_A being Avogadro's number [17].

As the lateral extension of a cascade is described by the radiation length, the Moliere radius ρ_M describes the radial extension of an electromagnetic cascade. A cylinder with a radius of ρ_M will contain 90 % of the energy of the cascade (99 % if the radius of the cylinder is 3.5 ρ_M). The Moliere radius is given by [17]:

$$\rho_M = E_s \frac{X_0}{E_c}. \quad (2.7)$$

with the scale energy E_s defined as $m_e c^2 \sqrt{4\pi/\alpha}$, which equals 21.2 MeV.

2.2 Charged heavy Particles traversing Matter

As described in section 2.1, the absorption of high energy electrons is a multi step process, which leads to the full absorption of these particles in relatively small amounts of matter. This is different for muons, although, as electrons, they also undergo only the electromagnetic interaction and not the strong interaction. Up to very high energies of 100 GeV, ionization is the main source of energy loss for muons (and other heavy charged particles) when traversing a dense medium. Although they can also emit Bremsstrahlung, which then partially also converts into e^+e^- -pairs, this plays a role only at much higher energies, since this is suppressed by a scale-factor $(m_\mu/m_e)^2 \approx 40000$. However, since ionization results typically only in an energy loss of 1-2 MeV g⁻¹cm² it takes substantial amounts of material to absorb the energy of these particles completely.

The mean energy loss per path length $\langle -\frac{dE}{dx} \rangle$ for a heavy charged particle traversing a medium with atomic number Z and atomic mass A can be described with the Bethe-Bloch-formula:

$$\langle -\frac{dE}{dx} \rangle = K z^2 \frac{Z}{A} \frac{1}{\beta^2} \left(\frac{1}{2} \ln \frac{2m_e c^2 \beta^2 \gamma^2 T_{max}}{I^2} - \beta^2 - \frac{\delta(\beta\gamma)}{2} \right) \quad (2.8)$$

where K equals $4\pi N_A r_e^2 m_e c^2$, T_{max} represents the maximum kinetic energy that can be transferred to an electron in a single collision, I is the mean excitation energy and δ describes the density effect. Figure 2.3 shows this energy loss for muons in copper as a function of the particle momentum. At momenta of $\beta\gamma \approx 3-4$ the mean energy loss distribution shows a broad minimum. Particles with these momenta are referred to as minimum

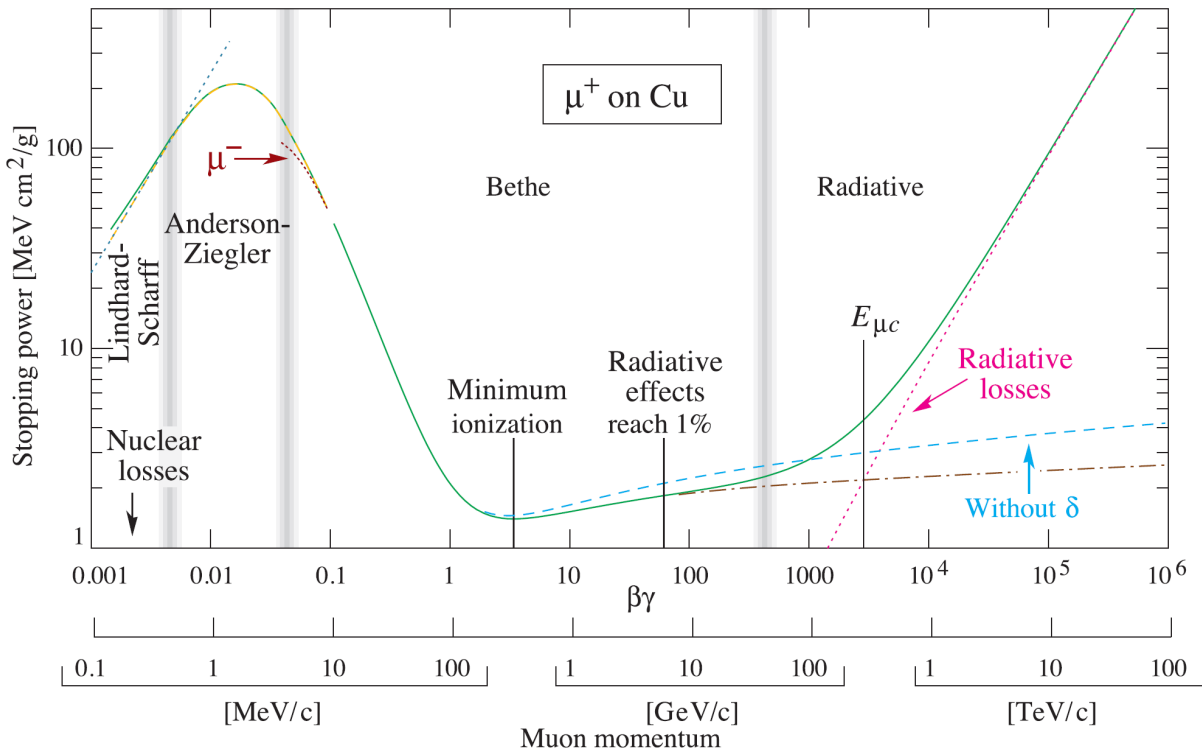


Figure 2.3: Mean energy loss per path length, also called “Stopping power” $\langle -\frac{dE}{dx} \rangle$ for positive muons in copper as a function of $\beta\gamma = \frac{p}{Mc}$ [17]. Solid curves indicate the total stopping power, vertical bands indicate boundaries between different approximations. The short dotted lines labeled “ μ^- “ illustrate the “Barkas effect,” the dependence of stopping power on projectile charge at very low energies.

ionizing particles (MIPs).

However, the mean energy loss does not reveal the full picture and is not well-defined experimentally, since the energy loss distribution for muons traversing moderate amounts of material like scintillator tiles of the AHCAL (see chap. 3) differs substantially from a Gaussian distribution and can instead be described by a Landau [21] or Landau-Vavilov [22] distribution if the mean energy loss in a scintillator tile is small in comparison to the maximum energy transfer in a collision T_{max} . The most probable value (MPV) for the energy loss of this distribution is below the value of $\langle -\frac{dE}{dx} \rangle$ in figure 2.3, but the distribution also has a long tail to high energy losses for several reasons: The production of knock-on electrons (δ -rays), when in an ionization a significant amount of the muon kinetic energy is transferred in a single collision; Small electromagnetic showers initiated by Bremsstrahlung photons, which becomes more important at higher energies, but also contributes at lower energies; And photo-nuclear reactions, where the muon electromagnetically interacts with a nucleus of the material, which also gives very high local energy deposits [17].

2.3 Hadron Showers

Charged hadrons also lose energy via ionization as described in section 2.2, but additionally they may interact strongly with the nuclei of the medium, whereas neutral hadrons deposit their energy only via strong scattering processes. At high energies of several GeV down to some MeV both the hit nucleus and the projectile hadron will typically change their identity during the scattering. During this scattering additional particles are created or released from the hit nucleus.

The most likely process to occur, when a hadron interacts strongly with a nucleus, is spallation, but also fission or nuclear break-up may take place. The spallation process can be described as a two stage process with very different time scales [18]: In a first step, the intra-nuclear cascade takes place, where some of the nucleons may be released from the nucleus. Typically also pions are created if the energy is above the pion production threshold. The timescale of this cascade is of the order of 10^{-22} s, and several different approaches exist to model this stage (see chapter 5). The manifold variety of possible end states of this step reaches from just some created pions to the release of many nucleons and combinations of both. Typically many of these final states have cross sections in the same order of magnitude. However, the details also strongly depend on the identity of the hit nucleus.

In the second stage of scattering, the de-excitation, typically on timescales of 10^{-18} s and much longer, the nucleus will change further to reach a stable configuration after the intranuclear cascade. For lighter nuclei, this happens via the evaporation of neutrons and de-excitation via the emission of γ s. For heavier nuclei, even nuclear fission may take place to bring the nucleus to a stable configuration. Also several models exist to describe this de-excitation and evaporation stage (see chapter 5).

The released protons and charged pions will lose their energy via subsequent hadron interactions or ionization. This is different for the released neutrons as they can lose their kinetic energy only via hadron scattering until they either leave the detector, decay, or are captured by another nucleus. Typically neutrons will undergo a series of elastic scatterings, where the average energy transfer per scattering is very low, but increases with decreasing size of the nucleus, until they are eventually captured by some nucleus, since the cross section for neutron capture is highest for neutrons at rest. This leads to very late energy depositions from neutrons and the time of the energy deposition often exceeds the readout time of a detector. The most extreme case is neutron decay with a half-life time of about 15 minutes.

In the intranuclear cascade, on average one third of the produced pions are neutral pions, which decay almost instantly into two photons, which results in electromagnetic sub-showers inside the hadron cascade. The fraction of the total hadron cascade energy that is deposited by these electromagnetic sub-showers is called electromagnetic fraction f_{EM} and varies strongly from event to event between 0 and 1. However, on average one third of the available energy of a hadron scattering is carried by this electromagnetic component

per hadron collision. If the initial projectile had sufficient energy for several generations of hadron interactions in the cascade, on average the total electromagnetic fraction after n generations of hadron scatterings equals to:

$$f_{\text{EM}} = 1 - \left(1 - \frac{1}{3}\right)^n. \quad (2.9)$$

Nevertheless, this is just a simplified model and in reality the situation is more complex as not only π mesons are produced and the $\frac{1}{3}$ should be taken as an upper limit [18] for the average electromagnetic fraction.

The energy that is needed to account for the binding energy of the released nucleons in hadron showers is lost for the measurement process and therefore called invisible energy. Also this invisible energy fluctuates strongly from interaction to interaction. However, one may regain a fraction of this energy by the use of absorber materials which have either high fission cross sections like uranium or by materials with high neutron cross section like tungsten.

Since this invisible energy or gaining energy by fission only occurs in hadronic showers, the response of a calorimeter to hadrons is in general different than the response to electrons of the same energy. The response to a pion π can then be described as the weighted sum of an electromagnetic shower part e and a purely hadronic part h , where the weight is the mean electromagnetic fraction f_{EM} :

$$\pi = e \cdot f_{\text{EM}} + h \cdot (1 - f_{\text{EM}}) \quad (2.10)$$

The hadronic cascades show different topology than the electromagnetic cascades and are described on the scale of the nuclear interaction length λ_{int} which is defined as the mean length that a hadron traverses through the medium before a strong interaction takes place. It is typically much larger than the radiation length. The interaction lengths for compound materials can be calculated in the same way as the radiation length for compound materials [18]:

$$\frac{1}{\lambda_{\text{int}}} = \sum_i \frac{V_i}{\lambda_{\text{int},i}}, \quad (2.11)$$

where $\lambda_{\text{int},i}$ is the interaction length of the i -th component and V_i the fraction of the total volume for this component.

2.4 Calorimeters

A calorimeter is a device consisting of a block of matter to absorb and measure the energy of the cascade initiated by a high-energy particle and thereby measuring the initial energy of this particle. The fact, that the shower length increases only logarithmically with energy, makes it possible to contain most (or all) of the cascade energy even for very high-energy particles, which are encountered in collisions at modern high energy particle accelerators,

within reasonable amounts of matter.

In general one distinguishes between two construction principles for calorimeters: the homogeneous calorimeters, where showers are initiated and detected by the same material (e.g. CMS ECAL with PbWO₄ crystals [23]), and heterogeneous calorimeters, where different materials are used to initiate the cascades (absorber) and for the detection of the shower energy (active material), like the CALICE AHCAL discussed in this thesis (chapter 3). The most common approach to the construction of heterogeneous calorimeters is the sandwich calorimeter, where absorber material is typically placed in layers interleaved with layers of the active material. However, these heterogeneous calorimeters can detect by construction only a fraction of the total cascade energy, the energy deposited in the active layers. This fraction is called sampling fraction, which is defined as the energy of a minimum ionizing particle that is deposited inside the active material in comparison to the total energy deposit inside the calorimeter [18].

The freedom to chose absorber and active materials independently for heterogeneous calorimeters has some decisive advantages: Absorber materials can be chosen with high density to minimize the thickness of the total calorimeters, while maintaining the same shower containment. At the same time active materials, like scintillator or gas, can be chosen for special properties. For example, organic scintillators which include a high fraction of hydrogen, can serve to efficiently moderate neutrons from hadron interactions. So the neutrons can be absorbed and contribute to the measured energy and thereby improve the overall energy resolution by reducing the average invisible energy. This freedom helps also to minimize the total material costs, an important factor for the construction of realistic 4π detectors for accelerator experiments. However, there is also the disadvantage that energy resolution is in general worse for heterogeneous calorimeters due to sampling fluctuations in the energy deposit.

In modern high energy collider experiments the calorimeters are mostly segmented and optimized for their individual purposes: typically the calorimeter system is divided into a fine grained electromagnetic calorimeter (ECAL), measuring electrons and photons, followed by a coarser calorimeter for the measurement of hadrons (HCAL). The hadron calorimeters have generally a reduced granularity, as hadron cascades suffer much more from fluctuations in the energy deposit, and could not benefit from increased granularity as much as electromagnetic calorimeters. Since electromagnetic showers scale with X_0 and hadron showers scale with λ_{int} which is typically much larger, the cost of such an optimized calorimeter system are in general drastically reduced in comparison to a single all-purpose calorimeter.

As described in section 2.1 inside an electromagnetic cascade, in principle, all the cascade energy can be measured. In contrast to this hadronic showers involve processes, where part of the energy is not detectable (invisible energy, see section 2.3). In addition the mean electromagnetic fraction increases non-linearly with the energy of the shower-initiating particle. This leads to a ratio $\frac{e}{h}$ of the calorimeter response to electromagnetic and to hadronic processes which is in general $\neq 1$. This ratio can be adjusted by a careful choice of active and absorber materials and their fraction of the total volume [24]. By using e.g. absorber

Calorimeter	Energy resolution (stochastic term only)
CMS ECAL	2.8%/ \sqrt{E} [28]
ZEUS HCAL	35%/ \sqrt{E} [25]
CMS HCAL	125%/ \sqrt{E} [29]
ATLAS HCAL	54%/ \sqrt{E} [29]

Table 2.1: *The single particle energy resolution for the barrel region of several built calorimeters.*

materials like tungsten with a high neutron capture cross section, one may regain part of the invisible energy by neutron capture. Also uranium absorber material with high fission cross section has been used for adjusting the $\frac{e}{h}$ ratio. Calorimeters with a $\frac{e}{h}$ ratio equal to one are called compensating calorimeters. Examples for almost compensating calorimeters with depleted uranium as absorber are the HCAL of the ZEUS detector [25], the HCAL of the AFS experiment at the CERN ISR [26] and the HELIOS experiment at the CERN SPS [27].

However, the ratio $\frac{e}{h}$ can not be measured directly. Instead the ratio of the response of the calorimeter to pions and electrons of the same energy can be measured, which is related to the $\frac{e}{h}$ by:

$$\frac{e}{\pi} = \frac{\frac{e}{h}}{1 - f_{em}(1 - \frac{e}{h})}. \quad (2.12)$$

The ratio $\frac{e}{\pi}$ is energy dependent due to the energy dependence of f_{em} .

The most important figure of merit for a calorimeter system is typically the relative energy resolution $\frac{\sigma_E}{\langle E \rangle}$, which can be parametrized as the quadratic sum of three terms:

$$\frac{\sigma_E}{\langle E \rangle} = \frac{a}{\sqrt{E}} \oplus b \oplus \frac{c}{E}, \quad (2.13)$$

were the a denotes the stochastic term. The constant b term takes into account calibration uncertainties and response inhomogeneities of the calorimeter. The third term c describes effects like electronic noise, which are energy independent. At very low energies, the noise term limits the calorimeter resolution, while at high energies the resolution is limited by the constant term. Several examples for the energy resolution of the central regions of build calorimeters are given in table 2.1. The examples include the CMS ECAL as a modern ECAL with very good energy resolution, the ZEUS HCAL as the hadron calorimeter with the best single particle energy resolution achieved so far, and the HCALs from the CMS and ATLAS experiments as examples for currently used hadron calorimeters at modern experiments.

2.5 Particle Flow concept

Conventional hadron calorimetry in high energy physics has basically reached the achievable limit in single particle energy resolution with the development of the ZEUS calorimeter, since the resolution is limited by the strong fluctuations in hadron showers. The ZEUS

calorimeter was almost compensating and was exceptionally thick in terms of nuclear interaction lengths. It thereby minimized the resolution degradation due to leakage effects, but it had a very coarse granularity with no longitudinal segmentation. However, with the given resolution of the ZEUS hadron calorimeter for all hadrons it is not possible to achieve the jet energy resolution required by modern linear collider experiments (chapter 1), since the jet energy resolution is worse than the single hadron energy resolution (see fig. 2.4). Therefore novel approaches to calorimetry had to be developed. One is the dual-readout technology which utilizes two different active materials, one sensitive to cherenkov light, the other conventional scintillator, to estimate the electromagnetic fraction for every hadron shower and therefore correct the energy measurement accordingly. A prototype with this technology is described in [30].

A second approach is the Particle Flow concept, which is also the design paradigm of the currently planned detectors for future linear colliders, but was first used in a less sophisticated version at the ALEPH detector at LEP. The fact, that the energy of charged particles can be measured with much greater accuracy by tracking systems, gives the possibility to measure the energy of charged particles with the good energy resolution of the tracking system, and measure only the neutral particles with the calorimeters. Thus, the energy of charged particles has to be subtracted from the energy measurement in the calorimeter system (see figure 2.5). Therefore the calorimeters need to have sufficient granularity to distinguish the contributions from the individual particles inside the jet. Several huge experiments like CMS at CERN [31] or H1 at DESY [32] have shown that the use of particle flow algorithms improves the achievable jet energy resolution even if the detectors were not specifically designed for this.

The CALICE collaboration has developed highly granular calorimeters, which give the possibility to identify individual clusters of energy depositions from the showers of individual particles inside a jet. Together with the tracking system it is possible to identify clusters belonging to showers of neutral particles by the use of the Pandora Particle Flow algorithm [33, 34] and measure only the energy of the neutral hadron part of a jet with the moderate energy resolution of the HCAL, whereas photons are measured with the ECAL and all charged particles are measured with the excellent resolution of the tracking system. The performance of the Pandora Particle Flow algorithm has been evaluated with testbeam data from CALICE detectors [35].

The total jet energy resolution can then be described by a quadratic sum of the individual detector resolutions weighted by the average fraction of the particle types inside a jet:

$$\begin{aligned} \sigma_{\text{jet}}^2 = & \sigma_{\text{TRACK}}^2 \cdot f_{p^\pm} + \\ & \sigma_{\text{ECAL}}^2 \cdot f_\gamma + \\ & \sigma_{\text{HCAL}}^2 \cdot f_{h^0} + \\ & \sigma_{\text{conf}}^2 + \sigma_{\text{thr}}^2 + \sigma_{\text{loss}}^2, \end{aligned} \quad (2.14)$$

were the σ_{TRACK} , σ_{ECAL} , σ_{HCAL} denote the different sub-detector resolutions which are weighted by their average fraction of the particle type inside a jet. On average, $f_{p^\pm} \approx 60\%$

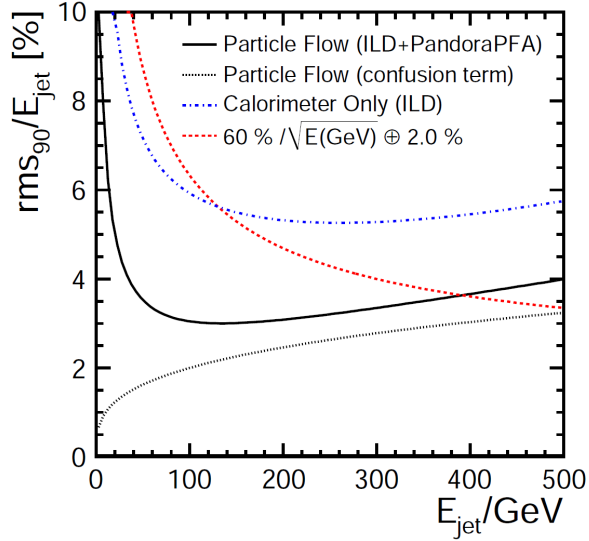


Figure 2.4: The empirical functional form of the jet energy resolution obtained from PFlow calorimetry [34]. The estimated contribution from the confusion term only is shown (dotted). The dot-dashed curve shows a parametrization of the jet energy resolution obtained from the total calorimetric energy deposition in the ILD detector. An indication of the resolution achievable by using a traditional calorimetric approach is given by the dashed curve ($\frac{60\%}{\sqrt{E(\text{GeV})}} \oplus 2.0\%$).

of the energy of a jet is carried by charged particles, $f_\gamma \approx 30\%$ of the energy is carried by photons and the remaining $f_{h^0} \approx 10\%$ are carried by neutral hadrons. The σ_{thr} describes effects from detector readout thresholds, the σ_{loss} describes contributions due to undetected particles. The CALICE detector granularity has been optimized to minimize contributions from the confusion term σ_{conf} , which describes the effects of wrongly attributed clusters of energy deposition and is the limiting term for the resolution at high energies (see fig. 2.6).

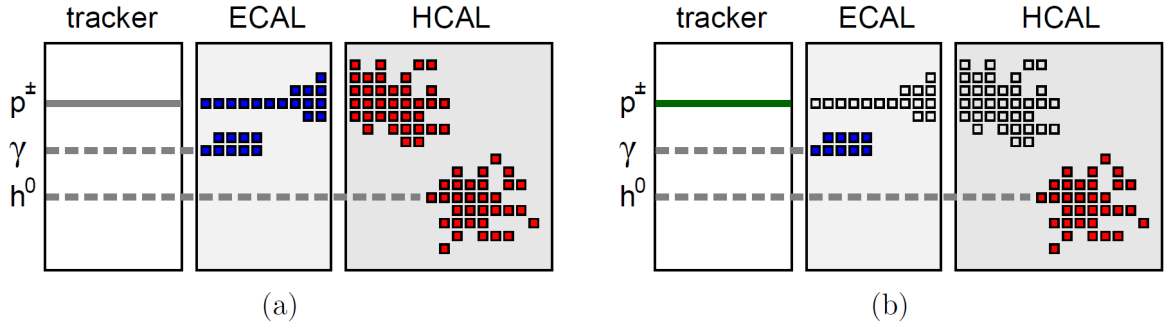


Figure 2.5: (a) *Simple calorimetry*: The calorimeters (ECAL+HCAL) measure the total energy deposited by all particles in a jet (charged particles p^\pm , photons γ , and neutral hadrons h^0). The track momentum measurement from the tracker is not used. (b) *Particle Flow approach*: The tracking system measures the energy of all charged particles and associated energy depositions are removed from the energy sum in the calorimeters. Photon energies are measured with the ECAL and only neutral hadron energies are measured by the HCAL. (data used for reconstruction of events is shown in color) [11].

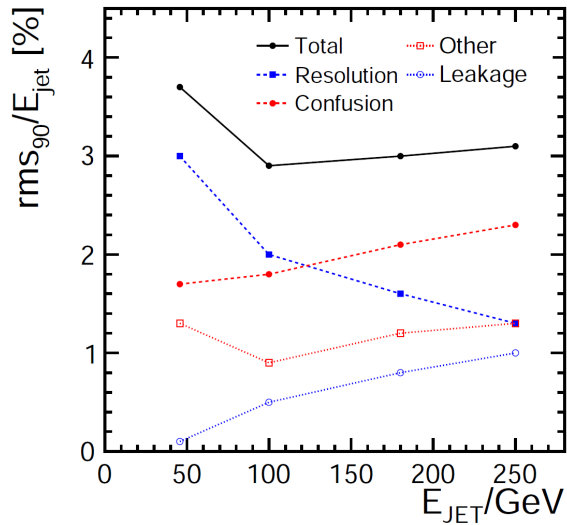


Figure 2.6: The contributions to the Particle Flow jet energy resolution obtained with PandoPFA as a function of energy. The total is (approximately) the quadrature sum of the components [34].

CHAPTER III

THE CALICE AHCAL PHYSICS PROTOTYPE

The CALICE Analog Hadron Calorimeter physics prototype (AHCAL) [36], shown in figure 3.1, is a scintillator-absorber sandwich calorimeter, covering approximately one cubic meter in volume in a classical layer design – 38 active layers called modules, which are interleaved with absorber layers, where the layers are oriented perpendicular to the incoming particles. The novel Silicon Photomultipliers (SiPM) were chosen as read out technology, making this prototype the first experiment using these new devices in large numbers. It was designed as a prototype to prove the physics measurement capabilities of a Particle Flow hadron calorimeter in a future high-energy linear collider. Two different options of absorber material, iron and tungsten, have been evaluated in testbeam campaigns (see chapter 4). This chapter describes the details of the prototype, its electronics, and the two different absorber options.

3.1 The Active Layers

The active layers consist of 5 mm thick quadratic tiles of different size made up of the organic scintillator BASF 143 from UNIPLAST, which is essentially polystyrene. Figure 3.2 shows the chemical structure of polystyrene. The scintillation light is generated by the decay of excited states of the delocalized π -electrons in the benzene rings. The electrons are excited by ionizing charged particles traversing the scintillator. Additionally the energy loss of muons in polystyrene is given in the same figure.

The tile structure of the layers is the following: In the central core, consisting of ten times ten tiles, the tiles are $3 \times 3 \text{ cm}^2$ size, followed by three rings of $6 \times 6 \text{ cm}^2$ size tiles (96 tiles) and then by $12 \times 12 \text{ cm}^2$ size tiles as outermost ring consisting of 20 tiles. The last eight of the 38 layers do not have the $3 \times 3 \text{ cm}^2$ tiles in the core, but also $6 \times 6 \text{ cm}^2$ tiles. This results in total in 7608 readout channels for all tiles in the AHCAL (6480 channels in the first 30 finely segmented layers). The layout of the tiles for the finely segmented layers and a single tile with SiPM is shown in figure 3.3.

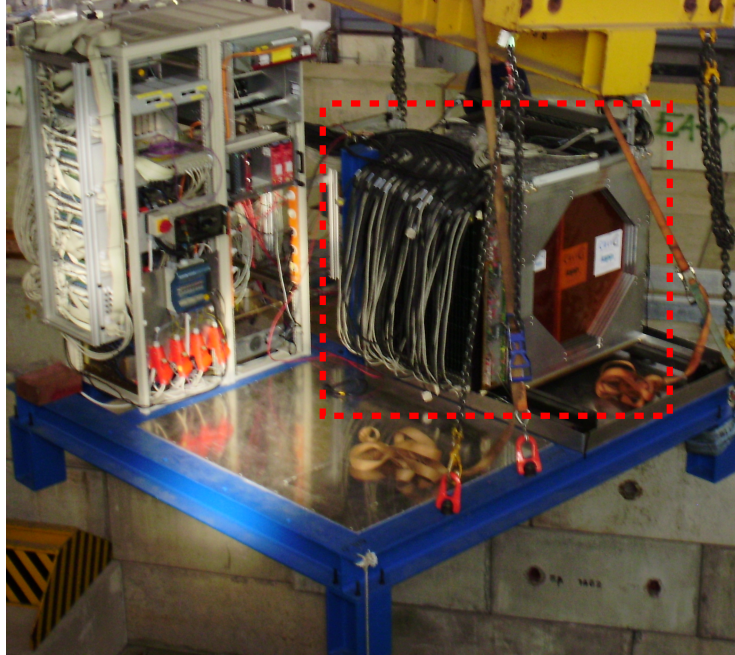


Figure 3.1: The setup of the detector at CERN PS. The calorimeter (in the red box) is mounted on a support platform. Left to the calorimeter is a crate containing the front-end electronics and the power supplies.

The edges of the tiles have undergone a chemical treatment to minimize the light leakage into neighboring tiles (inter-tile crosstalk), whereas the top and bottom of the tiles are covered with reflective foil (VN2000 super-radiant from 3M). A measurement of the inter-tile crosstalk is described in section 6.9. There is also a small groove molded into each tile which houses a wavelength-shifting fiber (Y11, 300 ppm from Kuraray) to collect the scintillation light, shift the collected light to a peak wavelength of 500 nm and to guide it to the SiPM readout. The other end of the fiber is covered with a mirror.

Each layer has also five temperature sensors which allow a continuous monitoring of the temperature inside the layer and two temperature sensors next to the very-frontend electronics, which are attached to the modules. The whole setup is enclosed in a steel cassette with a wall thickness of 2 mm. The position of the sensors is shown in figure 3.4. The calibrations system (see section 3.2.4) is mounted to the side of the module.

3.2 Read-out Electronics

The readout-out electronics of the AHCAL start with the SiPMs, which measure the energy deposits. They continue with the very-frontend electronics, where the signals from the individual cells are further processed by read-out chips. These chips integrate and shape the SiPM signals and they also amplify, multiplex and transfer the signals via SCSI bus to a VME crate with the CALICE Readout Cards (CRC). The CRC boards convert the analog signal into a digital signal, which is then stored on a computer. This is shown

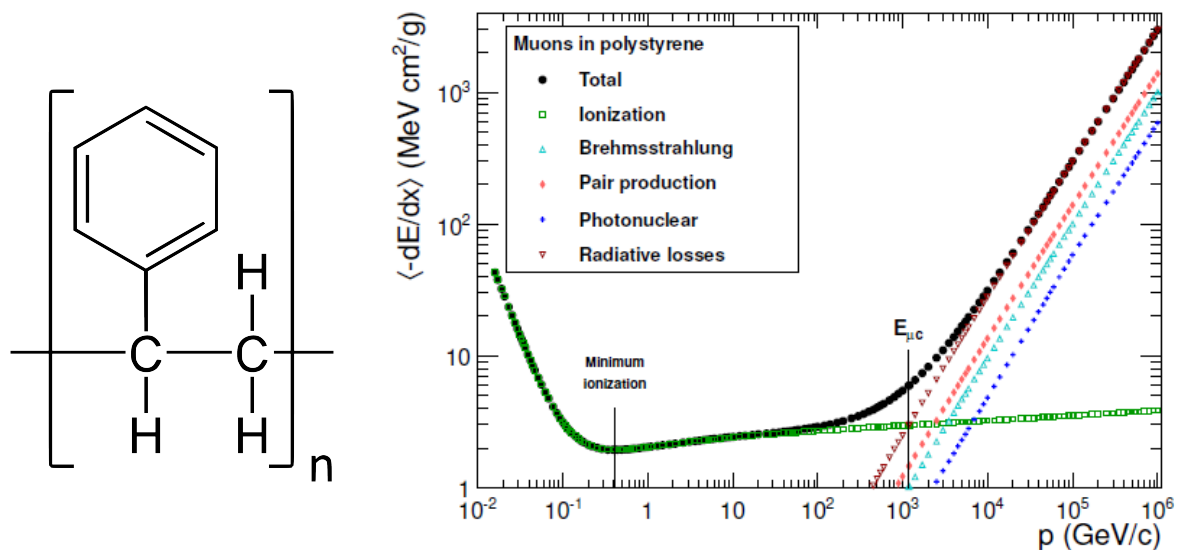


Figure 3.2: The chemical structure of polystyrene (left) and the average energy loss of muons in polystyrene (right) [37], data compiled from [38]

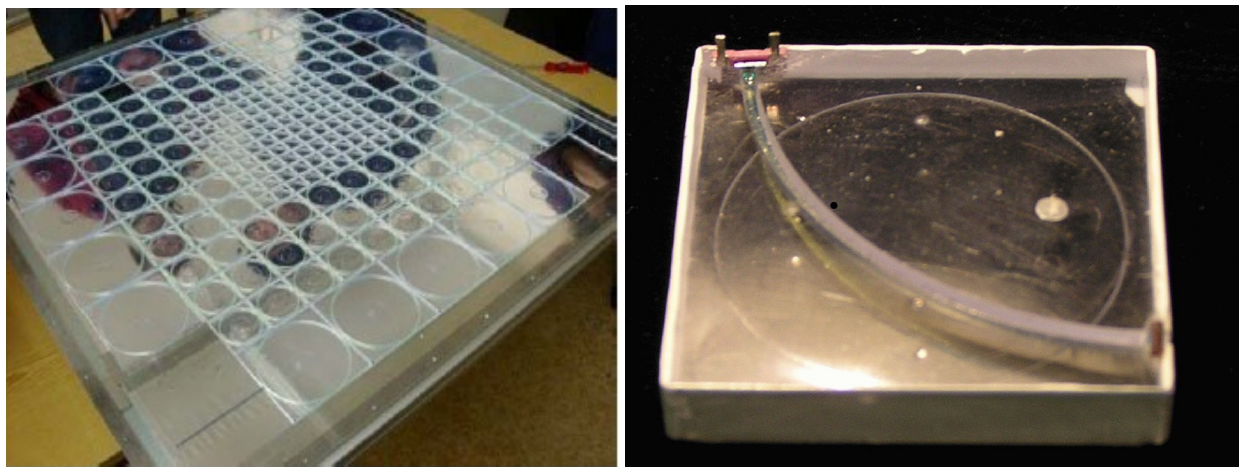


Figure 3.3: Shown are the tiles of an active layer (left) and a single scintillator tile with a size of 3×3 cm² (right).

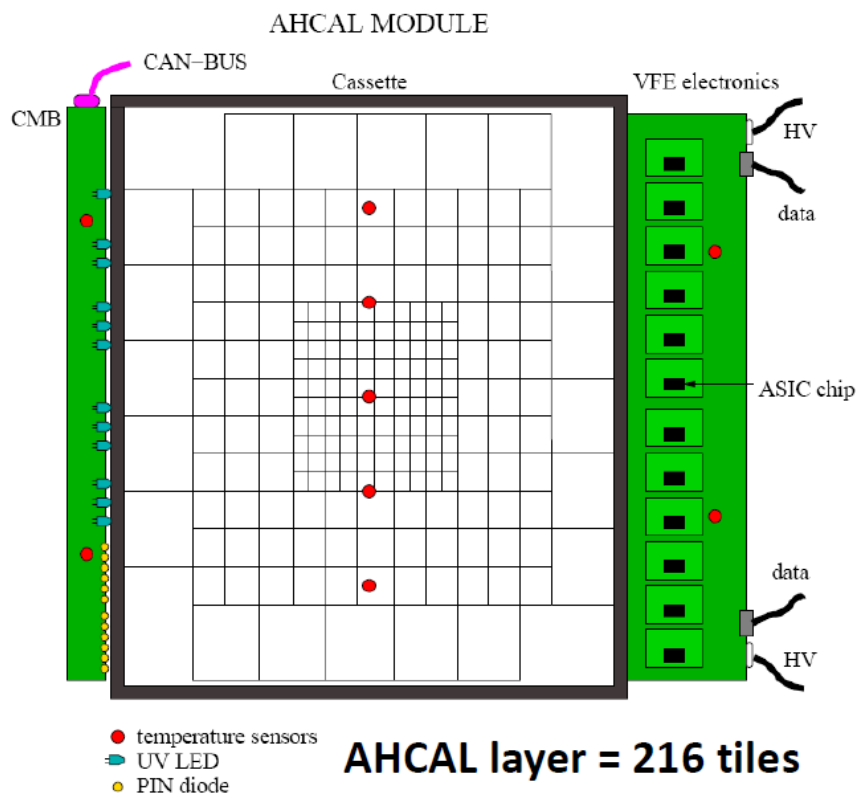


Figure 3.4: Schematic overview of a module. Visible are the tile pattern, the very-frontend electronics (VFE) and the calibration and monitoring board (CMB) attached to the side of the module. Temperature sensors are shown as red dots (two in the CMB, two in the VFE, and five inside the module) [36].

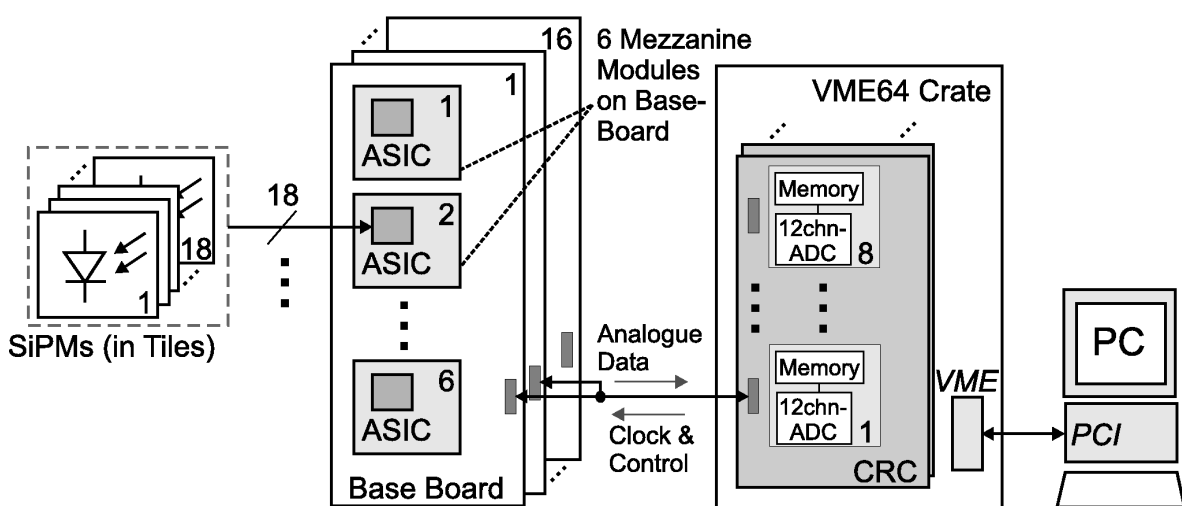


Figure 3.5: Schematic view of the read-out and data acquisition [36].

schematically in figure 3.5.

3.2.1 Silicon Photomultiplier

The active layers are read out with Silicon photomultiplier (SiPM) devices [39, 40], which have been produced by a collaboration of the National Research Nuclear University MePhI and Pulsar Enterprise. SiPMs are used instead of photomultiplier tubes due to the insensitivity to magnetic fields [41] and their small size, which allows to have the full read-out integrated into the detector, minimizing non-active material. In addition to their small size and their insensitivity to magnetic fields, they require only a bias voltage below 100 V in comparison to photomultiplier tubes which need high voltage (typically in the order of kV). SiPMs are a rather new technological development, and the AHCAL is the first experiment in high energy physics to use them in a large number, although other big experiments like CMS also plan their use [42].

A SiPM is essentially a matrix of pn-diodes, which are the pixels. Each pixel works like an avalanche photo diode (APD) in Geiger mode. When an electron-hole pair is created in the drift region of a pixel the electron and the hole will be accelerated by the applied electrical field and move to the multiplication region where it creates additional electron-hole pairs by ionization of the silicon. These secondaries again are accelerated by the electric field, create further electron-hole pairs, and this way an avalanche is generated. The avalanche continues until it is quenched by some high ohmic resistor. The time to build up the electrical field again, which is the minimum time interval between two avalanches in a single pixel, is called recovery time. In addition the resistors also decouple the individual pixels electrically from each other. However, due to the finite number of pixels of a SiPM and the recovery time of the individual pixels, the measured SiPM signals need to be corrected for saturation effects.

The SiPMs used for the AHCAL consist of 34x34 individual pixels (1156 in total) on an area of about 1 mm². A pixel has a 50 fF capacitance and a quenching resistor of 2-20 MΩ yielding a recovery time between 100-1000 ns. They are operated at reverse bias voltages in the range of between roughly 40 V to roughly 80 V, which is a few Volts above breakdown voltage, resulting in a gain in the order of 10⁶ photoelectrons per pixel. The geometrical efficiency is between 20 and 35 % and their quantum efficiency, which is a chance of a hit pixel starting an avalanche, is about 80 %. The tiles have been tuned by adjusting the operation voltage such, that the energy deposit of a minimal ionizing particle corresponds to 15 pixels (lightyield LY = 15 $\frac{\text{pix}}{\text{Mip}}$), which leads to an acceptable dynamic range and a reasonable signal-to-noise ratio. However, the SiPM gain and the response show a significant voltage and temperature dependence [43].

3.2.2 Very-frontend Electronics

The very-frontend electronics (VFE) consist of the Application Specific Integrated Circuit (ASIC) chips and the HCAL Base Boards (HBAB), which group the readout of up to six ASIC chips (one half module) and transfer the multiplexed data via a SCSI bus to the CRC boards in the VME crate. The ASIC chip is based on the ASIC chips of the CALICE Si-W ECAL [36].

Each ASIC can read out up to 18 channels for which the chip amplifies and shapes the signals from the SiPMs individually as explained schematically in figure 3.6. Each time a pixel of a SiPM fires a small charge is emitted, which is collected by a capacitor. The charge and discharge curve of the capacitor is then further shaped so that the maximum of the signal curve (hold curve) is proportional to the total signal. The signal curve is then sampled only at one point, which is the maximum for all signal strengths.

A schematic view of the ILC ASIC chip is shown in figure 3.8. The chip offers the option to choose one out of 16 preamplifier gains between 1 and 100 $\frac{\text{mV}}{\text{pC}}$ and one of sixteen CR-CR² shapers with shaping times between 40 ns and 180 ns per channel. Due to the shaping the signals from the SiPMs can be delayed such that the maximum of the signal is only reached after the generation of a trigger decision in a testbeam setup. The delay between trigger input and sampling of the shaped signal, the so called hold value, is adjusted per module due to the production tolerances of the electronic parts of each channel (see fig. 3.7). The large plateau region of the hold curves allow sufficient tolerance in adjusting this value per module, although the hold curves for the individual channels differ even inside a module [44].

In the AHCAL setup the ASIC is operated in two different modes with different amplification and shaping time. The physics mode (PM) which is used for data taking has a measured amplification of $G^{PM} = 8.2 \frac{\text{mV}}{\text{pC}}$ and a shaping time of 150 ns [36], which gives a sufficient dynamic range to record energy deposits from muons, which leave only a very small signal in every cell, as well as from electrons, which give the highest signals inside a single cell. In contrast to this the calibration mode (CM) has a gain of $G^{CM} = 92 \frac{\text{mV}}{\text{pC}}$ in order to resolve single pixels from single photon spectra, but only a shaping time of 40 ns, since LED pulses from the CMB system are short and no waiting for a trigger decision

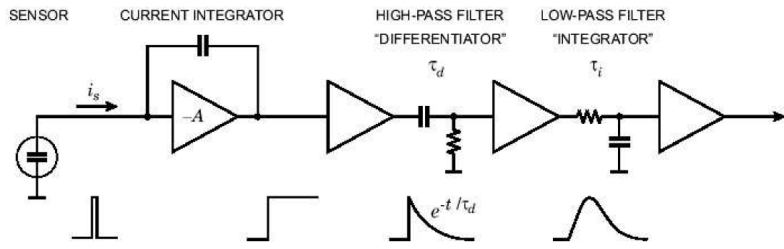


Figure 3.6: A simple pulse shaper using a CR differentiator as a high-pass and an RC integrator as a low-pass filter [44]. The illustrated signal shapes are valid for a delta-function like input pulse.

is necessary. The ratio of the response to a given signal in a cell in physics (A_i^{PM}) and calibration mode (A_i^{CM}) is called the intercalibration factor IC_i and can differ from the ratio of the amplifications due to the different shaping times:

$$IC_i = \frac{A_i^{PM}}{A_i^{CM}}$$

The ASIC chips also route the necessary bias voltages for the SiPMs. Since only a single external bias voltage is provided per half module, the ASIC chips have the ability to adjust this applied bias voltage for every SiPM by up to -5 V. The SiPMs of a half module have been selected to have breakdown voltages within this interval. The HBABs which house the ASICs amplify the signal by an additional factor of 2.

3.2.3 The Data Acquisition

The main component of the CALICE data acquisition system (DAQ) are the CALICE Readout Cards (CRC) which are build into a VME crate and connected to a common back-end panel. These cards comprise a 16 bit analog-to-digital-converter (ADC) for each of the 12 ASICs read out per layer, which digitizes the analog signal from the VFE before it is transferred to a computer for storage. The backplane has the possibility to read in trigger information from external detectors (cherenkov detectors, scintillator counters, etc) and distribute these trigger signals to all CRCs to have a common trigger decision and ensure the synchronous readout of the whole detector. The CRC boards also have an internal memory which can store the information of up to 2000 events, before the data needs to be transferred to the computer for storage. This buffer minimizes dead times in a testbeam measurement due to the read-out of the DAQ. The data is transferred to a computer using a fiber link.

3.2.4 The Calibration and Monitoring Boards

The Calibration and Monitoring Boards (CMB) are a calibration system that can be attached to the side of each of the active layers [45]. It was designed to determine calibration

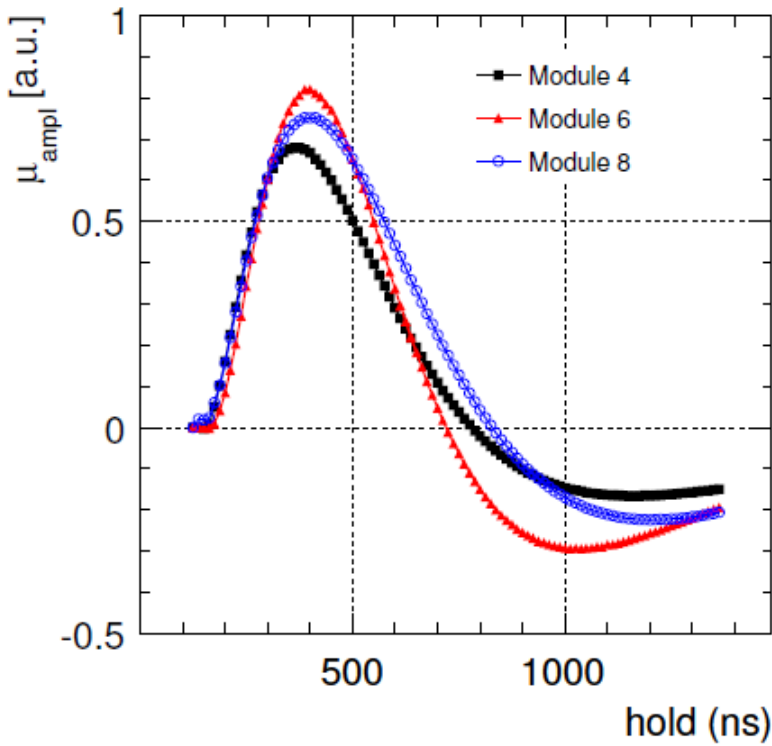


Figure 3.7: The hold curves in physics amplification mode for three different modules [44].

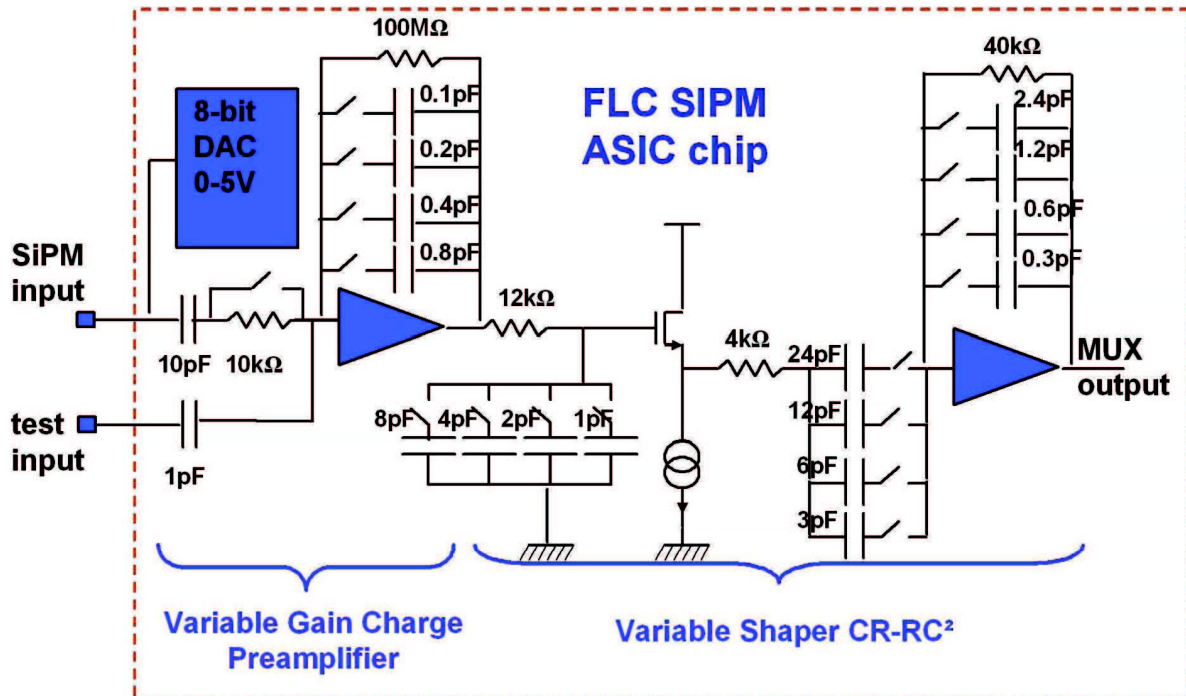


Figure 3.8: Block diagram of the ASIC chip for a single channel [36].

constants and saturation curves for every SiPM read-out channel. Each of the CMBs consists of an electronics board with a specially designed LED driver circuit steering 12 LEDs which can all be turned on separately. Each of the LEDs provides light for 18 tiles, which is routed via optical fibers to the individual tiles. Another fiber per LED is routed to a PIN diode to monitor the stability of the light output from the LEDs, but after installation of the PIN diodes it became clear that the measurement accuracy of the PIN diodes was not sufficient. Therefore information from the PIN diodes is not used in this analysis. The LED driver circuit was designed to provide short pulses (around 10 ns) with a nearly rectangular shape (fall and rise time around 1 ns), which are triggered by the DAQ to ensure synchronization of the emitted pulses with the read-out.

To fulfill its requirements, the CMB system must provide sufficient dynamic range in light output: it must be able to emit only a few photons into a cell to record single photon spectra, which are needed for the gain calibration of cells (see chapter 6), but it must also provide sufficiently high light intensities to fully saturate each SiPM. The system must also provide several light intensities in between these two extremes to determine precisely the saturation curves of each readout channel. It also gives the possibility to measure the response to a fixed LED light intensity in both amplification modes (CM and PM) of the ASIC, and can therefore be used to determine the intercalibration factors. The option to turn the LEDs individually on and off made it possible to measure the inter-tile crosstalk (see 6.9).

The second function of the CMB is the readout of the temperature sensors inside the active layers as well as the readout of two additional temperature sensors inside the CMB.

3.3 The Absorber

The active layers of the AHCAL have been operated with two different absorber structures: One is made up of approximately 1.7 cm thick iron plates, the other is made up of approximately 1 cm thick tungsten plates (see fig. 3.9). The properties of both materials are given in table 3.1. The exact setup of the absorber stacks is described in chapter 4. The iron plates are made of massive iron and fully cover the active layers, whereas the tungsten layers are made from tungsten alloy (92.99% tungsten, 5.25% nickel, 1.76% copper) due to mechanical reasons. For cost reasons they do not have quadratic shape but octagonal shape, so the tungsten plates do not cover the corners of the active layers [46]. The thicknesses of the absorber plates have been chosen such, that one absorber layer has approximately the same thickness in interaction length λ_{int} . But this results in very different thickness in radiation length X_0 .

Material	[unit]	Iron	Tungsten
Atomic number		26	74
Atomic mass	[g / mol]	55.845	183.84
Density	[g / cm ³]	7.87	19.3
Minimum ionization	[MeV / cm]	11.43	22.10
Nuclear collision length	[cm]	10.37	5.719
Nuclear interaction length λ_{int}	[cm]	16.77	9.946
Pion collision length	[cm]	13.59	6.936
Pion interaction length	[cm]	20.42	11.33
Radiation length X_0	[cm]	1.757	0.3504
Critical energy	[MeV]	21.68 (e ⁻) 21.00 (e ⁺)	7.97 (e ⁻) 7.68 (e ⁺)
Molière radius ρ_M	[cm]	1.719	0.9327
Muon critical energy	[GeV]	347.0	150.0

Table 3.1: Nuclear properties of iron and tungsten [17].



Figure 3.9: The tungsten absorber stack. It consists of 1 cm thick tungsten plates where the active layers are mounted in between.

CHAPTER IV

THE TESTBEAM SETUPS

This thesis investigates the differences of pions showers in two different absorber materials. But since both datasets were recorded at different testbeams at different particle accelerators it is crucial to identify the differences which are due to the different beamlines and detector setups. The following chapter will summarize both testbeam setups, at the FNAL MTest beamline for iron absorber testbeam data and at the CERN PS accelerator for tungsten absorber testbeam data, and the differences.

4.1 The FNAL 2008 and 2009 Testbeams

During the years 2008 and 2009 CALICE performed several testbeam campaigns with the AHCAL physics prototype, equipped with 38 iron absorber plates (see sec. 3.3) and the CALICE TCMT (Tail Catcher and Muon Tracker). Some of the testbeam campaigns were taken with CALICE ECAL prototypes mounted in addition in front of the AHCAL. The data was recorded at beam momenta from 1 GeV to 32 GeV. The detectors were placed on a movable stage, to record also showers, where the incoming particle is not perpendicular to the layers of the detector. This thesis will evaluate pion shower data taken at beam momenta from 2–10 GeV taken in July 2008 and electron shower data at the same beam momentum range recorded in May 2009. During both periods no ECAL was mounted before the AHCAL. In addition muon events recorded in September 2008 will be used for calibration purposes (see sec. 6.6).

The detector has been installed in sector MT6-2B at the MTest beamline of the Fermilab Testbeam Facility FTBF [47] (FNAL), together with auxiliary beam instrumentation. This additional beam instrumentation (see fig. 4.1) consisted of two $10 \times 10 \text{ cm}^2$ scintillators read out with photomultiplier tubes, three wire chambers, a $20 \times 20 \text{ cm}^2$ scintillator read out with a photomultiplier, and four scintillator plates of $40 \times 60 \text{ cm}^2$, each read out with a photomultiplier. The coincidence of the $10 \times 10 \text{ cm}^2$ scintillators was used as main trigger for the detector read-out, the $20 \times 20 \text{ cm}^2$ scintillator was used as multi-particle veto. The four large scintillator plates were assembled together to form a $1 \times 1 \text{ m}^2$ plate with a $20 \times 20 \text{ cm}^2$ hole in the center, utilized as beam halo veto. However, at least two sectors of the beam halo veto were read out with low efficiency, also the multi-particle counter was not

read out with high efficiency [11]. For the muon calibration runs, two scintillators with an area of $1 \times 1 \text{ m}^2$ each were installed, one in front and one behind the calorimeter. Their coincidence served as main trigger for the detector read-out during muon calibration data recording. For all other recorded data, the upstream scintillator has been removed from the beamline. The wire chamber information, which could provide information about the number of incoming particles and the beam size, cannot be used due to problems with the readout and calibration of the wire chambers.

The additional triggers, a beam halo muon veto and a multi-particle veto, are necessary due to the beam structure at the FNAL MTest beamline. Figure 4.2, which shows the beam composition during runs with an ECAL mounted in front of the AHCAL as a function of the beam momentum, already proves that there is a non-negligible amount of multi-particle events. There is no indication, that the beam for the runs recorded without an ECAL in front of the AHCAL, which will be analyzed in this thesis, have a composition that differs drastically from the one shown in the figure. The evaluation was done with one of the CALICE ECALs, which have a higher granularity than the AHCAL and can therefore identify two incoming tracks with much greater accuracy than the AHCAL. But since the ECAL testbeam prototypes covered only an area of roughly $30 \times 30 \text{ cm}^2$, this represents only the multi-particle events, in which particles arrive at the center of the AHCAL. Chapter 7 will show that in addition there is a huge number of showers, which are also accompanied by additional muons coming from the beam halo and depositing their energy in the outer region of the AHCAL.

The beamline provided also a differential cherenkov detector upstream of the experimental site, to tag the incoming particles [48]. Cherenkov detectors make use of the fact, that particles, that traverse a medium with a velocity which is faster than the velocity of light in this medium, will generate cherenkov light. The emitted light is then identified by a photomultiplier. The cherenkov detector at this beamline offers the possibility to set two separate thresholds for particle tagging (see details of the chrenkov detector in [11]). Typically those are set, such that one can distinguish particles lighter than a muon and pion and particles that are heavier than those [49]. However, at beam momenta of 6 GeV and below, only the lower of the two thresholds could be used due to the pressure limit of the gas tank and the safety regulations which allow only certain gas types to used. Typically the efficiency of the cherenkov detector to tag particles is close to one. Only at lowest momenta, the gas pressure of the cherenkov detector for the electron tagging has to be set so low, that eventually electrons do not generate sufficient amounts of cherenkov light. This leads to a small contamination of electrons in the pion samples at these energies.

4.2 The CERN 2010 Testbeam

At the end of 2010 the AHCAL, equipped with tungsten absorber, was used in a testbeam campaign at the CERN PS accelerator [50] to record particle shower data with a particle beam of mixed content in the energy range from 1 GeV to 10 GeV. This was complemented with an additional high energy testbeam at the CERN SPS to extend the range of recorded

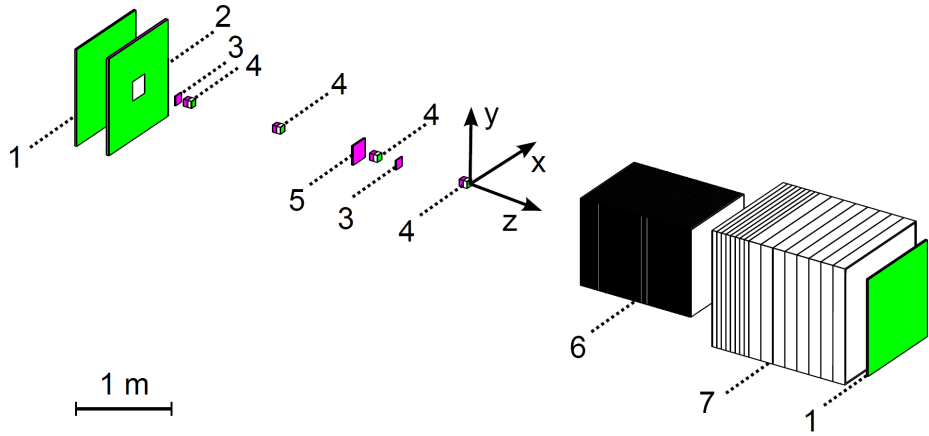


Figure 4.1: The experimental setup at MTest: (1) $1 \times 1 \text{ m}^2$ scintillators, (2) $1 \times 1 \text{ m}^2$ veto wall, (3) $10 \times 10 \text{ cm}^2$ scintillators, (4) drift chambers, (5) $20 \times 20 \text{ cm}^2$ multiplicity counter, (6) AHCAL, and (7) TCMT. While operated, the Si-W ECAL or the Sci-ECAL are located upstream of the AHCAL. The upstream $1 \times 1 \text{ m}^2$ scintillator is only installed during muon measurements. The z-axis indicates the beam position and direction. This figure is a visualization of the test-beam geometry implemented in the Mokka simulation explained in chapter 8 [11].

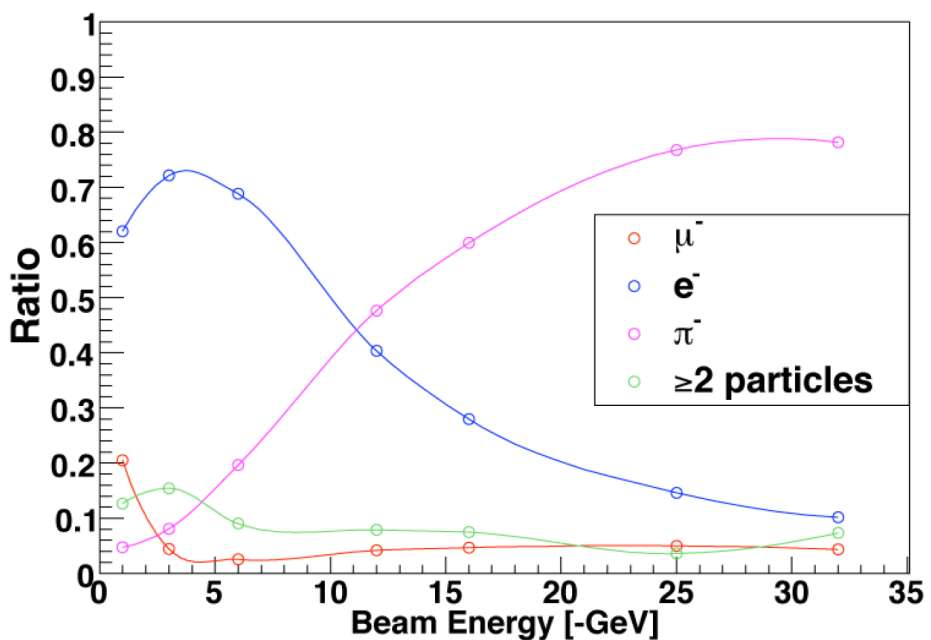


Figure 4.2: MTest secondary beam composition (in low-energy pion mode) measured with the CALICE detectors [11].

Momentum	Electron	Muon	Pion	Kaon	Proton
[GeV]					
1	0.0003	13.61	23.91	-.-	-.-
2	0.0001	3.38	5.92	-.-	-.-
3	0.0000	1.50	2.63	33.40	-.-
4	0.0000	0.84	1.48	18.64	-.-
5	0.0000	0.54	0.94	11.88	43.68
6	0.0000	0.38	0.66	8.24	30.11
7	0.0000	0.28	0.48	6.04	22.02
8	0.0000	0.21	0.37	4.62	16.81
9	0.0000	0.17	0.29	3.65	13.26
10	0.0000	0.14	0.24	2.96	10.73

Table 4.1: Tabulated Cerenkov pressures for CO₂ [46]

particle showers up to the energy of 300 GeV [46], but this high energy data is not evaluated in this thesis.

The testbeam period is split into a repair and commissioning time, taking place from September to the beginning of November in the T7 experimental area of the PS accelerator. At the end of this period also the muon calibration data was recorded (see sec. 6.6). During November the shower data was recorded for approximately three weeks, after moving the detector to the T9 area.

The CALICE AHCAL was mounted together with VME crates containing the read-out electronics and power supply on a steel platform, together with additional beam optics placed just in front of the detector. The detector consisted of 30 active layers, interleaved with tungsten absorber plates of 1 cm thickness (see sec. 3.3). The additional beam instrumentation mounted on the platform (fig. 4.3) consisted of two 10 x 10 cm² scintillators read out with photomultiplier tubes, which were used in coincidence as main trigger for the readout-out of the detector for beam events. Additionally three wire chambers were installed, but their information is not used in this thesis.

Upstream of the detector there was additional beam instrumentation provided by the testbeam facility, consisting of another unused wire chamber as well as two threshold cherenkov gas detectors, which provide the information on the particle identity during the recording of particle showers. However, due to safety regulations these could only be filled with CO₂, which limited in conjunctions with the pressure limits of the Cerenkov gas tanks (adjustable between bar 0 and 3.5 bar) the possibilities to set thresholds accordingly to calculations given in table 4.1. Also the cherenkov detectors have limited efficiency if the gas pressure is too low (see fig. 4.4), which affects the efficiency of the electron tagging at 2 GeV (see chap. 7).

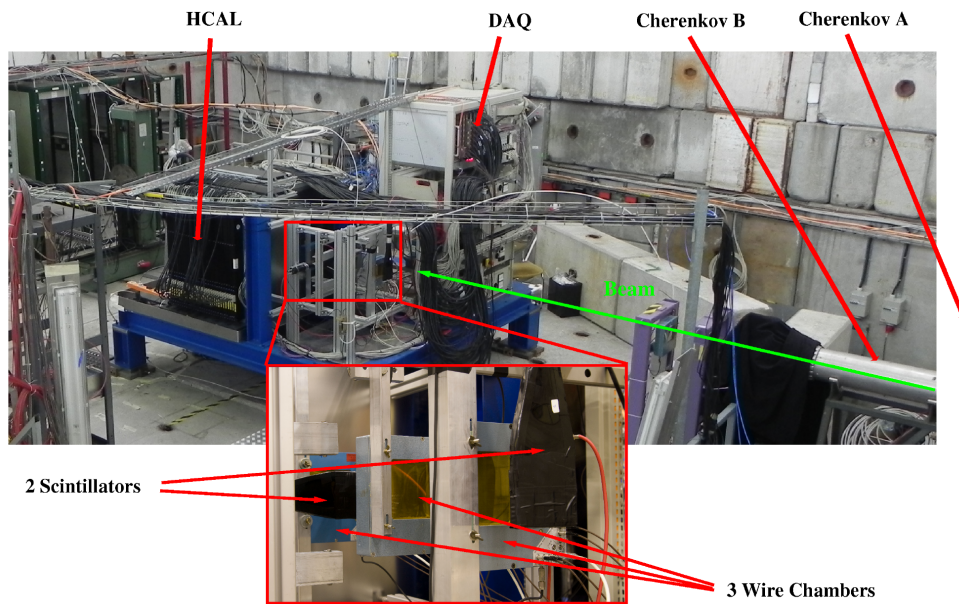


Figure 4.3: *Photograph of the experimental setup in the T9 beam line. The zoom-in shows a picture of the trigger telescope with three wire chambers and two scintillators [46].*

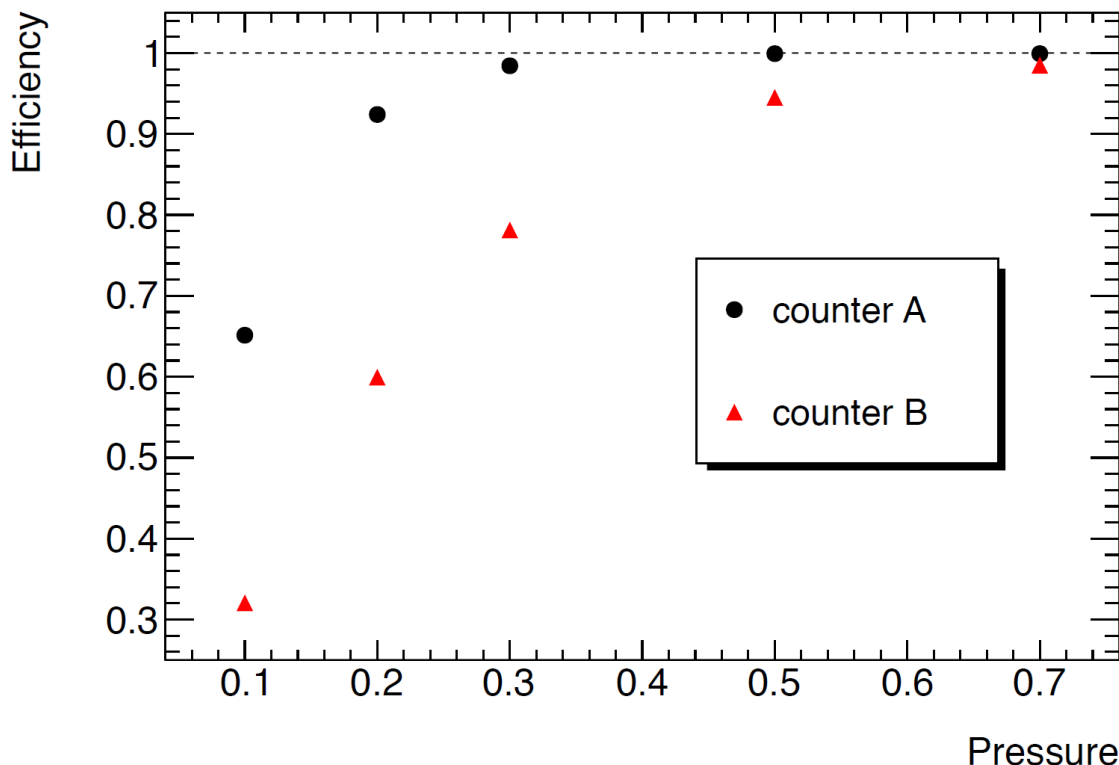


Figure 4.4: *Tagging efficiency of Cerenkov counter A and B as a function of the gas pressure (in bar absolute), obtained with electron samples at a momentum of 1 GeV [46].*

CHAPTER V

PHYSICS SIMULATION

In modern particle physics as well as in other research areas simulations have become an indispensable tool. They are not only used to investigate and cost efficiently optimize various design options, but can, to a limited extend, also be used as a guideline for the analysis of data. In this thesis the simulations will also guide the development of rejection criteria for events of the recorded data to select data subsamples that contain shower data of only one particle type (see chap. 7).

The GEANT4 framework [51] for the simulations of the physics processes inside a particle shower in conjunction with the MOKKA framework [52] for the simulation of detector geometries with realistic material compositions provides a set of tools necessary for the simulation of physics processes occurring in calorimeters during particle showers. The full simulation software is explained in detail in chapter 8, whereas this chapter will focus on different models to simulate hadronic interactions.

Electromagnetic interactions are calculated in GEANT4 by the standard EM package and a low-energy EM package [53]. Due to the manifold variety of different processes that can occur when a hadron hits a nucleus the simulation of hadronic interactions is much more complicated than the simulation of electromagnetic interactions, where only electrons, positrons and photons are involved (see chap. 2). Therefore several different models for the simulation of hadron interactions are provided by the GEANT4 framework, as well as several simulation backends for the treatment of the residual nuclei.

5.1 Hadron Cascade Simulation

Hadronic showers are more difficult to simulate than purely electromagnetic ones, due to the composite nature of both the projectile, which has a quark substructure, and the substructure of the hit nucleus, which is made up of nucleons, which also have a quark substructure. Also additional hadrons may be generated during the interaction, if the interaction energy is sufficient, resulting in a very large phase space of possible final states. Although several models exist to describe hadronic interactions, up to the present day there is no model that describes hadronic interactions in agreement with experimental data over

the full energy range.

Which aspects of the system dominate the interaction depends on the energy of the projectile. This can be illustrated in the simplified picture where the incoming particle is described by its deBroglie wavelength $\lambda_B = \frac{h}{p}$. With increasing projectile energy the wavelength becomes shorter and smaller structures become more important for the description of the interaction.

GEANT4 provides several hadronic interaction models, each valid for a given energy range, which are combined to “physics lists” (see sec. 5.3) to provide a description over the full energy range. These models are described in the following.

5.1.1 Cascade Models

If the particle energy is above a few hundred eV and does not exceed a few GeV, then the quark substructure of the nucleons can still be neglected, although the deBroglie wavelength of the projectile is comparable to the size of nucleons. In this case, the hadronic interaction can be described with the cascade models provided by GEANT4.

The cascade models track the path of the incoming projectile and that of secondaries emerging from the interaction through the nucleus (see fig. 5.1). The path length between interactions inside the nucleus is calculated from the modeled nucleon densities and parametrized cross-sections. The cascade is stopped when all particles are either absorbed, leave the nucleus or have an energy below a threshold. In this thesis only physics lists are investigated that use either the Bertini (BERT) or the Binary (BIC) cascade model, which differ in modeling of the nucleon densities and the treatment of hadron-nucleon interactions.

The GEANT4 implementation of the Bertini intra-nuclear cascade model [54] features not only the model of the cascade itself, but also modeling of excitons, a pre-equilibrium model, a nucleus explosion model for light nuclei, a model for Fermi break-up, a phenomenological fission model and an evaporation model at equilibrium. Its validity ranges from 200 MeV, where it is supplemented with a pre-equilibrium model, up to 5-10 GeV (dependent on the physics list), where the picture of the intra-nuclear cascade breaks down.

The Bertini model describes the nucleus as three concentric spheres with constant nucleon density with nucleons that follow a Fermi-gas momentum distribution at zero Kelvin to approximate the continuously changing nucleon density in nuclear matter. For each collision the model calculates the momentum of the struck nucleon, the type of reaction, and the four momenta of the reaction products, as long as the particle energy $E_{particle} > E_{cutoff} = 2$ MeV. The evaporation of the resulting highly excited nucleus is then treated by the built-in pre-equilibrium model using the exciton configuration as input parameter.

In contrast to this, the Binary intra-nuclear cascade model [55] features no built-in models for the treatment of pre-equilibrium or de-excitation and the exciton configuration

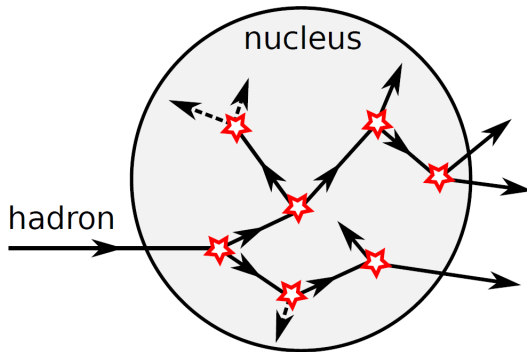


Figure 5.1: Schematic working principle of the cascade models: The projectile hadron and all secondaries emerging from the interactions are tracked through the nucleus and have further interactions calculated until they are absorbed or leave the nucleus [11].

has to be transferred to external models provided by GEANT4 for the treatment of corresponding processes. The validity range extends from 75 MeV up to 10 GeV (for pions only 1.5 GeV).

The Binary cascade model describes a nucleus as made up of nucleons with defined momentum and position. The momentum is chosen randomly between zero and the Fermi momentum, whereas the position is sampled from a Woods-Saxon distribution for heavy nuclei ($A > 16$) or from a harmonic oscillator shell model for light nuclei. In this model the interaction is treated using an intermediate step of short lived nuclear resonances which decay into the secondary particles emerging from the interaction. If no particle is above this kinetic energy threshold or the mean energy of the interaction participants drops below 15 MeV, the cascade is stopped and the remaining nucleus is further treated by the native GEANT4 pre-equilibrium and de-excitation models.

5.1.2 String Parton Models

The string parton models [56] in GEANT4 are used to simulate the inelastic scattering of particles with nuclei at energies beyond the validity range of cascade models where the quark substructure of nucleons must be taken into account. Instead of cascade models, a string excitation model is used to calculate the scattering. At the moment GEANT4 provides two different string excitation models, the diffractive string model or Fritiof model (FTF) and the quark gluon string model (QGS).

In the initial state of parton string models a nucleus is built, consisting of individual protons and neutrons. Each nucleon has position and momentum configuration sampled from either a density distribution of Wood-Saxon form for heavy nuclei ($A > 16$) or from a density distribution of a harmonic oscillator model for light nuclei, respectively. The result of an interaction between the primary particle and the nucleon are one or more excited strings, consisting of two endpoints with a defined quark content, which carry energy and

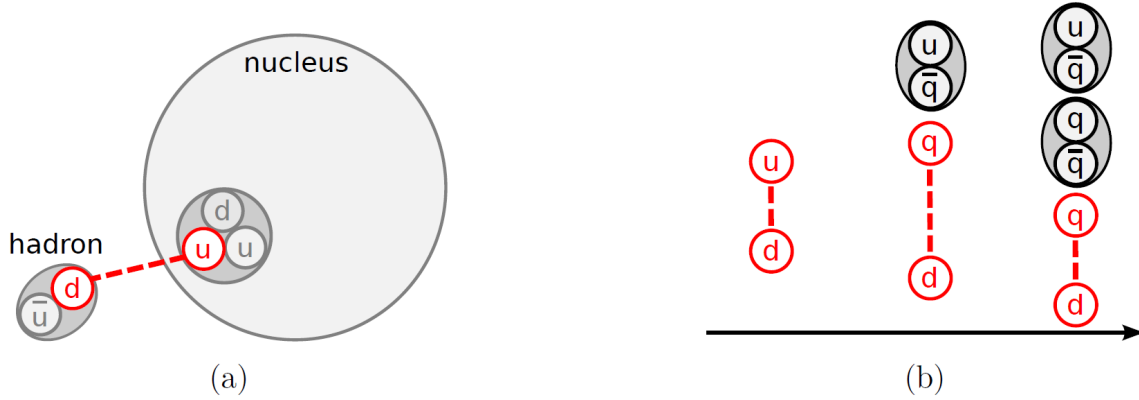


Figure 5.2: Schematic working principle of the string parton models: A string is formed between one of the projectiles and one of the targets quarks (left). The string then fragments via the generation of quark-antiquark pairs into hadrons (right) [11].

momentum, and an excited nucleus. The fragmentation of the strings into hadrons is handled by a fragmentation model, the interactions of secondaries with the excited nucleus are calculated by a cascade model and the simulation of de-excitation of the nucleus is done by the native GEANT4 nuclear fragmentation, pre-compound and nuclear de-excitation models. This is schematically shown in figure 5.2

Both models differ in the approach of modeling the string formation and the fragmentation function they use for string fragmentation. In the diffractive model the interaction probability is calculated based on the impact parameter, the center of mass energy of the interaction, and the elastic and diffractive cross sections, with scattering particles only exchanging momentum. A string is then formed and the quarks of the original hadron are assigned randomly to one of the two string endpoints. In contrast to this, the quark gluon string model uses two types of strings, longitudinal strings, which represent the momentum transfer, and transverse strings, which model color exchange via pomerons.

5.1.3 Chiral Invariant Phase-space Model

The chiral invariant phase space model (CHIPS) is a quark-level event generator for the fragmentation of hadronic systems into hadrons [57]. Since the phase space refers to the phase space of massless partons, only the three lightest quarks (u, d and s) are considered in this model. The model uses Quasmons, an excited intermediate state of massless quarks that are asymptotically free, to model the excited nuclear matter. This is similar to the QGS model, but with an additional string-at-rest object, the Quasmon. It uses a different split up of the projectile and the target into partons and the partons are massless in contrast to the QGS model. The Quasmon is initially formed from the partons assuming some critical energy of the system. An increase of the Quasmon energy beyond this critical energy results not in a further increase of the temperature of the system, but instead of the generation of new quark-antiquark pairs. The Quasmon then decays gradually via quark

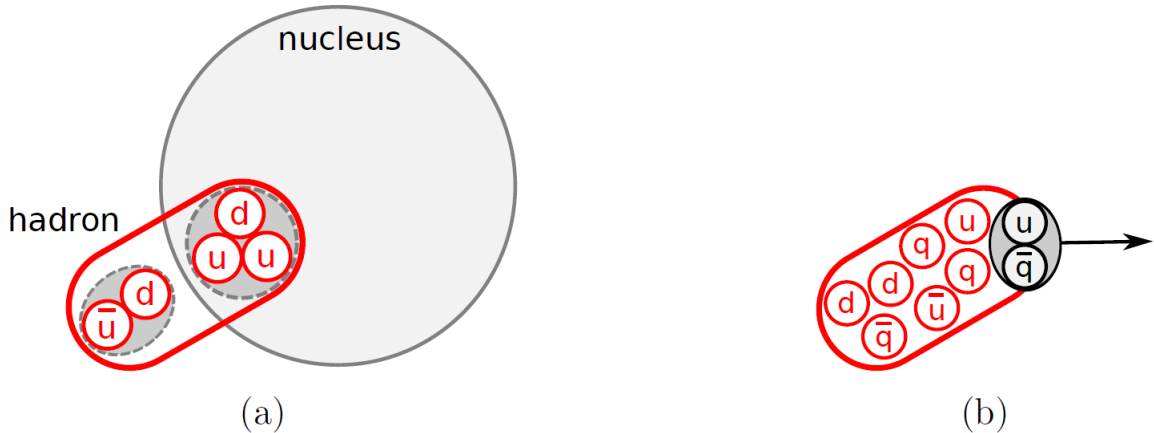


Figure 5.3: Schematic working principle of the CHIPS model: The Quasmon is formed from the quarks of the projectile and the target (left) and it decays via quark fusion (right) [11].

fusion and emission of hadrons and by double quark exchange with neighbor nucleons (see fig. 5.3).

This model is applicable over the full energy range since it describes the interactions both at the nucleon and at the quark level and can also handle the de-excitation of the nuclei. It is also used in other models to describe processes that cannot be treated in these models like photo nuclear reactions.

5.1.4 LEP

The low energy parametrized model LEP is a model which utilizes fits to experimental data instead of a theoretically motivated hadronic model. It is an adaptation of the old GEISHA hadronic package to C++, with several corrections and improvements. No detailed interactions are calculated and energy is only conserved on average but not for each individual event. Therefore this model is nowadays only used because of its low computation time and to fill gaps of validity ranges of other models (transition region between parton-string and cascade models). It is also used for particles which cannot be described by other models, e.g. long-lived hyperons [58].

5.2 GEANT4 Pre-compound and De-excitation Models

The native GEANT4 pre-compound and de-excitation models are used as backends for the parton string models and for the binary cascade and handle the fragmentation of residual nuclei. The pre-compound model is based on a semi-classical exciton model and describes the emission of protons, neutrons, and light compound fragments up to α -particles until the nuclear system reaches equilibrium. Further emission of evaporation particles, like

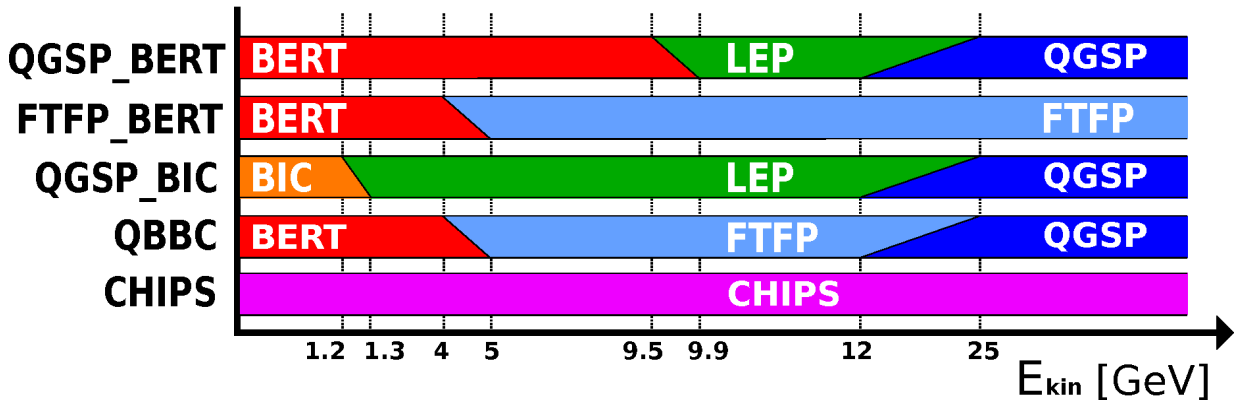


Figure 5.4: Schematic representation of the model content of the investigated GEANT4 physics lists. In the overlap regions one of the two models is chosen at random.

photons and nuclear fragments, as well as fission and nucleus explosive break-ups are then simulated with the native GEANT4 equilibrium de-excitation models [59].

5.3 Physics Lists

The physics lists QGSP_BERT, FTFP_BERT, QGSP_BIC, and QBBC all combine several of the above mentioned hadron physics models, each used in a given energy range. The different lists used for this thesis models are shown in figure 5.4 with the validity ranges of the individual models for pions [60]. The CHIPS physics list uses the CHIPS model over the full energy range. In addition to the models used for the inelastic hadron scattering, all physics lists include also models for elastic scattering, ionization, and various other processes which occur in a hadron shower.

5.4 Precision Neutron Calculations

The physics lists QGSP_BERT, FTFP_BERT, and QGSP_BIC offer the option of high precision neutron tracking (_HP option), but at the cost of increased computation time. This increased accuracy of the neutron description is achieved by using high-precision data based lookup tables for the cross sections of neutron interactions below 20 MeV. It is expected, that using this additional information yields a much better description of the showers in neutron rich materials like tungsten. The physics list QBBC has a comparable neutron tracking part with less precision, but also with less computation time needed. The CHIPS physics list is somewhat special, since it has also its own neutron transport calculations, however this is much simpler than the HP-package and also neutron capture is not modeled as a separate process, but as part of the CHIPS neutron inelastic package.

CHAPTER VI

DETECTOR CALIBRATION AND CHARACTERIZATION

The data recorded by the CALICE DAQ system for the energy deposit in a single cell is measured in ADC counts, but this scale cannot be directly compared between different channels. Therefore the measured amplitudes are converted a physics related energy scale. The conversion of a cell amplitude in ADC counts to a physics related energy scale like MIPs or GeV depends on the electronics chain of this individual channel as well as on environmental parameters like temperature. For the AHCAL the energy of a minimal ionizing particle (MIP) has been chosen as energy scale. The conversion requires a calibration of every individual channel to equalize the individual energy measurements in ADC counts to the common MIP scale, which relates the cell amplitudes to a well understood physical process, which is almost independent of the environmental conditions. The MIP scale differs from the GeV scale by a constant factor (see chap. 8).

One of the challenges of a highly granular calorimeter with analog readout like the CALICE AHCAL physics prototype with SiPMs is the synchronous and stable calibration of the high number of readout channels. However, due to the large number of channels, and SiPMs originating from different production batches, this procedure must be automated and therefore requires robust algorithms to extract the calibration data. Besides a temperature dependent factor to convert from the ADC to the MIP scale, the amplitudes are also corrected for saturation effects of the SiPMs, due to their limited number of pixels. The cell amplitudes are converted to the pixel scale, then the saturation correction is applied, and afterwards the desaturated amplitudes are converted back to the ADC scale and finally to the MIP scale. The full calibration can be expressed as:

$$A_i[\text{MIP}] = f_i^{-1} \left((A_i[\text{ADC}] - \text{Ped}_i[\text{ADC}]) \cdot \frac{\text{IC}_i}{G_i[\frac{\text{ADC}}{\text{PIX}}]} \right) \cdot \frac{G_i[\frac{\text{ADC}}{\text{PIX}}]}{\text{IC}_i} \cdot \frac{1}{M_i[\frac{\text{ADC}}{\text{MIP}}]}, \quad (6.1)$$

where A_i is the amplitude, f_i^{-1} is the inverse of the saturation function, Ped_i is the pedestal, IC_i , G_i , M_i are the intercalibration, gain and MIP constants of the i -th cell. Each factor, and how they are obtained, is described in the following paragraphs.

Also described is a measurement of the inter-tile crosstalk and a procedure to identify non-working or dead and very noisy readout channels, which will be excluded from analysis. These measurements are also used for the simulation of the detector (see chap. 9).

All used calibration constants can be found in the official CALICE database. The location of the individual database folders is given in Appendix A.

6.1 Offline Calibration of the Temperature Sensors

In addition to an online calibration of each temperature sensor, which is just an offset, an offline calibration is applied. This is necessary since occasionally the measured values of individual sensors show unphysical jumps. This jumping sensor behavior was already observed at earlier testbeams and points to an instability of the temperature sensors. However, the procedure is slightly different for both testbeam setups. For the CERN data the temperature readings are filtered by checking if the read temperatures are within the interval from 0°C to 45°C. If not, these readings are replaced with the module average temperature. For the FNAL data all the temperature readings are then replaced with the module median temperature. Since the temperature correction of the calibration needs only the difference to a reference temperature where the calibration was recorded, a precise measurement of the absolute temperature is not necessary.

Figure 6.1 shows the mean layer temperature as a function of the layer for a single run from each testbeam setup. The CERN data has been recorded at lower temperatures and shows also a more pronounced profile along the detector. Figure 6.2 shows the mean detector temperature as a function of the time from the start of the testbeam campaign. There is a huge difference in the average detector temperature between the runs recorded at CERN and the runs recorded FNAL, both in summer 2008 and in winter 2009. Also visible are the day and night cycles. The individual runs used for the analysis are also marked (for CERN data, electrons and pions are selected from the same runs). Both plots indicate that a temperature correction has to be applied to the recorded data for a precise calibration.

6.2 Pedestal Subtraction

The pedestal values used for the pedestal subtraction in formula 6.1 are obtained from the individual data taking runs. Every data taking run starts with 500 pedestal trigger events, where the cell amplitudes are read out at random times when no particles are showering in the detector. In addition there are small periods, typically after 10000 beam events, in which 500 events with pedestal triggers are recorded (the exact numbers were set to match with the spill structure of the beam and are therefore different for every testbeam). The value Ped_i in ADC counts used for pedestal subtraction is then the mean amplitude of the

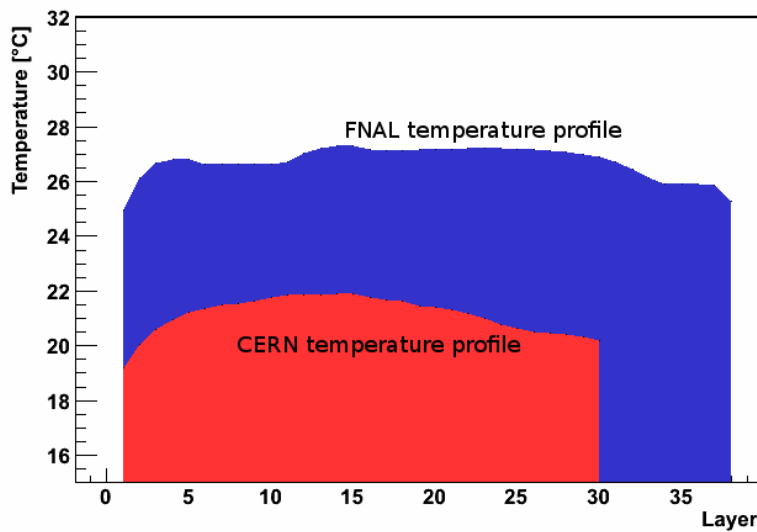


Figure 6.1: The average longitudinal temperature profiles for the AHCAL for a single run from the CERN testbeam (red) and from the FNAL testbeam (blue).

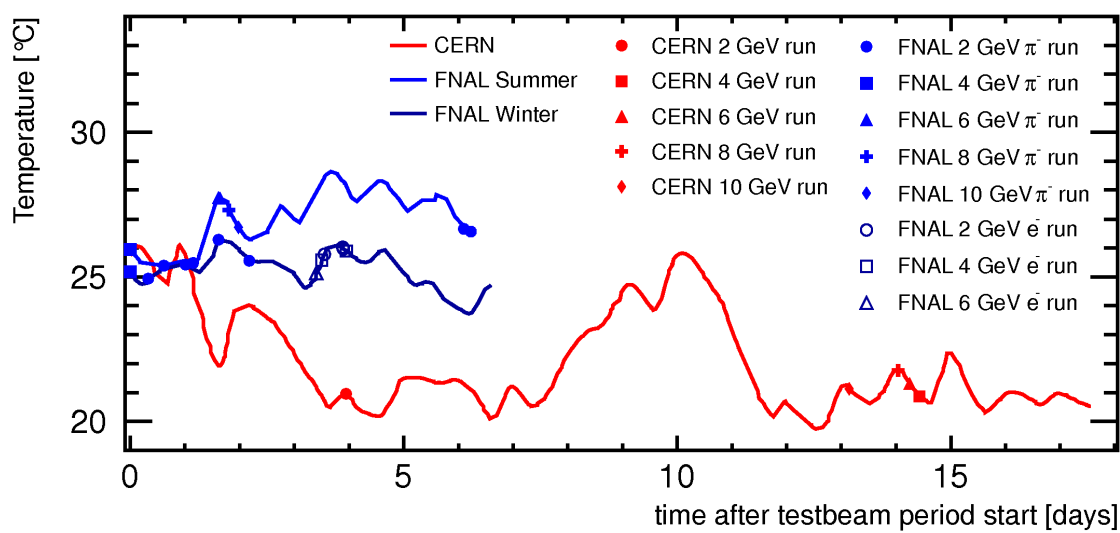


Figure 6.2: The mean detector temperature as a function of time from the beginning of every testbeam campaign. Also marked are the individual runs used for analysis. For the CERN testbeam electrons and pions are selected from the same runs.

last period of pedestal events for every individual channel i .

6.3 Gain Calibration

The gain constants G_i describe how many ADC counts are measured per fired pixel for a single cell. It is measured by injecting very small light intensities with the CMB system (see sec. 3.2.4) into each of the tiles, while using the high amplification of the calibration mode of the readout electronics (see sec. 3.2.2). This measurement is done in calibration mode to achieve the amplification needed to resolve single pixels (see fig. 6.3), which are then fitted with a sum of Gaussians. The algorithm used to fit these single photon spectra is described in detail in [61]. The distance between two consecutive peaks is the gain of a single measurement at a given cell temperature. All the measurements for a given channel are then averaged to have an average gain constant $G_{i,0}$ at an average cell temperature $T_{i,0}$.

In addition, the gain of a given cell i has a significant dependence on the temperature T_i which needs to be corrected for. It can be described by a linear function:

$$G_i(T) = \left(\frac{dG}{dT} \right)_i \cdot (T_i - T_{i,0}) + G_{i,0} \quad (6.2)$$

This dependence $(\frac{1}{G} \frac{dG}{dT})_i$ has been measured and found to be on average $-1.7 \frac{\%}{K}$ with a low spread of $0.3 \frac{\%}{K}$ [43]. This mean value is then applied as the slope of the linear correction for all cells.

Figure 6.4 shows the channel-wise comparison of gain constants G_i used for the calibration of the FNAL and CERN testbeam data. Both sets have been corrected to a temperature of 25°C . Both calibration sets are in good agreement with each other taking into account, that damaged ASICs and HBABs were exchanged during the commissioning at CERN. This also proves, that the temperature correction works well, since the temperatures of the calibration data differed by several degree Kelvin. Channels for which no gain constant could be measured, e.g. due to broken LEDs, are assigned with a default value of $400 \frac{\text{ADC}}{\text{PIX}}$ at a temperature of 25°C .

6.4 Inter-Calibration

The inter-calibration constants IC_i describe the ratio of the two amplification modes of the readout electronics for every individual channel.

$$IC_i = \frac{\text{Amp}_{\text{calib-mode}}}{\text{Amp}_{\text{phys-mode}}} \quad (6.3)$$

They are measured by injecting several fixed light intensities, which are in the linear response range of the SiPM, into the tiles in both amplification modes. The responses in both

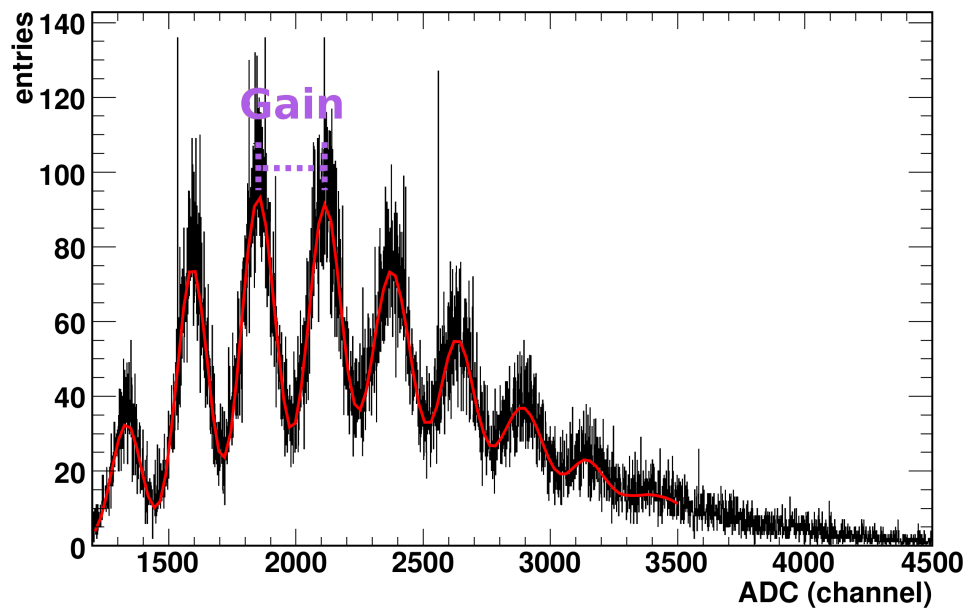


Figure 6.3: An example of a single pixel spectrum of a SiPM with a multi-gaussian fit [61]. The distance between two consecutive peaks is the gain constant.

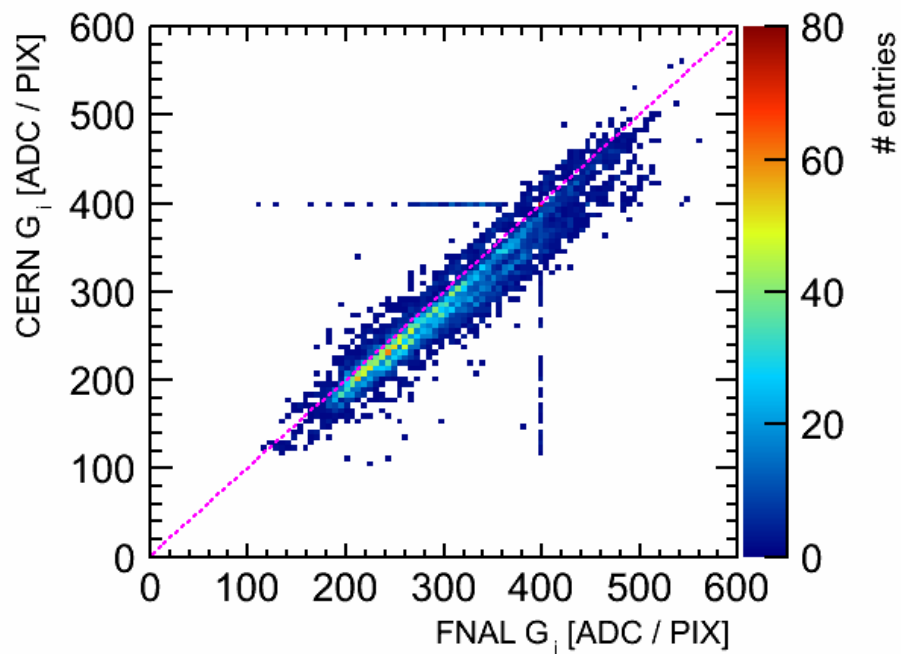


Figure 6.4: Comparison of the gain constants $G_i(25^\circ C)$ at CERN and FNAL testbeams.

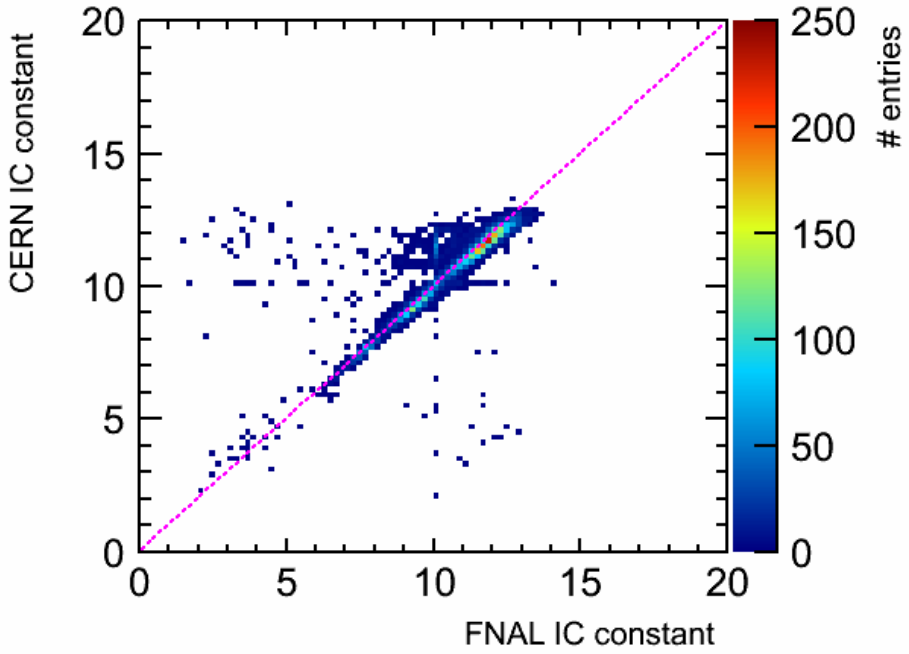


Figure 6.5: Comparison of FNAL and CERN inter-calibration constants. If no value could be measured a default ratio of 10 is used between the physics and the calibration amplification modes.

modes are then approximated with a linear function. The inter-calibration constant is then the ratio of the two slopes in both amplification modes. If no value could be measured, e.g. due to a broken LED, a default IC constant of 10 is used [11]. Figure 6.5 shows the comparison of the inter-calibration constants for both testbeam periods. Like for the gain constants a good correlation between the constants from both testbeam periods is found.

The inter-calibration constants are then used to calculate the corresponding gain constants for the physics amplification mode, since the gain constants can only be measured with the high calibration amplification mode.

6.5 Saturation Correction

Since the SiPMs incorporate only a finite number of pixels and a recovery time for every pixel, one has to correct saturation effects of every cell response. The saturation curves of the bare SiPMs, not mounted to tiles, have been measured at ITEP. Since only the curves for the bare SiPMs are known, these saturation curves have to be adjusted for the geometrical mismatch of the WLS-fiber of the tile and the SiPM surface after they have been glued to the tiles. This mismatch results in pixels that cannot be illuminated by light from the WLS. However, the maximum number of pixel for a SiPM is then no longer a well defined number, since inter-pixel crosstalk may fire pixels that are not directly illuminated by the WLS-fiber. In previous analyses the saturation curves for the bare SiPMs are all scaled with a factor of 0.8. Instead, a measurement of these scaling factors for individual

cells is presented and applied for this thesis.

To estimate the scaling factors for every SiPM individually, LED data has been evaluated: In special calibration runs, the LED light output is increased stepwise until the maximum light intensity is reached. However, this measurement cannot be used to determine the saturation curves directly as the non-linear dependence on the LED light output on the LED voltage is not sufficiently known. The runs are fully reconstructed (pedestal subtracted, conversion to the MIP scale and temperature corrected) but no saturation correction is applied. Since the maximum pixel amplitude is smeared by noise, not the highest response measured is used, but the highest peak in the response. In order to remove those channels, which did not reach saturation, this highest peak is only taken if the peak is at maximum 10 MIP lower than the maximum response measured for this cell, otherwise the measurement for this channel is discarded. The measured maximum amplitude is then converted to the pixel scale using the temperature corrected gain values. The saturation correction scale factor is the ratio of maximum amplitude in pixels and the nominal number of 1156 total pixels of a SiPM.

For some channels the ADC gets saturated before all pixels of a SiPM are illuminated, but those channels are easy to identify since the bin with the highest amplitude shows a much higher number of entries, than the surrounding bins and this peak is not smeared by noise. Figure 6.6 shows two example channels: one where SiPM saturation is reached and one where ADC saturation is reached before. If no saturation correction scale factor could be estimated (due to broken LED, discarded measurement, etc) or ADC saturation was reached first, a default scaling factor of 0.8 is used, which is also used for cells, where a scaling factor below 0.4 was measured. Cells for which a factor > 1 was found were replaced with a factor of 1. Factors above 1 are either due to rounding (measured factor < 1.1), or a default value for the gain constant or the inter-calibration was applied for this cell. Figure 6.7 shows the measured 5833 saturation correction scale factors which could be extracted from a single run. Further filtering and the combination of more data could increase the number measured saturation correction factors.

In parallel the scaling factors for a handful of central cells have been estimated using electrons at higher energies [35]. These values show a good agreement with the estimation from LED data and are used for those few cells where they are available.

The scaled saturation curves are fitted with a double exponential function described in [61] and 250 points for every function are stored. The last two points are extrapolated with a linear function to higher values. The inverse of these points, together with the linear extrapolation is used for the desaturation. If the amplitude that has to be desaturated is in between these stored points, the desaturation factor is calculated by a linear interpolation of the closest two stored points. The linear extrapolation of the saturation curves ensures the existence of a desaturation factor also for large amplitudes. For the relatively low hit energy densities encountered for shower energies investigated in this thesis, the systematic error introduced by the extrapolation should be negligible.

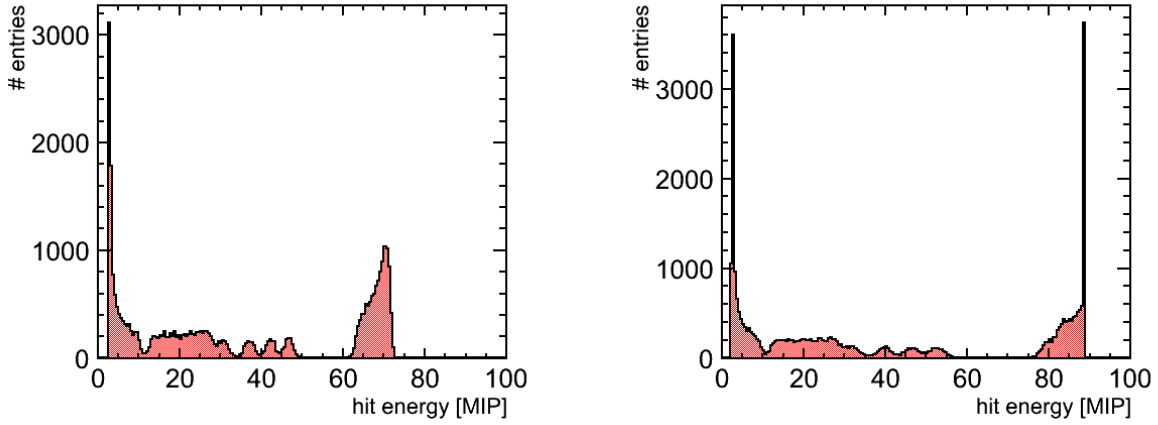


Figure 6.6: Two examples for saturation in readout channels for a run with LED light of increasing intensity: the left plot shows a channel were the SiPM gets saturated, whereas the channel on the right reaches ADC saturation before the SiPM is saturated.

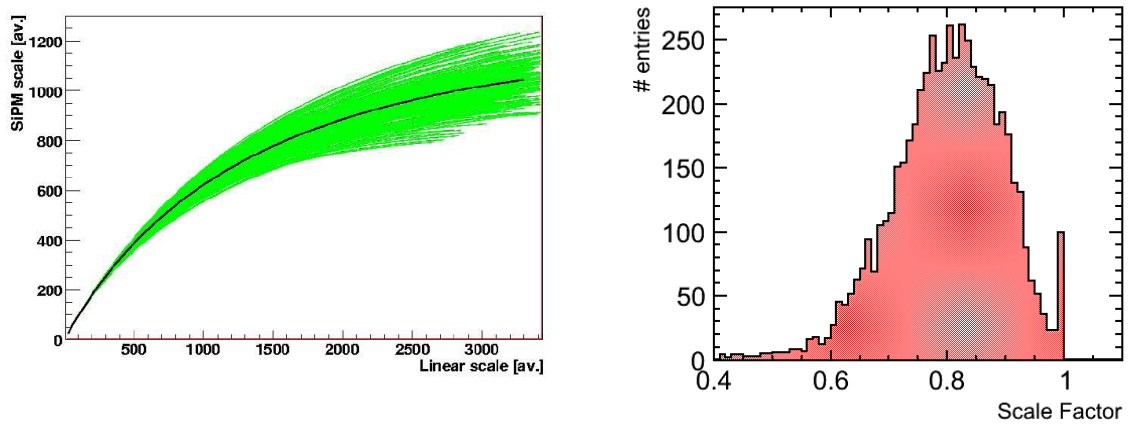


Figure 6.7: Left: Response of 500 arbitrary SiPMs from the AHCAL (green lines) and their mean response (black line) with respect to a linear photomultiplier tube scale [62]. Right: The distribution of 5833 saturation correction scale factors measured in a single run. Scale factors below 0.4 are replaced with a default value of 0.8 (not included in plot) and scale factors above 1.0 are replaced with this value (see text).

6.6 Cell Equalization with Muons

Since every channel has its individual ADC scale, all channels need to be normalized to a common physics scale. The AHCAL utilizes muons as minimum-ionizing particles for this normalization. Therefore long data taking runs with muons only are recorded. The response of a single cell to these muons is approximated with a convolution of a Landau and a Gaussian. The most-probable-value (MPV) extracted from this convoluted function is the MIP constant $M_i(T_0)$ of the i -th channel.

However, if all hits from muon runs are considered, this includes also noise hits. If a convolution of a Gaussian and a Landau distribution is used as approximation for these spectra, this will lead to unstable fits and wrong MPV fitting results, since the spectrum of a single cell will also contain hits due to noise. Therefore a filtering based on an existing CALICE tracking algorithm is applied first. This algorithm finds track segments consisting of at least three hits in a straight line (see sec. 7.5 for more details). Only the hits which are found to be on a track are further evaluated. However, this filtering could be improved with a more sophisticated algorithm for muon track identification.

The fitting procedure is very sensitive to initial parameters of the fit. Two consecutive Gaussian fits are used (second one in the range of $\pm 1\sigma$ around the mean of the first fit) to estimate the initial value for the MPV. The initial values of the other free fit parameters are the total number of entries in the spectrum, the natural width of the Landau (0.06 times the initial MPV) and the width of the second Gaussian fit. The spectrum of the filtered hits is fitted for every channel in the range from 0.6 to 2.0 times the initial MPV (fig. 6.8) and the MPV of the convoluted function is extracted and used as MIP constant. All fits have been inspected manually. Cells for which the fit failed are added to the list of bad cells.

As the gain constants, also the MIP constants show a significant temperature dependence, which can be described by a linear function for the temperature differences which occur in the data analyzed in this thesis (see [11]):

$$M_i(T) = \left(\frac{dM}{dT} \right)_i \cdot (T_i - T_{i,0}) + M_{i,0} \quad (6.4)$$

The mean value of the temperature dependence $\langle \frac{1}{M} \frac{dM}{dT} \rangle$ has been measured as $-3.7 \frac{\%}{K}$ [11]. However, due to the limited muon data, there is not sufficient statistics to measure the slope for every channel individually with the necessary precision.

Another method that has been developed in the past is the application of layer-wise slopes. These slopes are estimated with muon events from the normal data taking. But since the muons from the normal runs hit only few cells in each layer (the beam size is typically not larger than 2-3 cells in diameter), this method cannot provide reliable results for the outer cells [63].

Therefore a different method has been developed for this thesis: LED events, which are constantly recorded during data taking, and which are available for every cell with sufficient statistics, are used to measure the relative MIP constant temperature dependence for the

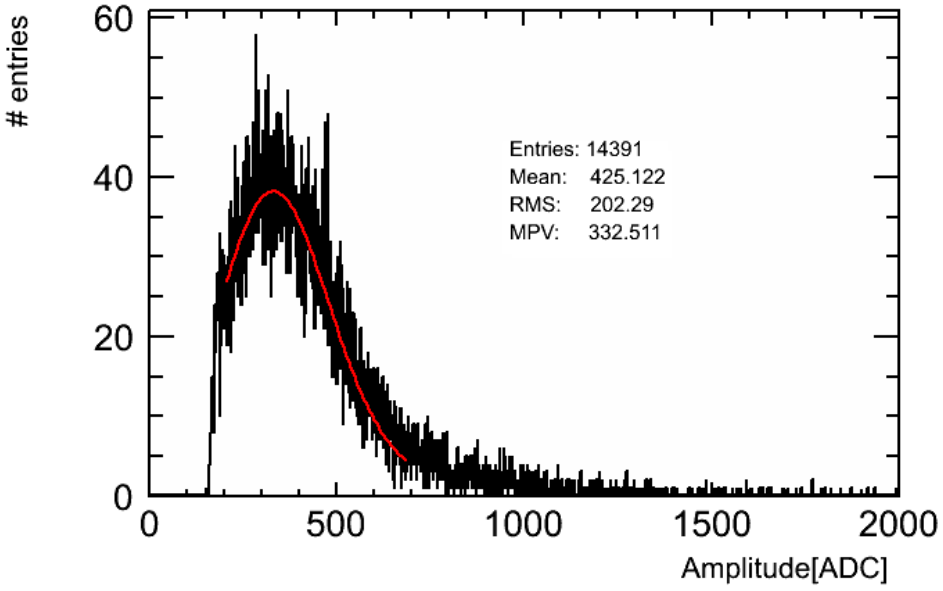


Figure 6.8: The distribution filtered hits in muon calibration data of a single channel in ADC counts. The distribution has been fitted with a convolution of a landau and a gaussian distribution. The mean and the RMS of the histogram are given as well as the most probable value of the fit.

individual channels. LED events can be used instead of muon events, as the relative MIP constant temperature dependence is equal to the relative temperature of any signal of fixed strength if both are measured at the same temperature. The events undergo the full CALICE reconstruction chain except for the MIP temperature correction. For every run, the mean amplitude of the LED events is stored and studied as a function of the mean cell temperature (the uncertainty on the temperature measurement of a single cell is unknown).

Due to instabilities of the LED system, the values have to be filtered for unreasonable jumps of the mean amplitude between runs. This is done with a very simple algorithm, which calculates the mean M_{tot} and the RMS R_{tot} of the distribution of the mean LED amplitudes. It also calculates the mean M_σ and the RMS R_σ of the distribution of those mean LED amplitudes which are within $\pm 1 R_{\text{tot}}$ of M_{tot} . If $R_{\text{tot}} > 2 R_\sigma$, then all mean amplitudes which are outside of the interval $M_{\text{tot}} \pm 5 R_{\text{tot}}$ are excluded, otherwise all mean amplitudes outside the interval $M_\sigma \pm 5 R_\sigma$. The mean response as a function of temperature is then approximated with a linear function (see fig. 6.9) and the slope of the fit relative to the MIP constant s^{rel} is used to calculate the absolute slope in ADC counts:

$$\left(\frac{dM}{dT} \right)_i = s_i^{\text{rel}} \cdot M_{i,0} \quad (6.5)$$

However, the amplitudes of LED events do not only have the temperature dependence of the SiPM but instead a convolution of the SiPM temperature dependence with the temperature dependence of the light output of the LED system, which is unknown. To estimate the temperature dependence of the LED system, the convoluted slopes calculated with the LED events are used to reconstruct pion runs of a given energy. It is assumed that the temperature dependence of the LED system can be linearized for the temperature

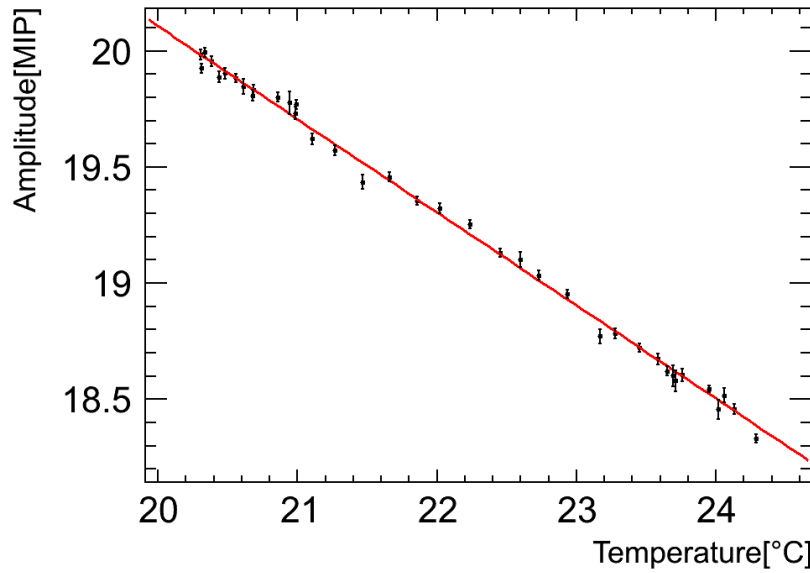


Figure 6.9: Shown is the mean amplitude of LED events as a function of the mean cell temperature of that LED events for a single cell. The error bars are purely statistical, since the error on the temperature measurement of a single cell is unknown. The red line shows the linear approximation.

intervals needed for this thesis. The remaining relative dependence of the mean amplitude of the pion events on the temperature $s_{\text{LED}}^{\text{rel}}$ has been measured to be $-1.13 \frac{\%}{K}$ and is added to each of the measured relative slopes from the LED events:

$$\left(\frac{dM}{dT} \right)_i = (s_i^{\text{rel}} + s_{\text{LED}}^{\text{rel}}) \cdot M_{i,0}. \quad (6.6)$$

Figure 6.10 shows the mean pion event amplitudes reconstructed with the convoluted slopes and a linear approximation, which shows a remaining temperature dependence as well as the deconvoluted slopes with the linear approximation, which are consistent with no remaining temperature dependence.

The distribution of the resulting relative slopes is shown in figure 6.11 and the mean value agrees with $-3.7 \frac{\%}{K}$. The width of the distribution cannot be explained with the quality of the fits alone and supports the hypothesis, that a cell-wise relative temperature correction will improve the calibration accuracy.

Both set of MIP constants for the FNAL and the CERN testbeams periods have been measured as described above. However, due to too large instabilities of the LED amplitudes during the FNAL testbeam, not the individual slopes have been used, but instead the slope in ADC counts is calculated with the mean slope of $-3.7 \frac{\%}{K}$. Also for the CERN testbeam data, 19 broken LEDs were found (10 in layer 18), as well as 96 channels, where the fits failed. Those cells are attributed with a default relative slope of $-3.7 \frac{\%}{K}$ and their respective absolute slopes. However, due to the small temperature range that is covered by the analyzes CERN data, no significant difference is observable between the LED based cell-wise MIP temperature correction and the global MIP temperature correction.

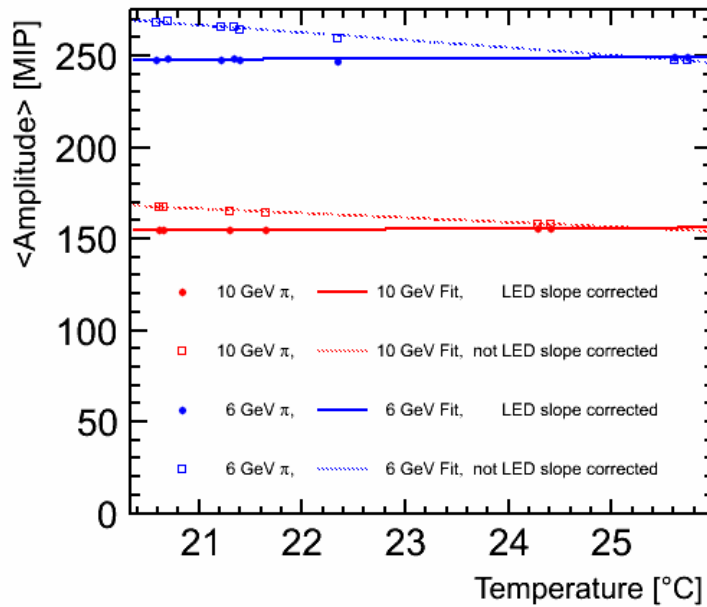


Figure 6.10: Shown are the mean amplitudes of reconstructed pion runs for 6 GeV (red) and 10 GeV (blue) without the LED system temperature slope correction (squares) and with the additional correction (circles), as well as their linear fits (dotted lines without correction, solid lines with correction applied).

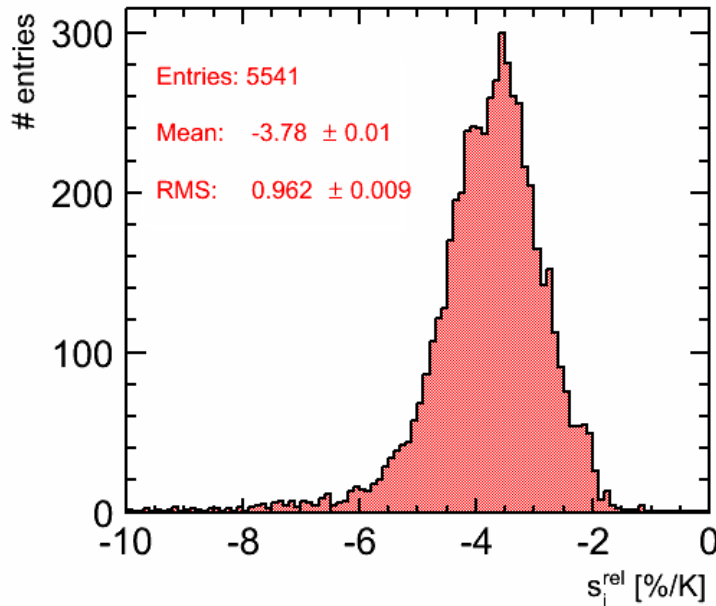


Figure 6.11: Shown is the distribution of the measured cell-wise relative MIP temperature dependence s_i^{rel} measured with LED events and corrected for the temperature dependence of the LED system. Excluded are dead channels, channels connected to broken LEDs and channels where the fits failed.

Both calibration sets have also been tested for individual cells. Therefore muon from normal beam runs have been selected (see sec. 7.6). These muons and the muon calibration runs have been reconstructed with the calibration applied. Then the same MIP fit has been applied to the track hits found in the muon events. This is done only for the 9 central towers, as the muons from the normal data taking are only recorded in this area because of the size of the main trigger. Then the MPV on the MIP scale is extracted. The distribution of these MPVs is shown in figure 6.12.

The figure shows for the CERN data the distribution of the fitted MPVs for the central towers for a single muon calibration run and for muons inside a hadron run. Both sets peak at a MPV of one within 1% uncertainty which proves that the calibration works in general. For the iron data the MPV distribution also peaks around one for the muon calibration run, proving that the calibration is consistent in itself. However, if this calibration set is applied to muons from normal hadron runs, the peak is shifted to higher values by approximately 6-7% (dependent of the actual run). This effect has been studied intensively with the result, that the peak position of the MPVs is increased by approximately 6% for all electron and hadron runs during the FNAL testbeam campaign if this calibration is applied. Additionally, a second muon calibration set, which has been recorded also at FNAL, but at different bias voltages of the SiPMs, shows the same increased mean MPV if the MIP constants are rescaled to the corresponding bias voltage of the first calibration set.

In principle such a shift of the mean MPV could be caused by either a wrong bias voltage applied or a wrong temperature monitoring. However, neither option seems realistic to explain this shift, as the voltages and the temperature are both monitored continuously and no problem could be found. Also the shift is visible for hadron runs recorded a day before and after the muon calibration runs, but it does not occur for the two muon calibration sets recorded with several months in between. Nevertheless there is a crucial difference in the recording of the muons runs and all other beam data: the muon runs were triggered with $1 \times 1 \text{ m}^2$ scintillators, whereas all other runs were triggered by the $10 \times 10 \text{ cm}^2$ scintillators, which also had different photomultipliers for read out (see sec. 4.1). The delay between trigger signal and readout, called hold value (see sec. 3.2), needs to be adjusted individually for each of the trigger types. If the trigger delay for the muon trigger was adjusted wrongly, then exactly such a shift of the mean MPV is observable.

To correct this shift, probably caused by a wrong trigger delay, all MIP calibration constants have been scaled by a factor of approximately 1.067, so that the mean MPV extracted from muon cell spectra from muons in hadron runs becomes one (shown in fig. 6.12). The temperature correction has been calculated according to the scaled MIP constants with $-3.7 \frac{\%}{\text{K}}$.

The rescaling is done globally and based only on the MPVs of the single cell spectra of muons of the 9 central towers, since only these cells provide sufficient statistics within a single hadron runs for a reasonable approximation. The exact hold curves and therefore the correct time delay is different for every module (in principle also for every read-out channel). Since the calibration is on average off by 6-7%, this implies that for some channels the amplitude is no longer measured in the plateau region of the hold curve. However, it would require individual rescaling factors, which cannot be estimated due to the low statistics, to correct fully for the wrong time delay between trigger signal and read-out. Therefore an increased calibration uncertainty can be expected for some of the modules.

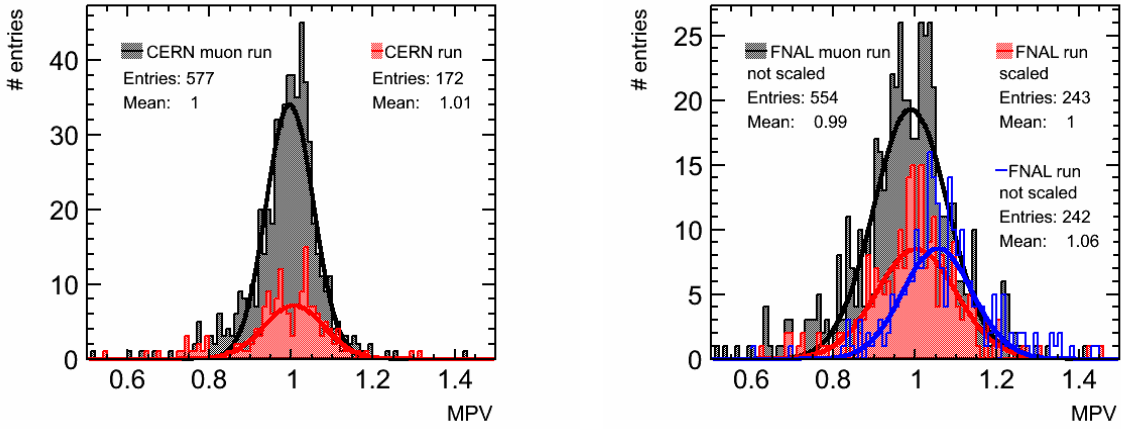


Figure 6.12: Extracted MPVs from the MIP fits for CERN (left) and FNAL (right) data as crosscheck of the MIP calibration (see text for details). The mean stated is the mean of the Gaussian approximation.

Figure 6.13 shows the comparison of both MIP calibration sets shifted to a temperature of 25°C and shows that both sets are in reasonable agreement, taking into account, that hardware was replaced and both sets were recorded at different temperatures.

6.7 Identification of Bad Channels

After several years of testbeam campaigns at DESY, CERN and FNAL some of the readout channels of the AHCAL are broken (dead) or show a very high noise occupancy (noisy). These channels, together with channels for which no valid muon peak could be found (see sec. 6.6), are called bad channels and are excluded from the analysis of data and simulations.

The dead channels do not show any signals above the pedestal level, which is mostly due to broken pins of the SiPMs. In addition some channels have been disconnected due to high noise occupancy. They are identified by the very small width of their pedestal distribution. Following the definitions given in [11], channels with a pedestal RMS of lower than 20.5 ADC counts are considered to be dead. In contrast to the dead channels, the noisy channels have an increased width of the pedestal distribution. These channels are also removed because on average they would contribute significantly to the total energy sum and thereby distort topological observables like shower profiles. Also for noisy cells the definition given in the reference is used, resulting in the removal of cells from the analysis, which have a RMS of larger than 120 ADC counts in pedestal events. The dead and noisy channels are about 2% of the total channels for both testbeam setups. However, the channels inside a given layers are not the same for both testbeams, as the order in which the modules were placed in the absorber structures differed for both testbeams. In addition some channels were repaired in between the two testbeams and some additional broke.

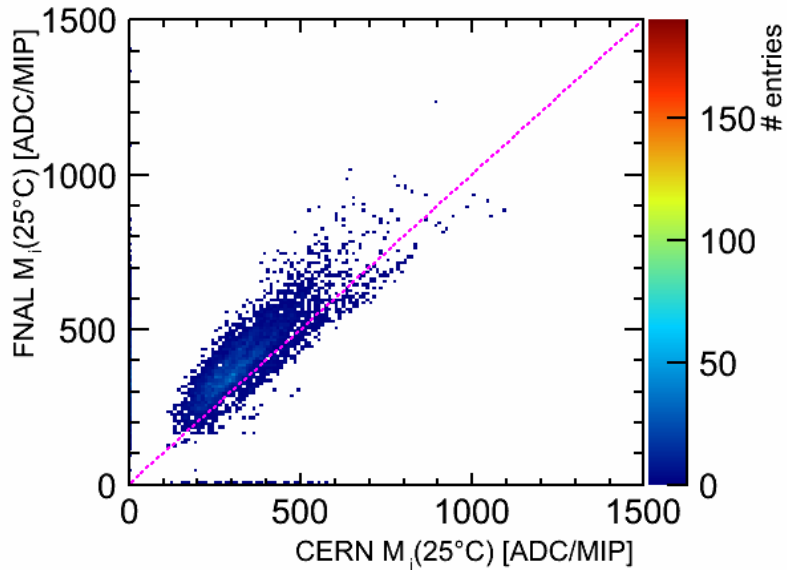


Figure 6.13: Shown is the channel-wise comparison of the MIP calibration used for CERN and for FNAL testbeam data.

Figure 6.14 shows the percentage of channels which are marked as bad per layer. The calorimeter region, where on average the most shower energy from hadron showers is deposited, has the least fraction of bad cells for both testbeam setups. The large difference in the total number of bad channels between the two setups is due to the large number of channels, for which no valid MIP calibration for the CERN testbeam was found, due to insufficient statistics. However, a map of the z-projection of the bad channels shows that most of these channels are located in the outer part of the calorimeter. Therefore no significant bias on the total energy and on longitudinal shower profiles is expected. Nevertheless, an impact on the tails of the radial shower profiles for the CERN setup cannot be excluded.

6.8 Noise after Calibration

The electronics noise would give a significant contribution to the total detector response if it is not suppressed. Therefore all cell amplitudes below 0.5 MIP are removed from analysis to limit the impact of electronics noise on the detector response. It has been shown that with this threshold only around 5% of all muon cell energy depositions are suppressed, while at the same time the contribution from electronics noise to the detector response is drastically reduced [36]. Nevertheless the noise cannot be fully removed, due to the limited signal-to-noise ratio of the first generation SiPMs used in the AHCAL prototype. The 0.5 MIP threshold has the same temperature dependence as the MIP calibration itself. However, the mean noise of the electronics in ADC counts has almost no temperature dependence. Therefore, the noise after suppression becomes inherently temperature dependent, since the fraction of the electronics noise that is removed depends on the temperature dependent threshold.

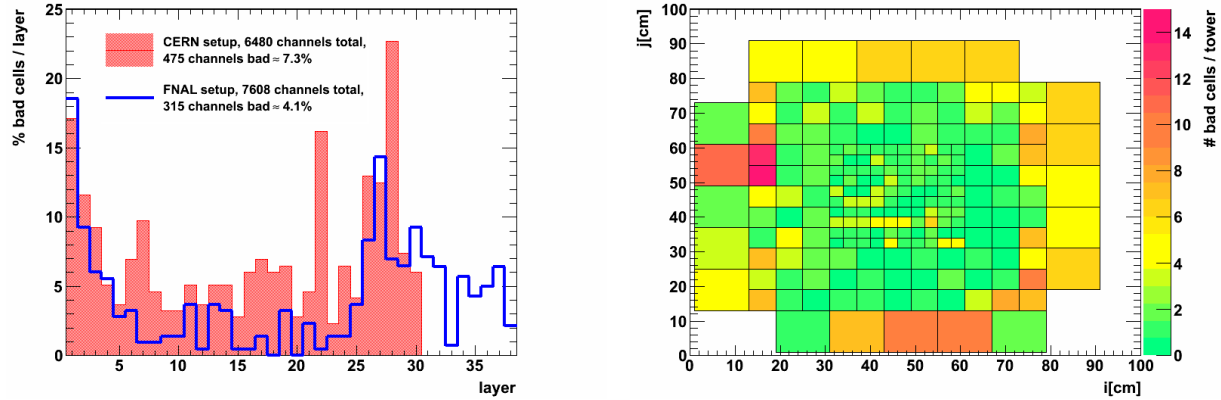


Figure 6.14: The percentage of cells that is excluded from analysis per layers for CERN and FNAL testbeam setups (left) and a map of the z-projection of the bad cells (right) for the CERN setup. The color of the cell indicates the number of bad cells in the respective tower.

Figure 6.15 shows the mean number and the mean energy sum of the hits above the 0.5 MIP threshold for pedestal events from individual data runs as a function of the mean run temperature. For both testbeam setups there is a strong dependence on temperature for the mean number and the mean energy sum of the hits above threshold in pedestal events observable. This strong temperature dependence of the noise would require the noise to be subtracted for each run individually if it should be removed from the data. However, the noise is not subtracted for this analysis, since it is not clear how to subtract noise from shower data. This is due to the fact, that the even small additional energy depositions from a shower might bring the amplitude above threshold. Additionally the noise for all cells that have sufficient energy depositions from showers is added to the total detector signal. So the total contribution from noise to the detector response is different in noise-only events than in shower events. Also the correct in-spill noise for the CERN data is unknown. Instead of subtracting the noise from data, it is added to the simulation for each simulated run individually (see chap. 8). This strong temperature dependence of the noise as well as the the total noise itself could be drastically lowered with modern SiPMs with better signal-to-noise ratios.

6.9 Inter-tile Crosstalk

The inter-tile crosstalk X_t describes the amount of light that leaks from one tile into an adjacent one:

$$X_t = \frac{A_{\text{Neigh}}}{A_{\text{Sum}}}, \quad (6.7)$$

where A_{Sum} is the theoretical response of the cell with no crosstalk to a given energy deposition, and A_{Neigh} is the response of an adjacent cell, where a signal is only generated by optical crosstalk. The crosstalk is mainly caused by the imperfect reflection properties of the tile edges, but also by a not tightly attached reflective foil which covers the two large

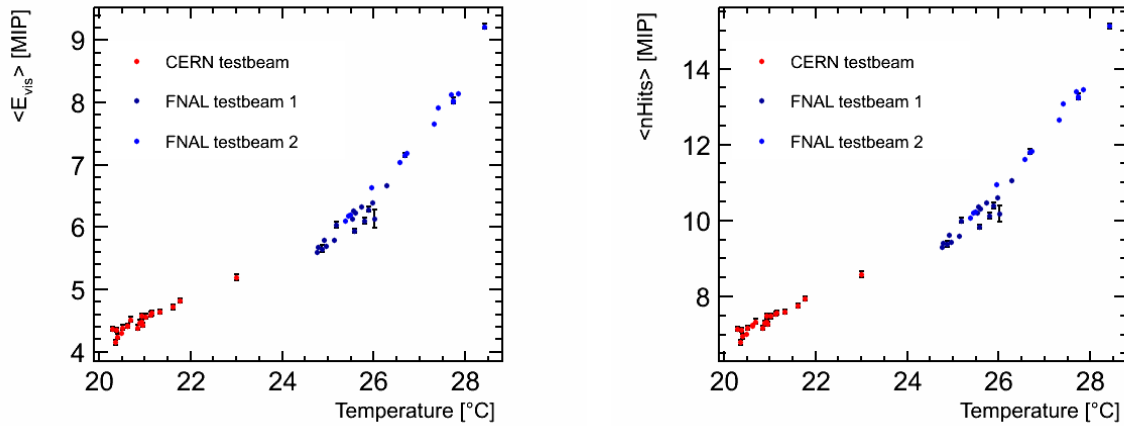


Figure 6.15: The mean energy $\langle E_{vis} \rangle$ (left) and mean number of hits $\langle nHits \rangle$ (right) of pedestal events from individual runs from the CERN and both periods of the FNAL testbeam as a function of the mean run temperature.

sides of the tiles. To measure the light leakage, a simplified model of the true crosstalk will be used. In this model the boundaries of the cells are considered to be semi-transparent mirrors without any absorption.

In the past the inter-tile crosstalk has just been measured for a sample of two tiles before they were built into the detector, giving an average inter-tile crosstalk of 2.5 % per tile edge [64], but it was also found out, that badly attached foil would increase the light leakage between cells. The following section will explain the measurement of this property for a much larger set of tiles.

In order to measure the inter-tile crosstalk, special calibration datasets have been recorded, where only one LED per layer was turned on, resulting in 12 LED runs per dataset. Each of the LEDs lights 18 cells, which are more or less in a row. In addition runs with pedestal triggers have been recorded before, after all, and after half of the LED runs, to have data for the pedestal subtraction of the channels and to exclude pedestal shifts during the data-taking. Three different datasets have been obtained this way, the first has been recorded at DESY during commissioning of the detector for testbeam preparation (dataset 1). For this set the active layers were horizontally stored on wooden plates and not inside the absorber structure. The other two datasets (datasets 2&3) have been recorded at CERN in the testbeam setup of the detector in between data taking periods. For these two datasets, the active layers were mounted vertically inside the tungsten absorber structure.

The inter-tile crosstalk can then be measured in the following way: To estimate the crosstalk for a single cell, only an array of 3 times 3 cells (see fig. 6.16), centered on the investigated cell, is considered, where none of the cells must be dead, and the middle row of cells is lit by a single LED. Cells with neighboring tiles with different size are ignored. All amplitudes from the cells of this array are then pedestal subtracted. If the average amplitude of the central cell exceeds 10000 ADC counts or is below 3000 ADC counts it is ignored to limit impact from SiPM saturation, which is not corrected in this simple analysis

and to make sure that this cell is lit, since some of the LEDs were broken. The amplitudes in ADC counts are then converted to a common MIP scale with a MIP calibration. The inter-tile crosstalk X_t for a single tile edge of cell A_i is then in a first step estimated as:

$$X_t = \frac{A_i}{A_i + A_{j1} + A_{j2}} \quad (6.8)$$

where A denotes the amplitude of the cell given in figure 6.16 with $j1$, $k1$, and $k2$ being the lit cells. However, this approach assumes that there is the same amount of light leaking from one lit cell to another one, which is not true due to the fact, that the cells connected to a single LED do not receive the same light when only one LED is turned on. Therefore, this result is used for a second iteration, which takes also the neighboring lit cells into account:

$$X_{t,final} = \frac{A_i}{A_i + A_{j1} + A_{j2} + X_t \cdot (2A_{j1} - A_{k1} - A_{k2})} \quad (6.9)$$

Since this second iteration results only in a correction at the percent level of the first iteration, no further iterations are done. The results for all three datasets are shown separately for cell sizes of $3\times 3\text{ cm}^2$ and $6\times 6\text{ cm}^2$ in figure 6.17 with just the statistical errors. To also take into account systematic uncertainties, the impact from using different MIP calibrations and the impact of saturation has been studied.

Different MIP calibrations have been used for all datasets to estimate the uncertainty on the crosstalk due to the used MIP calibration. This is especially important for the first dataset for which no MIP calibration from the same data taking period (native MIP calibration) exists. Figure 6.18 shows the crosstalk for dataset 3 for the native MIP calibration (MIP set 3) and two other MIP calibration sets from earlier testbeam periods (set 1 from 2007, set 2 from 2008). The result is almost independent from the used MIP calibration and a conservative estimate of 0.1% is used as uncertainty due to the used MIP calibration. To estimate the impact of saturation on the result, the cell responses have been divided into bins of 1000 ADC counts (see fig. 6.18) The crosstalk is stable within the interval from 3000 to 10000 ADC counts and also an estimate of 0.1% as uncertainty is used. The upper threshold could be set lower to exclude any impact from SiPM saturation, but this would further increase the statistical error in the same order of magnitude. An unforeseen feature of the CMB system is the main reason for the low statistics: The light of a single LED is no longer uniformly distributed among the fibers if only a single LED is lit per CMB. This feature was reproducible, however, it is not understood and would require additional debugging of the CMB electronics.

The statistical and the systematic errors are added in quadrature. The results from dataset 2 and 3 of $4.5 \pm 0.2\%$ crosstalk per tile edge are consistent, dataset 1 gives a lower mean crosstalk of $3.5 \pm 0.2\%$ per tile edge for the $3\times 3\text{ cm}^2$ cells. For the $6\times 6\text{ cm}^2$ cells all three datasets give a consistent result of $2.6 \pm 0.3\%$ crosstalk per tile edge. Figure 6.19 shows a comparison of the individual cell border measurements between dataset 1 and dataset 2, respectively dataset 2 and dataset 3. Almost all cells show an increased crosstalk in dataset 2 in comparison to dataset 1, whereas measurements for the individual cells in datasets 2 and 3 are consistent with each other. This comparison gives further indication, that the spread of the measured crosstalk values, is real and not due to measuring inaccuracy.

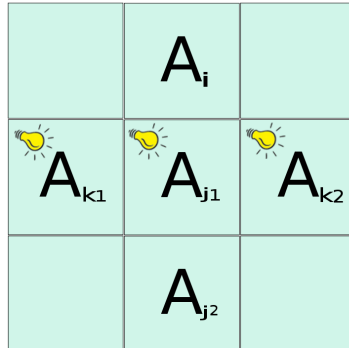


Figure 6.16: Scheme of a 3 times 3 cell array for the inter-tile crosstalk calculation. The cells in the middle row are lit by fibers from the same LED.

The cause for the increase crosstalk for the $3 \times 3 \text{ cm}^2$ cells between the datasets can only be guessed. Aging or scratching of the tiles edges seems very unlikely. Instead, the difference between the datasets for the $3 \times 3 \text{ cm}^2$ cells is interpreted as being due to a not tightly attached reflective foil on the cells for the setup in datasets 2 and 3, where the layers were placed vertically in the absorber stack. For dataset 1 the layers were placed horizontally on wooden plates. In the vertical position there might be enough space between tiles and cover, that the foil might bend away from the cells, especially in the middle of the layer where the $3 \times 3 \text{ cm}^2$ cells are located. Further indication for this hypothesis is from the direct comparison of the measurements for the individual tile edges (see fig. 6.19). A strong dependence of the inter-tile crosstalk on a correctly attached reflective foil was also reported from [64], and lab measurements with tiles indicate the same problems [65].

The measured crosstalk values have been cross checked with some cells that have two lit neighbors, and those cells see roughly twice as much light as the single lit cells. However there are very few of these double lit cells and therefore this crosscheck has a huge statistical uncertainty. The 4.5% crosstalk per tile edge will be used for the detector simulation, since this setup was closest to the data taking setup, and its impact is studied and compared to a simulation with the original crosstalk value of 2.5% per tile edge in the simulation validation chapter (see chap. 9).

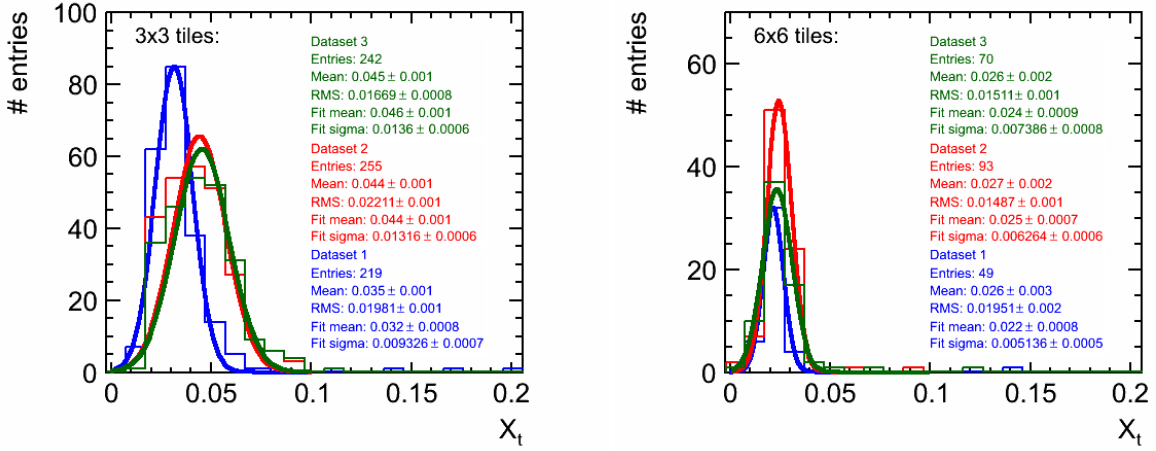


Figure 6.17: Distributions of the measured inter-tile crosstalk for the $3 \times 3 \text{ cm}^2$ (left) and $6 \times 6 \text{ cm}^2$ (right) tiles for all three data sets.

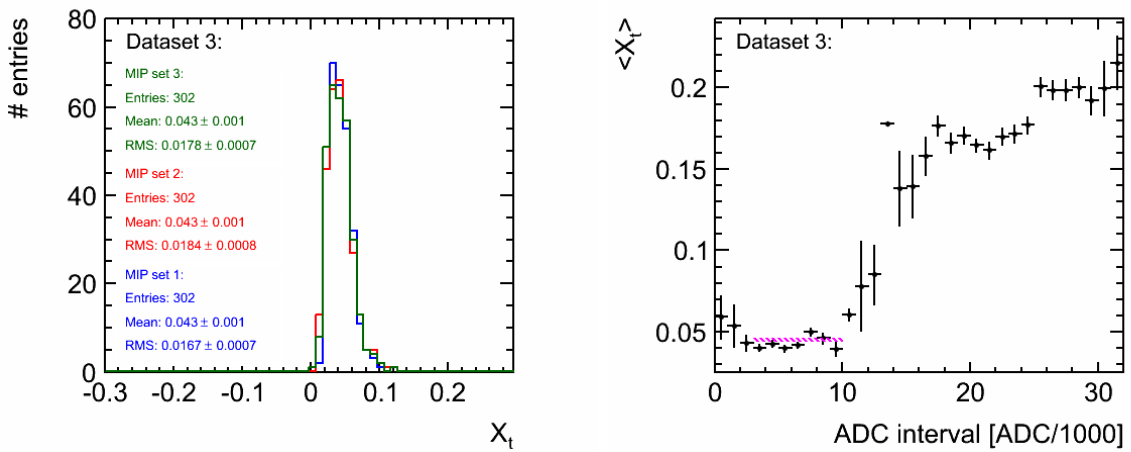


Figure 6.18: Dependence of the crosstalk measurement on different MIP calibrations used for dataset 3 (left) and the average crosstalk $\langle X_t \rangle$ for signals with different size (right). Between 3000 and 10000 ADC counts the result is stable, which is indicated by the purple dotted line showing the mean in this interval. At higher values, the impact from SiPM saturation on the result is visible.

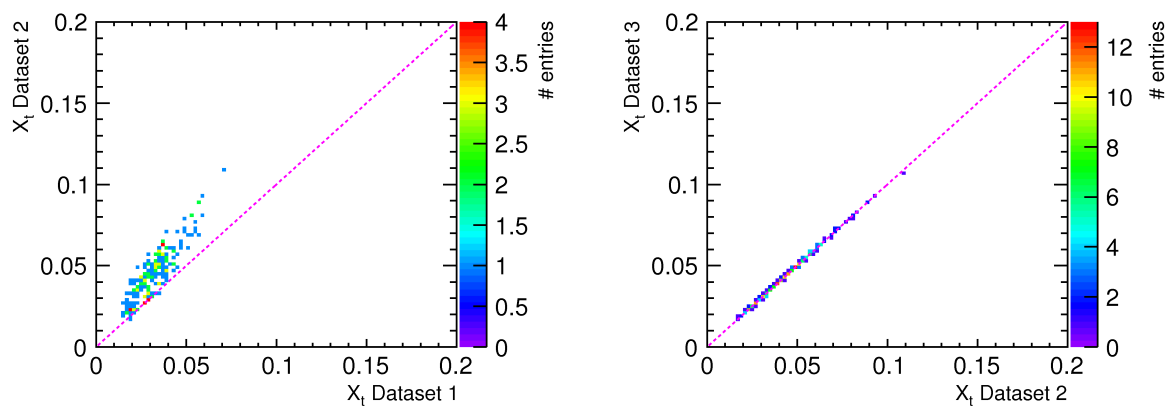


Figure 6.19: Comparison of the crosstalk measurement for the individual tile edges in different datasets.

CHAPTER VII

EVENT SELECTION

The particle beams provided at the CERN PS and the FNAL MTest beamlines comprise not only a single particle type, but instead a mixture of electrons, muons, and hadrons. Figure 7.1 shows the energy sum for all events recorded during a single 10 GeV run at CERN and at FNAL. The multi-peak structure indicates that there is more than one particle type interacting. Also the long tail for the FNAL data suggests additional contamination of the events. Therefore it is mandatory to filter the recorded datasets for events that were initiated by just one particle type, so they can be compared to simulations, or to compare both absorber types with each other.

However, the existing particle selections for the CERN [63, 12] and FNAL data [11] had to be modified, since this thesis will investigate differences in particle showers for two different absorber materials, and therefore aims to get as clean single particle shower samples as possible. At the same time, as little events as possible of the given particle should be rejected to ensure that the samples are not biased. Also the selection should be as similar as possible for both absorber setups. While the main part of the particle identification is done with the external cherenkov counters, additional software filters, called cuts, are needed. They are necessary not only to distinguish particles with similar mass (e.g. pion and muons), but also improve the data quality, and to remove multi-particle events, especially in case of the FNAL data, which are not addressed in previous selections for this data. Unless it is mentioned otherwise, the cuts are applied to both CERN and FNAL testbeam data and the simulation. The exact values of cuts can be found in Appendix B.

7.1 Beam Events

During the data taking, not only events that contain particle showers are recorded, but there is also the continuous recording of calibration events in the same run. These calibration events include pedestal events and LED events. For every event special trigger bits are set during the data taking, which are available for analysis, e.g. the beam bit for particle showers, the pedestal bit for random noise triggers, and the calibration bit for LED events. Therefore the first and trivial cut that is applied to the event selection of muon, electron, or pion samples is requiring that an event has a beam bit set to clear the data samples

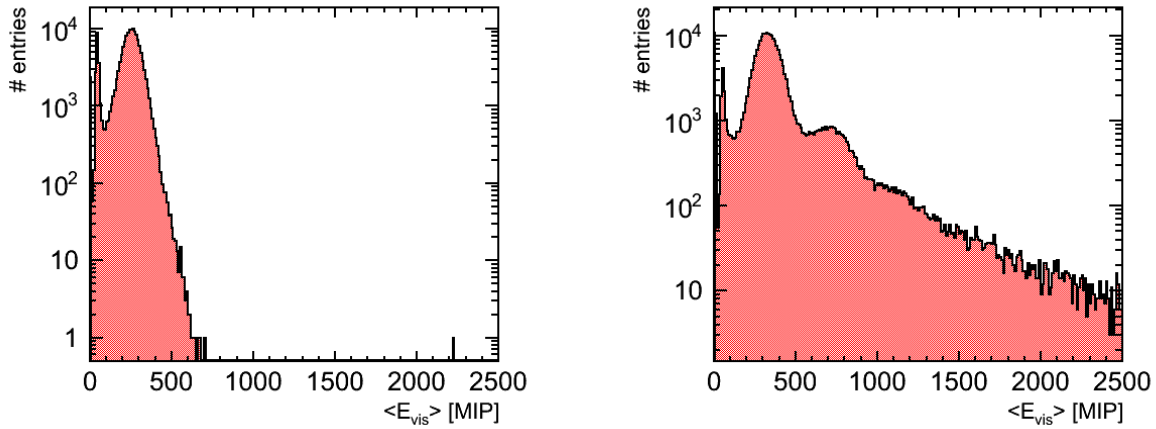


Figure 7.1: The mean visible energy for a single CERN (left) and FNAL (right) run at 10 GeV without any selection applied.

from noise and calibration events. This cut is only necessary for data since the bits are not set in the simulation.

7.2 Events with LED flashes

At the CERN testbeam in 2010 one of the CMBs was not working properly (CMB of module 9). Sometimes there were unforeseen LED-triggers in this module, resulting in random LED light flashes in all cells of this module. But since all cells in this module have an unreasonable high energy deposit and also the hit multiplicity for this module is high due to simultaneous flashes in all cells, these events could be easily removed by requiring that the hit multiplicity in this layer should be below 100. Although only a few events are removed by this cut, these events would bias the width of the energy sum distributions and hit multiplicity distributions. One of these events is visible in the CERN data in figure 7.1 with a visible energy sum of more than 2200 MIPs. This cut is only applied to the CERN data, since it does not remove any events in the FNAL data or in either simulation.

7.3 Empty Events

To ensure that in every event of the particle data samples there is at least one particle depositing energy in the calorimeter, a rejection criteria for empty events has been developed in [11]: The total energy deposit in the 3x3 cm² tiles of the first 5 layers must be at least 4 MIPs. This cut has very little impact on the recorded dataset, where a coincidence trigger of the two 10x10 cm² scintillators is required for the detector readout, making it almost impossible that a particle is scattered to the side in the distance between the second trigger scintillator and the detector. Also in the simulation the particle gun has been placed just upstream of the main scintillators and the tracking chambers. Nevertheless, the response

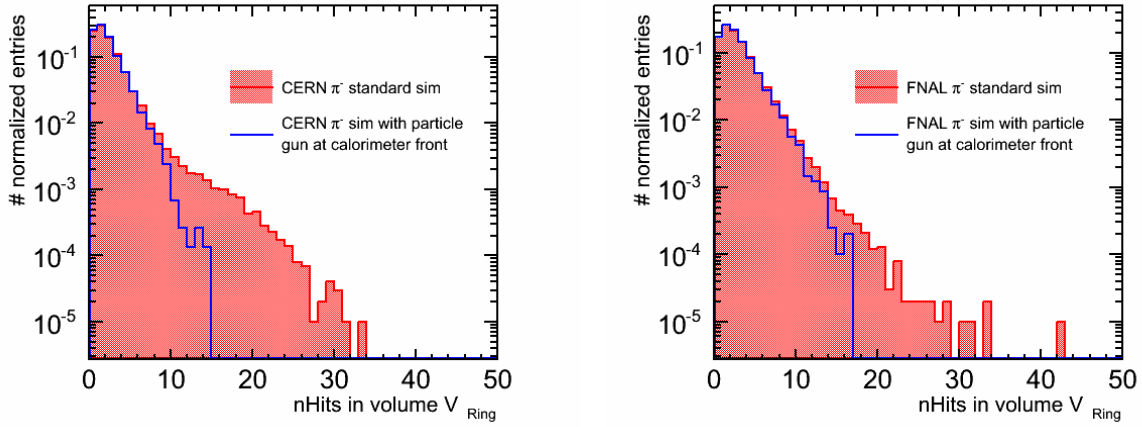


Figure 7.2: The number of hits in the volume V_{Ring} ($6 \times 6 \text{ cm}^2$ and $12 \times 12 \text{ cm}^2$ cells in the first five layers) for the normal 6 GeV simulation and a second simulation, where the particle gun was placed a few centimeters before the calorimeter front for the CERN setup (left) and the FNAL setup (right).

of the scintillators is not simulated. Therefore some particles are scattered away and do not reach the calorimeter in the simulation. The cut removes these events from the simulated data samples.

7.4 Upstream Interactions

For an incoming particle there is a chance that it may interact upstream of the calorimeter and start a shower already before it reaches the calorimeter. Since the energy of these particles or their remains is not well defined, these events also need to be removed from the data samples. This is done by requiring to have a low hit multiplicity in the $6 \times 6 \text{ cm}^2$ and $12 \times 12 \text{ cm}^2$ cells in the first five layers of the calorimeter, a volume which will be called V_{Ring} . The hit multiplicity in this volume of the normal simulation is compared with the hit multiplicity in the same volume of a dedicated simulation, where the particle gun was placed only a few centimeters in front of the calorimeter, so that these particles do not traverse any beam instrumentation and only need to traverse a minimum distance in air. The hit multiplicity in the volume V_{Ring} for the normal simulation and the dedicated one are displayed in figure 7.2. All events with more than 15 hits in the volume V_{Ring} are removed from the pion samples for 4 GeV and above. For 2 GeV the distributions of both simulations overlap completely and no additional cut was found for this energy.

7.5 Additional Algorithms

For the particle identification and especially for the multi-particle event rejection two additional algorithms are utilized and briefly described in the following. A tracking algorithm

which identifies track segments [66] and a clustering algorithm used for shower start finding [67]. The track segment finding algorithm tries to merge hits to clusters which are on a straight line and are therefore track candidates. The algorithm starts with isolated hits as seed hits for track finding and then tries to merge additional isolated hits in subsequent layers which are inside a small cone with the tip being the seed hit. A valid track segment is at least three hits long and therefore traverses at least three subsequent layers. However, the algorithm is incapable of finding track segments which are (almost) perpendicular to the beam axis.

The clustering algorithm identifies clusters of energy deposition in neighboring cells which can be a potential shower start, which is defined as the first inelastic scattering of the incoming hadron. The algorithm first tries to identify regions of interest, which are calorimeter hits exceeding a certain energy threshold. Then the energy depositions around this cluster seed hit are added, or clustered up. The cluster which is closest to the origin of the incoming particle and which meets certain requirements in size and shape is then considered as the shower start cluster. The shower starting point is then calculated from the position of the cell with the highest energy deposition in the cluster. However, previous investigations with simulated events indicate, that the agreement of the calculated shower starting point with the actual one which is also stored in the simulation is worse than a layer at energies below 10 GeV. Nevertheless, the clustering information and information if a shower start was found inside the calorimeter can still be utilized for the event selection.

7.6 Particle Identification

Both testbeam facilities at CERN and FNAL deliver a particle beam with an energy dependent mixed particle content. In order to study muon, electron and pion data separately the incoming particles have to be identified. This is done with the calorimeter itself as well as with additional beam instrumentation as cherenkov detectors. The external cherenkov detectors provided in both testbeam setups are able to tag particles heavier than a given mass, within a certain energy regime. In case of the CERN PS testbeam it was possible to apply separate tags for electrons, for pions and muons and for particles that are heavier at all energies. Pions and muons can not be separated by the cherenkov detector reliably, because of their similar mass. In case of the FNAL testbeam it was only possible down to 8 GeV to give particles heavier than a pion a separate tag. For lower energies, it was only possible to give two kinds of tags - electron or heavier (see chap. 4). Since pions and protons cannot be separated event by event with the calorimeter itself, there is a small fraction of protons in the pion samples at 6 GeV and below. But since this fraction is small and the proton shower topology is similar to the pion shower topology no significant bias is expected. For both testbeam setups the efficiency of the electron tagging with the cherenkov detectors decreased at 2 GeV. At these energies electron and pion showers look almost the same, however an estimation of the remaining electron contamination is done once the final pion selection is complete.

Since muons and pions cannot be separated reliably with the cherenkov detectors, a different strategy had to be developed. For energies above 4 GeV the combination of the

Beam Energy [GeV]	Pion Sample		Muon Sample	
	Pion Selection Efficiency	Muon Rejection Efficiency	Muon Selection Efficiency	Pion Rejection Efficiency
2	0.91 (0.91)	0.82 (0.82)	0.80 (0.80)	0.95 (0.95)
4	0.67 (0.63)	1.00 (1.00)	0.85 (0.85)	0.96 (0.96)
6	0.93 (0.92)	0.97 (0.97)	0.89 (0.90)	0.96 (0.96)
8	0.94 (0.94)	0.96 (0.96)	0.80 (0.81)	0.97 (0.97)
10	0.94 (0.94)	0.96 (0.96)	0.85 (0.85)	0.97 (0.97)

Table 7.1: The selection and rejection efficiencies for the muon-pion separation for simulated CERN data. The simulation used 18% crosstalk and the physics list QGSP_BERT_HP, the values in brackets are given for a simulation with 10% crosstalk.

number of hits and the longitudinal center of gravity of an event is used to distinguish between muon and pion events. This is shown for simulated particles in the upper two plots in figure 7.3. The muons can be well separated from the electron and pion events. Nevertheless, there is a small fraction of pion events looking like muons. These are either pions that decayed into a muon during the flight to the detector or pions that traverse the calorimeter without initiating a shower, and therefore have the same calorimeter signature as muons. Both types of events are also removed from the pion samples. The resulting selections for 6 GeV runs are shown in the lower two plots in figure 7.3. For the CERN data, the resulting distributions look as expected. However, the electron and pion selections at FNAL show a significant tail to higher hit multiplicities. This is a hint for some additional contamination of the samples which requires further filtering.

At energies of 4 GeV and below muons and pions cannot be distinguished with the above selection alone anymore, because the pion showers become smaller and have less hits. This results in an overlap of the distributions. Therefore, as additional criterion, it is required, that the energy deposit in the last layers does not exceed a certain threshold, since the energy deposition at the end of the calorimeter is typically very low for pion showers of these energies, while muons still reach the last calorimeter layers. Additionally, the shower start finding algorithm must not detect a shower start.

The cut efficiencies for the muon-pion separation are given in table 7.1 and table 7.2. They have been estimated with simulated data samples. However, as the energy deposit per layer in simulated particle showers depends on the used crosstalk parameter (see sec. 9.2), so does the cut efficiency at low energies. Therefore the efficiencies have been estimated with a simulation with 18 % crosstalk and a simulation with 10 % crosstalk. The separation is worst at 4 GeV. However, a low muon contamination of the 4 GeV pion sample could only be achieved at the price of a small bias on the sample.

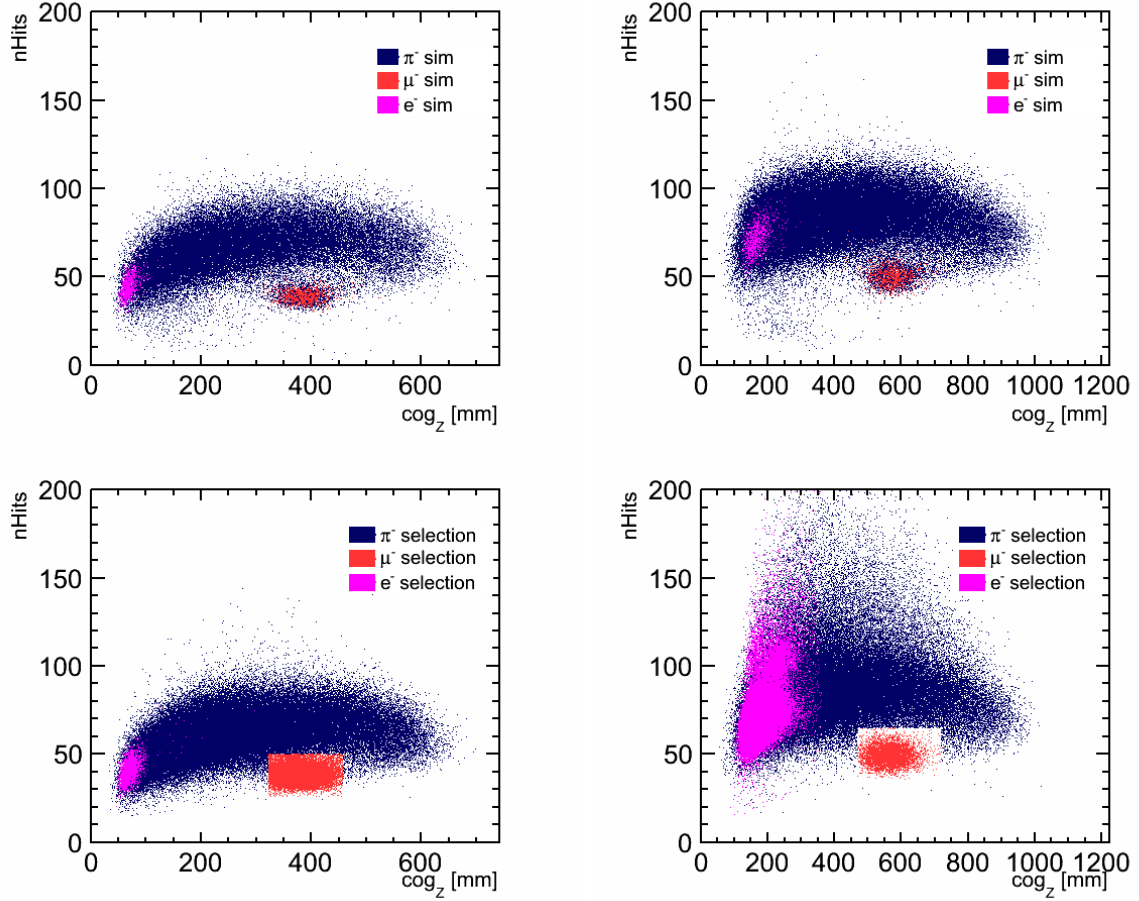


Figure 7.3: The number of hits versus the center of gravity from the calorimeter front for the CERN tungsten absorber setup (left) and the FNAL iron absorber setup (right) for simulated 6 GeV e⁻ (1000), μ⁻ (1000) and π⁻ (10000) events (upper two). The number of events has been chosen such, that the overlap regions remain visible. The two bottom plots show the same distribution for the cherenkov selected e⁻ and π⁻ samples and the selected muon sample. The data quality cuts have been applied in addition (see text).

	Pion Sample		Muon Sample	
	Pion Selection Efficiency	Muon Rejection Efficiency	Muon Selection Efficiency	Pion Rejection Efficiency
Beam Energy [GeV]				
2	0.77 (0.75)	1.00 (1.00)	0.72 (0.68)	0.95 (0.95)
4	0.82 (0.76)	0.99 (0.99)	0.69 (0.66)	0.98 (0.98)
6	0.94 (0.92)	0.98 (0.98)	0.68 (0.66)	0.98 (0.98)
8	0.95 (0.95)	0.97 (0.97)	0.67 (0.65)	0.98 (0.98)
10	0.95 (0.95)	0.97 (0.97)	0.67 (0.64)	0.99 (0.99)

Table 7.2: The selection and rejection efficiencies for the muon-pion separation for simulated FNAL data. The simulation used 18% crosstalk and the physics list QGSP_BERT_HP, the values in brackets are given for a simulation with 10% crosstalk.

7.7 Multi-Particle Events

As already shown in the particle identification section, there is a significant contamination for the FNAL data with events with a large visible energy sum and high hit multiplicities, most likely due to multi-particle events. In contrast to this, there was basically no multi-particle event contamination recorded for the CERN data. However, there is not only the case of two or more centrally incoming particles as mentioned in section 4.1, but there is also a significant number of events, which contain a centrally showering particle as well as one or several additional muons which traverse the outer tiles of the calorimeter at the same time as the central particle showers (see fig. 7.4). Additionally many events contain also remnants from particles interacting upstream of the calorimeter.

To remove those events which contain one or more additional muons, the track segment finding algorithm is utilized. Those events which contain a track (almost) parallel to the beamline, which traverses only $6 \times 6 \text{ cm}^2$ or $12 \times 12 \text{ cm}^2$ cells, are removed from the analysis, since for electron showers, tracks in this calorimeter region do not occur, and for pion showers it is very unlikely that a secondary hadronic inelastic scattering has such a signature.

Events containing more than one centrally showering particle are much harder to remove. For electrons all events are rejected, that contain more than one shower cluster, found by the clustering algorithm. However, this is not an option for the pion showers, as hadronic showers can contain multiple clusters of energy deposition, each originating from a hadronic inelastic scattering. If both particles shower directly on top of each other, not an increased number of clusters is found, but clusters containing a huge amount of energy. Therefore also pion events are rejected, that contain clusters exceeding a certain amount of energy or a certain size. The actual cut parameters depend on the beam energy and are given in appendix B. However, the one and two or more particle events show a significant overlap for these distribution and not all contamination can be removed.

The removal of events containing additionally remnants of other particles which interacted upstream of the calorimeter is the most difficult type of multi-particle contamination to get rid off. These events typically show an increased activity at the calorimeter front, however, these additional energy deposits are almost impossible to distinguish from noise fluctuations. Therefore, no dedicated rejection criterion is applied for this type of contamination. For muons, the multi-particle rejection is included in the box-cut from the particle identification, for electrons the rejection works also well, because of the small size of the showers, but for pions works worse, due to the large fluctuations of the showers. The percentage of events that is rejected by the additional offline multi-particle cuts in relation to the number of events, that is selected without the additional offline rejection is given in table 7.3.

Figure 7.5 shows the energy sum and hit multiplicity for 6 GeV pions at FNAL with only the online multi-particle rejection applied and with the additional offline multi-particle rejection applied. The online rejection consists of the trigger bits from the multi-particle scintillators and the muon-veto-scintillators (see sec. 4.1). The right-handed tails in both distributions could be significantly reduced with the additional offline rejection.

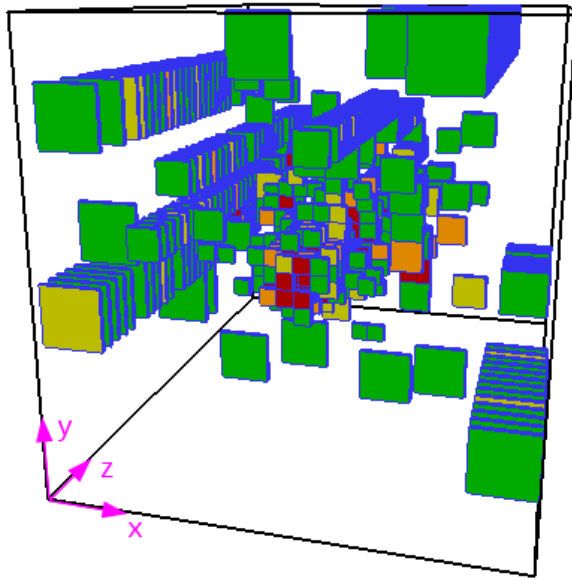


Figure 7.4: Event Display from an Multi-particle event. Shown are only those tiles, which exceed the 0.5 Mip threshold and their color represents the energy deposit of the tile (from green to red). Visible are several tracks in the outer part of the calorimeter, which are most likely additional muons. Also the size of the central shower indicates more than one showering particle in the central region.

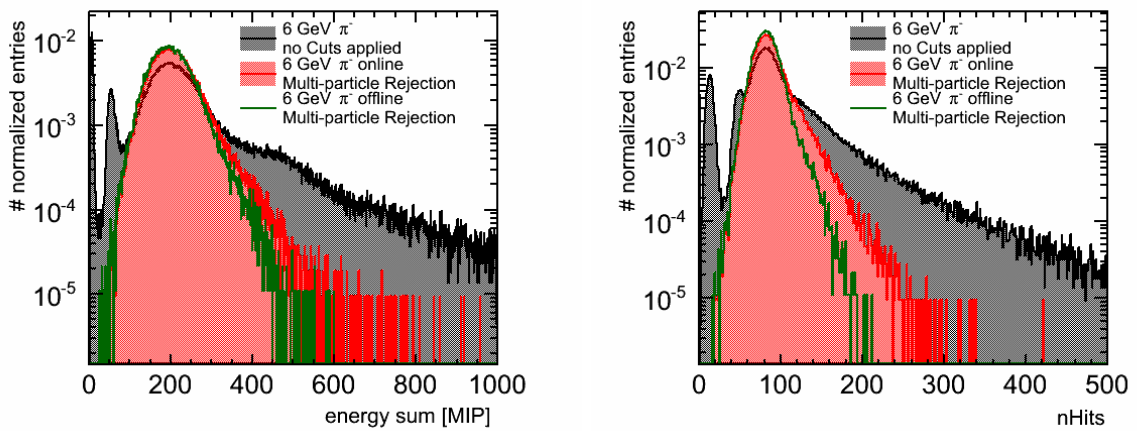


Figure 7.5: The energy sum (left) and hit multiplicity (right) for 6 GeV pions at FNAL with and without the additional offline multi-particle rejection applied.

Electrons		
Energy [GeV]	Simulation	Data
2	0.3 (0.3)	42,0
4	1.2 (1.3)	63,0
6	2.6 (3.0)	74,0
Pions		
Energy [GeV]	Simulation	Data
2	3.3 (5.8)	9.1
4	0.5 (0.4)	9.8
6	0.8 (0.8)	12.0
8	1.2 (1.0)	8.3
10	1.4 (1.1)	9.5

Table 7.3: Percentage of events that is removed by the additional offline multi-particle rejection for simulation and data for electrons and pions at FNAL. The simulation used QGSP_BERT_HP and 18% (10%) crosstalk.

7.8 Selection of the Tungsten Data Samples

The final selection for the CERN tungsten data includes muons from 4 GeV to 10 GeV, electrons from 2 GeV to 6 GeV and negative pions from 2 GeV to 10 GeV. Although also runs at 8 GeV and 10 GeV have been recorded, the number of electrons that they contain is not sufficient for a precise analysis. Additional electron data points at uneven energies (1 GeV, 3 GeV, 5 GeV) are not considered for this thesis, as the same energy points are not available for iron data. The selection cuts applied to these datasets include the data quality cuts discussed above as well as the particle identification discussed above. From the 6 GeV electron sample a single multi-particle event is removed by hand, and no further indications of multi-particle contamination could be found.

Figure 7.6 shows distributions of the visible energy sum for the electron and pion samples. The electron samples have been fitted with a Gaussian distribution with a range of $\pm 3\sigma$ of a previous Gaussian fit and show a very good agreement between the data and the Gaussian fit. Also beyond the three standard deviations there is a good agreement with a Gaussian shaped response, proving that the electron samples contain only a negligible amount of contamination.

The pion distributions have been fitted with a Novosibirsk distribution [68] instead, since this describes the energy sums far more accurate. The asymmetry of the visible energy sum distribution is caused by the suppression of low cell energy deposits and therefore is strongest at the lowest energies. However, as the pion distributions naturally show a much larger spread due to the fluctuations in the shower development, they have just been fitted in a range of $\pm 2\sigma$ of an initial Gaussian fit. Within this range the distributions are very well described by the fit. Only for the 8 GeV and 10 GeV samples a tail to lower energies, which extends beyond the Novosibirsk function, can be observed. This tail is most likely caused by pion showers not fully contained inside the calorimeter (see sec. 9.3). Also, this effect is enhanced in comparison to the iron absorber setup by the limited length of the tungsten absorber setup with 30 layers only. The number of events passing the selection

for all particle types and energies are given in table 7.8.

The response of electrons and pions as a function of the incident energy is fitted with a linear function:

$$\langle E_{\text{vis}} \rangle = u \cdot E_{\text{avail}} + v \quad (7.1)$$

The fit resulted for electrons is $u_e = 28.1 \pm 0.3 \frac{\text{MIP}}{\text{GeV}}$ and $v_e = 4.2 \pm 1.0 \text{ MIP}$. For pions the approximation gives $u_\pi = 25.5 \pm 0.2 \frac{\text{MIP}}{\text{GeV}}$ and $v_\pi = 3.7 \pm 0.7 \text{ MIP}$. The u factors agree within uncertainty for electrons and pions with the ones from previous analysis, but the offsets only agrees for pions with previous analysis [63]. The difference is most likely due to the calibration improvements. For both particle types, also the deviation from the linear response has been calculated (see fig. 7.7). The response of the electrons deviates at all energy points below 0.5% from linearity, which is an improvement to previous results, where the deviation from a linear response was only below 2-4% for electrons [12]. For the pions the deviation from linearity is largest at 4 GeV, nevertheless it does not exceed 3%, which is similar than in previous analysis. However, differences in the comparison for particles with opposite charge in the previous analysis [63, 12] point already to unsolved problems in the calibration of data in the previous analysis.

Additionally, the remaining contamination of the samples is estimated. The electron samples cannot contain pion contamination as a signal in the cherenkov counter is required, and the noise triggers of the photomultiplier practically never coincide with the beam triggers. However, the pion samples can contain electron contamination at low energies, as the gas pressure of the cherenkov detector for electron tagging has to be set very low (see chap. 4) and electrons may traverse the cherenkov detector without generating sufficient amounts of light to trigger the photomultiplier. To estimate the remaining electron contamination the distribution of the ratio of the energy deposit in the first 3 layers E_3 divided by the total energy deposit E_{30} has been plotted for 100000 simulated electrons, pions, and the finally selected pion events. This distribution in data is then approximated with the TFractionalFitter of the ROOT analysis framework by a weighted sum of the distributions for simulated electron and pions (see fig. 7.7). The resulting fit is consistent with no electron contamination.

7.9 Selection of the Iron Data Samples

The final selection for the FNAL iron absorber data samples is done for the same particles and energies as the CERN tungsten data. It is also based on the same selection strategies with only variations of the cut parameters. However, this dataset contains a significant multi-particle event contamination. Therefore the multi-particle event rejection cuts are applied in addition.

Figure 7.9 shows the visible energy sum E_{vis} for selected electron and pion event samples. The distributions have been fitted with the same functions and within the same ranges as for the CERN tungsten data. The electron samples for 4 GeV and 6 GeV are

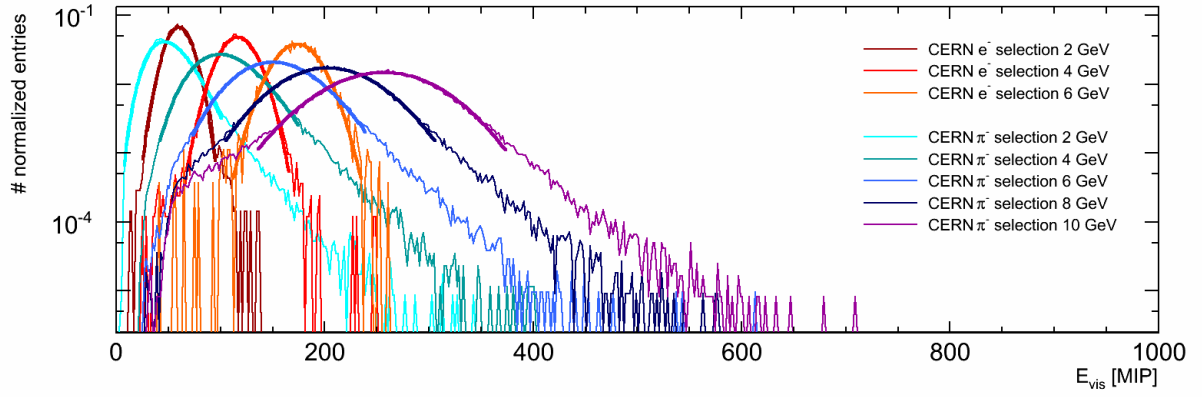


Figure 7.6: The sum of the visible energy E_{vis} in MIPs for the selected electron events from 2 GeV to 6 GeV and the selected pion events from 2 GeV to 10 GeV for the CERN testbeam data with all cuts applied. The thick lines indicate the fit results (see text for details).

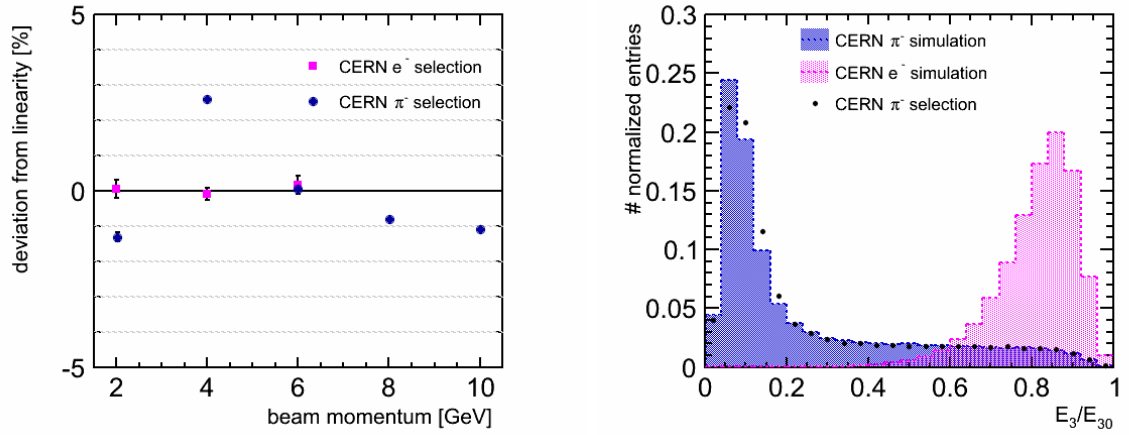


Figure 7.7: The deviation from a linear response of electrons and pions at CERN as a function of the beam momentum (left) and an estimation of the remaining electron contamination in the selected pions at 2 GeV at CERN.

Beam momentum [GeV]	μ^-	e^-	π^-
2	-..	6839	116336
4	16762	8220	70620
6	15284	2714	104724
8	11539	-..	111768
10	9761	-..	121734

Figure 7.8: The number of events passing the selection criteria used for the tungsten data analysis.

well described by the fit within the fitting range of three standard deviations. Beyond this range, non-Gaussian tails become apparent. This is due to the limitations of the multi-particle rejection and additionally due to electrons which lose significant amounts of energy upstream of the calorimeter. The low energy tail is even more pronounced for the 2 GeV electron sample, where no rejection for the upstream showering particles can be applied (see sec. 7.4).

The visible energy sum for the pions is well approximated by the Novosibirsk function. However, also for the pions tails in the energy sum are observable, showing also for pions the limitations of the event selection. Also for the iron absorber pion samples significant low energy tails are present above 6 GeV, which are also caused by shower leakage. The number of events for the different particles and energies that passed the selection are given in table 7.11.

The responses for electrons and pions for the iron absorber setup have also been fitted with a linear function. The calculated fit parameters for electrons are $u_e = 41.0 \pm 0.5 \frac{\text{MIP}}{\text{GeV}}$ and $v_e = 8.5 \pm 1.4 \text{ MIP}$. For pions the fit parameters have been calculated as $u_\pi = 33.7 \pm 0.3 \frac{\text{MIP}}{\text{GeV}}$ and $v_{pi} = -1.7 \pm 0.9 \text{ MIP}$. The negative offset extracted from the fit is most likely an artifact from the calibration errors, especially those caused by the shift of the MIP constants, and remaining multi-particle contamination (see chap. 6 and chap. 9). The conversion factor u for electrons agrees within errors with a previous result [11], but the offset w , which was consistent with 0 in previous analysis, is higher in this analysis and does not agree with the previous one. This can most likely be attributed to improvements achieved in calibration and event selection. The deviation from the linear response (see fig. 7.10) is similar as in the CERN data case. It is well below the percent level for electrons. For pions the deviation is also slightly bigger than for the CERN tungsten data. This can most likely be attributed to the worse sample purity and calibration errors. This is a clear improvement in terms of linearity of the electron response in comparison to previous analysis [11], which showed linearity within 2%.

Also for the iron 2 GeV pions a possible electron contamination is estimated. Instead of the ratio of the energy sum in the first three layers and the total energy sum, the ratio of the energy deposit in the first five layers and the total energy sum used, as electrons showers in iron extend further into the calorimeter (see chap. 9). In contrast to the tungsten absorber pion sample, an indication for a small contamination of the 2 GeV pion sample with electrons is found. Although, this contamination is expected to have a non-significant impact on the integral detector observables like visible energy sum or hit multiplicity, it can affect topological observables like shower profiles, since these are very different for the two particle types. The result of a previous analysis [11] which found significant electron contamination also at higher energies could not be verified. This is most likely due to the improved calibration and the additional multi-particle rejection.

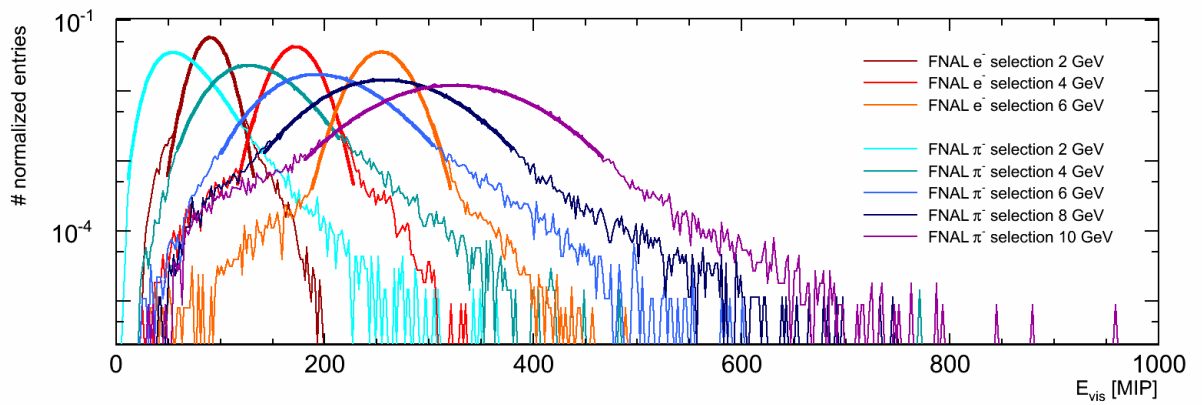


Figure 7.9: The sum of the visible energy E_{vis} in MIPs for the selected electron events from 2 GeV to 6 GeV and the selected pion events from 2 GeV to 10 GeV for the FNAL testbeam data with all cuts applied. The thick lines indicate the fit results (see text for details).

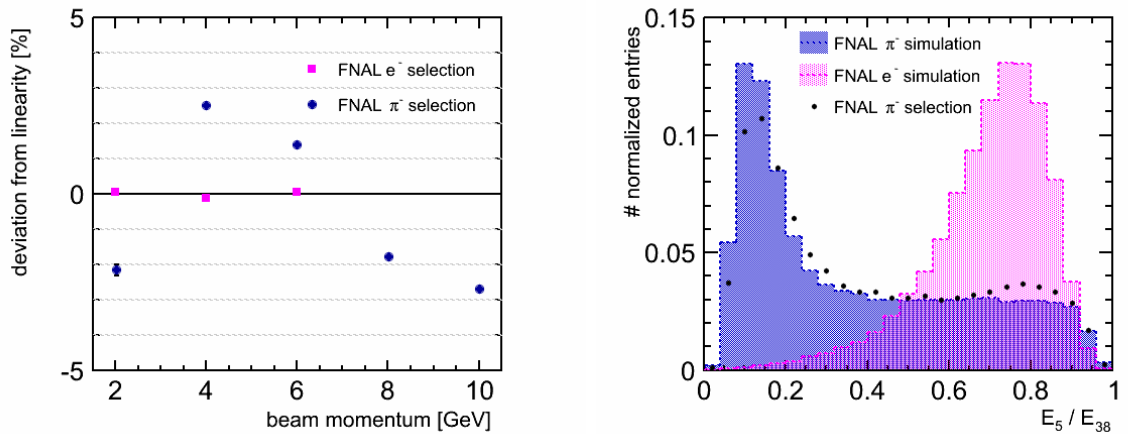


Figure 7.10: The deviation from a linear response of electrons and pions at FNAL as a function of the beam momentum (left) and an estimation of the remaining electron contamination in the selected pions at 2 GeV at FNAL.

Beam momentum [GeV]	μ^-	e^-	π^-
2	-.-	101443	68503
4	4920	109412	69643
6	5565	126746	91949
8	3397	-.-	87783
10	4116	-.-	113042

Figure 7.11: The number of events passing the selection criteria used for the iron data analysis.

CHAPTER VIII

DETECTOR SIMULATION

This chapter will explain how particle shower data are simulated for the AHCAL prototype. The simulation is done with common Monte-Carlo tools like the GEANT4 toolkit [51] (Version 9.5) in conjunction with the MOKKA framework [52], to model the physics processes for a given detector model, and the additional CALICE simulation software implemented in the MARLIN framework [69], to model the detector response to these simulated processes. After this procedure this simulated data is calibrated and reconstructed in the same way as recorded showers from testbeams by applying the same calibration software. In addition a MOKKA software plugin created for this thesis will be described, which can decompose hadron showers into different shower components.

The values for all simulation parameters are given in Appendix C.

8.1 Simulation of the Physics Processes

The physics processes that occur when a high energy particle hits the calorimeter are simulated with GEANT4 (see chap. 5) in conjunction with the MOKKA framework which provides implementations of the simulated detectors with realistic material compositions. These implementations, so called MOKKA drivers, are available both for the FNAL [70] and the CERN testbeam setups [63], including the actual calorimeter as well as additional beam instrumentation like tracking chambers, scintillators, etc. MOKKA also simulates the beam position and spread with a GEANT4 particle gun. However, the particle gun emits all particles parallel to the z-axis of the detector and assumes a gaussian beam profile, which is only an approximation of the real beam, since e.g. at the CERN T9 beamline the last beam optics magnet upstream of the detector focuses the beam on the detector. This can result in small deviations of the radial shower profiles.

A timing cut of 150 ns is applied to the simulation, to model the readout time window of the AHCAL electronics. This is especially necessary in case of tungsten absorber, where late energy deposits from neutron processes (see chap. 2) give a significant contribution to the total energy deposit. Also effects for scintillators at high ionization densities $\frac{dE}{dx}$ are taken into account, described by Birks Law [71], resulting in a non-linear light yield per

unit length $\frac{dL}{dx}$:

$$\frac{dL}{dx} \propto \frac{dE}{dx} \cdot \frac{1}{1 + k_B \cdot \frac{dE}{dx}} \quad (8.1)$$

using a Birks factor $k_B = 0.007943 \frac{\text{cm}}{\text{MeV}}$ [72].

Event samples for electrons, negatively charged muons, and negatively charged pions containing 100000 events each were generated with the software described above for the beam momenta 2,4,6,8, and 10 GeV for both testbeams (no 8 GeV electrons for FNAL). For the pions, the physics list QGSP_BERT, FTFP_BERT, QGSP_BIC, with and without _HP extension, as well as QBBC and CHIPS were used. The position of the particle gun and the run conditions (identified by the run number) used are given in Appendix C.

The output of the simulation, in the form of energy deposits in eV per virtual 1x1 cm² scintillator cells, is stored in the LCIO file format [73] to be further processed within the MARLIN framework.

8.2 Simulation of the Detector Response

Since the raw simulation output includes only the energy deposits inside virtual scintillator tiles, which neither reflect the true scintillator geometry nor take into account effects of the SiPMs, additional simulation software is used to model the readout of the AHCAL prototype. CALICE has additional detector simulation software based on the MARLIN framework called digitization software. This software emulates in several steps detector effects like inter-tile crosstalk, electronics noise, photon detection efficiencies and saturation of the SiPMs, and converts and adds the virtual cell energy deposits in eV from the MOKKA output into channel amplitudes in ADC as they are recorded during data taking [74]. This makes it possible to calibrate and reconstruct this digitized simulation data with exactly the same software as recorded testbeam data.

The first step of the digitization, called ganging, is the adding up of energy deposits in the virtual cells to energy deposits in the real scintillator tile sizes of the actual modules (see sec. 3.1). Once the energy depositions in the real cell geometry is calculated, these depositions in eV need to be converted to the ADC scale and thereby detector effects need to be simulated. Intuitively, the light distribution due to the crosstalk would be calculated first and only afterwards, the resulting energy depositions are converted to MIP scale with a global factor, called MIP2GeV factor, and from there to the individual ADC scales of the readout channels with the MIP constants. With this implementation, the two input parameters to the simulation, the inter-tile crosstalk and the MIP2GeV factor are correlated and cannot be tested separately. However, a second method that has been introduced in [62] allows the decoupling of the two parameters, for the simulation of muons. In this implementation, the cell energy depositions are directly converted to the MIP scale with a conversion factor MIP2GeV and only then the impact of the crosstalk is calculated. For the calculation of the crosstalk, the fraction of a cell energy deposition that is leaked

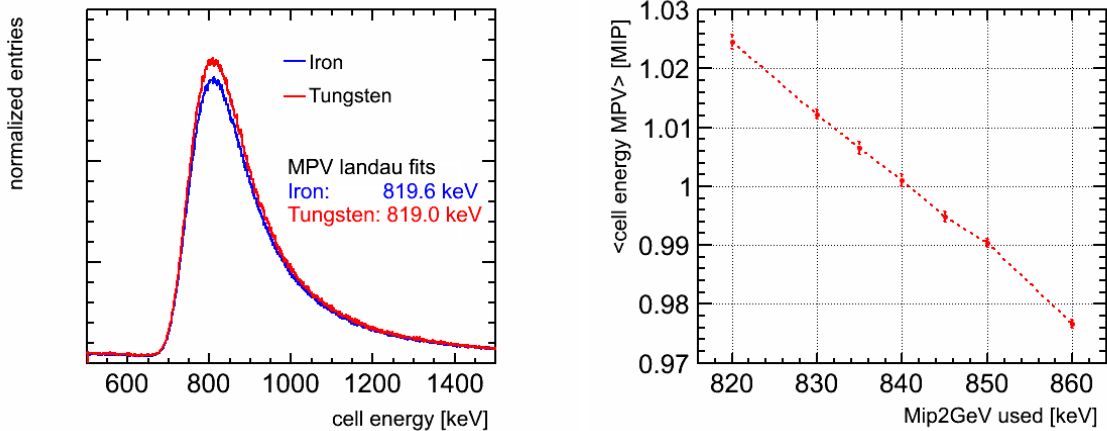


Figure 8.1: The energy deposits in the virtual 1 cm^2 cells from the raw simulation without any detector effects applied for $8 \text{ GeV } \mu^-$ for the two testbeam setup simulations (left). Each spectrum has been fitted with a pure Landau distribution and the MPV has been extracted. After the digitization the cell energy spectra have been fitted with a Landau convoluted with a Gaussian. The right plot shows the mean of a Gaussian fit of the distribution of these MPVs as a function of the MIP 2GeV factor.

to the four direct neighbors is calculated and added to the neighboring cells, but not subtracted from the original central cell. This leads effectively to a rescaling of the original MIP 2GeV factor to an effective factor MIP 2GeV^* :

$$\text{MIP } 2\text{GeV}^* = \text{MIP } 2\text{GeV} \cdot \frac{1}{(1 - X_t^{\text{cell}})} \quad (8.2)$$

with X_t^{cell} as the crosstalk for a whole cell (all 4 edges added up, see sec. 6.9). However, for simulated muons the leaked light in the cells surrounding the hit tile is always below the read-out threshold of 0.5 MIP and does not contribute to the measured detector response. This way, the simulation of muons is independent of the applied parameter for the crosstalk, and the MIP 2GeV factor can be estimated separately with muons.

Figure 8.1 shows, that there is no difference in the energy deposits of muons between the simulations with iron and the tungsten absorber. However, the simulated energy deposition cannot be compared to data directly. The detector effects need to be modeled and the calibration chain needs to be applied to the simulated data, in order to be comparable to recorded data. Therefore, the factor MIP 2GeV was chosen such, that the average MPV of a fit with a Landau distribution convoluted with a Gaussian of the individual cell responses (see sec. 6.6) is 1.0 after all detector effect have been applied. The dependence of the MPVs on the chosen MIP 2GeV factor for the cell energy deposit for 8 GeV muons is also shown in figure 8.1. According to this analysis, a MIP 2GeV factor of $840 \frac{\text{keV}}{\text{MIP}}$ was chosen. Different crosstalk values can be used for different tile sizes, since the measured values for the different tile sizes are very different (see sec. 6.9).

After calculating the energy deposits in MIPs for the real tile geometry, the SiPM photon detection is simulated. The energy deposition A_i in MIPs for the cell i is converted to

the pixel scale, using temperature corrected MIP M_i , gain G_i and intercalibration constants IC_i (see chap. 6 for details):

$$A_i[\text{PIX}] = A_i[\text{MIP}] \cdot \frac{M_i(T)}{G_i(T) \cdot IC_i} \quad (8.3)$$

Then the number of pixels is corrected with the scaled saturation function of this cell (see sec. 6.5) and smeared with a binomial distribution to model the statistical process of photon detection. Then the smeared saturation corrected number of pixels is then converted to the ADC scale with the temperature corrected gain and intercalibration constants:

$$A_{i,\text{sat}}[\text{ADC}] = A_{i,\text{sat}}[\text{PIX}] \cdot G_i(T) \cdot IC_i. \quad (8.4)$$

As last step, the noise of the read out electronics is overlaid to the simulated physics event. This is done by adding amplitudes in ADC from random trigger event data to the simulated ADC amplitudes for every individual cell. The random trigger events are taken from the same run as the run conditions for the simulation and were readout without any threshold applied.

8.3 Beam Profiles

One of the input parameters of the simulation is the position and width of the particle gun. It has to be placed such in x- and y-direction, that the actual beam sizes of the experiments are modeled to ensure that the same cells of the detector are hit in the simulation as during the data taking. Otherwise, the fact that different dead and noisy cells are hit would significantly bias the comparison of data and simulation. In the z-direction, the particle gun is placed just in front of the main triggers and wire chambers, which are located roughly a meter away from the detector. The gun is placed as close to the detector as possible to minimize scattering of the particles in air, which would broaden the simulated beam before it reaches the calorimeter.

The best way to estimate the beam sizes for each data run would be the analysis of the beam profile in the wire chambers mounted next to the main trigger. However, there is no wire chamber information for the FNAL testbeam data available, and to treat both setups consistently, the mean and the RMS of the center-of-gravity distributions in x- and y-direction in the AHCAL is used to estimate the beam size instead. This is done with electrons, since their showers are radially very symmetrical, and the center of gravity for an event will typically reflect the impact position of the electron on the calorimeter. The estimation of the beam sizes was done for every simulated run separately.

Figure 8.2 shows the agreement between the distributions of the center of gravity in x- and y-direction for data and simulation for a single electron run for each testbeam setup, which proves that the same tiles are hit with the simulated beam as during data taking. It is also visible that the beam of the FNAL setup was much broader than the beam at

CERN.

Although naively one would expect, that muons are better suited for the estimation of the beam size, since typically they do not shower, one has to keep in mind, that the beams are collimated before and after magnetic chicanes to achieve a small momentum spread of the beam. Muons, which can penetrate huge amounts of material, are not filtered away by these collimators. This muon beam halo is visible in figure 8.3. The figure also shows the beam profile agreement between data and simulation for a pion run from FNAL. Since the cherenkov information was included into the main trigger for the FNAL setup, the runs contain either electron events or pion and muon events. Therefore the beam sizes for the pion event simulation had to be estimated from pions events in data instead of electron events, although the beam settings are comparable.

The muon events are simulated with the same particle gun settings as for pions events (for CERN also electrons) of the same energy. The mean of the center of gravity distribution is extracted and used as initial value for the particle gun position. The spread of the gun position is set according to the RMS of this distribution. However, these input values do not reflect the true impact positions, since both values are biased by dead and noisy cells. Therefore the exact particle gun position had to be estimated iteratively by adjusting the position and the spread until a reasonable agreement in the center of gravity distributions was achieved.

8.4 Simulation of the Detector Noise

In section 8.2 it is described that the noise amplitudes that are added to the simulated response are extracted from random trigger events recorded during the same run. However, there are two different types of noise event triggers recorded by the AHCAL. The first, called Pedestal trigger, is typically used to measure the noise amplitudes for the simulation, by reading out all cells at random times. However this trigger always records a fixed number of events at once and always while there is no beam spill. The other noise event trigger, called CrcOscillator, is read out every second, independent of the spill signal.

The second trigger is combined with the beam spill trigger to compare the noise during a beam spill with the noise recorded off spill, since there might be a difference due to very late energy depositions from particle showers, e.g. from neutrons. Figure 8.4 shows the difference of the detector energy sum for both triggers for a single run for each testbeam setup for the energy sum and the number of hits above the 0.5 MIP threshold. The difference for the FNAL data is typically 0.2 MIPs on average for the energy sum and 0.4 hits for the whole detector. Because of this difference the in-spill noise triggers are used to estimate the noise amplitudes for the FNAL detector simulation. For the CERN testbeam the number of in-spill triggers is very low, because the beam bunch structure allowed a very continuous shower recording and the main triggers veto the CrcOscillator trigger. Although there is a clear indication that both the mean energy deposition and the number of hits is higher in-spill than off-spill, the pedestal trigger events are used, because the number of in-spill

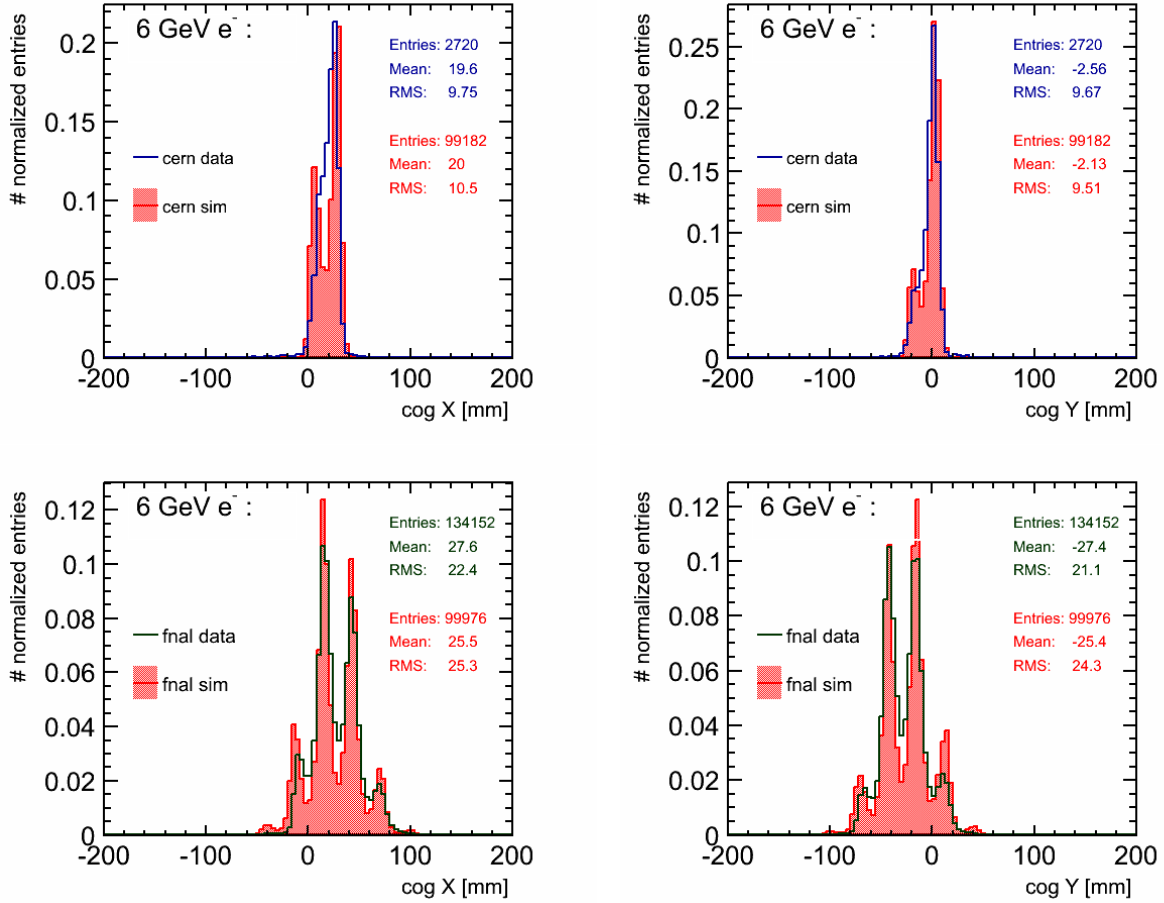


Figure 8.2: Beam profiles for 6 GeV e^- for data and simulation in x- and y-direction for the CERN(upper) and FNAL(bottom) testbeams. The simulation used 18 % crosstalk.

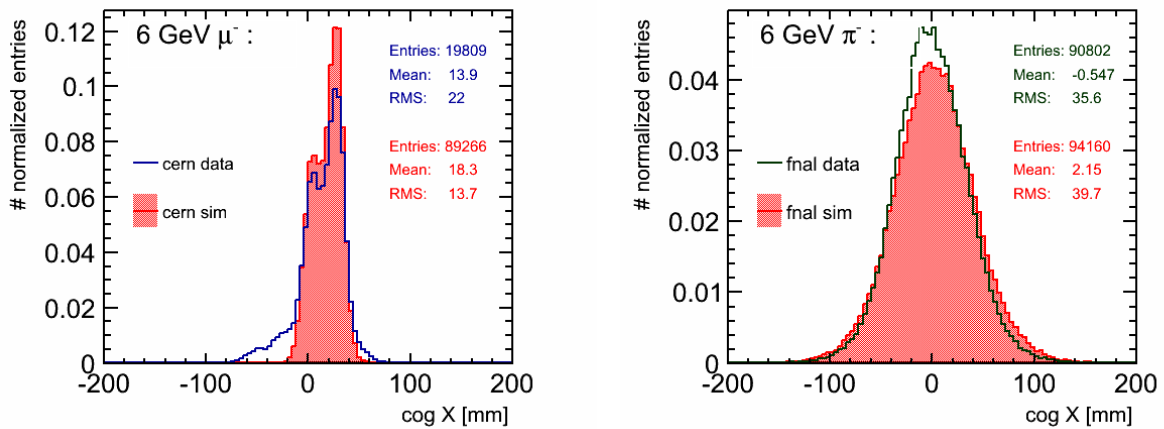


Figure 8.3: Beam profiles in x-direction for 6 GeV μ^- at CERN (left) and 6 GeV π^- at FNAL (right) in data and simulation. The simulation used 18 % crosstalk.

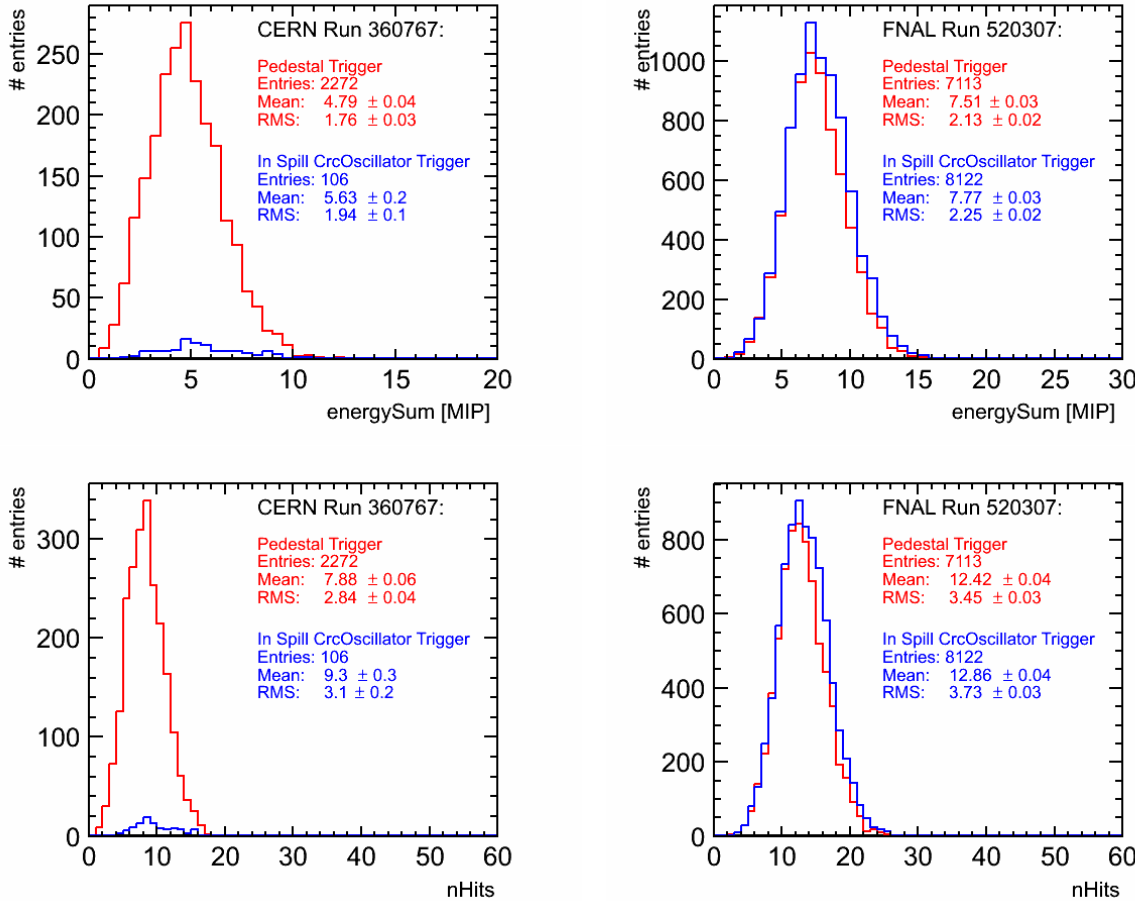


Figure 8.4: Comparison of noise recorded with two different triggers during data taking for a single CERN and FNAL run.

noise events is too low.

8.5 Hadron Shower Decomposition

Hadron showers can be decomposed into at least two different components, the electromagnetic and the hadronic component (see chap. 2). In addition neutrons play a crucial role in the difference of the shower development in iron and tungsten absorbers. However, it is not possible to measure these different shower components individually inside recorded data, but they can be extracted from the simulation. In order to understand differences in the shower development of particle showers in iron and tungsten a MOKKA plugin has been developed, which temporarily stores the full shower development tree from GEANT4 and decomposes the shower into different components by investigating the particle history for every energy deposition.

Almost all final energy depositions, which lead to an excitation of the scintillator and therefore generate scintillation light measured by the detector, are caused by ionization

from charged particles, independent of the processes that take place at intermediate steps of the particle shower [17]. Therefore it is necessary to evaluate the history of the ionizing particle inside the shower to determine the shower component, where the ionizing particle originates from.

In order to decompose the shower into different components, the plugin algorithm searches for every energy deposition inside the scintillator (sub-hit) in the simulation output of the shower development history until a certain particle ancestor is found. Then the interaction between the ancestor and the daughter particle is evaluated. The algorithm moves stepwise back in the shower history of an energy deposition. First it examines, if the final energy deposition was done by an electron, positron, or photon and if the ancestor of this particle in the history is a π^0 or η particle. When a π^0 or η ancestor is found, then this energy deposition is attributed to the electromagnetic shower component.

Second, the algorithm evaluates, if the ancestor was a neutron and attributes it to the neutron shower component accordingly. If a neutron ancestor is found, then the process it originated from is evaluated. The neutron component of the shower is further sub-divided into a neutron capture, a neutron elastic scattering, and a neutron inelastic scattering component. For energy depositions from the neutron elastic scattering component, it is furthermore investigated, if the neutron scattered with a proton, since this component is mostly measured due to the hydrogen in the scintillator and will be suppressed for readout materials with a smaller hydrogen amount (e.g. other readout technologies evaluated by CALICE).

If a particle that deposits energy in the scintillator can neither be attributed to the electromagnetic nor the neutron shower component, it is attributed to the according charged particle component (pion, proton, electron, etc).

This algorithm is illustrated in figure 8.5. It finally stores for every energy deposition the determined shower component together with energy, position, and hit time information.

Since the algorithm works on tracks simulated by the GEANT4 software, it cannot resolve the interactions taking place below the energy threshold for production of secondary tracks. This has no impact for charged particles, as they deposit their energy only via ionization. However, for low energetic neutrons this can lead to a wrong labeling on the energy depositions, as the energy depositions are attributed to the last interaction that generated a secondary track. The subsequent interactions are not calculated in detail and cannot be identified without significant changes to the GEANT4 and the MOKKA framework.

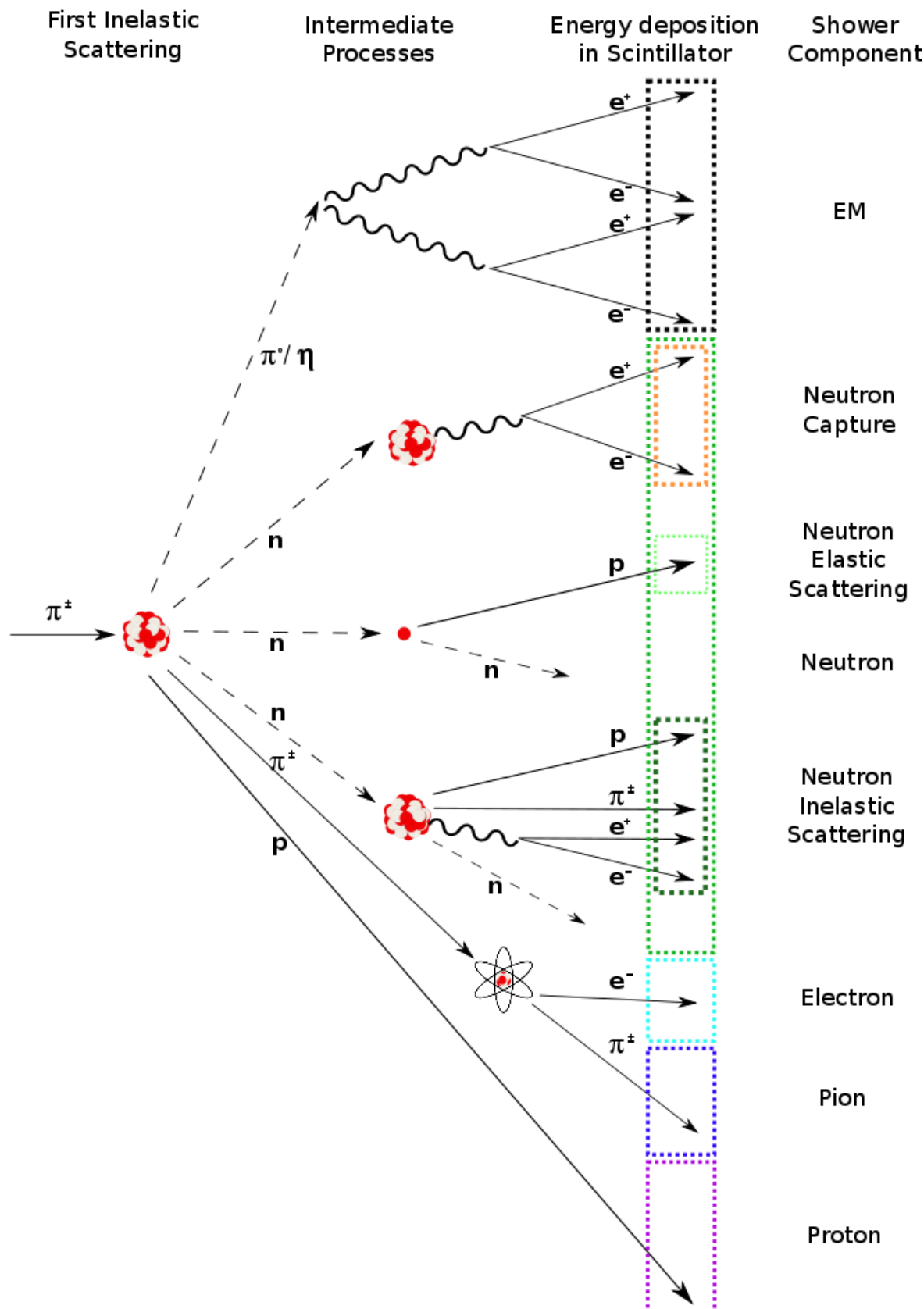


Figure 8.5: Schematic working principle of the shower decomposition algorithm from the Shower Decomposition MOKKA plugin. Excitations of the scintillator, which generate scintillation light, are only caused by charged ionizing particles (solid lines). Ionization from pions that leads to released electrons is shown schematically without the remaining nucleus.

CHAPTER IX

VALIDATION OF THE SIMULATION

In order to justify the shower decomposition into different components in simulations, a comparison of the predicted shower topology in simulations to the measured topology in recorded data is done as a validation of the shower simulation.

However, first muons in data and simulation are compared to validate the detector simulation itself, as well as the conversion factor between the GeV and the MIP scale. Also the calibration uncertainty is estimated with muons. In a second step electrons in data and simulation will be compared to investigate the modeling of the inter-tile crosstalk. At last, pions in data and simulation are compared to estimate which hadron shower simulation (physics list) describes the pion showers best.

9.1 Detector Validation with Muons

As a first step of the validation of the simulation, the distributions of the visible energy deposit E_{vis} and number of hits nHits from muons in data and in simulation in the energy range 4 GeV to 10 GeV are compared for both testbeam setups. For muons neither the saturation correction of the data has a significant impact, as the cell energy deposits are typically at the level 1 MIP, nor has the used crosstalk value for the simulation any impact because of the crosstalk implementation in the software (see sec. 8.2).

The comparison of the energy deposit and the hit multiplicity in data and simulation is used to validate the detector simulation. Figure 9.1 shows the visible energy sum E_{vis} and the number of hits above the 0.5 MIP threshold nHits for 8 GeV muons in data and simulation for the tungsten absorber setup. The peak of the energy sum distribution in data is well reproduced by the simulation, although the distribution in data is broader. The large right-hand tail in data can be explained by the use of the off-spill noise for the simulation, which on average gives less contribution to the detector response. However, the left-hand tail cannot be explained with noise. The most likely explanation is an unidentified dead cell, since this would lower the mean detector response. Also the hit multiplicity distribution in simulation shows a smaller tail towards lower multiplicities than in data, which supports the thesis of an non-identified bad cell. The peak position of the hit multiplicity is well reproduced by the simulation.

Figure 9.2 shows the mean energy deposits and the mean number of hits for muons of 4 GeV, 6 GeV, 8 GeV, and 10 GeV for data and simulation for the iron and the tungsten absorber setup. In addition both the mean of the energy sum and the mean hit multiplicity for those hits which are part of a track segment are given (see sec. 7.5 for track segment algorithm) to estimate the response with a minimal bias from noise. The noise that is removed by this selection is around 15 MIPs for the iron absorber setup and slightly smaller for the tungsten absorber setup since it features also less layers. For the CERN tungsten setup the energy sum in data is higher than predicted by the simulation at 4 GeV and at 10 GeV. At 4 GeV this is most likely an artifact of the event selection, as there is some pion contamination in the muon sample (see sec. 7.8). At 10 GeV an explanation might be the fact, that the off-spill noise is used for the simulation instead of the in-spill noise which also includes late contributions from neutron energy depositions, which are also expected to have more impact at higher energies.

The simulation agrees within 1.5% for CERN tungsten muon data for the energy sum for the hits, which are on a track fragment. For muons in the FNAL iron absorber the energy sum agrees within 0.8% for all hits as well as for the track hits only. These numbers are used as uncertainty of the total energy sum measured by the detector. The hit multiplicity for muons is reproduced by the simulation within 1 hit for both absorber setups. However, the agreement is worse for the track hit multiplicity for the CERN tungsten setup. The most likely explanation is a dead cell that has not been identified and is therefore not removed from the analysis in the simulation. Since the tracking algorithm searches for track fragments that consist of at least three consecutive hits, a single non-identified dead cell that is close to another bad cell can be the reason for a disagreement that is larger than one hit, as also the hits in between the two bad cells are discarded by the algorithm.

Investigations of the energy deposit per layer (see fig. 9.3) show that the simulation reproduces these depositions typically within 7% for the CERN setup and within 5% for the FNAL setup, only the last layers with a high number of dead channels show worse agreement. However, the layer-wise disagreement for the CERN data indicates, that there are not only calibration uncertainties but also an offset for almost every layer that is not observed for the FNAL data and that is most likely due to the use of the off-spill noise for the simulation (see sec. 8.4).

As an estimate for the systematic uncertainty of the energy deposit per layer, the distribution of the layer-wise ratios has been approximated with a gaussian. The width of this approximation is used as estimate for the systematic uncertainty on the layer energy measurement for the electron and pion showers. It is 5% for the CERN setup and 3% for the FNAL setup. For the CERN data, this is probably an overestimation, since the disagreement is mostly due to the underestimated noise contribution in the simulation, which is an offset instead of a relative uncertainty. However, this offset has larger impact on the small energy sums measured in traversing muons, than on the much higher energy sums measured in electron and hadron showers of the same energy.

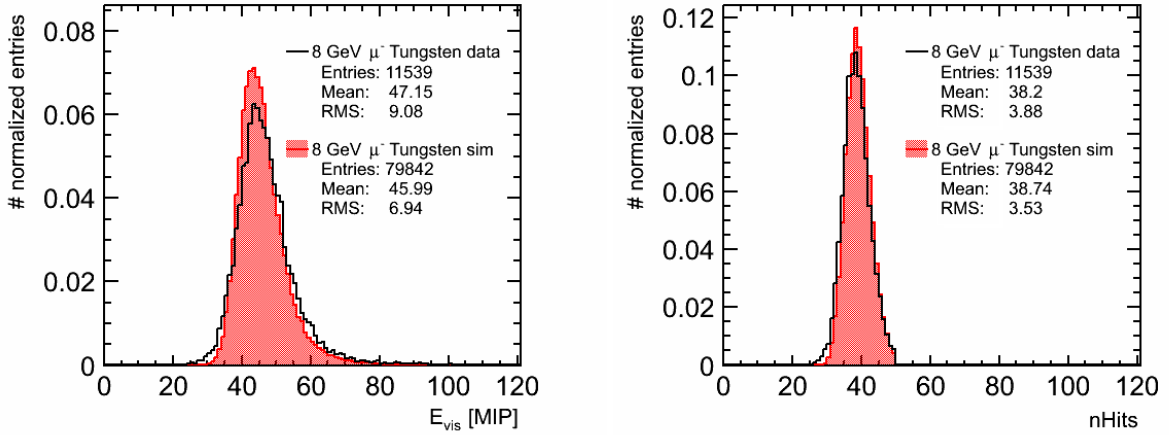


Figure 9.1: The visible energy deposit E_{vis} (left) and the number of hits $nHits$ (right) for 6 GeV muon data and simulation at CERN.

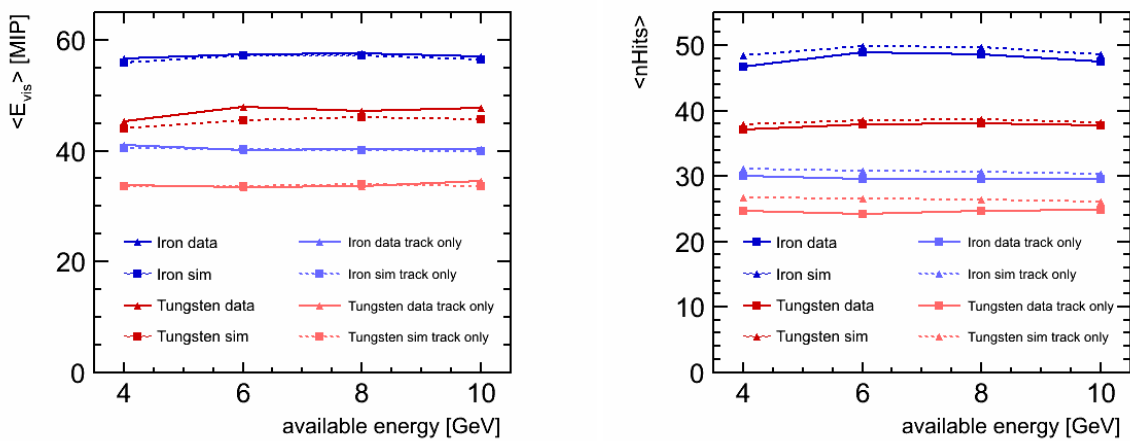


Figure 9.2: Comparison of the mean visible energy deposit $\langle E_{vis} \rangle$ (left) and the mean number of hits $\langle nHits \rangle$ (right) as a function of the available energy for muon data and simulation for both testbeam setups from 4 GeV to 10 GeV. The mean values are also compared for the hits that have been found on a track segment (see text for details).

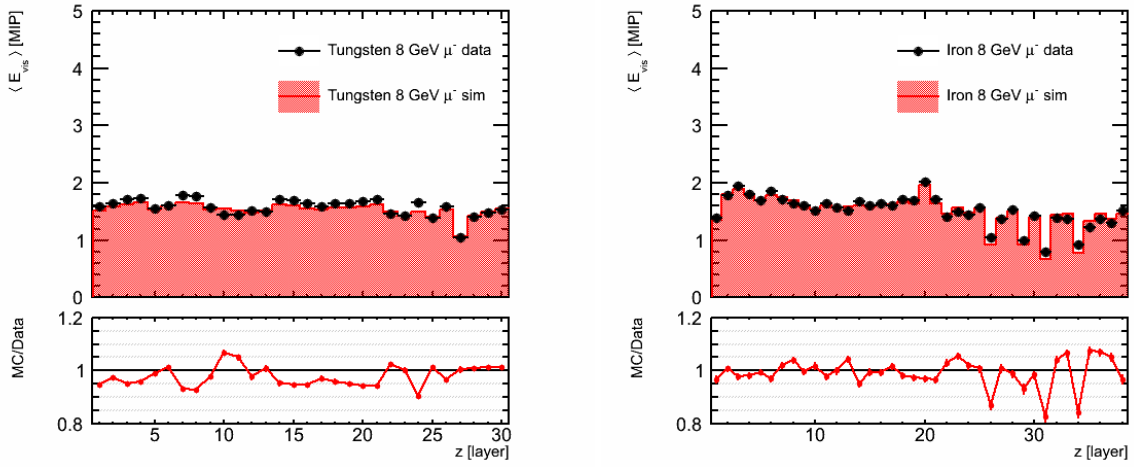


Figure 9.3: Longitudinal shower profiles for 8 GeV μ^- for data and simulation and their ratio for the tungsten (left) and the iron absorber setup (right).

9.2 Detector Validation with Electron Showers

The physics of electron showers is very well understood and can be simulated with negligible uncertainty. However, besides the adding of noise and the beam profiles, an additional effect must be taken into account for the detector response simulation of electron showers. Due to the higher cell energy deposits, the crosstalk parameter has significant impact on the visible energy sum and the number of hits above threshold of the simulation. Although the crosstalk simulation itself just distributes the energy deposition depending on the used crosstalk parameter and does not change the totally deposited energy, the 0.5-MIP threshold will suppress different cells and thereby change the total visible deposited energy. Additionally, the noise contribution to the visible energy sum in the simulation depends on the suppressed cells and thereby on the used crosstalk parameter, as even small additional cell energy deposits from leaked light can result in cells exceeding the 0.5 MIP threshold. Therefore electron showers provide an important tool for the validation of the detector simulation.

At the same time, the desaturation of the high cell energy deposits of electron shower data becomes important, whereas the average muon response is in the linear response range of the SiPMs. However, at the moment no method exists, that could verify the saturation correction for all channels, as the saturation curves that have been recorded during the data taking show not understood problems and cannot be used. Only for a handful of central cell, the saturation could be verified, as these cells reached full saturation also within recorded electron showers. For these central cells, the estimated desaturated maximum cell energies showed a reasonable agreements with the predictions from simulation. At the same time, these are the cells, where the desaturation correction has most impact, as most of the showers energy is deposited in the central cells. However, as mentioned above, the simulation itself has some uncertainties.

Figure 9.4 shows the distribution for the visible energy E_{vis} and the number of hits above threshold n_{Hits} for 4 GeV electrons for data and simulation for the tungsten ab-

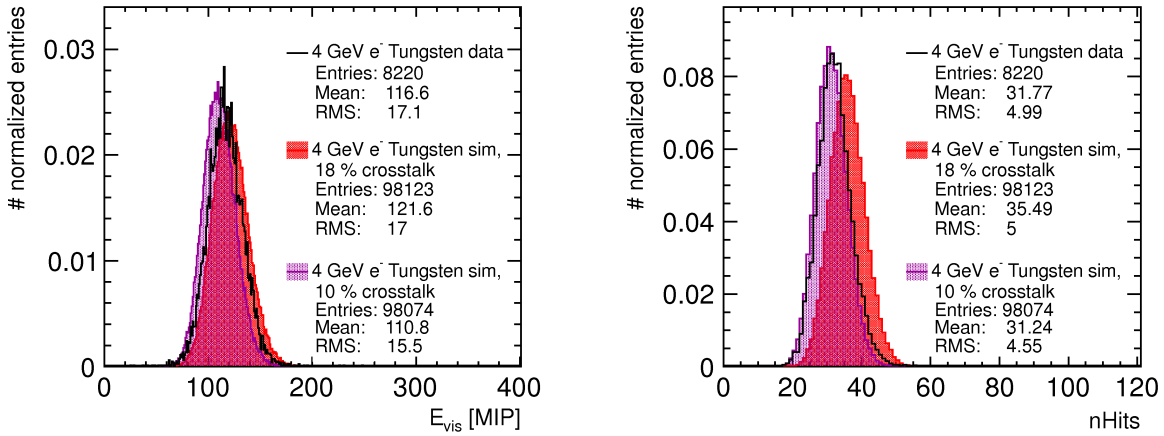


Figure 9.4: The visible energy deposit E_{vis} (left) and the number of hits $n\text{Hits}$ (right) for 4 GeV electron data and two simulations for tungsten absorber.

sorber setup. Two different versions of the detector simulation, with a crosstalk parameter X_t^{cell} of either 10% or 18% are shown. The 18% crosstalk were chosen, because this is the mean measured crosstalk (see sec. 6.9), whereas 10% crosstalk is the currently used default value for the AHCAL and reflects an earlier measurement of the crosstalk. However, this earlier measurement was done only for a single tile, whereas the new measurement did not only show an increased average crosstalk, but also a huge spread of the distribution of measured crosstalk values for the different tiles.

It is apparent that neither simulation does match the data for both observables. Although the hit multiplicity is very well described by the 10% crosstalk simulation, the visible energy distribution in data agrees better with the 18% crosstalk simulation. Since a single energy point can always be biased by calibration errors, problems specific for these runs etc, the agreement between data and simulation is studied as a function of the electron energy.

Figure 9.5 shows the average visible energy sum $\langle E_{\text{vis}} \rangle$ and the average number of hits $\langle n\text{Hits} \rangle$ for electron showers of 2 GeV, 4 GeV, and 6 GeV for both absorber setups for data and the two simulations with the different crosstalk parameter.

The visible energy sum for the tungsten data agrees at 2 GeV and 4 GeV better with the 18% crosstalk simulation, but at 6 GeV the agreement with the 10 % crosstalk simulation is slightly better. The hit multiplicity is generally better described by the 10% simulation, although an underestimation of the hit multiplicity is expected from the use of off-spill noise. For the iron data the 18% crosstalk simulation agrees better with data for both distributions and at all energies. However, the data does not agree within the estimated uncertainty for both distributions at once with either simulation with a global parameter for the crosstalk.

The investigations of the global observables did not lead to a conclusion which crosstalk parameter to use for the correct simulation, therefore the shower topology is studied in greater detail with two additional observables, as calibration errors, etc do not average out

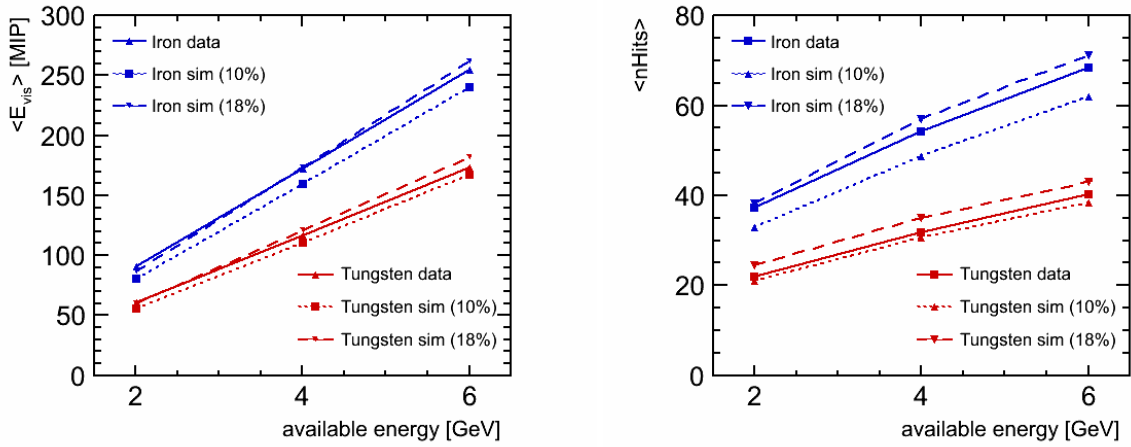


Figure 9.5: Comparison of the mean visible energy deposit $\langle E_{vis} \rangle$ (left) and the mean number of hits $\langle nHits \rangle$ (right) as a function of the available energy for electron data and two simulations with a different crosstalk parameter for both testbeam setups for 2 GeV, 4 GeV, and 6 GeV.

as much as for the global observables. The two additional observables are the longitudinal shower profile, which is the mean visible energy sum per layer, and the radial shower profiles, which describe the mean energy deposit per area as a function of the distance from the shower center of gravity.

Both observables are shown in figure 9.6 for 2 GeV, 4 GeV, and 6 GeV tungsten electron data and simulation. The longitudinal electron shower profiles show that most of the energy is deposited within the first four layers for the tungsten absorber setup and almost completely deposited within the first 7 layers. Later measurements of energy depositions are exclusively due to noise and therefore are omitted in the figure. The shower shape and the shower maximum, which is in layer two, agree well between data and simulation. However, there is a clear difference between the two simulations with the different crosstalk values observable. When data and simulation are compared layer-wise, it becomes apparent that some of the layers in data are well described by the 18% crosstalk simulation, whereas others are better described by the 10% crosstalk simulation. The seventh layer and (later ones) show a difference of more than 15% to the data, almost independent of the crosstalk value. This can be attributed to the limited accuracy of the noise simulation due to the use of the off-spill random trigger events.

The same figure shows also the radial electron shower profiles for the same energies. For the calculation of the radial profiles, the energy deposits in the actual cells have been distributed homogeneously into a $1 \times 1 \text{ cm}^2$ virtual cell grid. Then the energy within each radial bin of 3 cm width around the events center of gravity is summed up and normalized by the area of the bin. This average energy deposit per area is displayed as a function of the distance from the shower center (see [61] for details).

Almost all of the shower energy of electron showers in tungsten is radially contained within a circle of 10 cm radius around the shower center, with no visible energy dependence on the shower width. Beyond 10 cm radius only contributions from noise are visible. This is also reflected by the ratio which is given for both simulations. Both simulations show the same level of agreement with the data for the innermost bin, but the second bin is not described by any of the two simulations, instead a crosstalk parameter in between the two values

is suggested. The crosstalk also smears out the radial profiles, which are expected to be narrower from the moliere radius in tungsten of only roughly 1 cm. However, investigations of the radial profiles per layer indicate that the agreement with either simulation changes significantly for different layers. Beyond 10 cm distance from the shower center, the difference between the two simulations vanishes, because the signal is caused by noise and not by shower energy depositions. In this region the underestimation of the energy deposition by the simulation can be explained by the use of the off-spill noise for the simulation. A relative uncertainty of the same level as for the longitudinal profiles is assumed also for radial profiles, although a more realistic estimation must take into account the individual cell calibration uncertainties as only very few cells contribute significantly to the measured signal for electron showers at these low energies and only the uncertainty of these cells dominates the total uncertainty on the deposited energy.

The same distributions are given in figure 9.7 for the electron showers with iron absorber. Also for iron absorber, the shower shape and shower maximum of the longitudinal energy deposition are well predicted by the simulation. In contrast to the electron showers in tungsten, the electron showers in iron extend much further into the calorimeter (for a detailed comparison see next chapter). The shower maximum is in layer four and there is a significant energy deposit beyond layer 15. However, also for the iron absorber neither simulation describes the data over the full range. At 2 GeV the shower is only described by the 18% crosstalk simulation, whereas the data at higher energies also shows good agreement with the 10% crosstalk simulation for some of the layers. Additionally, the energy deposit in the first layer is significantly higher than in simulation, but this is most likely an artifact of the data sample, where especially in the first layer additional energy from remains of additional particles, that interact upstream of the calorimeter, is deposited. Also the disagreement at the end of the shower, especially at 2 GeV cannot not be attributed to a bad noise description in the simulation, since in-spill noise is used for iron, but instead to the remaining contamination of the electron samples from remnants of additional particles as the dominant effect (see sec. 7.9).

Also the radial profiles for electron showers in iron show a similar behavior to that in tungsten. The central bin is similarly well described by both simulations. The next two bins are better described by the 18% crosstalk simulation, however, this effect is most likely pronounced by the remaining multi-particle contamination of the events, as it was extremely difficult to remove contamination in the central region. This assumption would imply, that the agreement between data simulation for the radial shower profiles in iron gives almost exactly the same result as the one in iron. The underestimation of the energy deposit in the outer shower region by the simulation is also most likely an artifact of the remaining multi-particle contamination in the electron sample, since the iron simulations utilized the in-spill noise for the noise simulation and tails in the visible energy sum of the final electron selection are observable for iron .

The conclusion from these results is that the precision of the detector simulation for electron showers is limited by the crosstalk simulation and additionally for tungsten, by the simulation of the detector noise. The investigation of the tile crosstalk (see sec. 6.9) already indicated a huge spread for the measured values. This and the investigations of the longitudinal shower profiles indicate that a global crosstalk parameter cannot describe

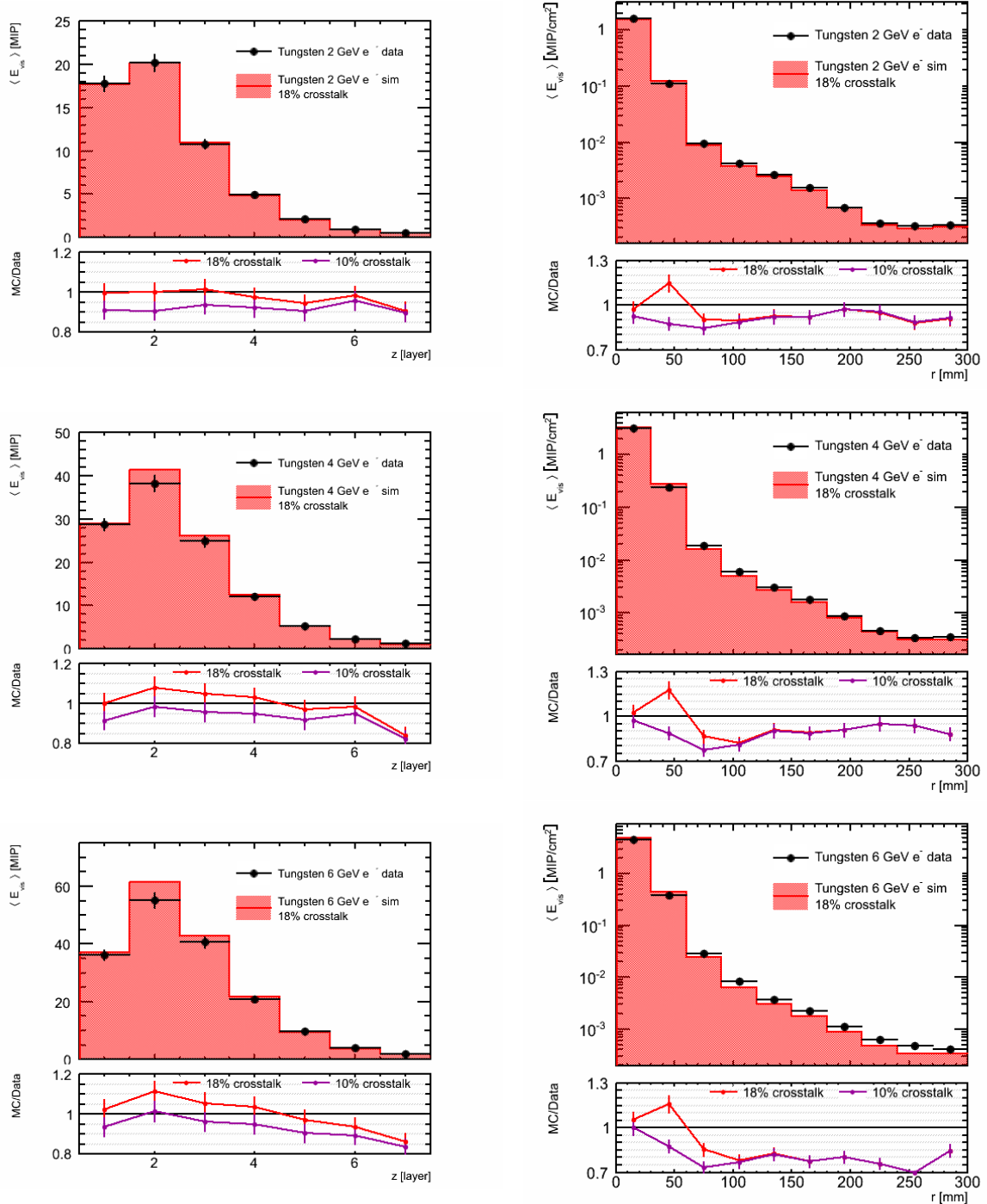


Figure 9.6: The comparison of data and simulation for the longitudinal (left) and radial shower profiles (right) for CERN e^- at 6 GeV, 4 GeV, and 2 GeV (from top to bottom). The ratio is shown for two simulations with different crosstalk values (10% and 18%).

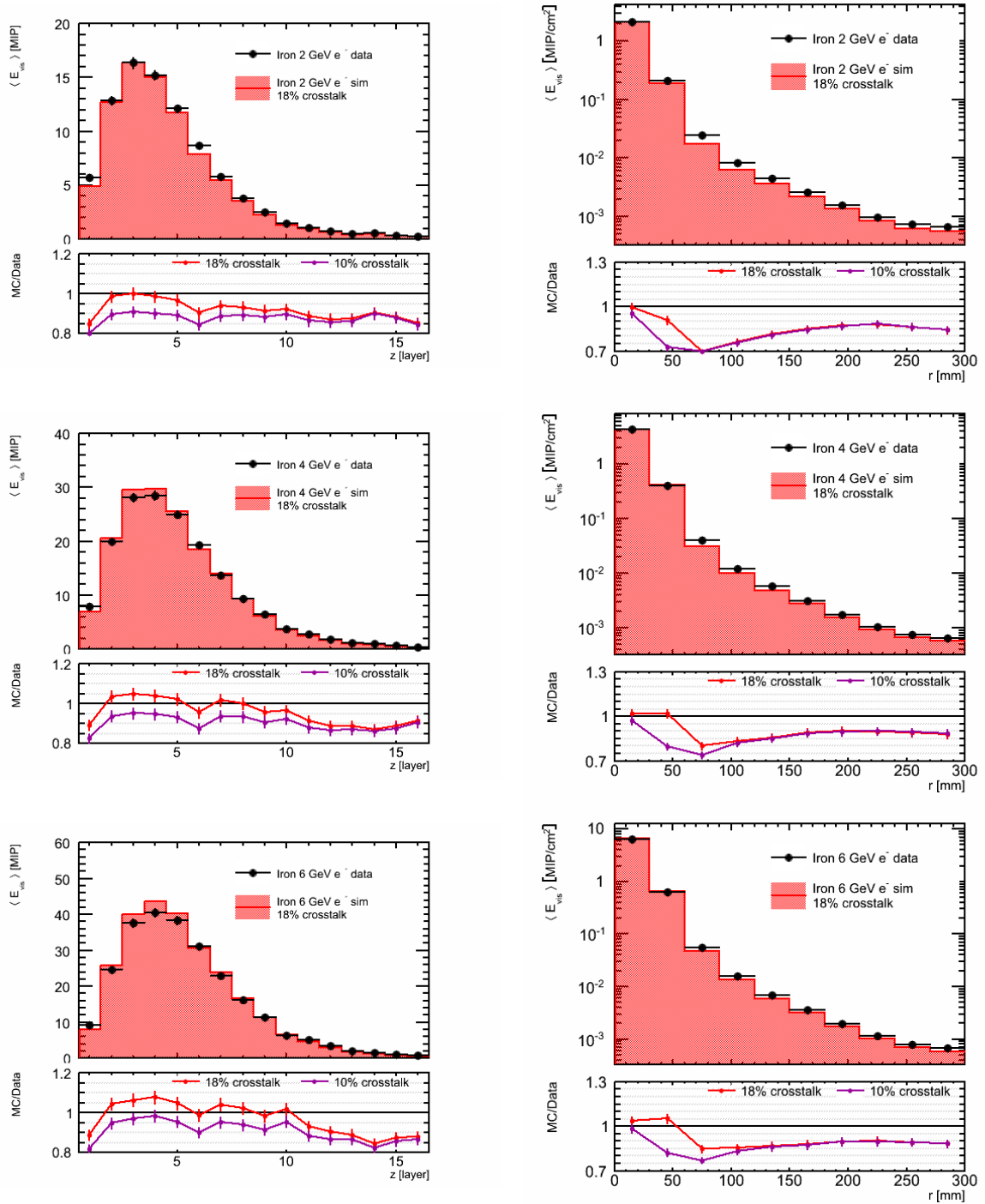


Figure 9.7: The comparison of data and simulation for the longitudinal (left) and radial shower profiles (right) for FNAL e^- at 6 GeV, 4 GeV, and 2 GeV (from top to bottom). The ratio is shown for two simulations with different crosstalk values (10% and 18%).

the detector precisely. Instead the crosstalk parameter has to be adjusted for each cell individually. However, a reevaluation of the cassette design seems more feasible for a future calorimeter.

At the same time, the reconstruction of data is limited by the desaturation of the high energetic cells. Since electron showers are small, only few cells contribute significantly to the detector signal, which makes it necessary to describe these few cells with utmost precision. However, besides these constraints the disagreement between recorded and simulated electron shower data does not exceed a few percent.

A similar validation study on electrons at higher energies has been done in parallel [35].

9.3 Validation of the Pion Shower Simulation

Since an understanding of the limitations of the detector description in the simulation is established, the different hadron shower implementations, or physics list, can be compared. This is necessary since the physics of hadron showers are less well understood than electron showers, and the simulation of hadron showers still undergoes significant improvements. It was shown that integral detector observables of the simulation like the visible energy sum or the hit multiplicity depends significantly on the crosstalk simulation. Therefore a comparison of the global observables between recorded data and simulation seems not a suitable tool to estimate the quality of the hadron shower simulation. Instead, a comparison of the predicted shower topologies can be used to distinguish the quality of different hadron physics simulations. This is done with the shower shape agreement parameter ξ [11] which can be calculated in both, the longitudinal or the radial direction:

$$\xi = \sum_i \min \left(\frac{E_i^{\text{Sim}}}{E^{\text{Sim}}}, \frac{E_i^{\text{Data}}}{E^{\text{Data}}} \right), \quad (9.1)$$

with E_i as the energy the i -th bin, and E as the total visible energy of the respective profile. The parameter ranges from 0.0 to 1.0, where 1.0 reflects perfect agreement of the simulated with the measured shower shape in the given direction. Figure 9.8 shows the longitudinal shape agreement ξ_{Lon} and the radial shape agreement ξ_{Rad} for pions showers of energies from 2 GeV to 10 GeV for the different investigated physics list for both absorber types and both crosstalk parameters.

The physics lists QGSP_BERT_HP, FTFP_BERT_HP and QBBC show the best shape agreement in the longitudinal direction for both absorbers, which all use the BERTINI model at low energies, whereas QGSP_BIC_HP and CHIPS show a significantly worse agreement of the shower shape in data and simulation. This is expected as QGSP_BIC_HP uses the old LHEP model at this energy and CHIPS has no precision neutron transport data. A decreased shape agreement, which is much more pronounced in tungsten than in iron, is also visible for the QGSP_BERT physics list without the HP extension, which is given as an example for a non-HP physics list. The quality of the shower topology prediction of the QGSP_BERT_HP list, which gives the best description in the longitudinal direction, is almost matched by the physics list QBBC, which performs even better at 10 GeV due to the used LHEP model for QGSP_BERT_HP at 10 GeV.

The situation is even more complex in the radial direction, where for tungsten CHIPS gives

the best shape description. In the radial direction the neutron transport calculations are less well visible as they shape agreement is dominated by the innermost bins, which are dominated by energy depositions from the electromagnetic shower core. For iron QBBC performs best, which also predicts the shower shape well for tungsten. The quality of the radial shape prediction from QGSP_BERT_HP is in the middle of the investigated lists. The shape agreement is generally worst for 2 GeV and the 4 GeV energy point is biased by the event selection. Nevertheless, these topological investigations are qualitatively almost independent of the used crosstalk parameter for the simulation, although the exact values for the shape agreement vary with the used crosstalk parameter for the simulation. Overall QGSP_BERT_HP gives the best shape prediction.

The shape agreement for the iron data is comparable to the shape agreement given in previous analysis [11]. However, in the previous analysis, the shape agreement was significantly worse if the electron contamination, that was found in the earlier analysis only (see sec. 7.9), is not subtracted. These improvements are due to the improved calibration and event selection.

Since the physics list QGSP_BERT_HP gives on average the best description of the shower topology, it is used for the investigation of the visible energy sum and the hit multiplicity. Figure 9.9 shows these distributions for pion showers of 8 GeV in tungsten. The mean values are displayed in figure 9.10 as a function of the available energy. The showers were again simulated with the two different values for the crosstalk parameter of the central tiles. The pion showers in tungsten agree better with the 18% crosstalk simulation for the visible energy sum, although, the hit multiplicity is better reproduced by the 10% crosstalk simulation. The iron data clearly favor the 18% crosstalk simulation, although this is most likely biased by a remaining contamination of the events with remains from additional particles, which can lead to a slightly increased energy sum. This also provides an possible explanation for the fact, that the energy sum in data even exceeds the energy predicted by the 18% crosstalk simulation.

The difference of the response in comparison to the analysis presented in [12], where a different MIP2GeV factor was used and a crosstalk parameter of 10%, can be explained with the changes in the simulation and the changes in the calibration and event selection. The difference of the response is at the percent level, whereas the agreement between data and simulation for the hit multiplicity is significantly better than in previous analysis [11], most likely due to the improved calibration and event selection.

Investigation of the longitudinal and radial shower profiles in tungsten show that pion showers reach much further into the calorimeter and are larger than electron showers (see fig. 9.11 and fig. 9.12). The shower maximum is in the third to fifth layer depending on the energy. The shape in total is reproduced well, however, layer seven shows an unphysical peak at all energies, which must be attributed to a calibration problem. Although this was investigated in great detail, the actual problem could not be found. Also for the pion showers, the agreement with both crosstalk simulations varies for each layer. However, the overall agreement is better for the 18% crosstalk simulation. At 4 GeV, the ratio differs drastically between the two simulations in the middle part of the shower. This can be explained with the crosstalk dependent purity of the pion sample (see sec. 7.6).

The radial pion shower profiles for tungsten show an agreement between data and simula-

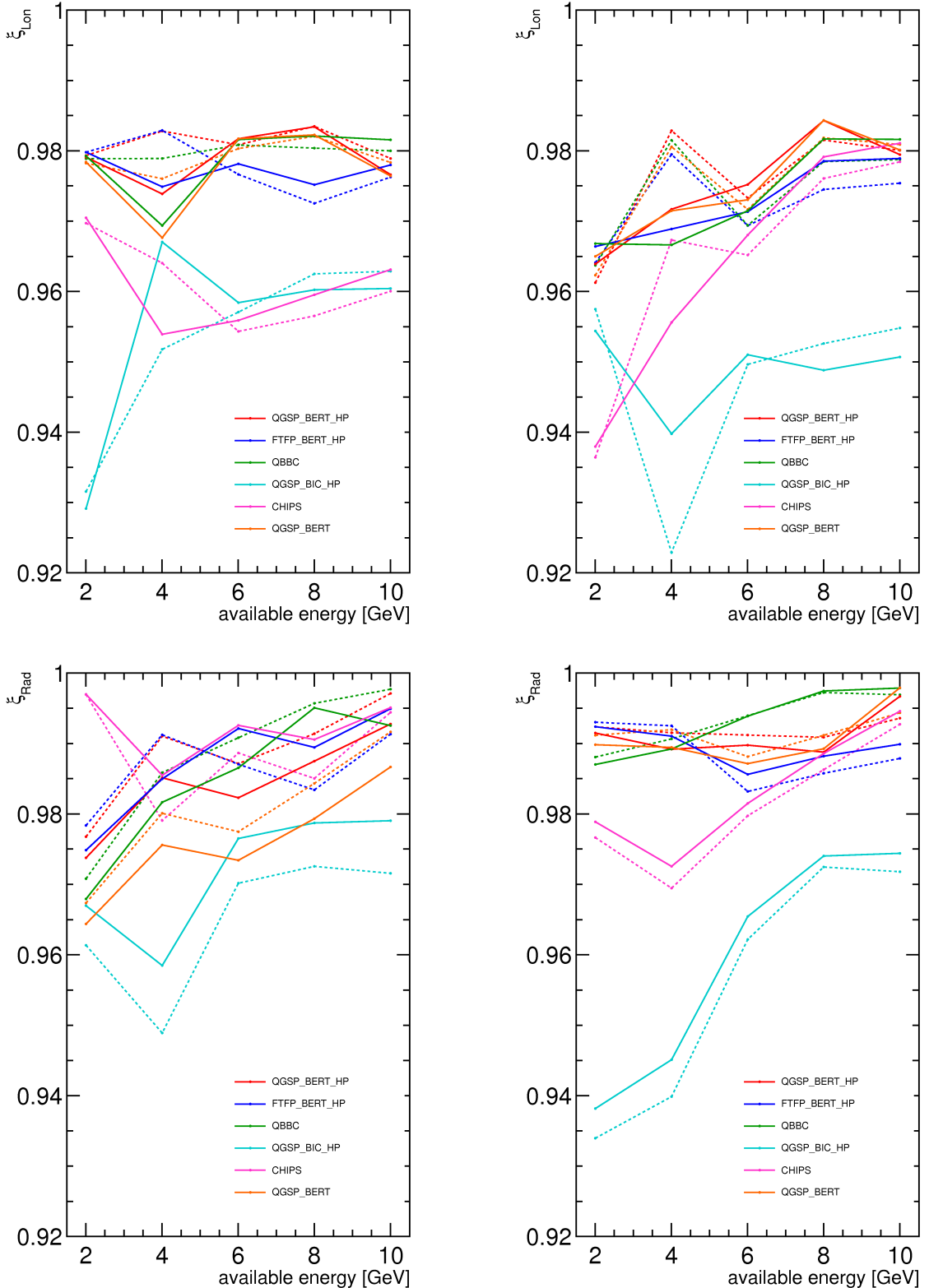


Figure 9.8: The longitudinal (top) shape agreement ξ_{Lon} and radial (bottom) shape agreement ξ_{Rad} for tungsten (left) and iron (right) data for several GEANT4 physics lists. The solid lines stand for a crosstalk parameter of 18% and the dashed lines for a crosstalk parameter of 10%.

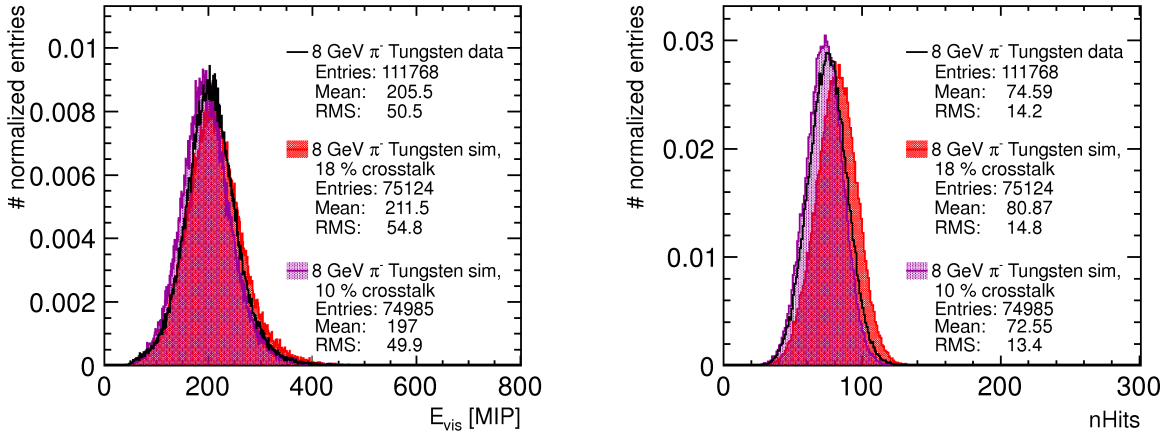


Figure 9.9: The visible energy deposit E_{vis} (left) and the number of hits $n\text{Hits}$ (right) for 8 GeV pion data and simulation for tungsten absorber.

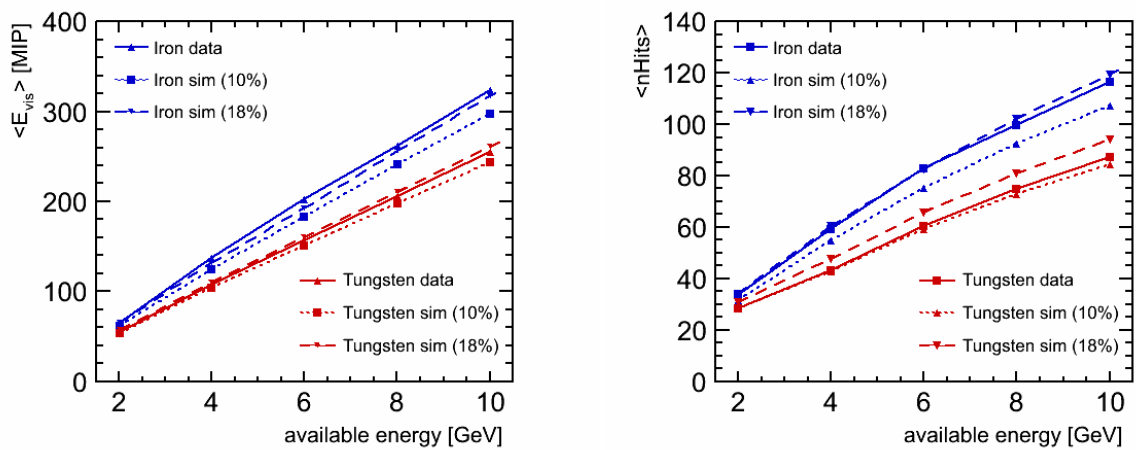


Figure 9.10: Comparison of the mean visible energy deposit $\langle E_{\text{vis}} \rangle$ (left) and the mean number of hits $\langle n\text{Hits} \rangle$ (right) as a function of the available energy for pion data and two simulations with the QGSP_BERT_HP physics list but with a different crosstalk parameter for both testbeam setups from 2 GeV to 10 GeV.

tion within 10%. The central part of the shower is better described by the 18% crosstalk simulation. However, with increasing radial distance from the shower center, there is typically an overestimation of the energy deposit in the simulation. This is worse for the 18% crosstalk simulation.

The shower shapes and the shower maximum also show a reasonable agreement between the iron data and simulation (see fig. 9.13 and fig. 9.14). The pion showers extend further into the calorimeter than for the tungsten absorber setup. The shower maximum is between the fifth and eighth layers depending on the total shower energy. The longitudinal pion shower profiles show in general a worse agreement of the shower shape with the simulation than for the tungsten absorber setup. Especially in the first ten layers, the energy deposit seems to be underestimated by the simulations, whereas the energy deposit in the last layers seems to be overestimated by the simulation. Most likely these features can be attributed to the shift of the muon calibration constants (see sec. 6.6). The shift of the calibration constants was done such, that the muon cell energy depositions have a MPV of one on average for the central cells. But it was already indicated that this shift might work badly other than the cells. Additionally the derived MIP temperature correction for these cells will also not work well, since it is based on the actual constants. This effect cannot be investigated with electron showers, as they are typically too small and involve too few cells. Similar to the tungsten data, the crosstalk dependent sample purity is observable for 4 GeV in the central shower part.

The radial shower profiles show the worst agreement between data and simulation in the shower center. This disagreement could be caused by a small remaining multi-particle contamination of the events, which is especially hard to filter for the central region. The further the distance from the shower center, the better is the agreement between data and simulation. In total, the 18% crosstalk simulation agrees better with the data.

So far, only the agreement of the mean shower profiles between data and simulation has been investigated. Since hadron showers, in contrast to electron showers, are subject to strong event to event fluctuations, it will also be investigated how well these fluctuations are described by the different physics lists. The events longitudinal center of gravity cog_z

$$cog_z = \frac{\sum_i E_i z_i}{\sum_i E_i} \quad (9.2)$$

is calculated with E_i as the energy and z_i as the z-position of the i -th hit. From this the standard deviation of the center of gravity in the z-direction is calculated to quantify the fluctuations in the longitudinal direction:

$$\sigma_z = \sqrt{\frac{\sum_i E_i \cdot (z_i - cog_z)^2}{\sum_i E_i}}. \quad (9.3)$$

The mean standard deviation is shown in figure 9.15 as a function of the available energy for tungsten and iron for data and the investigated physics lists. The dip at 4 GeV for tungsten is an artifact of the event selection. Besides this dip, the shower fluctuations are relatively stable for tungsten, whereas they increase with energy for iron. Also the showers generally fluctuate by roughly 50% stronger in the longitudinal direction for iron than for tungsten. Generally the mean standard deviation of the center of gravity in the

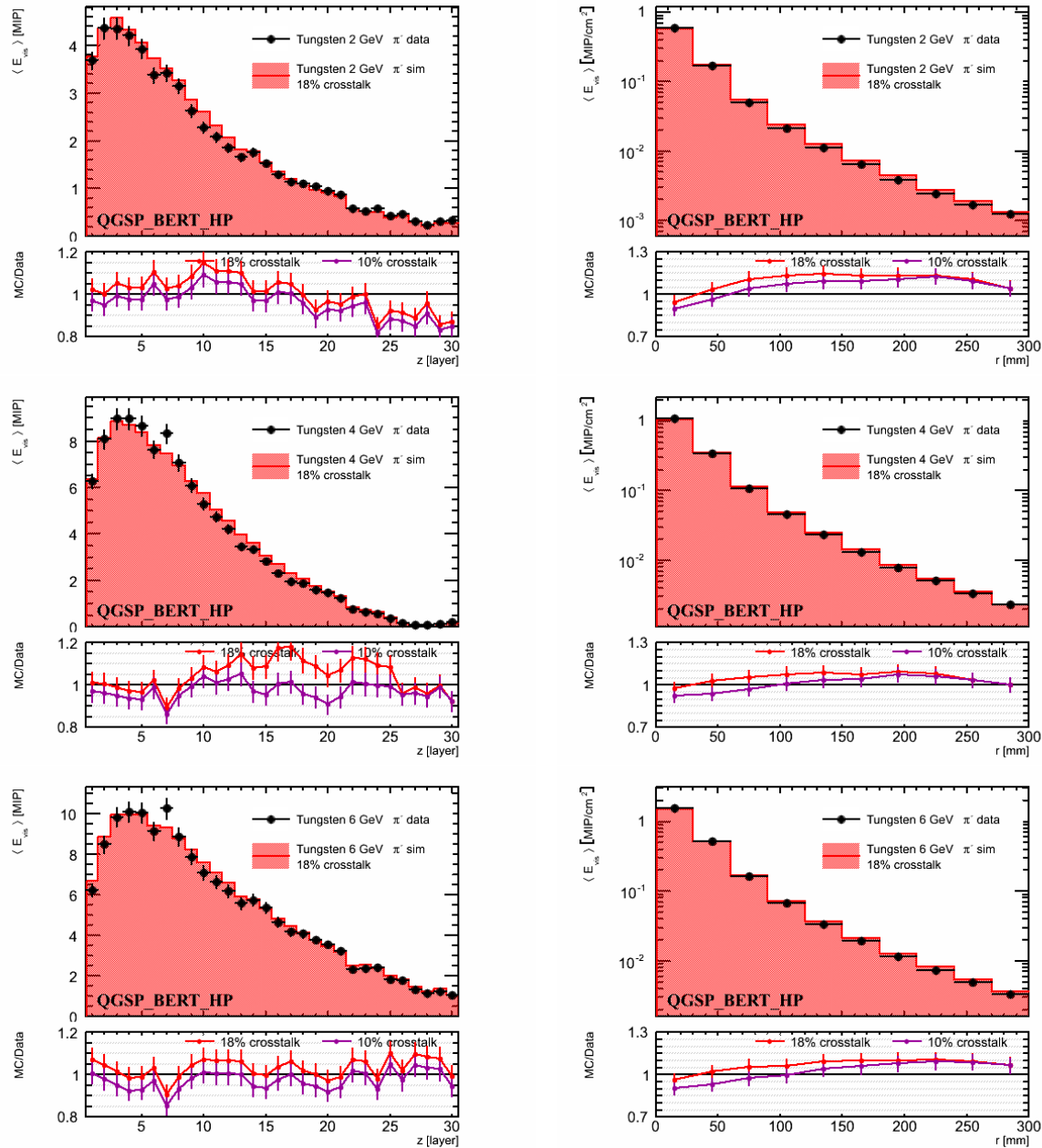


Figure 9.11: The longitudinal (left) and radial (right) shower profiles from 2 GeV to 6 GeV π^- in data and simulation for tungsten absorber.

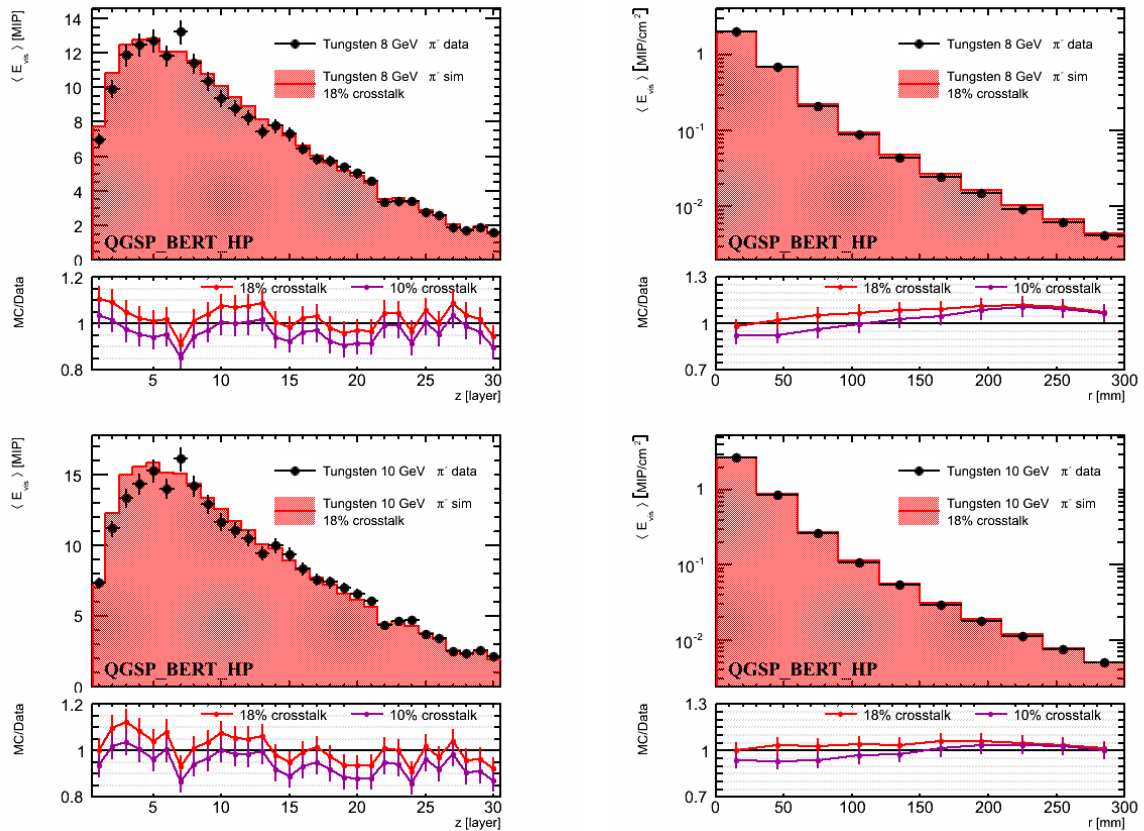


Figure 9.12: The longitudinal (left) and radial (right) shower profiles for 8 GeV and 10 GeV π^- in data and simulation for tungsten absorber.

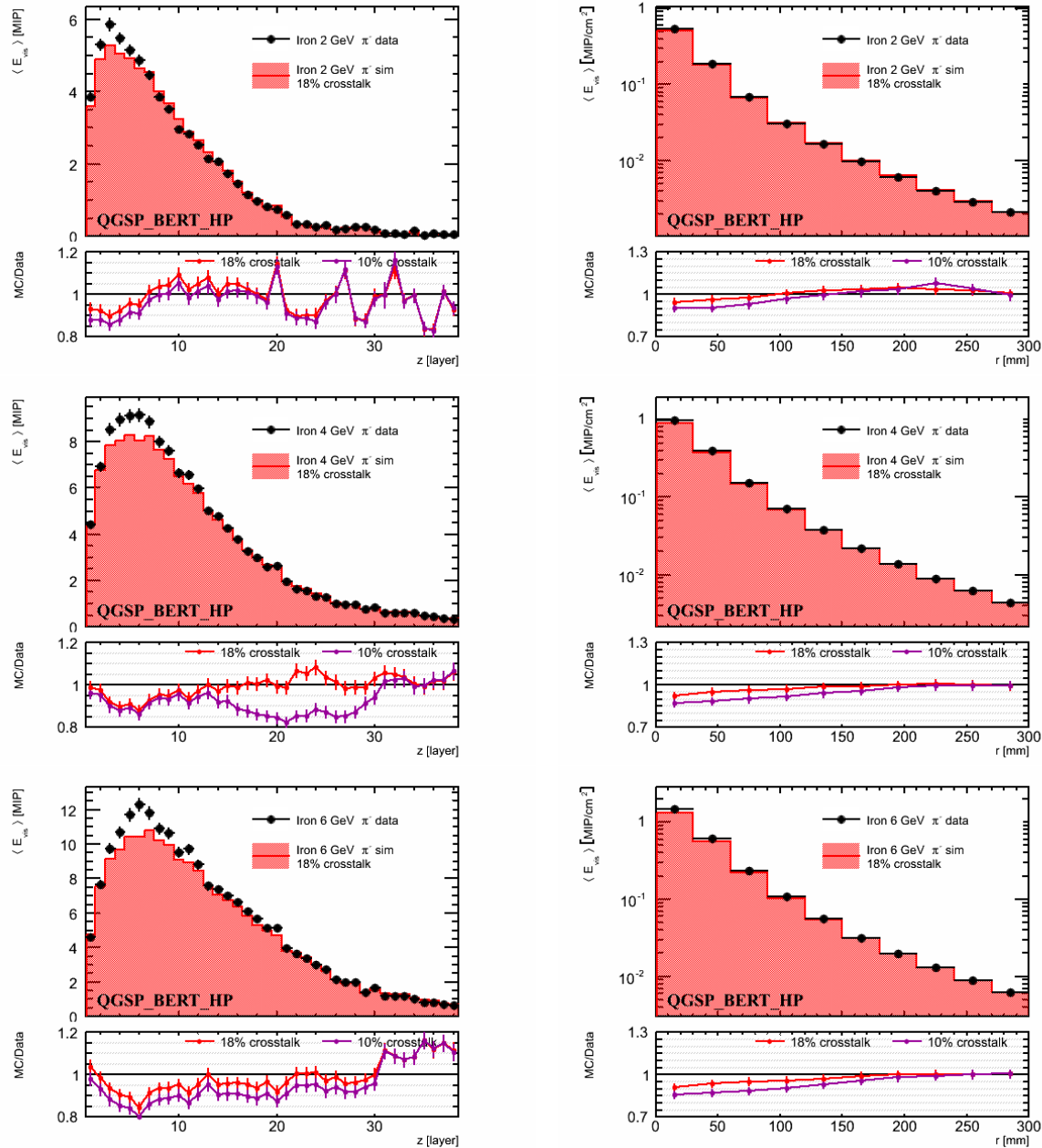


Figure 9.13: The longitudinal (left) and radial (right) shower profiles from 2 GeV to 6 GeV π^- in data and simulation for iron absorber.

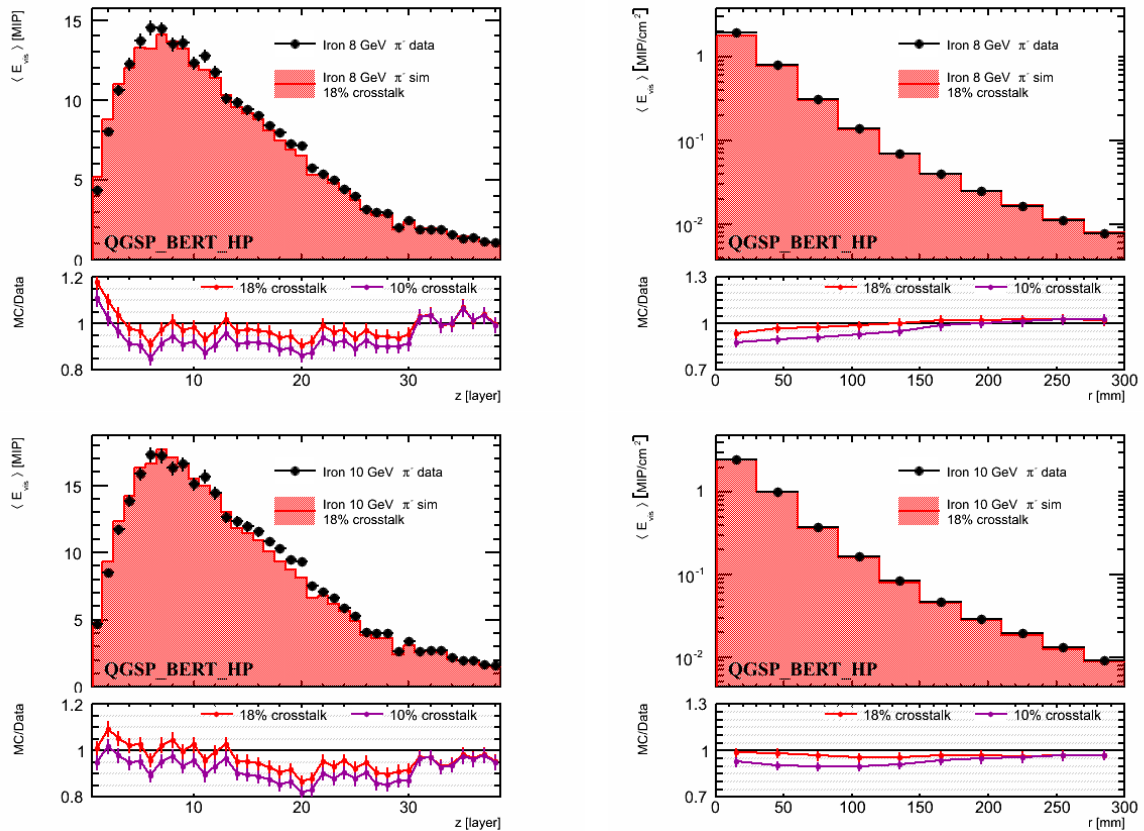


Figure 9.14: The longitudinal (left) and radial (right) shower profiles for 8 GeV and 10 GeV π^- in data and simulation for iron absorber.

longitudinal direction is well predicted by all physics lists, with QGSP_BIC_HP giving the worst description. For iron QGSP_BERT_HP gives the best description, whereas for tungsten QBBC performs best.

The shower fluctuations in the radial direction have been investigated in the same way. The center of gravity in the radial direction is calculated as:

$$\text{cog}_R = \frac{\sum_i E_i r_i}{\sum_i E_i} \quad (9.4)$$

with

$$r_i = \sqrt{(x_i - \text{cog}_X)^2 + (y_i - \text{cog}_Y)^2}. \quad (9.5)$$

To quantify the radial fluctuations the standard deviation from the radial center of gravity has been calculated:

$$\sigma_R = \sqrt{\frac{\sum_i E_i \cdot (r_i - \text{cog}_R)^2}{\sum_i E_i}} \quad (9.6)$$

The mean radial standard deviation of the center of gravity in the r -direction (see fig. 9.16) agree well between data and all simulations for both absorbers. QGSP_BERT_HP gives the best description for both absorbers, whereas the physics list QGSP_BIC_HP has the worst agreement, which underestimates the fluctuations. The fluctuations in tungsten are slightly smaller than in iron.

Despite the changes done in calibration and event selection, the results for iron are in very good agreement with previous results [11], both in terms of absolute numbers as well as for the predicted change of the cascade length and width fluctuations which changes with energy.

The results for the investigations of pion shower profiles with the QGSP_BERT_HP physics list support the hypothesis, that a global crosstalk parameter is not well suited to describe the light leakage among cells in the AHCAL physics prototype. It was also shown, that the agreement with either simulation varies with the layer for the longitudinal profiles. The radial profiles suggest a larger crosstalk parameter for the shower center and smaller ones for the outer parts of the calorimeter, which supports also the hypothesis that there is increased crosstalk for the central region of the modules due to a not tightly attached reflective foil. However, the global values gives generally a better description for pion showers than for electron showers since the showers are larger and involve more cells, which will smear out the uncertainties. A global description also works better for iron, where the showers are bigger than in tungsten.

The overall agreement of the pion showers in data and simulation, especially the good prediction of the shower topology and the shower fluctuations seem to justify the use of the simulated data for a further decomposition of the showers into components and a comparison of these components between the two absorber setups.

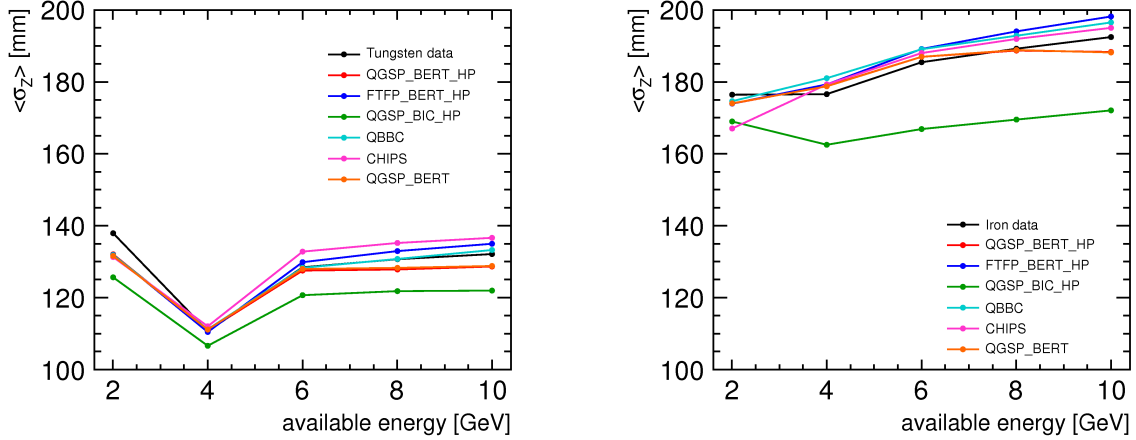


Figure 9.15: The mean of the events longitudinal standard deviation from the showers center of gravity in z-direction as a function of the available energy for tungsten (left) and iron (right) for data and several physics lists.

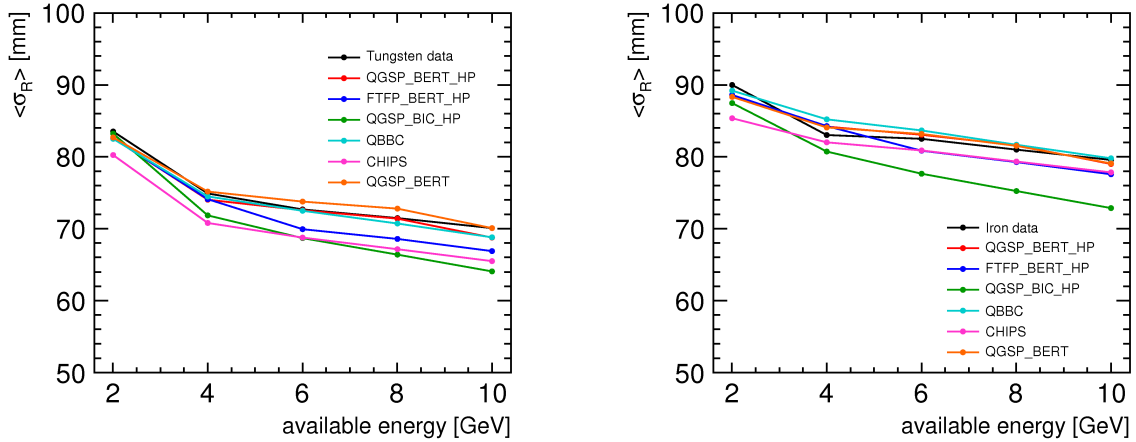


Figure 9.16: The mean of the events radial standard deviation from the showers center of gravity in radial direction as a function of the available energy for tungsten (left) and iron (right) for data and several physics lists.

CHAPTER X

COMPARISON

In this chapter the hadron shower simulation, which has been validated in the last chapter, is used to get a deeper understanding of the differences of hadron showers in tungsten and iron, since these details cannot be measured with currently available detectors inside a particle shower.

The first hadronic interaction is investigated in detail and the differences in the shower start are described. The topological differences for hadron showers in tungsten and iron are discussed with the longitudinal shower shapes. Additionally the shower is decomposed into different showers parts (see sec. 8.5) and all the visible energy is attributed to one of the showers parts. With this decomposition the differences between hadron showers in tungsten and iron can be explained. Also the time evolution of the showers is compared. This provides the tools to compare the two calorimeters in terms of energy resolution and the e/h ratio and understand the differences in their performance.

10.1 The First Hadronic Interaction and the Electromagnetic Fraction

Since the nuclei of tungsten and iron contain very different numbers of protons and especially neutrons, the number of particles emerging from the first hadronic interaction of the incident pions with the atoms of the absorber is investigated in the simulation. Therefore the first hadronic inelastic scattering is evaluated and the numbers of protons, neutrons, and pions released by the scattering are counted, if the scattering occurred inside the absorber volume of the simulation.

Figure 10.1 shows the distributions of the number of protons released by the first hadronic interaction in the absorber for 6 GeV negative pions. In case of iron a two peak structure is visible: the most likely process is the loss of either one or two, or 9 protons during the hadronic interaction. Also for tungsten the most likely is the loss of one or two protons due to the interaction. However, a second peak, which is also at a higher number of released protons, is much less pronounced. On average slightly more protons are released from the first hadronic interaction in tungsten than in iron. Nevertheless, no significant

difference in the mean visible energy deposited by protons in the shower is expected, as the mean fraction of the showers initial energy that is carried by protons after the first hadronic interaction is very similar (see Fig. 10.2) and the protons deposit their energy mainly via ionization losses.

Figure 10.1 also shows the number of neutrons from the first interaction. In contrast to the number of protons, the number of neutrons emitted from the first inelastic hadronic scattering is very different for iron and tungsten. This is expected due to the very different nuclei. Iron shows also for the number of emitted neutrons a two peak structure, with a first sharp peak at two released neutrons and a second, less pronounced peak at 12 released neutrons. For tungsten, the chance to emit few neutrons is in the same order of magnitude as the loss of more than 50 neutrons for a single hadronic interaction. Nevertheless, the fractions of the total energy that are transported by the protons and neutrons after the first inelastic scattering are similar for both absorber types and only minor differences are observable.

This means, that the neutrons will on average carry less kinetic energy for tungsten than in iron. However, in contrast to the proton component, this difference in the number of released neutrons is expected to result also in different visible energy depositions by this shower component, since the mechanisms of neutron energy deposition are much more complex than for protons and depend significantly on the neutron energy (e.g. the neutron capture cross section is highest for neutrons at rest). Minor differences in the fractions of the initial shower energy transported by the different particle types are also observable for neutral and charged pions, but for charged pions no impact on the visible energy is expected for the same reasons as for protons.

The neutral pions (and heavier neutral mesons) decay almost instantly into two photons, which then deposit the energy in small electromagnetic sub-showers, which form the electromagnetic component of the shower. However, for this shower component not only the first hadronic interaction must be taken into account but also subsequent ones. Therefore the electromagnetic fraction f_{EM} has been calculated for each event by adding up the energy of all neutral pions (and η -mesons) found inside the shower and dividing by the energy of the pion initiating the shower.

Figure 10.3 shows the distribution of the electromagnetic fraction for tungsten and iron for 6 GeV pions. The distribution ranges from zero, which means that the whole shower is transported via charged hadrons and neutrons, to one, which means that the whole energy is used to create neutral pions which decay almost instantly into photons and create electromagnetic sub-showers. However, there is a small difference between tungsten and iron, where the electromagnetic fraction is on average slightly increased for iron. The mean electromagnetic fraction is also shown as a function of the energy of the incoming particle. The mean fraction increases with energy as expected from the increasing number of subsequent generations of hadron interactions with increasing energy of the primary particle. Also the difference between tungsten and iron is observable. However, this difference is also visible if only the first interaction is investigated and is not only due to an on average higher number of subsequent hadronic interactions in iron.

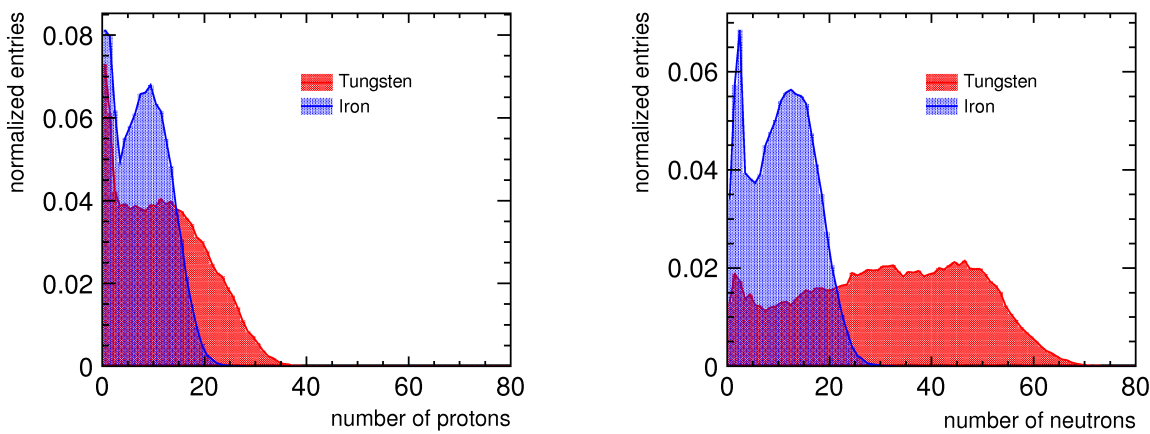


Figure 10.1: The number of protons (left) and neutrons (right) from the first hadronic interaction for 6 GeV pions in tungsten and iron. (normalized to the total number of events)

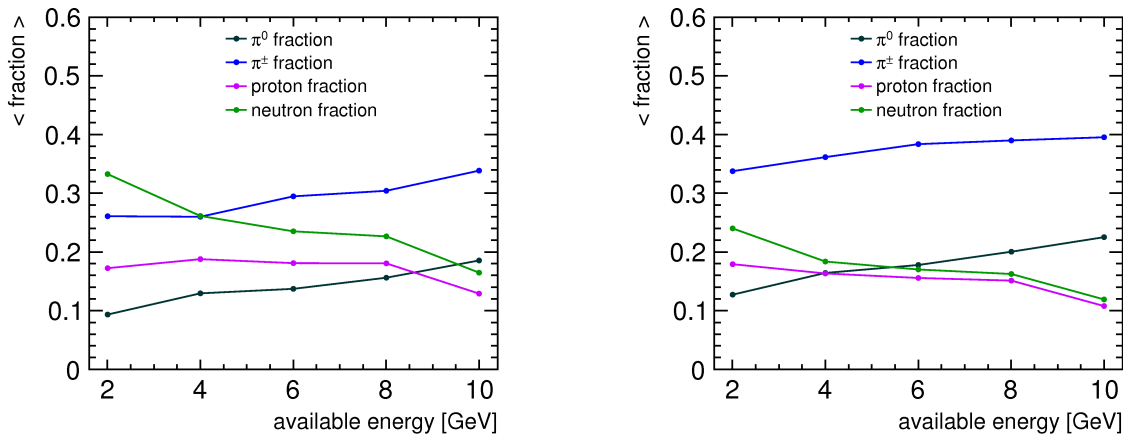


Figure 10.2: The mean fraction of the showering pions energy transported by different particles after the first inelastic scattering for tungsten (left) and iron (right) as a function of the available energy.

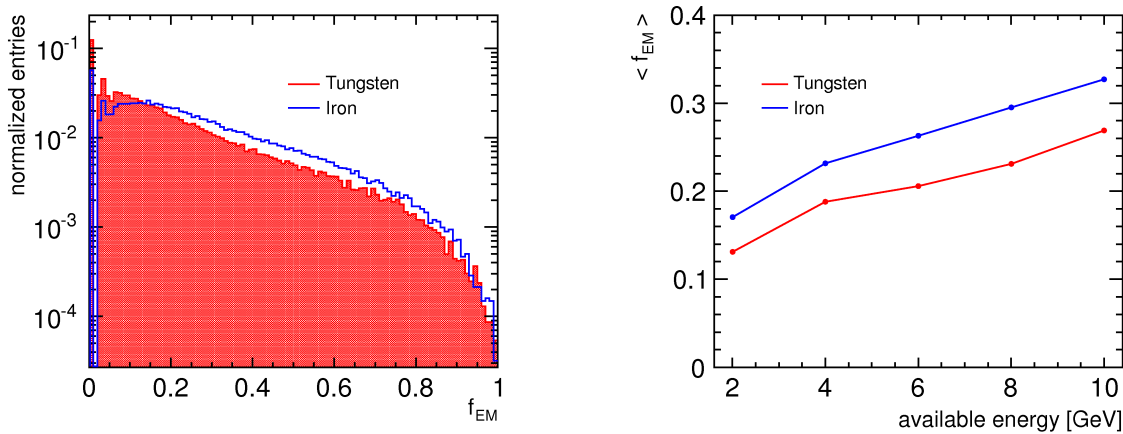


Figure 10.3: The electromagnetic fraction f_{EM} for 6 GeV pions (normalized to the total number of events) and the mean electromagnetic fraction as a function of the available energy for tungsten and iron.

10.2 Comparison of Shower Profiles

The last chapter showed that electron showers are larger in iron than in tungsten and involve therefore more cells. In the longitudinal direction the difference is best observable as the electron showers deposit almost all their energy within the first few layers in tungsten, whereas in iron the showers extend significantly further into the calorimeter. However, if the longitudinal shower shapes are compared on their natural scale, the effective radiation length X_0^{eff} , they should look almost identical and their shower maxima should agree. Only the measured total deposited energy is different, due to the different thickness of the tungsten and iron absorber plates in radiation lengths, which leads to a higher fraction of the total shower energy deposited inside the tungsten absorber plates, than in the iron absorber plates, and thereby to a different sampling fraction of the shower for both absorber configurations.

This is shown in figure 10.4, which displays the same 6 GeV electron shower profiles for tungsten and iron as in the last chapter. The profiles are given as a function of the effective radiation length instead of as a function of the layer. The effective radiation length is calculated with the numbers and material amounts given table C.1 in Appendix C and equation 2.4. The calculated effective radiation length for the tungsten absorber setup is $X_0^{\text{eff}}(\text{Tungsten}) = 0.87 \text{ cm}$ and for the iron absorber setup $X_0^{\text{eff}}(\text{Iron}) = 2.57 \text{ cm}$. Additionally the longitudinal profiles have been approximated with the parametrization given in equation 2.3. The shower maxima around $0.4 X_0^{\text{eff}}$ and the shapes of the profiles agree on the effective radiation length scale, if it is taken into account, that the approximation of the shower maximum for the tungsten data is biased to lower values. The fit is constrained by the absolutely small systematic error on the fourth layer and the low number of data points.

Figure 10.4 shows also the longitudinal shower profiles for 6 GeV π^- . In contrast to the electron showers profile, the pion shower profiles do not even agree on their native scale, the effective interaction length $\lambda_{\text{int}}^{\text{eff}}$, which has been calculated with table C.1 and equation 2.11. The calculated effective interaction length for the tungsten absorber setup is $\lambda_{\text{int}}^{\text{eff}}(\text{Tungsten}) = 19.11 \text{ cm}$ and for the iron absorber setup $\lambda_{\text{int}}^{\text{eff}}(\text{Iron}) = 23.28 \text{ cm}$.

The reason for this difference in the longitudinal shower shape for pions in tungsten and iron can be explained by decomposing the shower into the different shower parts (see sec. 8.5). Figure 10.5 and figure 10.6 show the same longitudinal shower profiles for pions in tungsten and iron absorber as section 9.3, but this time as a function of the effective interaction length instead of as a function of the layer. Additionally the mean energy deposit per layer for the different shower components is shown. The mean energy deposit has been calculated from the mean fraction per layer for each shower component multiplied by the total mean energy deposit per layer from the simulation with 18% crosstalk.

The fraction of the shower energy, that is carried by the electromagnetic component increases with increasing momentum of the showering particle and is the dominant visible shower component except for the lowest energies, where the proton component deposits equal amounts of visible energy. The comparison of the electromagnetic component shows that this shower component is significantly smaller in tungsten than in iron at all energies. Besides this difference in the totally deposited energy there is also a significant difference in the longitudinal shape of the electromagnetic component between the two absorber ma-

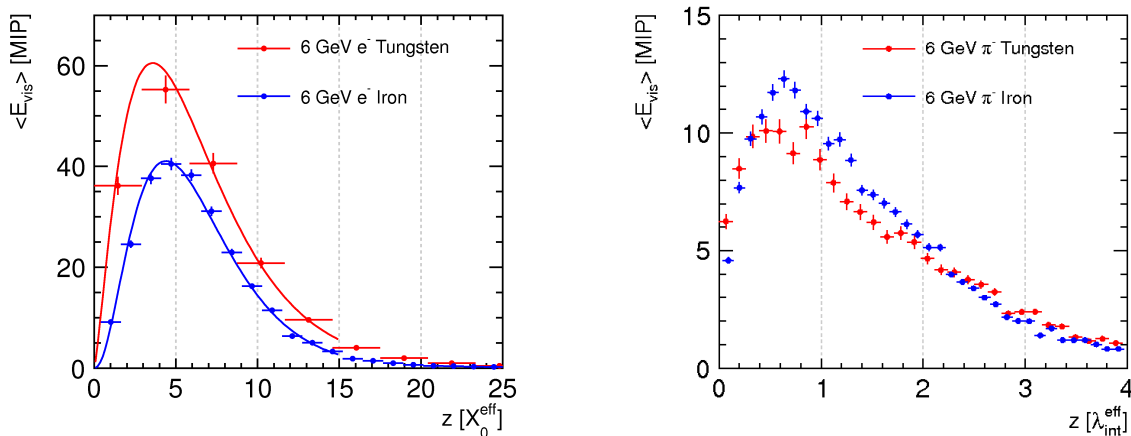


Figure 10.4: The longitudinal shower profiles for 6 GeV electrons as a function of the effective radiation length (left) and for 6 GeV pions as a function of the effective interaction length (right) for iron and tungsten absorber. The electron profiles have been approximated with a longitudinal parametrization (see text for details).

terials. In tungsten the maximum of the electromagnetic shower component is typically at around $0.5 \lambda_{int}^{eff}$, whereas in iron the maximum is around $0.8 \lambda_{int}^{eff}$. This difference is due to the fact, that the effective radiation length is the natural scale for any electromagnetic sub-shower inside the hadronic shower and is the dominant effect for the explanation of the different longitudinal shape of pion showers in tungsten and iron. This means that there is also a different sampling rate of the electromagnetic component in the two absorbers with the given absorber thicknesses.

Additionally there is a difference in the neutron component, which becomes more important for the later layers. This is studied in detail in the comparison of the shower components, since the differences are better visible for the total energy sums for the components (see sec. 10.4). The proton and pion component are very similar for both absorbers. This is also true for the additional electron component of the shower, which originates from collisions of charged pions and protons with electrons from the absorber with a huge momentum transfer.

10.3 Time evolution of the Shower

Additionally the time evolution of pion showers is studied and compared for both absorber materials. A precise understanding of the time structure of hadron showers is especially important for calorimeters for the CLIC detectors, as the foreseen bunch structure of the accelerator will lead to several subsequent primary collisions depositing energy in the detector within the readout time window. With sufficient knowledge of the time structure it is possible to disentangle the energy depositions into shower contributions from individual events. Additionally the time structure can help to get a four dimensional event reconstruction. Though the AHCAL physics prototype does not have the capability to measure the hit time of each individual sub-hit (see sec. 8.5), a possibility to measure at least the

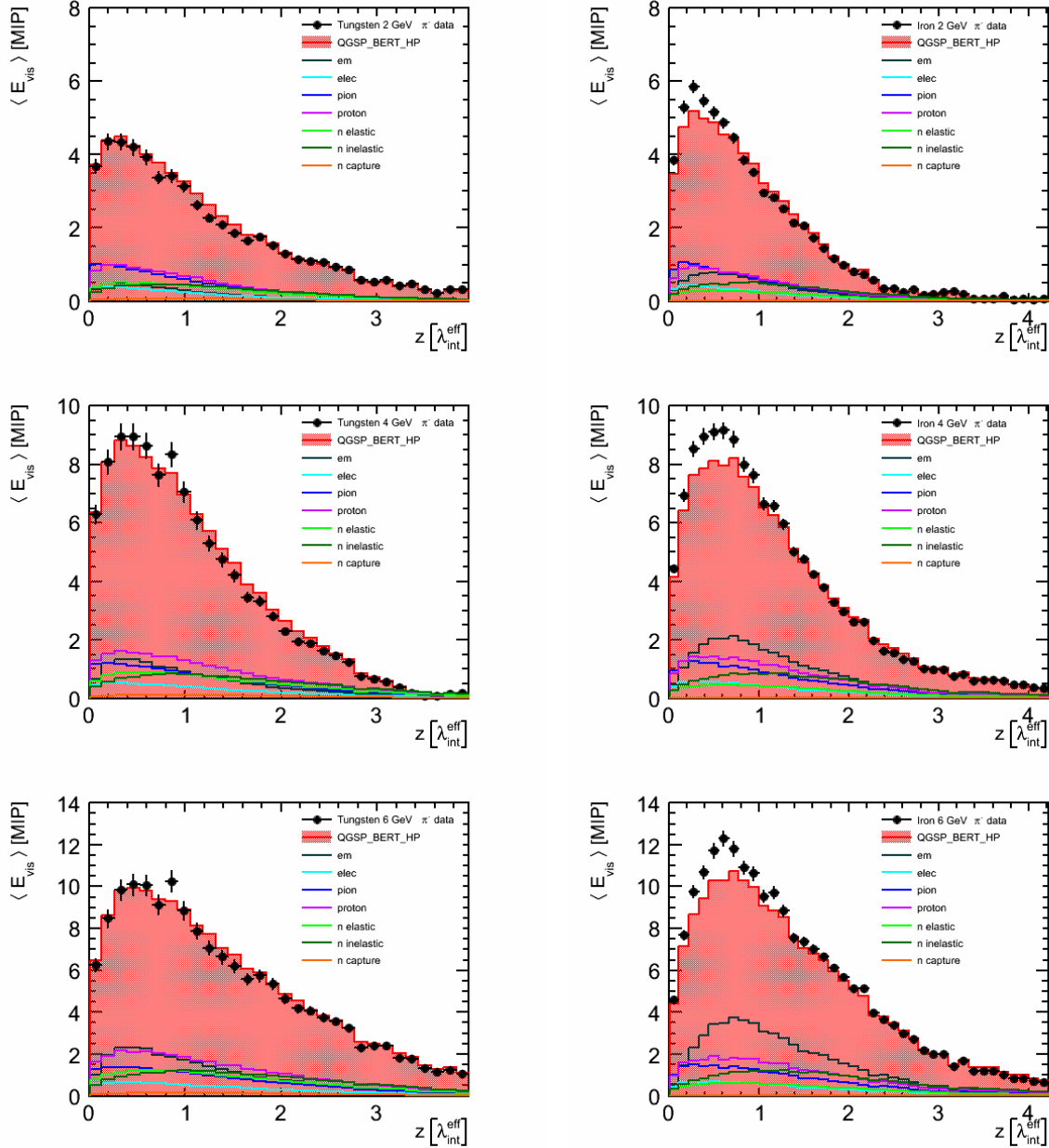


Figure 10.5: The longitudinal shower profiles for tungsten (left) and iron (right) for data and simulation for 2 GeV, 4 GeV and 6 GeV (top to bottom). For the simulation also the decomposition into the different shower components is shown. The simulation used QGSP_BERT_HP and 18% crosstalk.

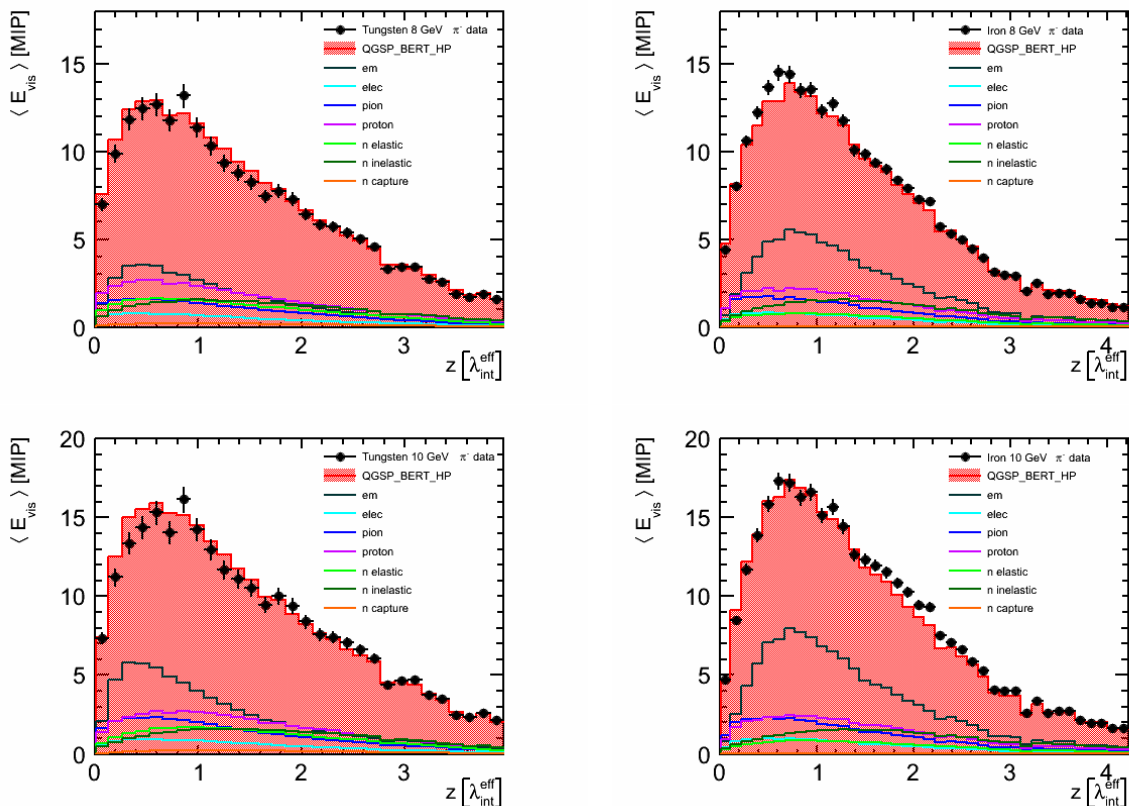


Figure 10.6: The longitudinal shower profiles for tungsten (left) and iron (right) for data and simulation for 8 GeV and 10 GeV (top to bottom). For the simulation also the decomposition into the different shower components is shown. The simulation used QGSP_BERT_HP and 18% crosstalk.

time of the first sub-hit in a cell is already included in the next generation of readout electronics for the AHCAL.

Figure 10.7 shows the number of sub-hits in the simulation leading to energy depositions in the active layers as a function of the deposition time from the entering of the primary pion into the detector for the full readout window of the AHCAL electronics of 150 ns. The cascade is dominated during the first nanoseconds by the electromagnetic component for both absorber types. Also the charged pions and protons released from the hadronic give significant contributions during the first nanoseconds. For iron, the initial part of the shower lasts longer, as the pions on average penetrate further into the calorimeter before interacting.

However, the electromagnetic component only gives significant contributions directly after the first inelastic hadronic interaction, as particles from this component have velocities close to the velocity of light and their energy is absorbed very fast. After a few nanoseconds the neutron components start to dominate the cascade. The neutron components start with a slow turn-on curve during the first nanoseconds, which is due to the fact, that, in contrast to the charged particles, the released neutrons do not immediately deposit energy via ionization. In the very beginning of this neutron time regime, the energy depositions from the neutron inelastic scattering dominate, but since this component falls off rapidly, there is a time interval of roughly 20-30 ns where the elastic scattering dominates. This is a feature of the active layers consisting of hydrogen-rich plastic scintillator polystyrene. If other readout materials like gas are used, then this neutron elastic component will be suppressed. After this intermediate regime of the neutron elastic scattering, the neutron inelastic and neutron capture shower components start to dominate the energy deposition. It is also well observable, that the neutron components give typically an order of magnitude more contributions to the deposited energy for tungsten, than for iron.

The late neutron inelastic tail is mostly an artifact of the decomposition algorithm, as these neutrons have typically an energy below the production threshold for secondary tracks. Therefore the last interaction that generated a secondary track is used for the labeling of these hits. In reality these hits must most likely be attributed to neutron elastic scattering and neutron capture instead.

The other shower components like the charged pion component, the proton component, and the additional electron component, which is a feature of the ionization simulation in GEANT, are very similar for both absorber types.

10.4 Comparison of the Shower Components for different Physics Lists

Although the comparison of the different hadron simulations to data in chapter 9 overall favored the QGSP_BERT physics list, this does not necessarily mean that also the individual shower components are described correctly or just better than for the other hadron simulations. Therefore the investigation of the shower components has been done for each of the used hadron physics lists. However, one can try to relate the different shower components, and the quality of their modeling to the shape agreement of the respective physics list. This distinction works only between the electromagnetic component and all other

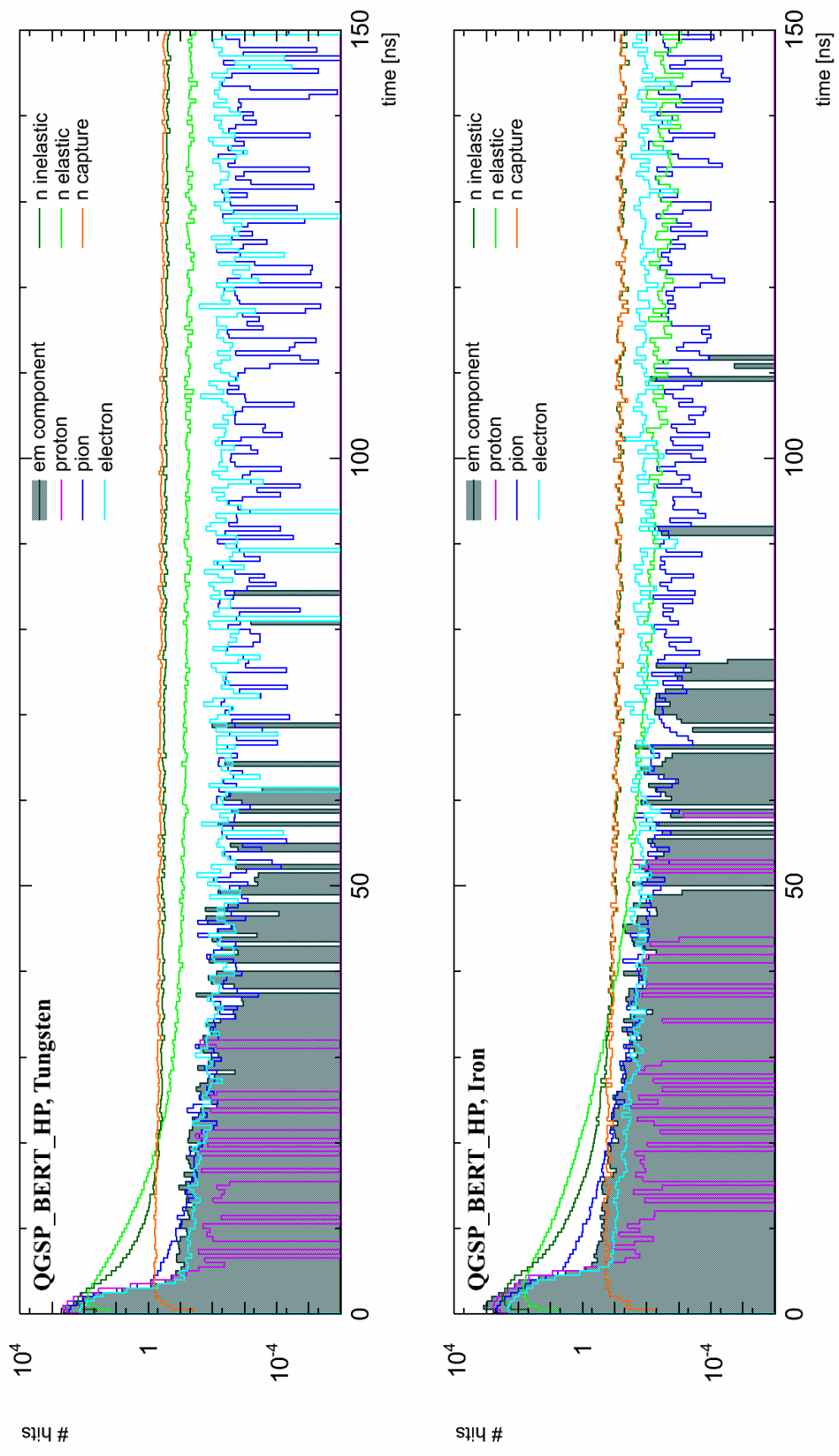


Figure 10.7: The number of energy depositions in the active layers as a function of the deposition time for the different shower components for tungsten (top) and iron (bottom).

components together, as most of the shower components deposit energy in the same region of the shower. The differences between the physics lists for the relevant shower components are small compared to the differences of the absorber materials. Therefore a quantitative statement of the shower component comparison between the two absorber setups can be given.

Figure 10.8 shows the mean visible energy deposited by the electromagnetic shower component $\langle E_{vis}^{EM} \rangle$ as a function of the pion energy, where the difference between both absorber types is well visible: The visible energy which was deposited via the electromagnetic shower component is almost twice as much in iron as in tungsten. However, it was also shown, that the mean electromagnetic fraction of the shower is only slightly increased in iron in comparison to tungsten (see fig. 10.3). This can be explained with the very different sampling of this shower component for the chosen absorber thicknesses, which leads in case of tungsten to a significantly higher amount of energy deposited inside the absorber and which is therefore not visible. The mean visible energy that is deposited by the electromagnetic shower component is predicted very similar by all physics lists, although QGSP_BIC_HP and CHIPS give a higher prediction.

The investigation of the first hadronic interaction showed also a difference between iron and tungsten in the number of neutrons released by this interaction. Therefore also a difference in the neutron component of the showers is expected. The same figure shows also the mean visible energy deposition via the neutron shower component for both absorber types as a function of the pion shower energy. Also for this shower component there is a difference between the two absorbers visible, however this time, the neutron deposits more visible energy for the tungsten absorber configuration. The neutron component is predicted lowest by the physics lists QGSP_BIC_HP and CHIPS, whereas the other lists predict a significantly higher neutron component. Also visible is a higher prediction for the neutron component in tungsten for the QGSP_BERT physics list in comparison to the same list with HP-extension, but almost no difference for these two lists for iron. The energy deposit via the other shower components shows no significant differences between the two absorbers.

The neutron component is also further decomposed into an inelastic scattering, an elastic scattering and a neutron capture component to understand the details of the different neutron components for the two absorbers (see fig. 10.9). However, the predictions for the individual neutron components cannot be related to the shape agreement, as the neutron components deposit their energy in the same shower regions. QBBC gives the highest prediction for the neutron inelastic component, whereas QGSP_BIC_HP gives the lowest prediction. The energy deposit via the inelastic neutron scattering does not show a significant difference between the two absorber types.

In contrast to this, the elastic neutron component is roughly a factor two higher in tungsten. This can be explained with the fact, that there are much more medium energetic neutrons inside the tungsten showers, as already expected from the higher number of neutrons which are released from the first interaction. The different physics lists give similar predictions for this component, with the prediction for highest energy deposit from QGSP_BERT_HP and the lowest from QGSP_BIC_HP.

The prediction for the visible energy deposit by the neutron capture component differs by roughly a factor of ten between the two absorber setups. However, from the comparison

of the cross sections for neutron capture one would expect an even stronger neutron capture component for tungsten as the cross section is (dependent on the exact energy) up to three orders of magnitude higher. Thus, the difference of only one order of magnitude for the visible energy for this shower component can be explained in the same way as for the electromagnetic shower component. Since neutron capture results in the release of one to several γ s, which will give electromagnetic sub-showers, a huge fraction of the energy of these sub-showers is also deposited inside the absorber in case of tungsten. The physics list QGSP_BERT_HP and FTFP_BERT_HP give almost identical predictions, whereas QBBC gives the lowest prediction and QGSP_BIC_HP is in between the three. Also well visible is the difference between the physics QGSP_BERT with and without the HP extension. Without the high precision neutron data, the energy deposition via neutron capture is predicted significantly higher for both absorbers, although the total contribution in iron is negligible. The CHIPS physics list shows zero contribution for neutron elastic scattering and neutron capture because it treats both processes inside its neutron inelastic scattering calculations. This also leads to an increased deposition for the neutron inelastic shower component, which is observable. However, disentangling for CHIPS would require a more sophisticated decomposition algorithm, which identifies the processes inside the neutron inelastic scattering calculations.

However, one must distinguish between differences in the shower development which is due to the absorber and effects that are caused by the active layers. An effect, that is enhanced by the choice of organic scintillator as active material is the elastic scattering of neutrons. The average energy transfer per scattering is larger the smaller the mass of the scattering nucleus. The average energy deposit per scattering is therefore largest for elastic scattering with single protons, or hydrogen atoms.

Figure 10.10 shows the mean visible energy that is deposited by the neutron elastic scattering shower component, for those scatterings that occurred with a single proton. The difference between tungsten and iron for this part of the neutron elastic scattering shower component is almost as big as the difference in the complete neutron elastic scattering component. Therefore a less significant difference is expected for the neutron elastic shower component if an active material with a low hydrogen density is chosen, e.g. gas for micromegas active layers. This would also affect the neutron capture component as the neutrons are less efficiently moderated and the neutron capture cross section depends on the neutron momentum.

10.5 Comparison of the Calorimeters

The two figures of merit for a hadron calorimeter are the e/h ratio and the single particle energy resolution. The small number of different energies that are evaluated by this thesis does not allow for a precise estimation of these parameters, as they are not constrained enough. Nevertheless the precision is sufficient for a qualitative comparison of both absorber configurations. However, the number given here can not be used to evaluate the performance of the AHCAL, and other studies show that a significantly better energy resolution can be achieved with this detector [75].

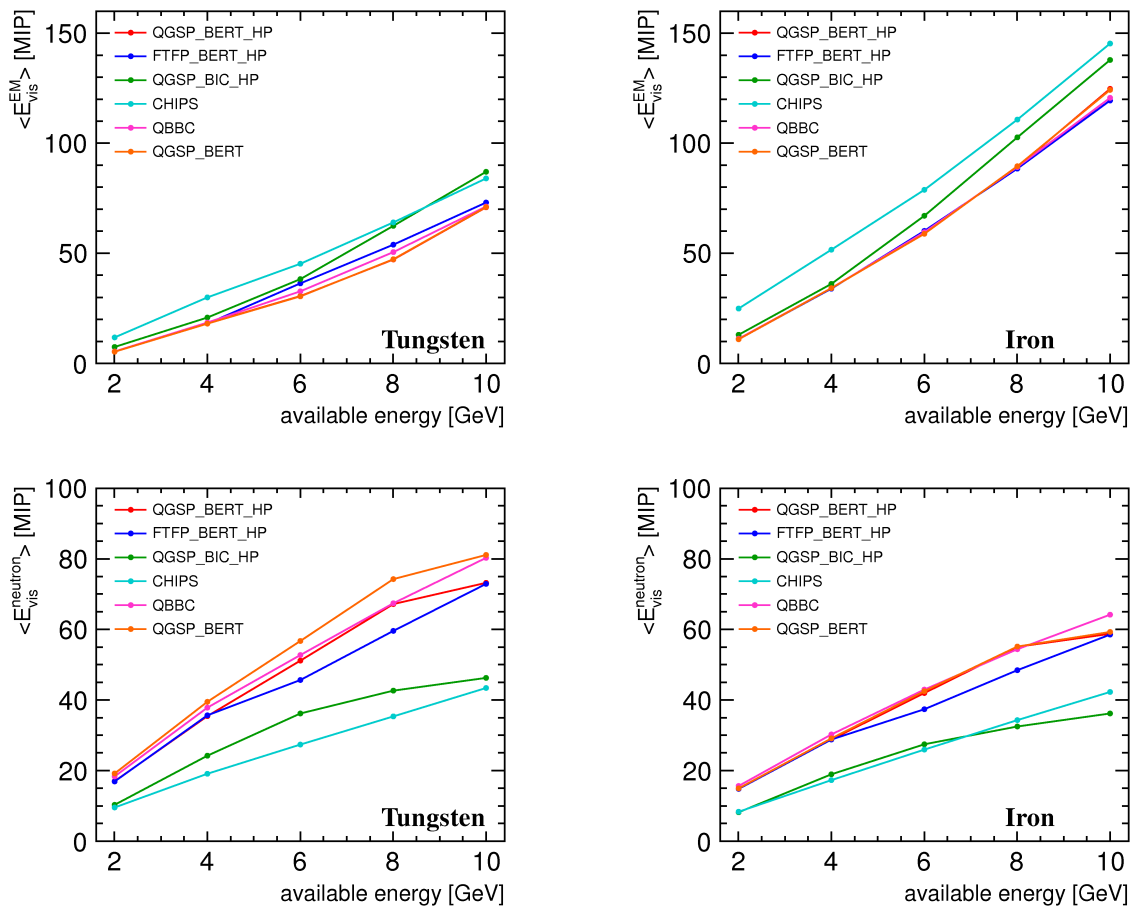


Figure 10.8: The mean visible energy deposition by the electromagnetic shower component (top) and the mean visible energy deposition by the neutron shower component (bottom) for 2 GeV to 10 GeV pions for tungsten (left) and iron (right) for different physics lists.

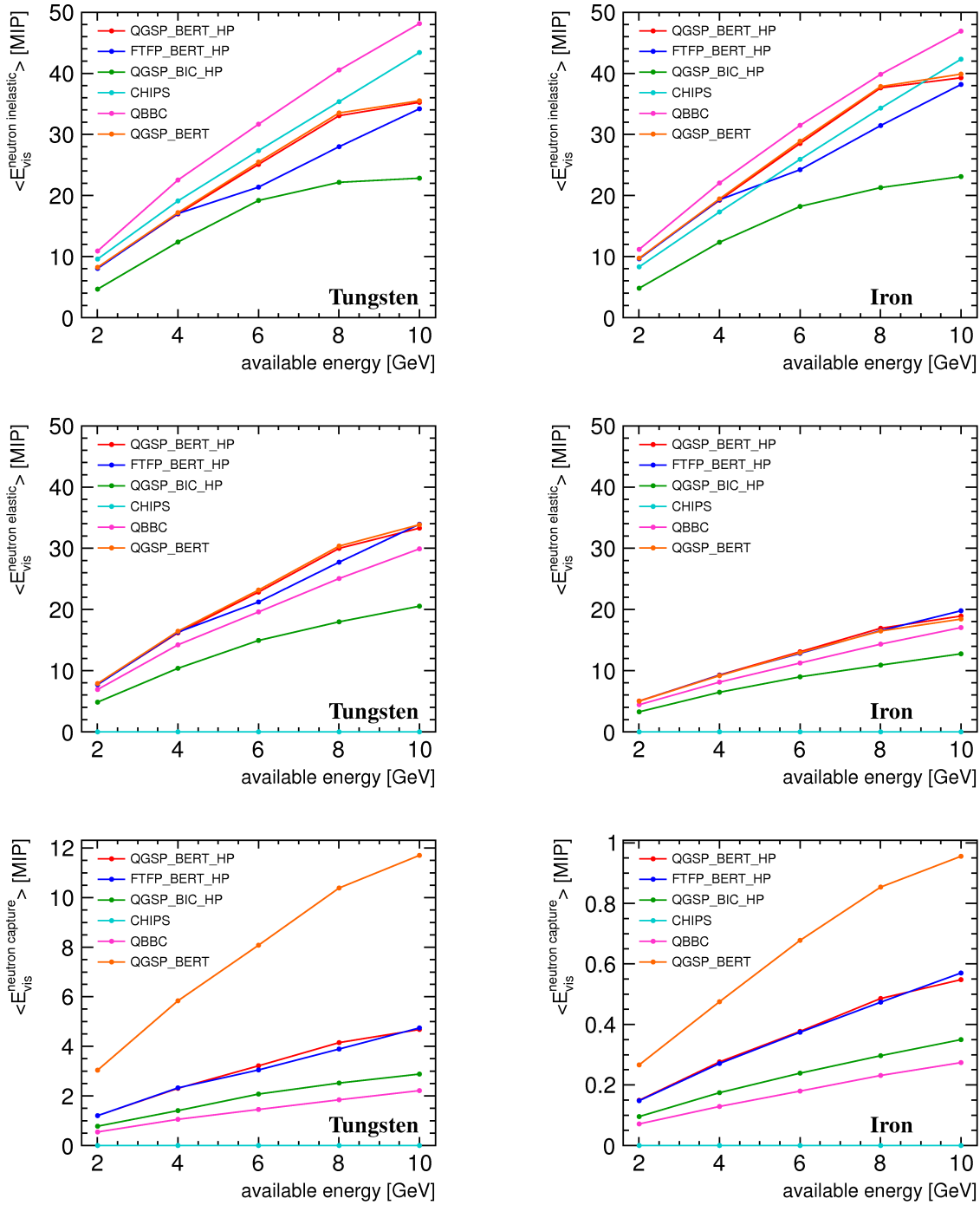


Figure 10.9: The mean visible energy deposit for the three neutron shower components inelastic scattering (top), elastic scattering (middle), and neutron capture (bottom) as a function for pions from 2 GeV to 10 GeV for tungsten (left) and iron (right). (Note the different y-scales for the neutron capture graphs.)

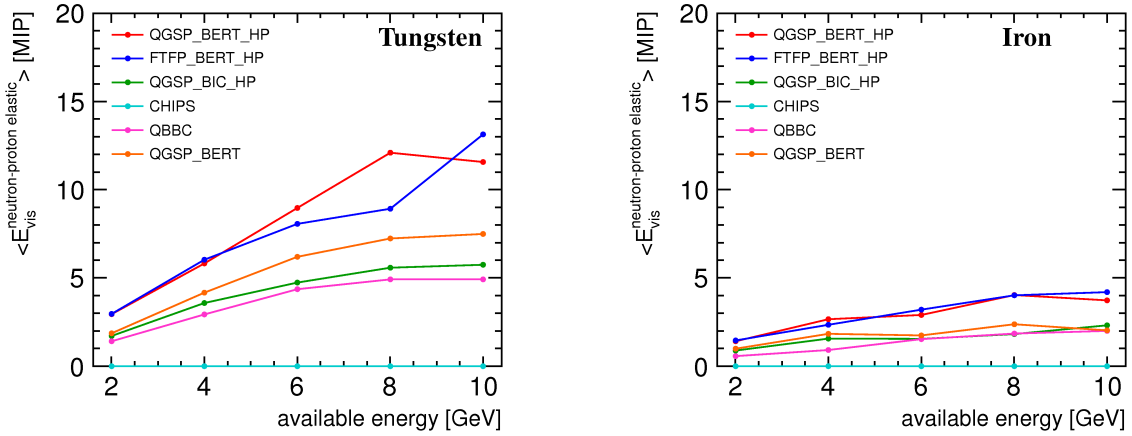


Figure 10.10: The mean visible energy deposition by the neutron elastic scattering with a single proton for 2 GeV to 10 GeV pions for tungsten (left) and iron (right) for different physics lists.

The e/h ratio describes the ratio of the response to electromagnetic showers and the response to purely hadronic showers with zero electromagnetic component in an energy independent way. So far only the e/π ratio could be extracted from the response of electrons and pions [75] as $e/\pi = 1.19$, with negligence of the energy dependence of this number. For the iron data a similar e/π ratio of approximately 1.2 can be extracted from this analysis. For the calculation of the e/h ratio as an energy independent characteristic of the calorimeter, additionally the knowledge of the electromagnetic fraction is necessary, which has been calculated with the shower decomposition tool. The e/h ratio can be calculated from equation 2.10 as:

$$\frac{e}{h} = \frac{e - (f_{\text{EM}} \cdot e)}{\pi - (f_{\text{EM}} \cdot e)} \quad (10.1)$$

with the measured electron response e and the measured pion response π and the mean electromagnetic fraction f_{EM} which has been extracted from simulations of pions of the same energy. The 6 GeV data has been chosen for this calculation as it gives the best compromise of all energy points, in terms of selection purity, no bias of the selection, and availability of both pion and electron data with reasonable statistics. The e/h ratio calculated as the mean of the 2 GeV, 4 GeV, and 6 GeV data points is 1.13 for the tungsten absorber configuration and 1.42 for the iron absorber configuration with an uncertainty of a few percent. Using the responses from data at lower energies or the responses from the simulation gives within uncertainty the same result. The tungsten absorber configuration is close to compensation, which is due to the suppression of the electromagnetic component and the strong neutron capture component, which reduces on average the invisible energy. However, a e/h ratio so close to compensation suggests an optimization of the thickness of the active and absorber layers to reach compensation since a compensating calorimeter will simplify the jet-energy calibration significantly in comparison to a non-compensating calorimeter.

The single particle resolution at a certain particle energy used in this thesis is defined as the ratio of the RMS and the mean of the full visible energy deposit distribution. The

resolutions for the different particle energies are then approximated with equation 2.13:

$$\frac{\sigma_E}{\langle E \rangle} = \frac{a}{\sqrt{E}} \oplus b \oplus \frac{c}{E}. \quad (10.2)$$

As already mentioned, the range for the approximation is small and contains only a few data points. Therefore the third parameter of the approximation function has been fixed to the RMS of the CRC-oscillator noise events, which has been converted from the MIP to the GeV scale with the respective measured $\frac{\text{MIP}}{\text{GeV}}$ factor from equation 7.1 from the response linearity approximation. However, the two first parameters of the resolution approximation are strongly correlated for the small fitting range.

For electrons both datasets are well described by the fit (see fig. 10.11), but a clear difference is observable for the single particle energy resolution between the two absorber configurations. The second parameter, or calibration term, of the fitting function is roughly 5% (see table 10.1), whereas the first parameter differs for both absorber configurations. For tungsten it is around 27% for iron only around 23%. The accuracy of these parameters extracted from the approximation is a few percent, with a high correlation between the two first parameters. However, even within this uncertainty, the single particle energy resolution for electrons is a few percent better at all energies for the iron absorber configuration, than for the tungsten absorber configuration. Since at these energies, electron showers are fully contained inside the detector and all the shower energy is in principle measurable, this difference in resolution is due to shower start fluctuations, which will then result also in fluctuations of the energy deposited inside the active layers. These fluctuations are more significant in tungsten, due to the thicker absorber layers in terms of radiation length. This is also in agreement with the observation that electron showers in tungsten deposit significantly less energy in the active layers, than electron showers of the same energy in iron.

The energy resolution has also been estimated for simulated electron showers. The estimated parameters are also summarized in table 10.1. The second parameter has been fixed to the estimation from the data approximation, so that the first parameter can be compared between data and simulation in spite of the large correlation between the fit parameters. It agrees with the estimation from recorded data within the uncertainty for both absorber configurations. However, the stochastic term extracted from the simulation seems to be slightly smaller than in measured data, which can be explained with a small remaining contamination of the data, which nevertheless has impact on the RMS of the visible energy distribution.

The estimation of the single particle energy resolution for pions is given also in figure 10.11. The 4 GeV data point has been excluded from the approximation of the energy resolution for pions in tungsten and iron, due to the strong impact of the event selection on the RMS of the visible energy distribution at this energy. The noise term has been estimated in the same way as for electrons and has been fixed to this value.

The estimated stochastic term for tungsten is roughly $\frac{58\%}{\sqrt{E}}$, whereas for iron this term is roughly $\frac{56\%}{\sqrt{E}}$. The second term is roughly two times higher than for electrons for both absorber setups. This is due to 8 GeV and 10 GeV data points, where a significant energy leakage was observable, which increases the RMS of the visible energy distribution. When

the second term is fixed in the order of 5%, the agreements, between approximation and data gets better for the low-energy data, but worse for the 8 GeV and 10 GeV data points. Additionally the first parameter increases. However, the energy resolution is worse for pion showers in tungsten data than for pion showers in iron data at all energies.

Also for simulated pion showers the energy resolution has been estimated for both absorber types with two simulations (10% and 18% crosstalk) and the estimated parameters are summarized in table 10.1. For tungsten the estimated parameters from both simulation agree well with data. For the iron setup, there is a better resolution estimated from simulations than from data (see fig. 10.11), which can be explained with remaining contamination of the pion sample. Also observable is an increased energy resolution for the simulation with 18% crosstalk in comparison to the one with 10% crosstalk. Since the crosstalk algorithm for simulated showers works effectively the same way as a blur filter is working for pictures, it can be understood why an increased crosstalk has negative impact on the energy resolution. This effect is much smaller for electrons as the showers are more compact and pronounced.

However, if the thickness of absorber and active layers is optimized to achieve an e/h-ratio of one, which leads on average to less invisible energy, and the sampling frequency is optimized to reduce the sampling fluctuations of the electromagnetic sub-showers, a sandwich calorimeter with tungsten absorber should be capable of achieving a better single particle energy resolution than a sandwich calorimeter with iron absorber and the same read-out technology.

The estimation of the single particle energy resolution for pions is given also in Figure 10.11. The energy resolution is worse for pion showers in tungsten data than for pion showers in iron data at all energies. The 4 GeV data point has been excluded from the approximation of the energy resolution for pions in tungsten and iron, due to the strong impact of the event selection on the RMS of the visible energy distribution at this energy (see chap. 7). The noise term has been estimated in the same way as for electrons and has been fixed to this value.

The estimated stochastic term for tungsten is roughly $\frac{58\%}{\sqrt{E}}$, whereas for iron this term is roughly $\frac{56\%}{\sqrt{E}}$. The second term is roughly two times higher than for electrons for both absorber setups. This is due to 8 GeV and 10 GeV data points, where a significant energy leakage was observable, which increases the RMS of the visible energy distribution. When the second term is fixed in the order of 5%, the agreements, between approximation and data gets better for the low-energy data, but worse for the 8 GeV and 10 GeV data points. Additionally the first parameter increases.

The extracted values for the constant term are significantly higher than in previous published analysis [75, 12], where the constant term is in the order of 1-2%. This difference can most likely be attributed to the remaining problem of calibration and event selection of the low-energy data and the extracted values of this low energy data cannot be used to estimate the performance of the AHCAL in general. The stochastic term for tungsten is in good agreement with previous analysis, but for iron a roughly 10% lower value has been shown in previous analysis, which is also most likely due to the remaining problems of the analyzed iron sample.

Also for simulated pion showers the energy resolution has been estimated for both absorber types with two simulations (10% and 18% crosstalk) and the estimated parameters

Data set	$a \left[\frac{1}{\sqrt{\text{GeV}}} \right]$	b	c [GeV]	χ^2
Electrons:				
CERN data	0.27	0.053	0.069	10.1
CERN sim (10%)	0.25	0.053	0.069	428
CERN sim (18%)	0.25	0.053	0.069	511
FNAL data	0.23	0.052	0.055	25.6
FNAL sim (10%)	0.20	0.052	0.055	202
FNAL sim (18%)	0.20	0.052	0.055	365
Pions:				
CERN data	0.58	0.13	0.076	5.25
CERN sim (10%)	0.59	0.13	0.076	184
CERN sim (18%)	0.61	0.13	0.076	210
FNAL data	0.56	0.11	0.066	1.86
FNAL sim (10%)	0.51	0.11	0.066	417
FNAL sim (18%)	0.53	0.11	0.066	769

Table 10.1: Parameters of the resolution approximation for electrons and pions in tungsten and iron. The third parameter (c) has been fixed and the second parameter (b) has been fixed for the simulation to the estimated value of the corresponding data set.

are summarized in table 10.1. For tungsten the estimated parameters from both simulation agree well with data. For the iron setup, there is a better resolution estimated from simulations than from data (see Fig. 10.11), which can be explained with remaining contamination of the pion sample. Also observable is an increased energy resolution for the simulation with 18% crosstalk in comparison to the one with 10% crosstalk. Since the crosstalk algorithm for simulated showers works effectively the same way as a blur filter is working for pictures, it can be understood why an increased crosstalk has negative impact on the energy resolution. This effect is much smaller for electrons as the showers are more compact and pronounced.

However, if the thickness of absorber and active layers is optimized to achieve an e/h-ratio of one, so that fluctuations of the electromagnetic fraction have no impact on the resolution, and the sampling frequency is optimized to reduce the sampling fluctuations of the electromagnetic sub-showers, a sandwich calorimeter with tungsten absorber should be capable of achieving a better single particle energy resolution than a sandwich calorimeter with iron absorber and the same read-out technology.

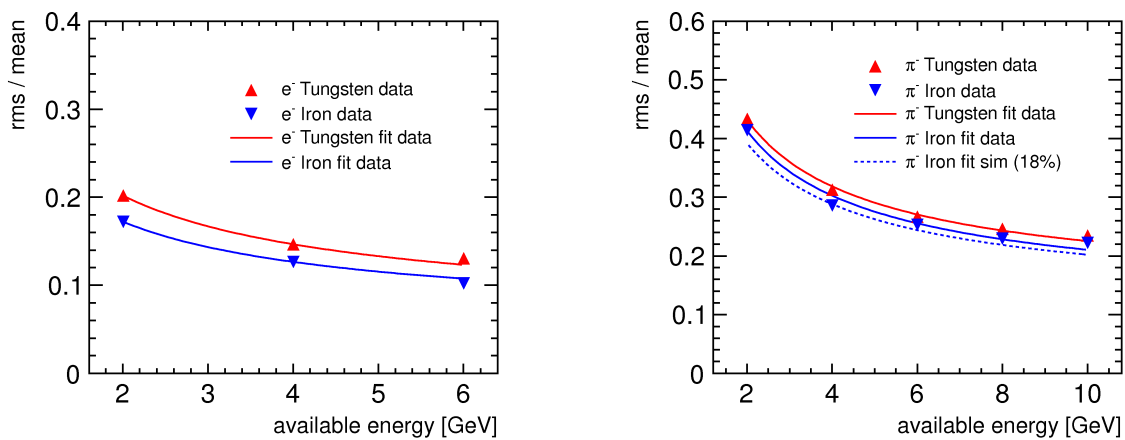


Figure 10.11: Single particle energy resolution as a function of the available energy for electrons (left) and pions (right) in iron and tungsten. The 4 GeV pion data points have been excluded from the approximation.

CHAPTER XI

SUMMARY AND OUTLOOK

The next generation of e^+e^- linear accelerators, ILC and CLIC, are developed for precision measurements of the Higgs-like particle found at CERN and for the search for physics beyond the standard model. The detectors, which record the collisions, will need unprecedented jet-energy resolution to achieve their physics goals. This performance goal can only be met with new approaches for the detector design and especially the design of the hadron calorimeters, which are in the classic calorimetric approach the limiting factor for achieving highest jet-energy resolutions.

The Particle Flow concept provides a suitable approach to meet the performance goals. The CALICE collaboration has developed several Particle Flow calorimeter prototypes with different read-out technologies. One of these prototypes is the AHCAL. However, the choice of the absorber material for the hadron calorimeters is not fixed, and well known absorber materials like iron are not suited for the CLIC detectors, as the use of iron in a reasonable thickness would result in an unaffordable magnet coil. Instead tungsten is suggested as absorber material for the CLIC hadron calorimeters, which is also an option for the ILC hadron calorimeters.

A prototype with a volume of 1 m^3 has been built for the AHCAL, which has been operated in several testbeam campaigns at CERN and FNAL to record shower data from muons, electrons and hadrons. Shower data from 2 GeV to 10 GeV from two testbeam campaigns has been evaluated for this theses. For one testbeam the AHCAL has been quipped with iron absorber layers, for the other testbeam the AHCAL has been equipped with tungsten absorber.

Both data sets have been analyzed before [11, 12], but both use different simulation parameters, which when applied to the other dataset lead to an unreasonable agreement between data and simulations. Therefore the simulation parameters had to be reevaluated. Additionally a number of improvements on the calibration and event selection of both existing analysis was found.

Calibration, Event Selection and Simulation Several new procedures for the calibration of the recorded data were developed for this thesis to improve the existing calibration chain. The existing methods for the identification of bad channels, for the extraction of

the gain constants and their temperature correction have been applied to the data. New methods for the temperature correction of the MIP calibration and for the estimation of the individual scaling factors for the saturation correction have been developed. The inter-tile crosstalk has been the least known parameter for the detector simulation. The inter-tile crosstalk was measured and a difference in the amount of leaked light between the horizontal and vertical placement of the $3 \times 3 \text{ cm}^2$ tiles was found. This problem is addressed with the new engineering prototype, most likely with a complete wrapping of the tiles. The strong temperature dependence of the noise over threshold has been studied. However, this dependence can most likely be significantly lowered with future SiPMs with an increased signal-to-noise ratio.

The event selection for the CERN and FNAL datasets needed to be modified in comparison to earlier analysis to have a similar selection strategy for the data sets from both absorber setups. The existing methods to remove empty events and events that start showering upstream of the calorimeter have been adapted and applied for the CERN data and the pion-muon separation has been equalized for both testbeams and further extended to lower energies. A significant multi-particle contamination of the events from the FNAL dataset has been found, which was not reported in earlier analysis. Most of this contamination could be removed with the specially developed rejection criteria. However, due to the uncertainty introduced by the mentioned calibration problems and the uncertainty of the simulation, a precise estimation of the remaining multi-particle contamination was not feasible.

The distributions of the visible energy sum have been approximated with either Gaussian or Novosibirsk distributions, which showed a good agreement within the fitting range. Only for the FNAL data, tails showing a remaining contamination of the events were observable. The deviation from linearity is typically $< 3\%$, only the 4 GeV data point for iron shows a higher deviation, which can be explained with the selection at this energy. A possible electron contamination of the CERN and FNAL pion showers has been investigated, based on an existing method. In contrast to earlier results, a small electron contamination of a few percent could only be found for the FNAL 2 GeV pions shower data and neither at higher energies nor for the CERN dataset.

Validation of the Simulation The achieved improvements for data and simulation allowed for the first time a consistent description of measured muons, electrons, and pions for both absorber types with simulations within reasonable uncertainties. This allows of a precise understanding of the quality of the detector simulation with comparisons of measured muons and electrons to simulated ones, as the physical processes that occur when these particle traverse the detector can be simulated with negligible uncertainty in comparison to the uncertainty of the detector simulation.

The energy sum and number of hits in data was well reproduced by the muon simulation. The layer-wise comparison of data and simulation for muons showed that the predictions of the simulation agree typically within 5% for the individual layers, with the worst agreement in the last 8 layers of the iron absorber stack.

The comparison of electrons in data and simulation is used to further study the quality of the detector simulation, as the crosstalk parameter has significant impact on electron (and hadron shower) responses. Additionally the measured deposited energy in data is affected by the desaturation correction, due to the typically higher cell-energy deposits, especially in the center of the showers.

Investigations of the mean response showed that neither the simulation with 10% crosstalk, nor the simulation with 18% describes the data accurately for any of the absorbers, but somewhere in between. Studies of the longitudinal shower profiles show that the agreement between data and simulation varies for each layer as for the electrons. Since electron showers are very compact, they can only be predicted correctly, when all affected cells are simulated with utmost precision. However, the measurement of the inter-tile crosstalk indicated already a huge spread of this parameter for different cells. Therefore the varying agreement for the individual layers can most likely be explained by the fact, that the correct inter-tile crosstalk for the actual cells, that are hit by the shower, is unknown and a global mean value is used instead. In addition, the uncertainty of the desaturation correction is unknown.

The physics of hadron showers is more complex and several models are available to simulate the hadronic scattering. Since the integral observables, like visible energy sum or number of hits above threshold, depend on the inter-tile crosstalk of the simulation, these observables are not well suited for a comparison of data and simulations to distinguish the quality of the shower predictions by the different physics list. Instead the shape agreement of the profiles between data and the different simulations has been calculated to distinguish the quality of the shower predictions of the different simulations. In general, the physics list QGSP_BERT_HP gives the best description of the measured shower topologies. This preference of the data for the physics lists QGSP_BERT_HP is consistent with earlier analyses of the low-energy tungsten and iron data.

The standard deviations of the longitudinal and radial center-of-gravity, which was already used before as a quantity to measure the fluctuations of pion showers, are best described for tungsten by the physics list QBBC, whereas for iron the best description is given by the physics list QGSP_BERT_HP, which is in agreement with the results of the previous iron analysis.

Comparison of Iron and Tungsten The individual shower components cannot be precisely distinguished in the data recorded by the AHCAL, therefore only simulations can be used to understand the difference of hadron showers in tungsten and iron. The predictive power of the simulations to describe the recorded shower topology, which is drastically affected by the strength of the individual shower components, is sufficient to justify the decomposition of the simulated showers into different shower components to gain further insight on the differences of the shower development between tungsten and iron. Additionally the first inelastic hadronic interaction has been studied and compared between the two absorber setups, to distinguish differences that originate from the first hadronic interaction and shower differences that are due to the transport of the components through the calorimeter.

The differences in the products of the first inelastic scattering affects mainly the neutron

shower component. The number of neutrons that are emitted on average is significantly larger than in iron. At the same time, the fraction of the total shower energy, that is transported by neutrons after the first inelastic hadronic scattering is less significant, so that the average energy per neutron is significantly lower in tungsten.

The longitudinal electron shower profiles agree for both absorber types when they are shown as a function of the effective radiation length, but a comparison of the longitudinal pion shower profiles as a function of the effective interaction length showed that the shower maxima for both absorber types do not agree. Instead the shower maximum in tungsten is at an earlier point of the cascade. The comparison of the longitudinal profiles on the effective-interaction-length scale with the decomposition of the deposited energy into the different shower fractions showed, that the difference in the shower topology can be explained with the drastically lower deposited visible energy from the electromagnetic shower component in tungsten. However, the reason for the lower visible energy deposit is the much worse sampling of this shower component of the tungsten absorber setup with a thickness of the absorber layer of almost $2.6 X_0$ in contrast to the iron layers which have a wall thickness of roughly $1 X_0$. Therefore more energy of the electromagnetic shower component is deposited inside the tungsten absorber plates than in the iron absorber plates. This leads also to more fluctuations of the visible energy sum.

A comparison of the time evolution of the showers shows beside the difference of the visible energy from the electromagnetic shower components, which dominate the first nanoseconds of the shower, also the strong differences of the neutron shower components, which dominate the rest of the shower. This leads in general to more late energy depositions in tungsten, which need to be taken into account for a CLIC detector, where there are particles from more than one $e^+ - e^-$ -collision at the time traversing the detector.

A detailed comparison of the shower components for both absorber types revealed not only the differences between the two absorber setups, but also the differences between the physics lists. The differences between pion showers in tungsten and in iron are a significantly lower visible energy deposition from the electromagnetic component for tungsten which is a result of the bad sampling of this shower component for the tungsten absorber setup. The second difference is in the neutron shower component, which is higher for the tungsten absorber setup. This can be explained with the higher number of low energetic neutrons, which lead to more energy deposit from neutron elastic scattering. Additionally the cross section for neutron capture is up to three order of magnitude higher. However, due to the bad sampling of the electromagnetic sub-showers that occur from the released photons after a neutron has been captured by a nucleus, this leads only to a visible energy deposition, that is a factor ten higher than in iron. Nevertheless, that is in total only roughly 2 % of the total visible energy deposited by the shower. A better sampling of the electromagnetic sub-showers would lead to a higher visible energy deposit from this shower component.

The $\frac{e}{h}$ ratio has been calculated for both absorber setups and is 1.13 for the tungsten absorber setup and 1.42 for the iron absorber setup with an uncertainty of a few percent. From previous CALICE analysis only the e/π ratio was known, which is also in agreement

with the e/π ratio extracted from this analysis. The value of 1.1 for tungsten, which is close to compensation, suggest an optimization of the thickness of active and absorber layers to achieve compensation.

The impact of the different sampling of electromagnetic showers for both absorber types and the thereby increased fluctuations of the visible energy sum for tungsten is directly visible from the comparison of the relative single particle energy resolution for electrons and results in a worse resolutions for tungsten. This has also impact on the relative single particle energy resolution of pion showers, as it leads also to increased fluctuations of the visible energy deposit for any electromagnetic sub-shower inside the hadron shower in tungsten and therefore to a worse energy resolution. Nevertheless, a better relative single particle energy resolution should be achievable with tungsten absorber in comparison to iron absorber, if the sampling of the electromagnetic sub-showers is equalized between setups due to less fluctuations of the invisible energy, as this setup is much closer to compensation. Additionally the ratios of active and absorber materials can be optimized to achieve compensation, which will further improve the energy resolution.

The extracted resolutions show an increased constant term with respect to previous analysis. This decreased performance can most likely be attributed to the remaining problems of the investigated data samples. Therefore, the estimated resolution can not be applied to other analysis and does not describe the performance of the AHCAL in general, which is significantly better for other data sets. It can only be utilized for a comparison of the two absorber types for the respective low energy data sets.

Outlook The investigation of the AHCAL physics prototype demonstrated the physics potential of the AHCAL technology. In addition to the AHCAL physics prototype, an engineering prototype is currently commissioned, to demonstrate the feasibility to built a full scale and fully integrated ILD/CLIC-detector with the AHCAL technology. This prototype addresses the remaining calibration problems and solutions for the crosstalk problem are investigated. Additionally also techniques for mass production are tested. This new engineering prototype uses also a next generation of read-out electronics, which have been specially designed for the AHCAL, and is housing an AHCAL dedicated an ASIC chip, the SPIROC chip that has also the capability to measure the time structure of a shower by measuring the time of the first hit for every read out channel.

APPENDIX I

DATA SETS & CALIBRATION

This Appendix will summarize data sets (run numbers) used for analysis in table A.1. Also the names of folders in the CALICE database containing the used calibration sets are given in table A.2 and table A.3.

	FNAL Runs	CERN Runs
2 GeV π^-	520291 529299 520300 520365 520369 580024 580044 580058	360463
4 GeV π^-	520283 520285 580012	360774
6 GeV π^-	520304 520305	360771
8 GeV π^-	520307	360767
10 GeV π^-	520308	360737
2 GeV e^-	580093 580102 580103	360463 360774
4 GeV e^-	580092 580104	360771
6 GeV e^-	580090	

Table A.1: *The run numbers of the individual runs used for the analysis.*

Calibration Set	Database Folder
Bad channel list	/test_cg_2010/BadCellMap_2010_final_v1
Gain constants	/test_cg_2010/gain_constants
Gain slopes	/test_cg_2010/gain_slopes
Inter-calibration constants	/cd_calice/Hcal/ic_constants (ahc_ic_constants_006)
MIP constants	/test_cg_2010/mipConsts_2010_final_v1
MIP slopes	/test_cg_2010/mipSlopes_2010_final_v1
Saturation curves	/cd_calice/Ahc/ResponseCurve (ahc_response_curve_002)
Saturation curve scalings	/test_cg_2010/satCorFactors
Temperature sensor calibration	/cd_calice_cernbeam/Hcal/AhcSroTempOffset_Diff

Table A.2: The CALICE database folder names of the CERN calibration sets used. If the folders are tagged, the tag is given in brackets.

Calibration Set	Database Folder
Bad channel list	/test_cg_2010/deadCellMap_forNewMip_FINAL
Gain constants	/cd_calice/Hcal/gain_constants (ahc_gain_constants_007)
Gain slopes	/cd_calice/Hcal/gain_slopes (ahc_gain_slopes_007)
Inter-calibration constants	/cd_calice/Hcal/ic_constants (ahc_ic_constants_006)
MIP constants	/test_cg_2010/newCalibFnal_v4_Const
MIP slopes	/test_cg_2010/newCalibFnal_v4_Slopes
Saturation curves	/cd_calice/Ahc/ResponseCurve (ahc_response_curve_002)
Saturation curve scalings	/test_cg_2010/satCorFactors
Temperature sensor calibration	/cd_calice/Hcal/tempSensors (ahc_tempSensors_001)

Table A.3: The CALICE database folder names of the FNAL calibration sets used. If the folders are tagged, the tag is given in brackets.

APPENDIX II

EVENT SELECTION PARAMETERS

This Appendix will summarize the event selection criteria used for the different particle samples for all energies. Cuts that are marked with an (*) after their name are only applied to data and not to the simulation.

Energy [GeV]	Cut Name	Cut
All	BeamCut(*)	beamBit = 1
All	Cherenkov Selection(*)	cherenkowBit = 0 & cherenkow2Bit = 1
All	Bad LED Event Rejection(*)	nHits in Layer 7 < 150
All	Empty Event Rejection	$E_{vis}^{First5layers} \geq 4$
All	Pre-Shower Rejection	nHits ^{GuardRing} < 15
All	Found Hits on Tracks	nHits ^{Track} > 0
All	Only central Events	-20 < cog _X < 40 &
All	Only central Events	-40 < cog _Y < 20
All	Pion Rejection	630 < cog _Z < 765 &
All	Pion Rejection	25 < nHits < 50
4	Pion Rejection	No Shower Start Found &
4	Pion Rejection	$E_{vis}^{Last5layers} \geq 2.5$

Table B.1: *Event selection criteria for the CERN muon sample.*

Energy [GeV]	Cut Name	Cut
All	BeamCut(*)	beamBit = 1
4, 6	Cherenkov Selection(*)	cherenkowBit = 0 & cherenkow2Bit = 0
8, 10	Cherenkov Selection(*)	cherenkowBit = 1 & cherenkow2Bit = 0
All	Empty Event Rejection	$E_{vis}^{First 5 layers} \geq 4$
All	Pre-Shower Rejection	nHits ^{Guard Ring} < 15
All	Pion Rejection	2000 < cog _Z < 2250 &
All	Pion Rejection	35 < nHits < 65 &
All	Pion Rejection	No Shower Start Found &
4	Pion Rejection	$5 < E_{vis}^{Last 8 layers} < 20$
6, 8, 10	Pion Rejection	$20 < nHits^{Track} < 38$
All	BeamHaloVeto (Online)(*)	vetoBit = 0
All	MultiVeto (Online)(*)	multiADC < 3800
All	MultiVeto (Offline)	No outer tracks parallel to beam
All	MultiVeto (Offline)	NTracks <= 8
All	MultiVeto (Offline)	nCluster = 0

Table B.2: *Event selection criteria for the FNAL muon sample.*

Energy [GeV]	Cut Name	Cut
All	BeamCut(*)	beamBit = 1
All	Cherekov Selection(*)	cherenkowBit = 1 & cherenkow2Bit = 1
All	Bad LED Event Rejection(*)	nHits in Layer 7 < 150
All	Cluster Cut	Number of Clusters = 1 &
All	Cluster Cut	$340 < \text{cog}_Z^{\text{Cluster}} < 400$
All	Muon Rejection	$\text{cog}_Z < 630$ or $\text{cog}_Z > 765$ &
All	Muon Rejection	nHits < 25 or nHits > 50)
2	Muon Rejection	2.5 MIP < energy in last 3 layers < 10 MIP
4	Muon Rejection	energy in last 5 layers < 2.5 MIP
4, 6	Muon Rejection	Shower Start Found
6	MultiVeto(Offline)(*)	eventNumber $\neq 9880$

Table B.3: Event selection criteria for the CERN electron sample.

Energy [GeV]	Cut Name	Cut
All	BeamCut(*)	beamBit = 1
All	Cherekov Selection(*)	cherenkowBit = 0 & cherenkow2Bit = 1
All	Cluster Cut	Number of Clusters = 1 &
All	Cluster Cut	$1620 < \text{cog}_Z^{\text{Cluster}}$
All	Muon Rejection	$\text{cog}_Z < 1892$
2	Muon Rejection	$\text{cog}_Z < 2000$ or $\text{cog}_Z > 2250$ &
2	Muon Rejection	nHits < 30 or nHits > 60)
4, 6	Muon Rejection	$\text{cog}_Z < 2000$ or $\text{cog}_Z > 2250$ &
4, 6	Muon Rejection	nHits < 35 or nHits > 65)
2	Muon Rejection	energy in last 6 layers < 3 MIP
All	Muon Rejection	energy in last 8 layers < 5 MIP
All	Muon Rejection	nHits in last 8 layers < 6
4	Muon Rejection	energy in last 6 layers < 3 MIP
4, 6	Muon Rejection	Shower Start Found
All	PreShower	nHits in first layer < 10
All	MultiRejection(Offline)	not more than 2 hits with energy > 18 MIP
All	MultiRejection(Offline)	not more than 2 track fragments
2	MultiRejection(Offline)	nHits(Cluster) < 40
4	MultiRejection(Offline)	nHits(Cluster) < 60
6	MultiRejection(Offline)	nHits(Cluster) < 80
2, 4	MultiRejection(Offline)	nHits - nHits(Cluster) < 40
6	MultiRejection(Offline)	nHits - nHits(Cluster) < 50
All	BeamHaloVeto (Online)(*)	vetoBit = 0
All	MultiVeto (Online)(*)	multiADC < 3800

Table B.4: Event selection criteria for the FNAL electron sample.

Energy [GeV]	Cut Name	Cut
All	BeamCut(*)	beamBit = 1
2	Cherekov Selection(*)	cherenkowBit = 0 & cherenkow2Bit = 0
4 - 10	Cherekov Selection(*)	cherenkowBit = 0 & cherenkow2Bit = 1
4 - 10	Pre-Shower Rejection	nHits ^{GuardRing} < 15
All	Empty Event Rejection	E _{vis} ^{First5layers} >= 4
All	Bad LED Event Rejection(*)	nHits in Layer 7 < 150
4 - 10	Muon Rejection	Shower Start Found
All	Bad Event Rejection(*)	energy < 1500 MIP
2	Muon Rejection	cog _Z < 630 or cog _Z > 765 &
2	Muon Rejection	nHits < 25 or nHits > 65) &
2	Muon Rejection	2.5 MIP > energy or energy > 10 MIP
4	Muon Rejection	cog _Z < 630 or cog _Z > 765 &
4	Muon Rejection	nHits < 25 or nHits > 65) &
4	Muon Rejection	2.5 MIP > energy
6 - 10	Muon Rejection	cog _Z < 630 or cog _Z > 765 &
6 - 10	Muon Rejection	nHits < 25 or nHits > 65)

Table B.5: *Event selection criteria for the CERN pion sample.*

Energy [GeV]	Cut Name	Cut
All	BeamCut(*)	beamBit = 1
2 - 6	Cherekov Selection(*)	cherenkowBit = 0 & cherenkow2Bit = 0
8, 10	Cherekov Selection(*)	cherenkowBit = 1 & cherenkow2Bit = 0
All	BeamHaloVeto (Online) (*)	vetoBit = 0
All	MultiVeto (Online) (*)	multiADC < 3800
All	Pre-Shower Rejection	nHits ^{GuardRing} < 15
All	Empty Event Rejection	E _{vis} ^{First5layers} >= 4
2	Muon Rejection	cog _Z < 2000 or cog _Z > 2250 &
2	Muon Rejection	nHits < 30 or nHits > 60)
2	Muon Rejection	energy in last 6 layers < 3 MIP
4 - 10	Muon Rejection	cog _Z < 2000 or cog _Z > 2250 &
4 - 10	Muon Rejection	nHits < 35 or nHits > 65)
4 - 10	Muon Rejection	Shower Start Found
All	MultiVeto (Offline)	NTracks <= 8
All	MultiVeto (Offline)	No outer tracks parallel to beam
All	MultiVeto(Offline) (*)	nClusters >= 1
2	MultiVeto(Offline) (*)	nHits(biggest Cluster) < 40
4	MultiVeto(Offline) (*)	nHits(biggest Cluster) < 60
6	MultiVeto(Offline) (*)	nHits(biggest Cluster) < 80
8	MultiVeto(Offline) (*)	nHits(biggest Cluster) < 90
10	MultiVeto(Offline) (*)	nHits(biggest Cluster) < 100
4	MultiVeto(Offline) (*)	nHits(Clusters) < 60
6	MultiVeto(Offline) (*)	nHits(Clusters) < 85
8	MultiVeto(Offline) (*)	nHits(Clusters) < 100
10	MultiVeto(Offline) (*)	nHits(Clusters) < 110

Table B.6: *Event selection criteria for the FNAL pion sample.*

APPENDIX III

SIMULATION PARAMETERS

This Appendix summarizes used material properties as extracted from the MOKKA simulation (table C.1) and the simulation input parameters (tables C.2, C.3, and C.4).

Material	Thickness [cm]	X_0 [cm]	λ_{int} [cm]
Absorber Layers:			
Steel	1.7	1.76	16.97
Tungsten alloy	1	0.39	10.81
Steel frame	0.05	1.76	16.97
Active Layers:			
Steel Casette	2x 0.2	1.76	16.97
3M Foil	0.0115	41.12	68.51
PCB	0.1	17.51	48.39
Cable-Fibre Mix	0.15	224.37	729.83
Scintillator	0.5	41.31	68.84
Air Gap	2x 0.125	30392.1	71013.7

Table C.1: Material properties for the simulation of the absorber layers (tungsten framed with steel or iron) and the active layers as extracted from MOKKA.

Run	Energy [GeV]	HCAL-shift x [mm]	HCAL-shift y [mm]	Beam x [mm]	Beam dx [mm]	Beam y [mm]	Beam dy [mm]	Beam z [mm]
360737	10	-13	-9	2.5	14	-3.14	15	-1200
360767	8	-13	-9	20.1	14.5	-2	14.5	-1200
360771	6	-13	-9	19.8	8	-2.9	8	-1200
360774	4	-13	-9	18.0	10	-3.4	11.7	-1200
360463	2	-13	-9	1.8	12	-3.14	12	-1200

Table C.2: The input parameters for the simulation with MOKKA for the CERN tungsten runs for all particle types.

Run	Energy [GeV]	HCAL-shift x [mm]	HCAL-shift y [mm]	Beam x [mm]	Beam dx [mm]	Beam y [mm]	Beam dy [mm]	Beam z [mm]
580087	10	0	0	14.63	21.04	-23.79	19.0	-1000
580090	6	0	0	26.33	25.57	-25.93	24.57	-1000
580092	4	0	0	25.69	29.7	-22.44	29.1	-1000
580093	2	0	0	35.49	37.29	-21.09	37.08	-1000

Table C.3: The input parameters for the simulation with MOKKA for the FNAL iron runs for electrons.

Run	Energy [GeV]	HCAL-shift x [mm]	HCAL-shift y [mm]	Beam x [mm]	Beam dx [mm]	Beam y [mm]	Beam dy [mm]	Beam z [mm]
520308	10	0	0	-2.67	20.07	8.40	20.81	-1000
520307	8	0	0	3.64	24.43	9.20	24.40	-1000
520305	6	0	0	2.45	29.87	7.68	29.96	-1000
520285	4	0	0	5.00	33.83	8.56	33.28	-1000
520291	2	0	0	9.34	35.02	7.68	35.54	-1000

Table C.4: The input parameters for the simulation with MOKKA for the FNAL iron runs for muons and pions.

APPENDIX IV

ADDITIONAL RESULTS

This Appendix gives the longitudinal profiles with the shower decomposition for the physics lists FTFP_BERT_HP (fig. D.1 and D.2), QGSP_BIC_HP (fig. D.3 and D.4), QBBC (fig. D.5 and D.6), and CHIPS (fig. D.7 and D.8), which were not shown in chapters 9 and 10.

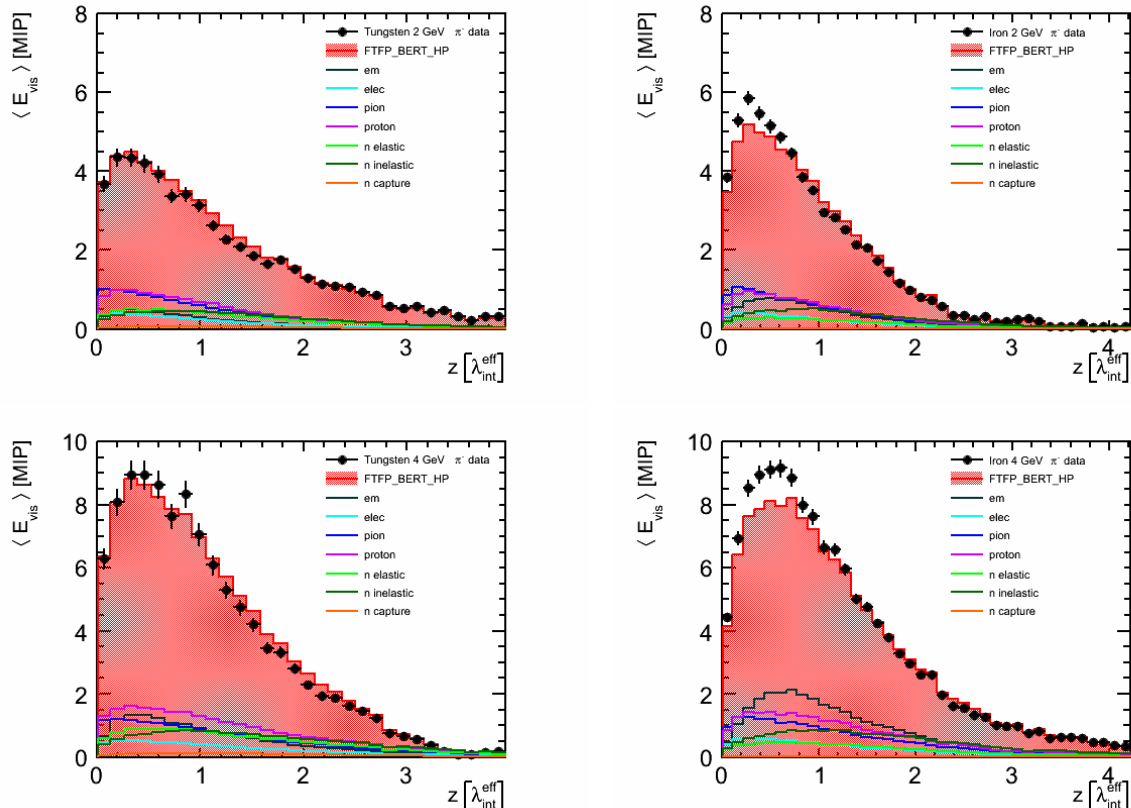


Figure D.1: The longitudinal shower profiles for tungsten (left) and iron (right) for data and simulation for 2 GeV (top) and 4 GeV (bottom). For the simulation also the decomposition into the different shower components is shown. The simulation used FTFP_BERT_HP and 18% crosstalk.

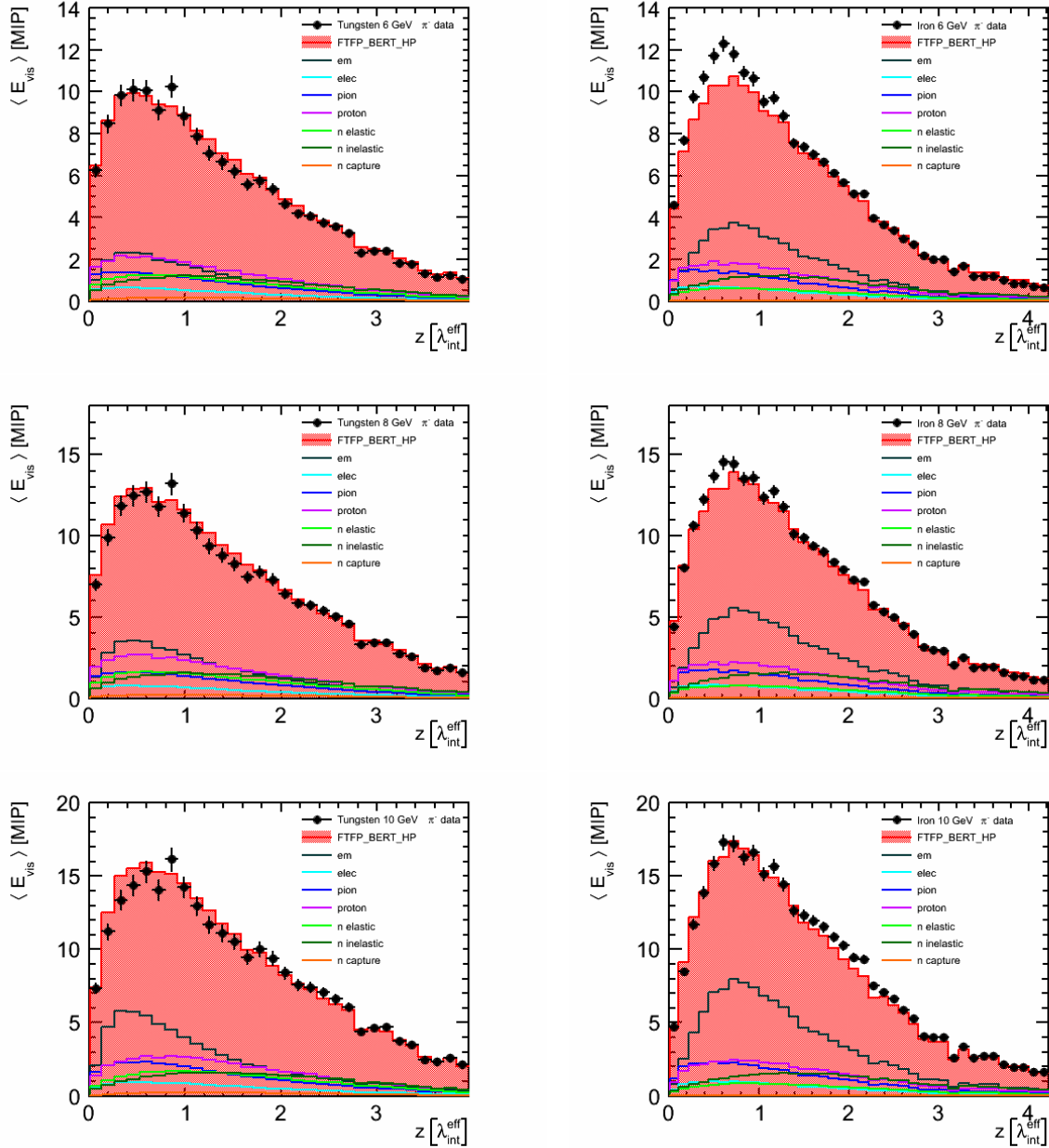


Figure D.2: The longitudinal shower profiles for tungsten (left) and iron (right) for data and simulation for 6 GeV, 8 GeV, and 10 GeV (top to bottom). For the simulation also the decomposition into the different shower components is shown. The simulation used FTFP_BERT_HP and 18% crosstalk.

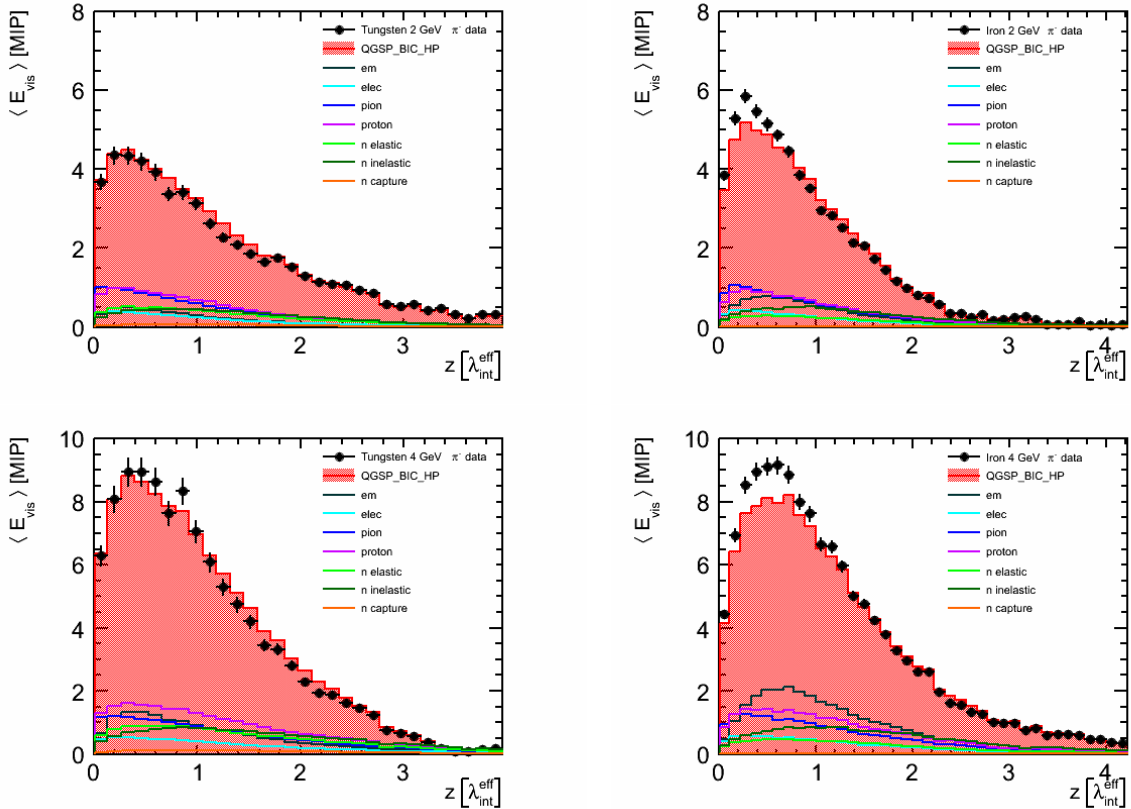


Figure D.3: The longitudinal shower profiles for tungsten (left) and iron (right) for data and simulation for 2 GeV (top) and 4 GeV (bottom). For the simulation also the decomposition into the different shower components is shown. The simulation used QGSP_BIC_HP and 18% crosstalk.

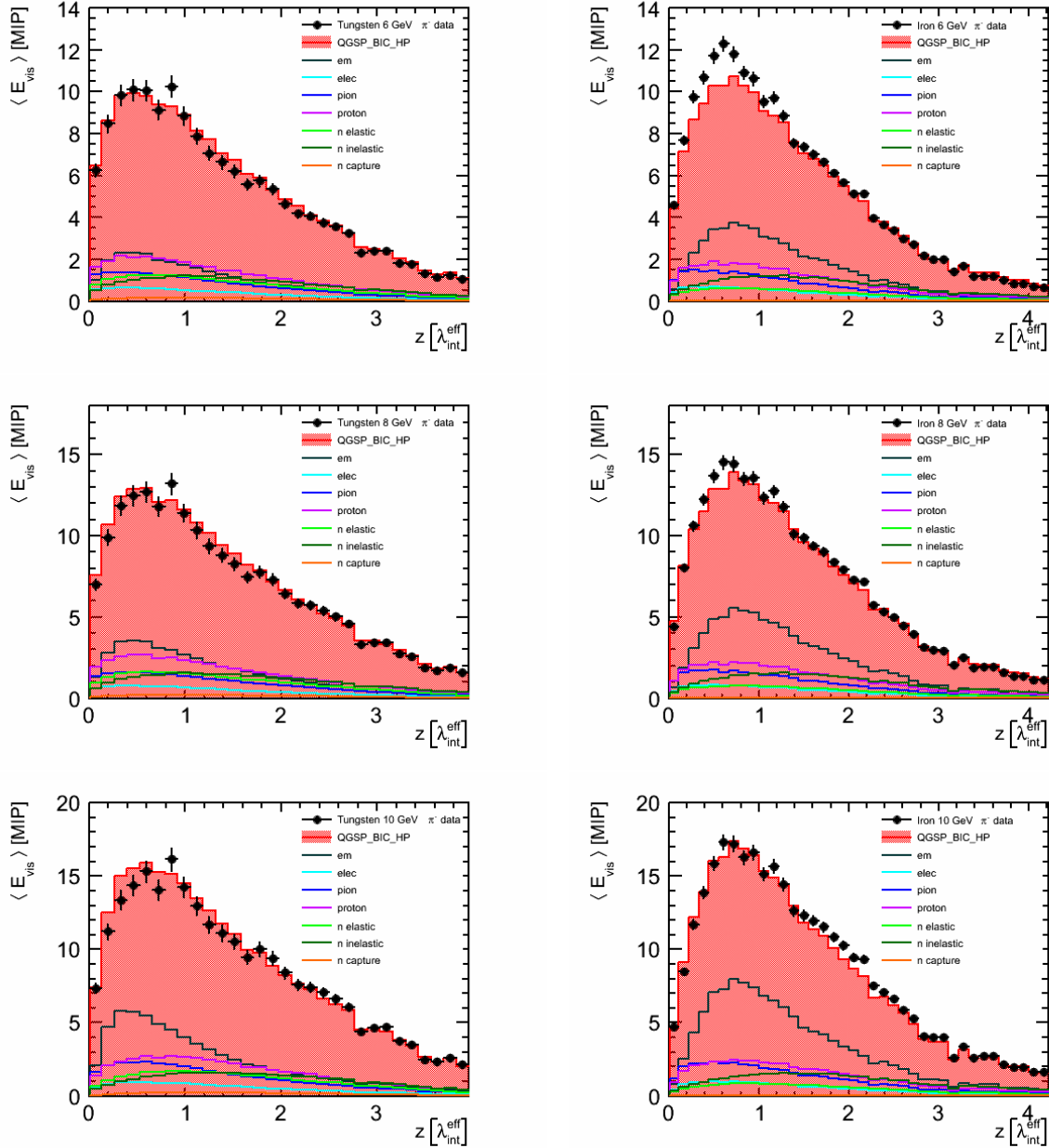


Figure D.4: The longitudinal shower profiles for tungsten (left) and iron (right) for data and simulation for 6 GeV, 8 GeV, and 10 GeV (top to bottom). For the simulation also the decomposition into the different shower components is shown. The simulation used QGSP_BIC_HP and 18% crosstalk.

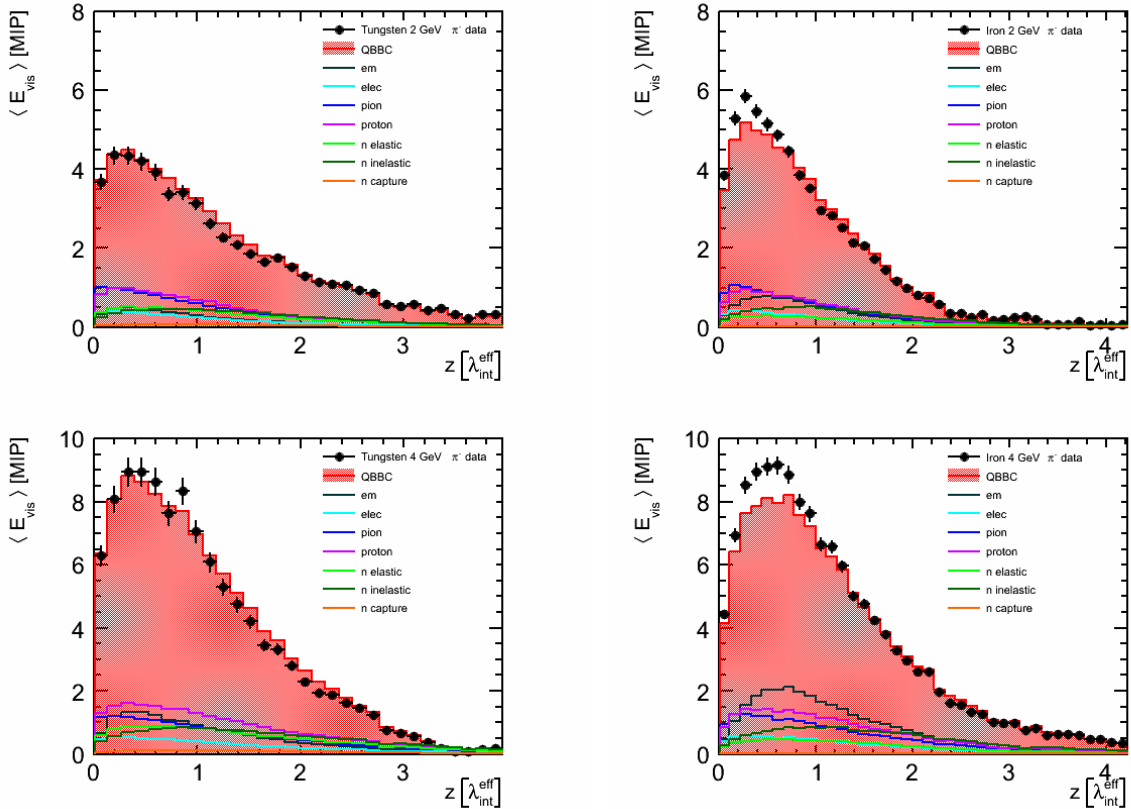


Figure D.5: The longitudinal shower profiles for tungsten (left) and iron (right) for data and simulation for 2 GeV (top) and 4 GeV (bottom). For the simulation also the decomposition into the different shower components is shown. The simulation used QBBC and 18% crosstalk.

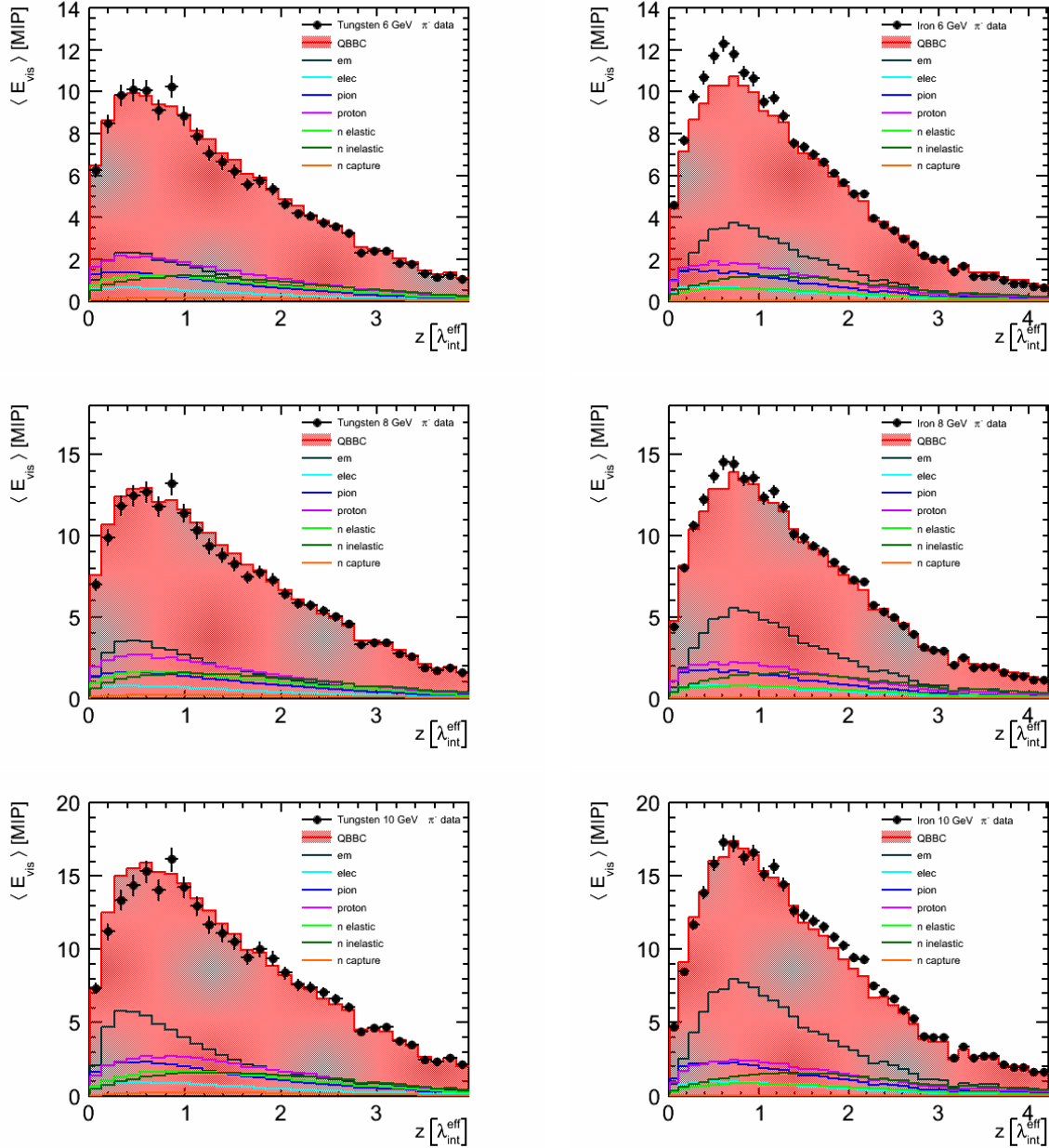


Figure D.6: The longitudinal shower profiles for tungsten (left) and iron (right) for data and simulation for 6 GeV, 8 GeV, and 10 GeV (top to bottom). For the simulation also the decomposition into the different shower components is shown. The simulation used QBBC and 18% crosstalk.

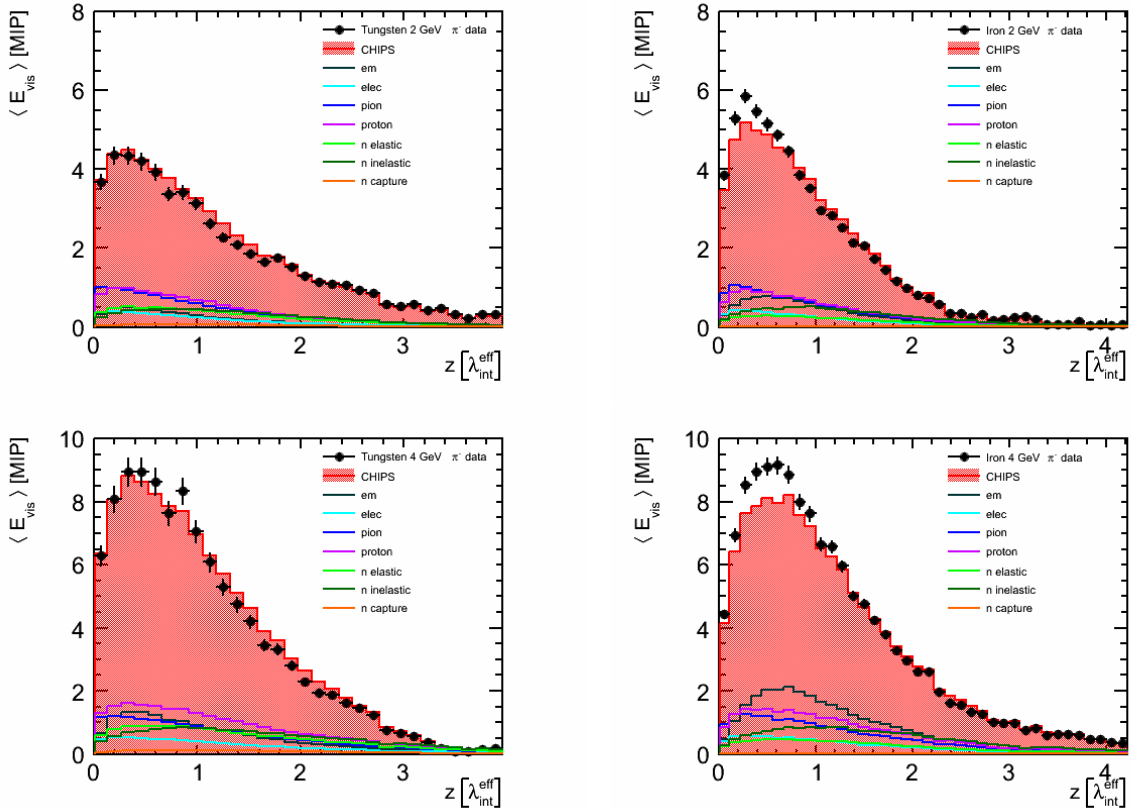


Figure D.7: The longitudinal shower profiles for tungsten (left) and iron (right) for data and simulation for 2 GeV (top) and 4 GeV (bottom). For the simulation also the decomposition into the different shower components is shown. The simulation used CHIPS and 18% crosstalk.

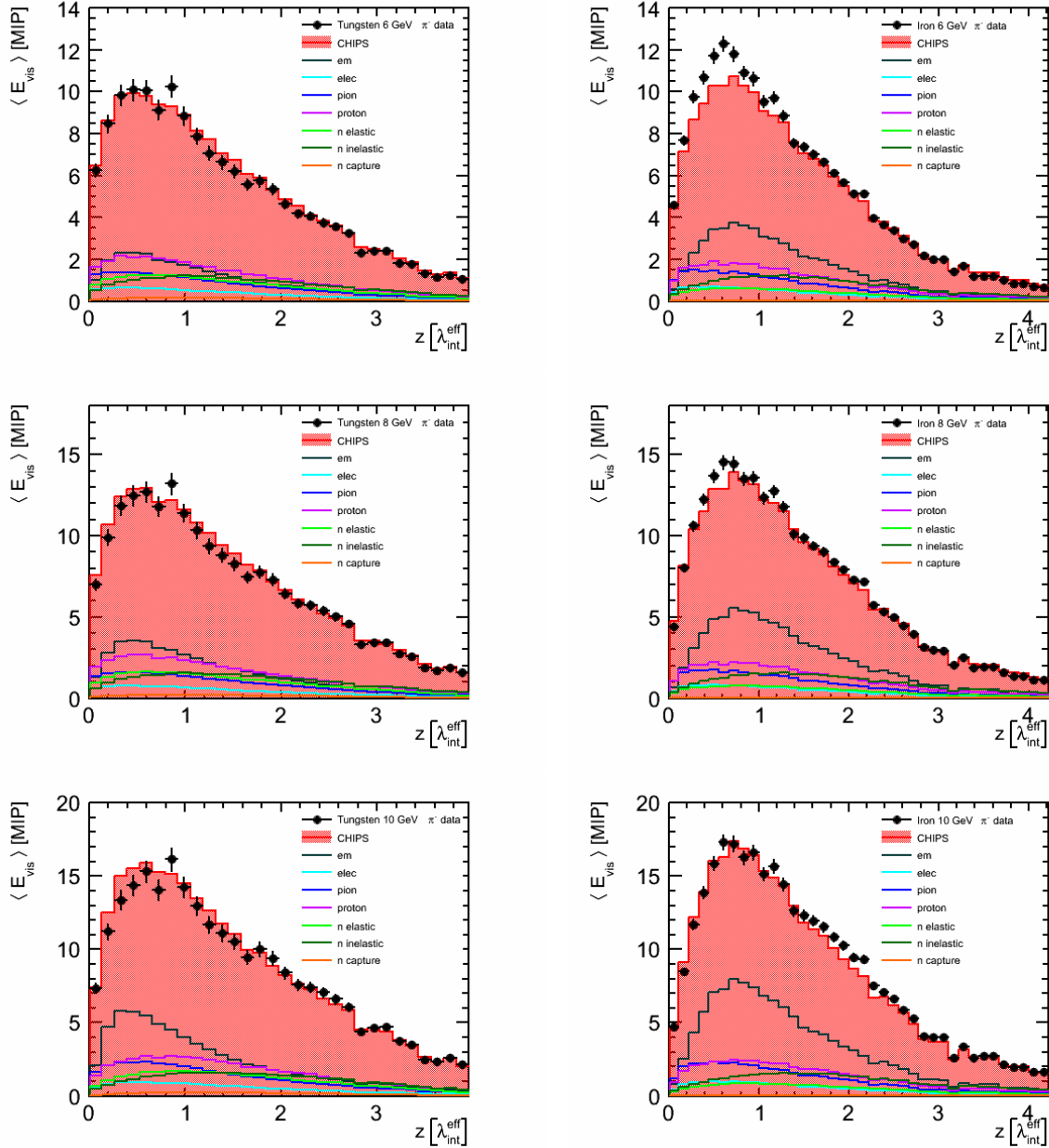


Figure D.8: The longitudinal shower profiles for tungsten (left) and iron (right) for data and simulation for 6 GeV, 8 GeV and 10 GeV (top to bottom). For the simulation also the decomposition into the different shower components is shown. The simulation used CHIPS and 18% crosstalk.

BIBLIOGRAPHY

- [1] A. Salam, “Elementary Particles,” *Contemp. Phys.*, vol. 1, pp. 337–354, 1959.
- [2] S. Glashow, “Partial Symmetries of Weak Interactions,” *Nucl. Phys.*, vol. 22, pp. 579–588, 1961.
- [3] S. Weinberg, “A Model of Leptons,” *Phys. Rev. Lett.*, vol. 19, pp. 1264–1266, 1967.
- [4] F. Englert and R. Brout, “Broken Symmetry and the Mass of Gauge Vector Mesons,” *Phys. Rev. Lett.*, vol. 13, pp. 321–323, 1964.
- [5] P. W. Higgs, “Broken symmetries, massless particles and gauge fields,” *Phys. Lett.*, vol. 12, pp. 132–133, 1964.
- [6] P. W. Higgs, “Broken Symmetries and the Masses of Gauge Bosons,” *Phys. Rev. Lett.*, vol. 13, pp. 508–509, 1964.
- [7] G. Aad *et al.*, “Observation of a new particle in the search for the Standard Model Higgs boson with the ATLAS detector at the LHC,” *Phys. Lett.*, vol. B716, pp. 1–29, 2012.
- [8] S. Chatrchyan *et al.*, “Observation of a new boson at a mass of 125 GeV with the CMS experiment at the LHC,” *Phys. Lett.*, vol. B716, pp. 30–61, 2012.
- [9] H. Baer *et al.*, “The International Linear Collider Technical Design Report - Volume 2: Physics,” 2013.
- [10] L. Linssen *et al.*, “Physics and Detectors at CLIC: CLIC Conceptual Design Report,” *ArXiv e-prints*, Feb. 2012.
- [11] N. Feege, “Low-energetic Hadron Interactions in a Highly Granular Calorimeter,” Ph.D. dissertation, University of Hamburg, 2011, DESY-THESIS-2011-048.
- [12] C. Adloff *et al.*, “Shower development of particles with momenta from 1 to 10 GeV in the CALICE Scintillator-Tungsten HCAL,” *JINST*, vol. 9, p. P01004, 2014.
- [13] L. Evans and P. Bryant, “LHC Machine,” *JINST*, vol. 3, p. S08001, 2008.
- [14] P. Lebrun *et al.*, “The CLIC Programme: Towards a Staged e^+e^- Linear Collider exploring the Terascale: CLIC Conceptual Design Report,” Geneva, Tech. Rep. CERN-2012-005, 2012.

- [15] T. Behnke *et al.*, “The International Linear Collider Technical Design Report - Volume 1: Executive Summary,” 2013.
- [16] T. Behnke *et al.*, “The International Linear Collider Technical Design Report - Volume 4: Detectors,” 2013.
- [17] J. Beringer *et al.*, “Review of particle physics,” *Phys. Rev. D*, vol. 86, p. 010001, Jul 2012. [Online]. Available: <http://link.aps.org/doi/10.1103/PhysRevD.86.010001>
- [18] R. Wigmans, *Calorimetry*, 1st ed. Oxford University Press, 2000.
- [19] M. Berger *et al.*, “National Institute of Standards and Technology Standard Reference Database XCOM: Photon Cross Sections Database,” April 2013. [Online]. Available: <http://www.nist.gov/pml/data/xcom/>
- [20] E. Longo and I. Sestili, “Monte Carlo Calculation of Photon Initiated Electromagnetic Showers in Lead Glass,” *Nucl. Instrum. Meth.*, vol. 128, p. 283, 1975.
- [21] L. Landau, “On the energy loss of fast particles by ionization,” *J.Phys.(USSR)*, vol. 8, pp. 201–205, 1944.
- [22] P. Vavilov, “Ionization losses of high-energy heavy particles,” *Sov.Phys.JETP*, vol. 5, pp. 749–751, 1957.
- [23] G. Bayatian *et al.*, “CMS physics: Technical design report,” 2006.
- [24] C. Fabjan *et al.*, “Iron Liquid-argon and Uranium Liquid-argon Calorimeters for Hadron Energy Measurement,” *Nucl. Instrum. Meth.*, vol. 141, p. 61, 1977.
- [25] I. Park, “Experience with the ZEUS Calorimeter,” in *Proc. Beijing Calorimetry Symposium*, Beijing, China, Oct. 1994.
- [26] T. Akesson *et al.*, “Properties of a Fine Sampling Uranium-copper Scintillator Hadron Calorimeter,” *Nucl. Instrum. Meth.*, vol. A241, p. 17, 1985.
- [27] T. Akesson *et al.*, “Performance of the Uranium / Plastic Scintillator Calorimeter for the Helios Experiment at CERN,” *Nucl. Instrum. Meth.*, vol. A262, p. 243, 1987.
- [28] P. Adzic *et al.*, “Energy Resolution of the Barrel of the CMS Electromagnetic Calorimeter,” *JINST*, vol. 2, p. P04004, 2007.
- [29] D. Froidevaux and P. Sphicas, “General-purpose detectors for the Large Hadron Collider,” *Ann.Rev.Nucl.Part.Sci.*, vol. 56, pp. 375–440, 2006.
- [30] N. Akchurin, F. Bedeschi, A. Cardini, M. Cascella, G. Ciapetti *et al.*, “Detection of electron showers in dual-readout crystal calorimeters,” *Nucl. Instrum. Meth.*, vol. A686, pp. 125–135, 2012.
- [31] S. Chatrchyan *et al.*, “Determination of Jet Energy Calibration and Transverse Momentum Resolution in CMS,” *JINST*, vol. 6, p. P11002, 2011.

- [32] R. Kogler, “Measurement of jet production in deep-inelastic e-p scattering at HERA,” Ph.D. dissertation, University of Hamburg, 2011, DESY-THESIS-2011-003.
- [33] V. L. Morgunov, “Calorimetry Design with Energy-flow Concept (Imaging Detector for High-energy Physics),” in *Proc. Tenth International Conference Pasadena*, California, Mar. 2002.
- [34] M. A. Thomson, “Particle Flow Calorimetry and the PandoraPFA Algorithm,” *Nucl. Instrum. Meth.*, vol. A611, pp. 25–40, 2009.
- [35] S. Morozov, “To be announced,” Ph.D. dissertation, University of Hamburg, 2014.
- [36] C. Adloff *et al.*, “Construction and Commissioning of the CALICE Analog Hadron Calorimeter Prototype,” *JINST*, vol. 5, p. P05004, 2010.
- [37] C. Lam, “Interactions of Particles with Momenta of 1-10 GeV in a Highly Granular Hadronic Calorimeter with Tungsten Absorbers,” Master’s thesis, Universiteit Twente, 2012. [Online]. Available: <http://essay.utwente.nl/63783/>
- [38] “Pdg atomic and nuclear properties of materials.” [Online]. Available: <http://pdg.lbl.gov/2011/AtomicNuclearProperties/>
- [39] P. Buzhan, B. Dolgoshein, A. Ilyin, V. Kantserov, V. Kaplin *et al.*, “An advanced study of silicon photomultiplier,” *ICFA Instrum.Bull.*, vol. 23, pp. 28–41, 2001.
- [40] D. Renker and E. Lorenz, “Advances in solid state photon detectors,” *JINST*, vol. 4, p. P04004, 2009.
- [41] E. Garutti, M. Groll, A. Karakash, and S. Reiche, “Magnetic field dependence studies for silicon photomultiplier,” 2004, LC-DET-2004-025.
- [42] P. La Rocca and F. Riggi, “The upgrade programme of the major experiments at the Large Hadron Collider,” *J.Phys.Conf.Ser.*, vol. 515, p. 012012, 2014.
- [43] N. Feege, “Silicon Photomultipliers: Properties and Application in a Highly Granular Calorimeter,” Master’s thesis, University of Hamburg, 2008, DESY-THESIS-2008-050.
- [44] M. Groll, “Construction and Commissioning of a Hadronic Test-Beam Calorimeter to Validate the Particle-Flow Concept at the ILC,” Ph.D. dissertation, University of Hamburg, 2007, DESY-THESIS-2007-018.
- [45] N. Wattimena, “Commissioning of an LED Calibration and Monitoring System for a Prototype of a Hadronic Calorimeter,” Master’s thesis, University of Hamburg, 2006, DESY-THESIS-2006-039.
- [46] D. Dannheim, W. Klempt, and E. van der Kraaij, “Beam tests with the calice tungsten analog hadronic calorimeter prototype,” Apr 2012, LCD-Note-2012-002.
- [47] The Fermilab Test Beam Facility. [Online]. Available: <http://www-ppd.fnal.gov/FTBF>

- [48] B. Lang *et al.*, “The Use of Cerenkov Counters at MTEST,” 2004. [Online]. Available: http://www-ppd.fnal.gov/FTBF/Facility/Inst_Cerenkov/cc_mtest.pdf
- [49] J. Litt and R. Meunier, “Cerenkov Counter Technique in High-energy Physics,” *Ann. Rev. Nucl. Part. Sci.*, vol. 23, pp. 1–44, 1973.
- [50] L. Durieu, O. Ferrando, J. Hemery, J. Riunaud, and B. Williams, “The CERN PS east area in the LHC era,” *Conf.Proc.*, vol. C970512, pp. 228–230, 1997.
- [51] S. Agostinelli *et al.*, “GEANT4: A Simulation Toolkit,” *Nucl. Instrum. Meth.*, vol. A506, pp. 250–303, 2003.
- [52] Mokka - a GEANT4 Application to Simulate the Full ILD Geometry. [Online]. Available: <http://polzope.in2p3.fr:8081/MOKKA>
- [53] V. Ivanchenko *et al.*, “Recent Improvements in GEANT4 Electromagneticx Physics Models and Interfaces,” in *Proc. Joint International Conference on Supercomputing in Nuclear Applications and Monte Carlo 2010*, 2010.
- [54] A. Heikkinen *et al.*, “Bertini Intra-nuclear Cascade Implementation in GEANT4,” in *Proc. Computing in High-energy and Nuclear Physics (CHEP 03)*, 2003.
- [55] J. Wellisch and G. Folger, “The Binary Cascade,” in *Proc. Computing in High-energy and Nuclear Physics (CHEP 04)*, 2005.
- [56] G. Folger and J. Wellisch, “String Parton Models in GEANT4,” in *Proc. Computing in High-energy and Nuclear Physics (CHEP 03)*, 2003.
- [57] J. Apostolakis *et al.*, “Validation of GEANT4 Hadronic Models Using CALICE Data,” EUDET-MEMO-2010-15.
- [58] H. Fesefeldt, “The Simulation of Hadronic Showers: Physics and Applications,” 1985, PITHA-85-02.
- [59] J. M. Quesada, “Recent Developements in Pre-equilibrium and De-excitation Models in GEANT4,” in *Proc. Monte Carlo Conference (MC 10)*, 2010.
- [60] A. Ribbon *et al.*, “Status of GEANT4 Hadronic Physics for the Simulation of LHC Experiments at the Start of LHC Physics Program,” CERN-LCGAPP-2010-02.
- [61] B. Lutz, “Commissioning of the Readout Electronics for the Prototypes of a Hadronic Calorimeter and a Tailcatcher and Muon Tracker,” Master’s thesis, University of Hamburg, 2006, DESY-THESIS-2006-038.
- [62] N. Wattimena, “Calorimetry at the International Linear Collider: From Simulation to Reality,” Ph.D. dissertation, University of Hamburg, 2009, DESY-THESIS-2010-006.
- [63] A. Lucaci-Timoce, “Shower development of particles with momenta from 1 to 10 gev in the calice scintillator-tungsten hcal,” May 2012, CAN-036.
- [64] V. Morganov, “Itep activity on hcal prototype cassette mass production,” Talk given at ECFA Workshop 2004, Durham, UK.

- [65] S. Laurien, private communication.
- [66] C. Adloff *et al.*, “Track segments in hadronic showers in a highly granular scintillator-steel hadron calorimeter,” 2013.
- [67] B. Lutz, “Hadron Showers in a Highly Granular Calorimeter,” Ph.D. dissertation, University of Hamburg, 2010, DESY-THESIS-2010-048.
- [68] M. Nakao *et al.*, “Measurement of the $B \rightarrow K^*$ gamma branching fractions and asymmetries,” *Phys. Rev.*, vol. D69, p. 112001, 2004.
- [69] Marlin - Modular Analysis and Reconstruction for the Linear Collider. [Online]. Available: <http://ilcsoft.desy.de/marlin>
- [70] A. Lucaci-Timoce, “HCAL Prototype in the Test Beam Mokka Model.” [Online]. Available: <http://www.desy.de/~lucaci/Others/hcalTBeam.pdf>
- [71] J. B. Birks, *The Theory and Practice of Scintillation Counting*, 1st ed. Macmillan, 1964.
- [72] M. Hirschberg *et al.*, “Precise Measurement of Birks kB Parameter in Plastic Scintillators,” *IEEE Trans. Nucl. Sci.*, vol. 39, pp. 511–514, 1992.
- [73] S. Aplin, J. Engels, F. Gaede, N. A. Graf, T. Johnson *et al.*, “LCIO: A Persistency Framework and Event Data Model for HEP,” *IEEE Trans. Nucl. Sci.*, vol. 60, pp. 2075–2079, 2013.
- [74] S. Richter, “Validation of the Calibration Procedure for a Highly Granular Calorimeter with Electromagnetic Processes,” Master’s thesis, University of Hamburg, 2008.
- [75] C. Adloff *et al.*, “Hadronic energy resolution of a highly granular scintillator-steel hadron calorimeter using software compensation techniques,” *JINST*, vol. 7, p. P09017, 2012.

ACKNOWLEDGEMENTS

I would like to thank Prof. Dr. Erika Garutti and Dr. Felix Sefkow for giving me the opportunity to write my thesis in such an interesting and supporting environment and for the numerous tips, discussions and suggestions and the invested time and effort. I would also like to thank especially Felix for his constant support and fairness.

In addition I would like to thank Prof. Dr. Eckhard Elsen and Prof. Dr. Johannes Haller for examining my thesis and Dr. Georg Steinbrück for chairing my disputation. I am also thankful for the helpful suggestions and discussions with my mentors Dr. Karsten Büscher and Dr. Marcel Stanitzki.

I am obliged to Dr. Mark Terwort and Dr. Katja Krüger for all the time they have invested, their guidance, the discussion, their suggestions, their motivation and the things I have learned from them over the years. And a special thanks to Katja for all the corrections. Most likely I would have never succeeded in finishing the thesis without the support of you two.

Throughout the last years it has been my pleasure to be part of the DESY FLC group and I would like to thank my group leader Dr. Ties Behnke and my colleagues for this great experience. I would like to thank Dr. Vassily Morgunov for his helpful tips and discussions, Dr. Shaojun Lu for his endless patience in fixing software problems and for the fruitful physics discussions. A similar amount of credit goes to Sergey Morozov for his never ending motivation to fix problems. I would also like to thank Ralf Diener for the numerous times he helped me and for the nice conversations. A special thanks goes to our secretaries Ramona Matthes and Andrea Schrader.

I would like to thank the members of the CERN Linear Collider Group from Dr. Lucie Linsen, especially Angela, Astrid, Christian, Erik, Dieter, Dominik, Martin, Stephane and Wolfgang, for the support and excellent teamwork, as well as for the warm welcome and the nice time during my visits at CERN.

Being part of the CALICE Collaboration has been a valuable, interesting, and enjoyable experience. I would like to thank the collaboration members for this experience, especially Marco, Sebastian, Lars, Christian, Frank, Katsu, Marina, Ivo, Jaroslav and Jiri.

Finally, I would like to express my gratitude towards my family, especially my parents, for their constant strong support over the years and to my friends for their patience, and especially Dr. Henning Gutzmann for the corrections.